Université Joseph Fourier - Grenoble I

Diplôme d'habilitation à diriger des recherches

présenté par

Pierre SARAMITO

Ingénieur ENSIMAG

Chargé de Recherche 1re classe au CNRS

Algorithmes et logiciels pour la simulation numérique en fluides non-newtoniens

soutenu le 21 février 2002 devant le jury composé de

Emil HOPFINGER	Président
Pierre ALART	Rapporteur
Roland GLOWINSKI	Rapporteur
Jean-Claude SAUT	Rapporteur
Georges-Henri COTTET	Examinateur
Claude VERDIER	Examinateur

Laboratoire de Modélisation et de Calcul (UMR 5523, CNRS - INPG - UJF)

Remerciements

Je tiens à adresser mes plus vifs remerciements aux membres de mon jury : Pierre Alart, Roland Glowinski et Jean-Claude Saut qui ont accepté d'être mes rapporteurs, ainsi que Georges-Henri Cottet, Emil Hopfinger et Claude Verdier que je remercie pour l'intérêt qu'ils portent à mes travaux

Les travaux décrits dans ce mémoire se développent actuellement au sein de l'équipe Équations aux Dérivées Partielles du Laboratoire de Modélisation et de Calcul de Grenoble. Je tiens à remercier encore Georges-Henri Cottet, chef d'équipe, pour l'accueil dans son équipe, ainsi que Jacques Blum, alors directeur de laboratoire, Alain Le Breton, directeur actuel, François-Xavier Le Dimet, responsable du projet INRIA IDOPT et Jean-Claude Paumier, responsable du projet IMAG SIGMAS. Ils m'ont offert un environnement scientifique idéal, très enrichissant et ouvert.

Je remercie chaleureusement les étudiants dont je dirige ou ai dirigé les recherches, et qui ont contribué à ces travaux, en particulier Jocelyn Etienne et Nicolas Roquet.

Un grand merci à Brigitte Bidegaray, Christine et Eugène Kazantsev ainsi que Laurence Viry pour leur aide et le soutien qu'ils m'ont apportés.

Table des matières

1 Introduction

Ce document correspond à onze ans de recherche, dont quatre dans le secteur privé et sept au Centre National de la Recherche Scientifique. Les sujets abordés, qui peuvent *a priori* sembler disparates, sont tous liés à la modélisation numérique, et les applications concernent principalement les matériaux non-newtoniens.

Après ma thèse de troisième cycle (1990) sur la simulation numérique des écoulements de fluides viscoélastiques (modèle d'OLDROYD), j'ai étendu la méthode proposée à d'autres modèles (modèles de PHAN-THIEN et TANNER, § 2), ce qui m'a conduit à obtenir des résultats sur le comportement asymptotique aux grands nombres de WEISSENBERG pour ce type de modèles. Ceci représentait à cette époque une véritable performance, qui n'a, à ma connaissance, encore aujourd'hui été relevée que par une autre équipe de recherche (Louvain-La-Neuve, CROCHET et MARCHAL), et ce, en mobilisant de très gros ordinateurs pendant des temps non-négligeables. En parallèle, je travaillais à la société CISI (compagnie internationale de services informatiques, aujourd'hui compagnie des signaux) sur la simulation de l'injection des matières plastiques dans les moules, dans le cadre du projet CLIP (club des logiciels de l'industrie plastique) soutenu par le ministère de la recherche et des entreprises concernées telles que Peugeot, Renault, Rhône-Poulenc, ... J'ai aussi eu l'occasion d'intervenir à CISI sur d'autres projets : la simulation de l'écoulement d'air autour des essieux de TGV ou la climatisation dans les wagons. J'y ai également initié un projet de recherche sur la génération de maillages en dimension trois.

En 1993, j'ai rejoint la société SGS-Thomson (aujourd'hui ST-microelectronics) dans sa division recherche et développement. Dans le cadre des recherches sur la simulation, la vérification et la synthèse des circuits intégrés, j'ai collaboré à des programmes de recherche européens ESPRIT 5075 (Philips, SGS-Thomson) et JESSI-AC3 (Bosch, CNET, SGS-Thomson) sur le sujet. J'ai diversifié mes activités en appliquant à ces problèmes certaines méthodes issues de la mécanique, et gagnant un sens de la conception des gros logiciels, ainsi que, par de nombreux voyages, une meilleure connaissance de l'Europe de l'informatique. Les outils logiciels que j'y ai réalisés continuent encore aujourd'hui à se développer et à évoluer dans la société depuis mon départ.

En effet, dans la même période, je candidatais au CNRS que je rejoignais à l'automne 1994 sur le thème de la modélisation numérique des matériaux en grandes

déformations : viscoélasticité, viscoplasticité, surfaces libres et tensions capillaires, et j'intégrais le laboratoire de rhéologie, récemment cré. Je développais avec la société GIST (groupement informatique scientifique et technique) et Richard MICHEL, ingénieur responsable des recherches dans cette société, une collaboration de recherche sur le thème des logiciels de simulation en viscoplasticité.

Dans le même temps, je répondais à l'invitation des professeurs Roland GLOWINSKI et Daniel D. JOSEPH, et partais pour un séjour de quatre mois aux États-Unis (Minneapolis, puis Philadelphie). Dans le cadre du projet de la National Science Foundation « *simulation directe des écoulements contenant des particules* », j'intervenais sur le « volet viscoélastique » du projet. Je voudrais souligner la richesse scientifique du projet, tant sur la mécanique des fluides non-newtoniens que sur le traitement numérique du problème. De plus, j'y nouais également de nombreux contacts et une meilleure connaissance de l'informatique parallèle et de la manipulation informatique des grandes matrices creuses.

De retour en France début 1997, je retrouvais aussi les questions de viscoplasticité, où Nicolas ROQUET, embauché par la société GIST sur une bourse CIFRE, démarrait sa thèse sur les fluides de type BINGHAM. Ce problème posait de véritables défis aux méthodes numériques, aucune méthode ne semblant « marcher » correctement en pratique, bien que toutes les méthodes proposées étaient justifiées par de solides résultats théoriques. Sa thèse s'orientera assez vite vers une approche algorithmique de type Lagrangien augmenté, combinée avec une adaptation énergique des maillages afin de capturer les zones rigides (§ 3).

Sur le thème voisin des écoulements de boue et débris en montagne (appelées aussi laves torrentielles), j'intervenais dans le cadre d'un programme européen sur les risques naturels. En effet, ces écoulements de débris peuvent être modélisés par des fluides à seuil avec surface libre, les équations étant alors moyennées dans l'épaisseur, avec une approche de type SAINT-VENANT.

Je quittais le laboratoire de rhéologie pour commencer à travailler début 2000 au laboratoire de modélisation et de calcul (LMC), où Jacques BLUM, directeur du laboratoire, me proposait un environnement et des moyens très propices au développement de mes activités de simulation numérique, notamment sur le projet SIGMAS de l'IMAG, avec les professeurs Jean-Claude PAUMIER, Ioan IONESCU et Annie RAOULT, et le projet IDOPT de l'INRIA, avec Jérôme MONNIER, maître de conférences. J'y découvrais un laboratoire de grande taille, où des équipes de mathématiciens, mécaniciens et informaticiens collaboraient de façon étroite. Nicolas ROQUET m'y rejoignait d'ailleurs très bientôt et soutenait[1] dans la même année une thèse sur la viscoplasticité. Il y présentait une quantification théorique des gains obtenus par l'utilisation des maillages adaptés. L'argument, entièrement

1. co-encadrement avec Jean-Claude PAUMIER, professeur à l'Université Joseph FOURIER.

nouveau, s'appuie sur une estimation *a priori* de l'erreur. En effet, ce type d'argument est généralement utilisé en maillages quasi-uniformes, les estimateurs locaux (ou *a posteriori*) étant habituellement utilisés en maillages adaptés. Cet argument était illustré par de nombreux exemples concrets de calcul. Une fois sa thèse soutenue, Nicolas ROQUET a rejoint la société UNILEVER, dans le cadre d'un programme européen et sur le thème de la simulation numérique de matériaux non-newtoniens pour l'agroalimentaire.

Les méthodes et logiciels développés dans le cadre de la viscoplasticité se prêtent à une généralisation assez naturelle à de nombreux autres problèmes, notamment ceux pouvant également se formuler en terme d'inéquations variationnelles, et, comme l'a fait remarquer Roland GLOWINSKI à l'occasion d'une publication, ceux traitant d'analyse d'image. Ces logiciels sont depuis 2001 entièrement accessibles par le réseau internet à l'ensemble de la communauté scientifique (§ 4). Une application à des problèmes d'avalanche (modèles de type granulaire) est actuellement à l'étude (§ 5).

2 Fluides viscoélastiques

Pour les fluides viscoélastiques à loi de comportement de type OLDROYD [Old50], le tenseur des contraintes totales de CAUCHY σ_{tot} est donné par :

$$\sigma_{tot} = -pI + 2\eta_1 D(u) + \tau$$

où p est la pression hydrostatique, $\mathbf{u}$ le champ des vitesses, $D(\mathbf{u}) = (\boldsymbol{\nabla}\mathbf{u} + \boldsymbol{\nabla}\mathbf{u}^T)/2$ le tenseur des taux de déformation, et $\eta_1 > 0$ une première viscosité. Le tenseur τ des contraintes supplémentaires satisfait une loi de comportement de type différentiel :

$$\lambda \overset{\square}{\tau} + \tau - 2\eta_2 D(\mathbf{u}) = 0 \tag{1}$$

où λ est le temps de relaxation, $\eta_2 \geq 0$ est une seconde viscosité et $\overset{\square}{\tau}$ est une notation pour la dérivée d'OLDROYD du tenseur τ :

$$\overset{\square}{\tau} = \frac{\partial \tau}{\partial t} + \mathbf{u}.\nabla\tau + W(\mathbf{u})\tau - \tau W(\mathbf{u}) - a\,(D(\mathbf{u})\tau + \tau D(\mathbf{u}))$$

où $W(\mathbf{u}) = (\nabla\mathbf{u} - \nabla\mathbf{u}^T)/2$ est le tenseur de vorticité et $a \in [-1, 1]$ est un paramètre de la dérivée d'OLDROYD. La loi de comportement (1) est couplée aux équations de conservation de la quantité de mouvement et de la masse :

$$\rho\left(\frac{\partial \mathbf{u}}{\partial t} + \mathbf{u}.\nabla\mathbf{u}\right) - \mathbf{div}\,\tau - \eta_1\Delta\mathbf{u} + \boldsymbol{\nabla}p = \mathbf{f} \tag{2}$$

$$\operatorname{div}\mathbf{u} = 0 \tag{3}$$

où ρ est la densité, supposée constante (écoulement incompressible). Les équations (1)-(3) étant posées dans un domaine Ω de $\mathbb{R}^N$, $N = 2, 3$, le problème aux inconnues $(\tau, \mathbf{u}, p)$ est complété par des conditions aux limites sur $\mathbf{u}$, sur le bord entrant pour τ, ainsi que des conditions initiales pour $\mathbf{u}$ et τ. Lorsque la frontière du domaine est régulière et les données assez petites, Collette GUILOPPÉ et Jean-Claude SAUT ont montré [GS87] l'existence globale de solutions.

Le cas limite $\lambda = 0$ correspond à un fluide newtonien. Pour $\lambda > 0$, ce modèle permet de décrire des solutions de polymère dans un solvant newtonien ou bien des mélanges de polymères. Cette loi peut s'étendre à d'autres modèles différentiels, tels que le modèle de PHAN-THIEN et TANNER [PTT77], de GIESEKUS [Gie82]. Par ailleurs ces résultats peuvent s'étendre à plusieurs temps de relaxation. Ce problème fait apparaître trois nombres sans dimension : We le nombre de WEISSENBERG, Re le nombre de REYNOLDS, ainsi que le paramètre $\alpha = \eta_2/(\eta_1 + \eta_2) \in]0, 1]$.

2.1 Algorithme par décomposition d'opérateur

Afin de simplifier l'analyse de la méthode numérique proposée, je supposerais l'écoulement lent, et négligerais dans la suite le terme d'inertie $\mathbf{u}.\nabla\mathbf{u}$ dans (2). Il s'agit d'une hypothèse classique dans ce type de simulation; la difficulté du problème porte désormais sur la non-linéarité dans l'équation (1) de la dérivée d'OLDROYD.

L'idée directrice consiste à séparer les termes de viscosité des termes de transport. On se ramène ainsi à résoudre deux sous-problèmes plus simples, l'un de type STOKES, l'autre de type transport du tenseur des contraintes supplémentaires. Le problème peut se mettre sous la forme :

(P): trouver $\mathcal{U} = (\tau, \mathbf{u})$ tel que :

$$S\frac{d\mathcal{U}}{dt} + A(\mathcal{U}) = \mathcal{F} \quad \text{et} \quad \mathcal{U}(0) = \mathcal{U}_0$$

où $S = \text{diag}\,(We, Re)$, $\mathcal{F} = (0, f)^t$, $\mathcal{U}_0 = (\tau_0, \mathbf{u}_0)^t$ et $A(\mathcal{U}) = A_1(\mathcal{U}) + A_2(\mathcal{U}; \mathcal{U})$ est donné par la décomposition suivante :

$$A_1(\tau, \mathbf{u}) = \begin{bmatrix} \nu\tau & - & 2\alpha D(\mathbf{u}) \\ -\text{div}\,\tau & - & (1-\alpha)P\Delta\mathbf{u} \end{bmatrix} \quad ; \quad A_2(\sigma, \mathbf{v}; \tau, \mathbf{u}) = \begin{bmatrix} \nu'\tau + We\,\mathrm{T}(\mathbf{v})\tau \\ 0 \end{bmatrix}$$

où $\nu' = 1 - \nu$ et $\nu \in [0, 1]$ est un paramètre de la décomposition et $P\Delta$ représente l'opérateur de STOKES. Dans la décomposition précédente, $\mathrm{T}(\mathbf{v})$ désigne l'opérateur de transport : $\mathrm{T}(\mathbf{v})\tau = \mathbf{v}.\nabla\tau + + W(\mathbf{v})\tau - \tau W(\mathbf{v}) - a\,(D(\mathbf{v})\tau + \tau D(\mathbf{v}))$.

Inspiré par les travaux de GLOWINSKI [Glo86] sur les équations de NAVIER-STOKES, introduisons à présent la semi-approximation de (P). Soit $\Delta t > 0$ un

pas de temps et θ un paramètre, $\theta \in]0, \frac{1}{2}[$. Considérons les notations $\theta' = 1 - 2\theta$, $\mathcal{U}^0 = \mathcal{U}_0$ et $\mathcal{U}^{n+\delta} \approx \mathcal{U}((n+\delta)\Delta t)$. Puisque A_1 et A_2 sont plus simples que A, utilisons cette décomposition pour résoudre (P) par le θ-schéma :

$$\frac{S\mathcal{U}^{n+\theta} - S\mathcal{U}^n}{\theta\Delta t} + A_1(\mathcal{U}^{n+\theta}) + A_2(\mathcal{U}^n; \mathcal{U}^n) = \mathcal{F}^{n+\theta} \quad (4)$$

$$\frac{S\mathcal{U}^{n+1-\theta} - S\mathcal{U}^{n+\theta}}{\theta'\Delta t} + A_1(\mathcal{U}^{n+\theta}) + A_2(\mathcal{U}^n; \mathcal{U}^{n+1-\theta}) = \mathcal{F}^{n+1-\theta} \quad (5)$$

$$\frac{S\mathcal{U}^{n+1} - S\mathcal{U}^{n+1-\theta}}{\theta\Delta t} + A_1(\mathcal{U}^{n+1}) + A_2(\mathcal{U}^n; \mathcal{U}^{n+1-\theta}) = \mathcal{F}^{n+1} \quad (6)$$

La résolution de (4) et (6) se réduit à celle d'un problème de type STOKES, et la résolution de (5), à celle d'un problème de type transport pour l'opérateur $I + \varepsilon\,\mathrm{T}(\mathbf{v})$, avec $\varepsilon > 0$. Cet algorithme se programme bien en pratique, et a fait l'objet de nombreuses publications [1, 20, 4, 5, 21, 6, 8, 14].

2.2 Un élément fini ultra-léger

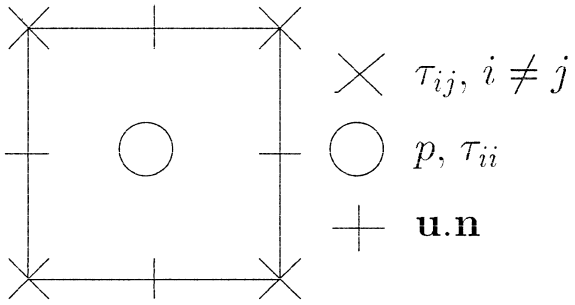

FIG. 1 – *Élément fini ultra-léger pour le problème de* STOKES *à trois champs.*

J'ai ensuite proposé une nouvelle méthode d'éléments finis mixtes pour approcher ce problème en espace. Cette méthode a l'avantage de n'utiliser que très peu de degrés de liberté pour un maillage donné : environ dix fois moins que les méthodes d'approximation proposées précédemment par l'équipe de CROCHET et MARCHAL [CM87] ou par FORTIN et FORTIN [FF89]. Il s'agit d'une combinaison de l'élément mixte de RAVIART et THOMAS [GR86] pour les vitesses-pressions, d'une approximation P_0 discontinue pour les composantes normales τ_{ii} des contraintes et d'une approximation continue et linéaire pour les composantes de cisaillement τ_{ij}, $i \neq j$. (voir FIG. 1). J'ai aussi montré que cette combinaison d'éléments satisfaisait deux conditions de BREZZI-BABUSKĂ [Bre74], conditions

nécessaires et suffisantes pour que le problème soit bien posé pour $We = 0$ et que la solution correspondante converge lorsque le pas du maillage tend vers zéro (voir aussi [BS92] pour l'élément proposé par FORTIN et FORTIN).

D'autre part, il était nécessaire de décentrer les termes de transport des contraintes $\mathbf{u}.\nabla\tau$. Pour les composantes normales τ_{ii}, approchées par un élément discontinu, j'utilisais la méthode de LESAINT et RAVIART tandis que le schéma de volumes finis de BABA et TABATA était approprié pour les composantes de cisaillement. Ces deux choix conduisent à des schémas décentrés monotones[2]. Cette propriété assure en particulier que les solutions approchées ne présenteront pas d'oscillations parasites. Je remarquais l'article de 1988 de GOODMAN [GL88] qui montrait que la méthode SUPG proposée par HUGHES et BROOKS [BH82] ne vérifiait pas cette hypothèse. De plus, les travaux de 1987 de CROCHET et MARCHAL [CM87] utilisant cette méthode présentaient des solutions avec oscillations parasites près des coins ré-entrants, dans le cas d'un écoulement en contraction brusque, où la solution est singulière.

Cet élément permettait alors de résoudre le problème sur des ordinateurs possédant une taille de mémoire modeste, ce qui n'avait pas été le cas jusqu'alors. Ceci a donné lieu a plusieurs publications [1, 4, 6]. La combinaison d'un algorithme robuste et d'un élément fini très économique a permis d'obtenir pour la première fois les comportements asymptotiques des modèles de PHAN-THIEN et TANNER, comme nous allons le voir dans le paragraphe suivant.

2.3 Propriétés élongationnelles et recirculations

Le problème-test de l'écoulement viscoélastique en contraction brusque possède l'avantage de mettre en évidence le comportement du modèle sur une très large gamme de taux de déformation: l'écoulement est élongationnel le long de l'axe et cisaillé près des parois. De plus, la singularité dûe au coin ré-entrant sollicite le modèle dans la plage des très grandes déformation et contraintes. Après avoir réalisé un logiciel pour un modèle viscoélastique d'OLDROYD (relation (1)), je l'ai étendu au modèle viscoélastique proposé par PHAN-THIEN et TANNER [PTT77, Lar88] :

$$\lambda \overset{\square}{\tau} + (1 + \varepsilon \mathrm{tr}\,\tau)\,\tau - 2\eta_2 D(\mathbf{u}) = 0$$

où $\varepsilon \geq 0$ est un paramètre du modèle. Ce modèle a l'avantage de prédire, pour un écoulement en élongation simple, une viscosité élongationnelle croissante [6, p. 203] et présentant un plateau, analogue à ce qui est observé pour les solutions de polymères. Les maillages utilisés sont donnés FIG. 2. La FIG. 3 présente la

2. en anglais, on dit aussi TVD, pour Total Variation Decreasing.

branche de solution pour des valeurs croissantes du nombre de WEISSENBERG, ce pour une contraction à géométrie axisymétrique. Ce calcul met clairement en

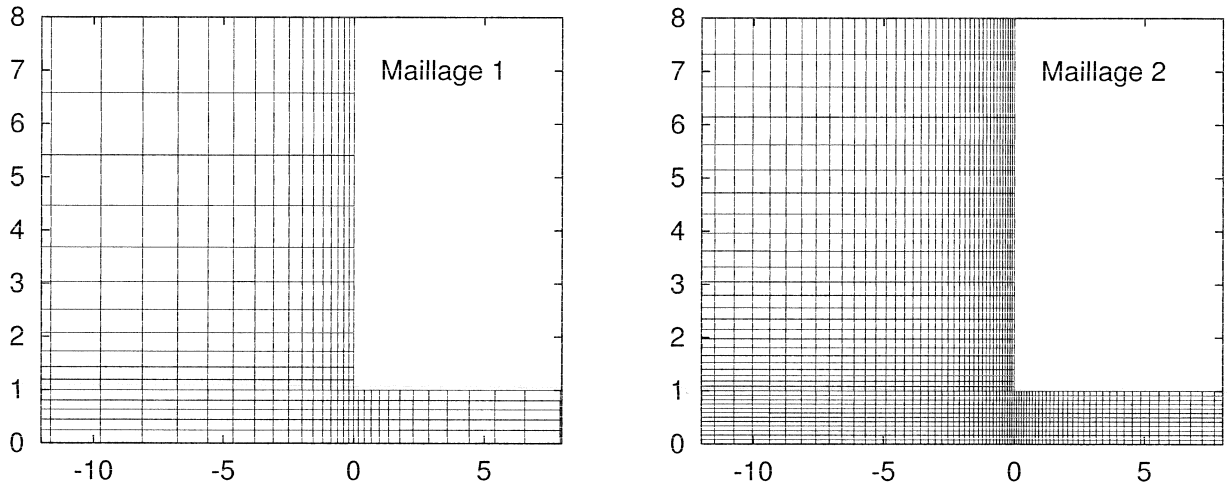

FIG. 2 – *Vue partielle des maillages pour la contraction brusque.*

évidence le développement d'une zone de recirculation située dans la partie amont de l'écoulement, cette zone tendant asymptotiquement vers une taille maximale (FIG. 3.d) pour les grandes valeurs de We. J'ai ensuite étudié une variante du modèle précédent :

$$\lambda \overset{\square}{\tau} + \exp(\varepsilon \operatorname{tr} \tau)\, \tau - 2\eta_2 D(\mathbf{u}) = 0$$

Ce modèle prédit une viscosité élongationnelle passant par un maximum puis décroissant [6, p. 203], ce qui correspond bien aux mélanges de polymères. Dans ce cas, la simulation prédit des zones de recirculation passant par un maximum, puis décroissant ensuite pour se résorber asymptotiquement aux grands WEISSENBERG. Ce travail met donc clairement en évidence les mécanismes de développement des recirculations et leur corrélation avec les propriétés élongationnelles du matériau, et a été poursuivi en étudiant la correction de COUETTE (perte de pression due à la contraction) pour les différentes variantes. Ceci a donné lieu aux publications [6, 7, 13, 14, 15].

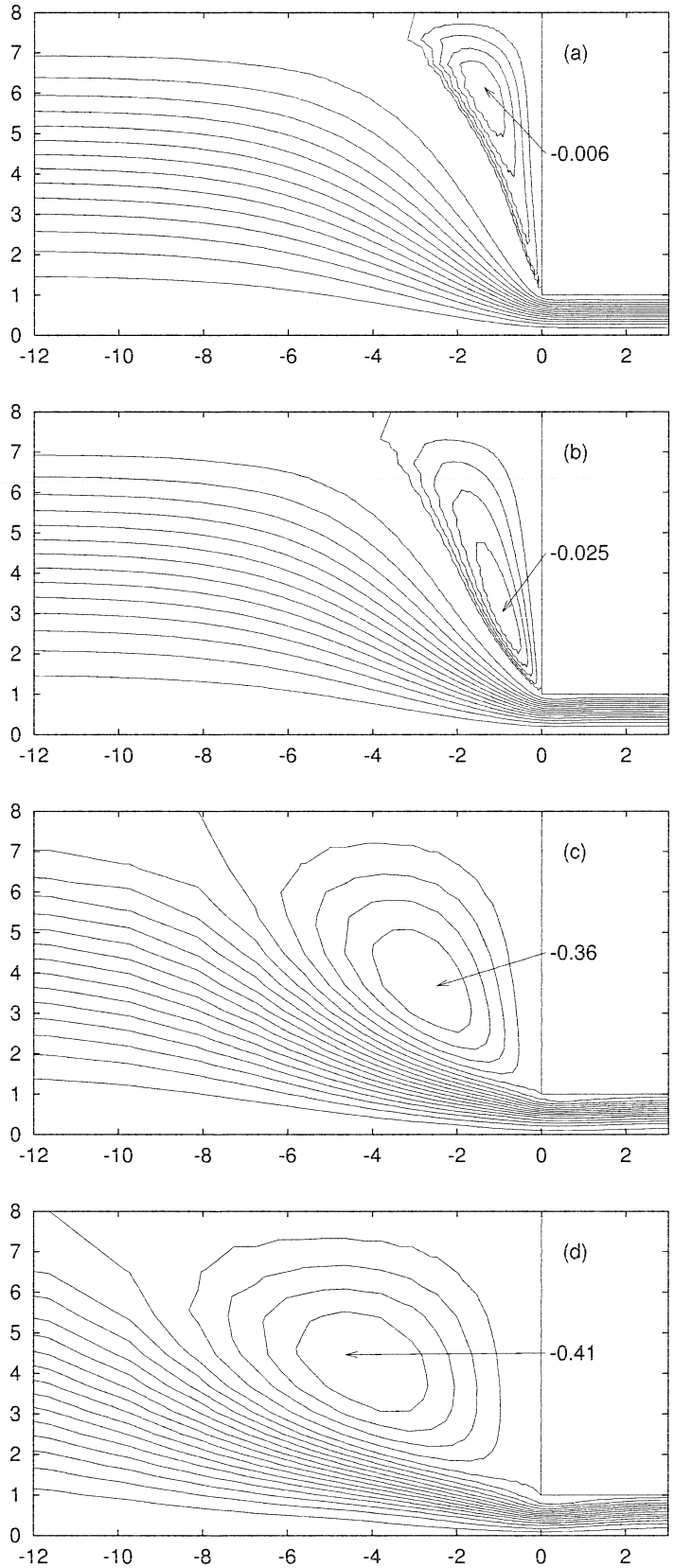

FIG. 3 – *Modèle de* PHAN-THIEN *et* TANNER *avec* $\varepsilon = 5 \times 10^{-4}$*: (a)* $We = 2.0$*; (b)* $We = 4.6$*; (c)* $We = 14$*; (d)* $We = 69$.

3 Fluides à seuil

Mon travail sur la simulation numérique pour les fluides viscoplastique à conduit à l'encadrement d'une thèse [49], de deux sujets de DEA [43, 46], un projet de fin d'études de l'ENSHMG [45] et de deux sujets de DESS [44, 47]. Ce travail a fait l'objet de nombreux rapports et publications [9, 10, 16, 17, 31, 32, 38, 39, 28, 29, 30]. Aussi j'ai choisi de présenter ici un résultat correspondant aux travaux de la thèse de Nicolas ROQUET, qui fait l'objet d'une publication en cours [11].

3.1 Aspect général de l'écoulement

Considérons l'écoulement d'un fluide viscoplastique autour d'un cylindre en mouvement uniforme tel que représenté sur la FIG. 4.

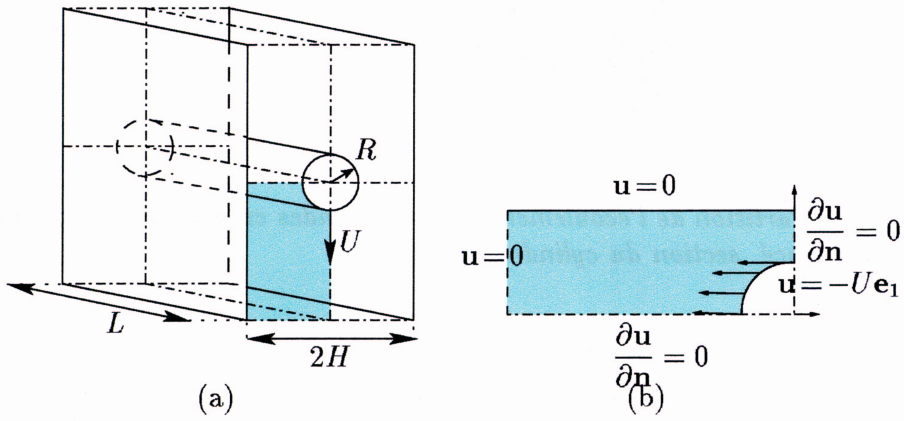

FIG. 4 – *Cylindre se déplaçant à vitesse constante entre deux plaque : (a) vue générale; (b) domaine de calcul.*

Concernant les travaux expérimentaux sur ce problème, on pourra consulter [YA73, BW69]. À notre connaissance, il n'existe pas de travaux de simulation numérique sur ce problème, les seuls travaux voisins existants portent sur le problème de la chute d'une sphère (cas axisymétrique) dans un milieu décrit par un modèle bivisqueux. Le remplacement du modèle de BINGHAM par un modèle bivisqueux induit des difficultés numériques supplémentaires, comme nous l'avons montré dans [10].

L'écoulement est partitionné en deux régions : les **régions rigides** ($D(\mathbf{u}) = 0$) et les **régions déformées** ($D(\mathbf{u}) \neq 0$). Dans notre cas, les régions rigides sont

composées de zones de type différent. Ces zones sont séparées entre elles par la région déformée. Afin d'identifier ces zones et d'en faciliter la compréhension, nous avons introduit une terminologie spécifique (voir aussi FIG. 5) :

- une **zone morte englobante** qui contient la zone déformée;
- deux zones rigides, en forme de **pointe**, situées sur le cylindre, dans l'axe du mouvement, l'une en amont, l'autre en aval, et toutes deux entourées par la zone déformée;
- deux zones ovoïdes, aux extrémités pointues, que nous appellerons **amandes**, à l'intérieur de la zone déformée. Elles sont situées entre le cylindre et la paroi, de part et d'autre du cylindre.

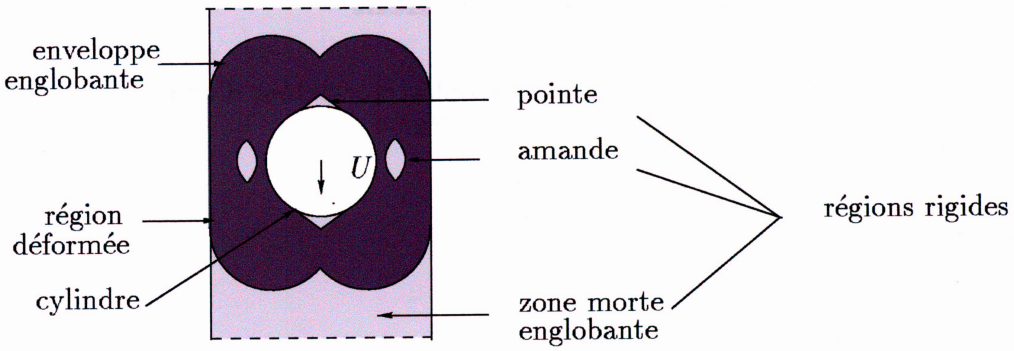

FIG. 5 – *Partition de l'écoulement : régions rigides en gris clair, région déformée en gris foncé, section du cylindre en blanc.*

Par ailleurs, l'enveloppe de la zone déformée autour du cylindre en mouvement est appelée **enveloppe englobante**. Cette enveloppe vient toucher la paroi lorsque celle-ci est assez proche du cylindre. L'existence de l'amande est ici entièrement nouvelle, tandis que les autres zones rigides avaient déjà été mises en évidence dans des travaux expérimentaux antérieurs [YA73, BW69].

3.2 Formulation du problème

Décomposons le tenseur des contraintes totales de CAUCHY suivant :

$$\sigma_{tot} = -p.I + \sigma,$$

où σ désigne sa partie déviatrice et p la pression. L'équation constitutive de BINGHAM [Bin22] s'écrit :

$$\begin{aligned} &\sigma = 2\eta D(\mathbf{u}) + \sigma_0 \frac{D(\mathbf{u})}{|D(\mathbf{u})|} && \text{si } |D(\mathbf{u})| \neq 0, \\ &|\sigma| \leq \sigma_0 && \text{si } |D(\mathbf{u})| = 0, \end{aligned} \tag{7}$$

où $\sigma_0 \geq 0$ est le seuil de contrainte, η la viscosité plastique, et $\mathbf{u}$ la vitesse. La notation $|\tau|$ représente pour tout tenseur τ la norme matricielle : $|\tau| = \sqrt{\tau : \tau}$.

La loi de comportement (7) est couplée aux équations de conservation de la quantité de mouvement et de la masse :

$$\rho\left(\frac{\partial \mathbf{u}}{\partial t} + \mathbf{u}.\nabla\mathbf{u}\right) - \mathbf{div}\,\sigma + \nabla p = 0 \tag{8}$$

$$\mathrm{div}\,\mathbf{u} = 0 \tag{9}$$

où ρ est la densité, supposée constante.

Remarquons que le cas $\sigma_0 = 0$ se ramène à un fluide newtonien incompressible. Pour $\sigma_0 > 0$, les régions rigides commencent à apparaître, et se développent lorsque σ_0 augmente. Les relations (7)-(9) sont complétées par les conditions aux bords indiquées sur la FIG. 4.b, et des conditions initiales. Ce problème fait apparaître deux nombres sans dimension : Bi, le nombre de BINGHAM et Re, le nombre de REYNOLDS. Dans la suite, le terme d'inertie $\mathbf{u}.\nabla\mathbf{u}$ dans (8) sera négligé, l'écoulement étant supposé lent.

3.3 Adaptation de maillage

Ce problème s'inscrit naturellement dans le cadre des inéquations variationnelles [GLT81, KO88], et nous avons utilisé la méthode du Lagrangien augmenté [GT89] combiné avec un algorithme de descente de type UZAWA pour résoudre le système.

Une des difficultés provient du fait que la solution est très peu régulière à la traversée des régions rigides-déformées. Ainsi, l'utilisation de maillages quasi-uniformes de pas h et de l'élément P_2-P_1 (par exemple) en vitesses-pression ne permet pas d'obtenir la précision attendue pour une solution régulière : la convergence est en $\mathcal{O}(h)$ en norme H^1 au lieu de $\mathcal{O}(h^2)$ pour la vitesse.

Pour compenser cela, une stratégie élégante consiste à adapter le maillage à cette perte de régularité. Cette approche présente ici un certain nombre d'avantages :

- les surfaces de transition rigide-déformée sont localisées géométriquement avec plus de précision, le maillage y étant plus fin : $h_{\mathrm{loc}} = \mathcal{O}(h^2)$;
- cela permet de récupérer la convergence globale optimale en $\mathcal{O}(h^2)$, où h est le pas de maillage quasi-uniforme hors du voisinage des surfaces de transitions;
- enfin, le surcoût en terme de nombres d'inconnues est globalement négligeable, le raffinement de maillage étant localisé.

Nous avons montré dans [9] ces affirmations pour l'écoulement d'un fluide de BINGHAM dans un tuyau, et ceci se vérifie encore ici. L'adaptation de maillage est obtenue par un cycle de calcul, représenté sur la FIG. 6. Partant d'un maillage initial, une première résolution est effectuée, à partir de laquelle on génère un premier maillage adapté [Hec97]. Un nouveau calcul est ainsi effectué, et ainsi de suite. Le maillage et la solution convergent assez rapidement vers un point fixe.

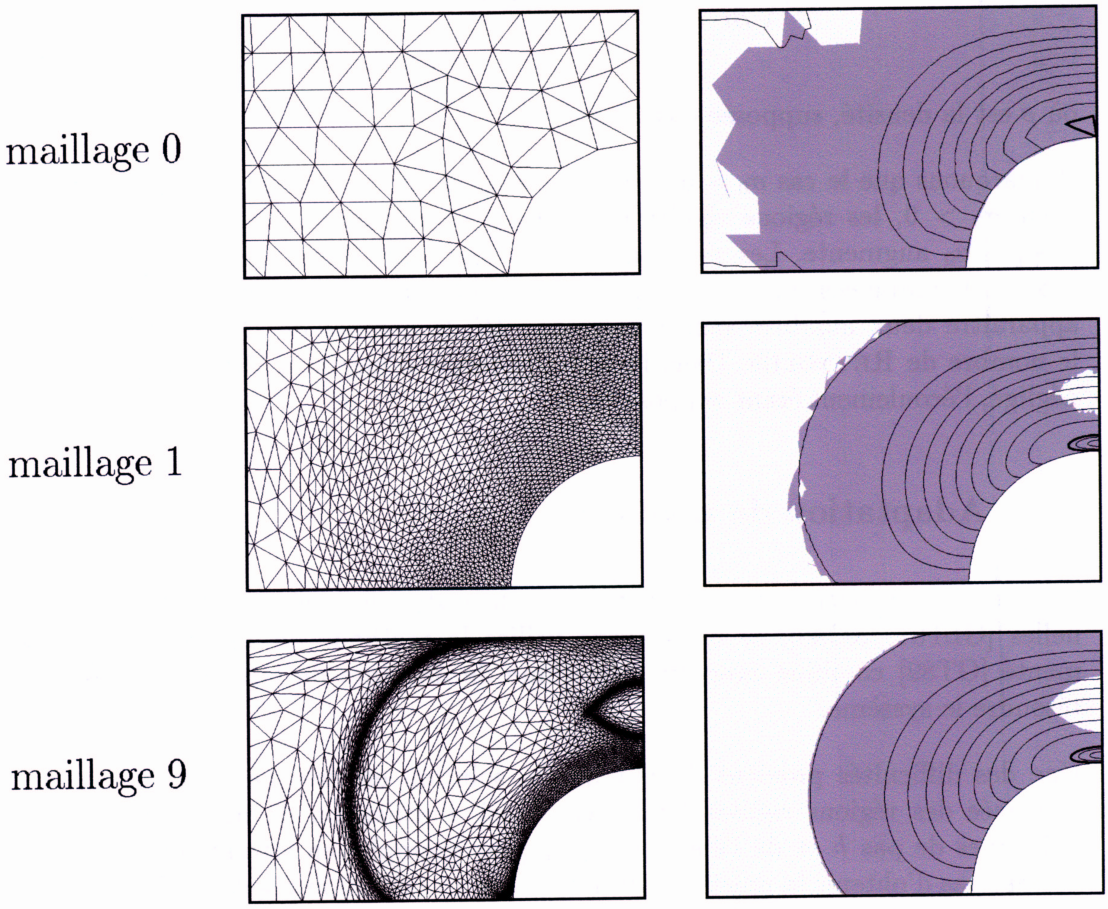

FIG. 6 – *Modèle de* BINGHAM *($Bi = 10$) : cycles d'adaptation.*

Sur la FIG. 7, on pourra apprécier la finesse de résolution des détails de l'écoulement. La légère concavité de la pointe apparaît clairement en FIG. 7.b, les lignes noires horizontales dans la pointe représentant les trajectoires de matière en translation solide à la même vitesse que le cylindre. La convexité marquée de l'amande s'observe en FIG. 7.c, où les trajectoires sont cette fois des arcs de cercle, la matière contenue dans l'amande étant en rotation solide. Enfin, une région de recirculation apparaît en détail en FIG. 7.d, tandis que le maillage est très concentré au sommet du cylindre, où la solution est singulière (contraintes

et taux de déformations exacts non-bornés). On y observe aussi le centre de l'écoulement de retour, provoqué par le déplacement du cylindre.

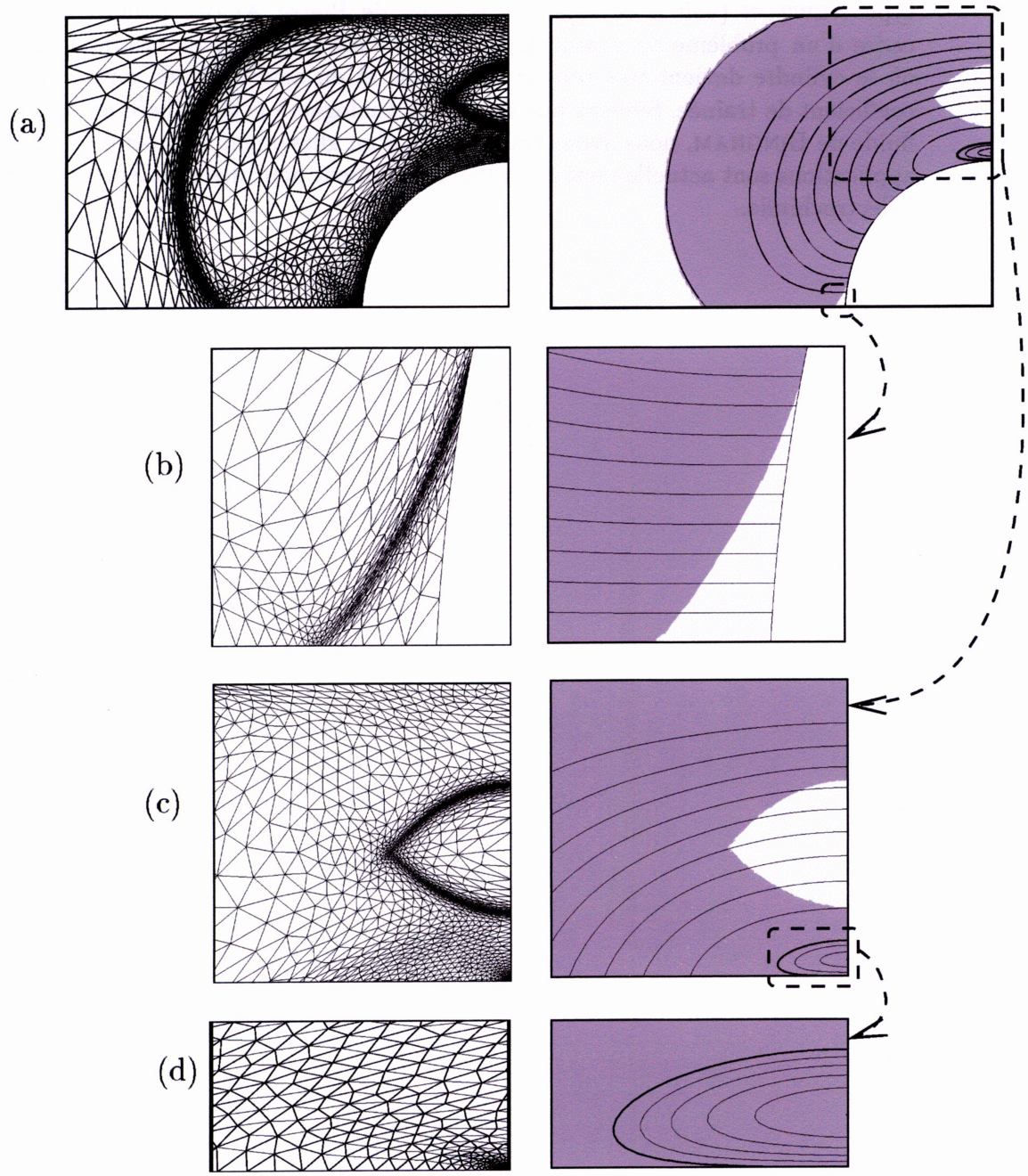

FIG. 7 – *(a) vue générale; (b) pointe; (c) amande; (d) recirculation.*

Les temps de calculs sont de l'ordre de l'heure sur station de travail pour les résultats présentés ici. Pour des problèmes plus volumineux, un gain substantiel pourrait être obtenu en remplaçant l'algorithme d'UZAWA par une méthode de type NEWTON (voir à ce sujet les travaux de Pierre ALART [Ala97] dans le cadre d'un problème de contact). Ce travail s'est poursuivi en étudiant le cas où le cylindre devient très proche des parois et en analysant les variations du coefficient de traînée. Suivant une démarche analogue à celle utilisée ici pour un fluide de BINGHAM, nous avons traité le cas d'un glissement avec seuil. D'autres applications sont actuellement à l'étude, notamment pour des problèmes issus de l'éléctrochimie.

4 Une librairie d'éléments finis

4.1 Motivation

Le développement la librairie `rheolef` [28] est issu du constat qu'il n'existait pas d'environnement logiciel satisfaisant pour la simulation numérique des fluides non-newtoniens. Les environnements disponibles offrent soit un interface au niveau matrice-vecteur, et ce sont les plus nombreux, soit leur interface est de type éléments finis, mais leurs fonctionnalités sont trop réduites pour notre propos (pas d'éléments finis mixtes, etc..) ou pas assez modulaires pour les applications en vue. Dans la deuxième catégorie, on trouve le très élégant interpréteur `freefem+` [PHBO01] d'Olivier PIRONNEAU ou bien la librairie `ofeli` [Tou01] de Rachid TOUZANI.

Par ailleurs, spécifier l'interface d'une librairie avait un double avantage :

i) conduire à un code modulaire et donc plus facile à maintenir;
ii) pouvoir utiliser cette librairie pour d'autres applications.

Aussi, avec Nicolas ROQUET, avons nous développé la librairie `rheolef` [28], disponible depuis janvier 2001. Le code fait actuellement environ 70 000 lignes, principalement en `C++`.

4.2 Réalisation et illustrations

L'interface s'appuie sur la formulation variationnelle du problème à résoudre. En plus des notions de **maillage** et de **matrice creuse** apparaissant habituellement dans ce type de code, nous avons introduit les notion d'**espace** d'approximation, de **forme** bilinéaire et de **champs**. Il s'agit a notre connaissance de la première librairie d'éléments finis s'apuyant sur un interface utilisant des concepts variationnels.

À titre d'exemple, considérons le très classique problème de POISSON avec une condition de DIRICHLET homogène sur le bord dans un ouvert borné $\Omega \subset \mathbb{R}^N$, $N = 1, 2, 3$.

(P): trouver u, defini dans Ω, telle que :

$$-\Delta u = 1 \text{ dans } \Omega \text{ et } u = 0 \text{ sur } \partial\Omega,$$

dont la formulation variationnelle s'écrit :

(FV): trouver $u \in H_0^1(\Omega)$ *tel que :*

$$a(u,v) = m(1,v),\ \forall v \in H_0^1(\Omega),$$

où les formes bilinéaires $a(.,.)$ et $m(.,.)$ sont définies par :

$$\begin{aligned} a(u,v) &= \int_\Omega \nabla u.\nabla v\, dx,\ \ \forall u,v \in H_0^1(\Omega), \\ m(u,v) &= \int_\Omega uv\, dx,\ \ \forall u,v \in L^2(\Omega). \end{aligned}$$

La forme $a(.,.)$ définit un produit scalaire dans $H_0^1(\Omega)$ et est appelée forme d'**énergie**. Elle est associée à l'opérateur $-\Delta$. La forme $m(.,.)$ est ici simplement le produit scalaire de $L^2(\Omega)$, et est appelée forme de **masse**. L'approximation par éléments finis de LAGRANGE s'obtient en introduisant $\mathcal{T}_h$, un maillage de Ω et V_h, l'espace des fonctions continues, polynomiales par morceaux de degré $k \geq 1$ et s'annulant sur le bord du domaine :

$$V_h = \{v \in H_0^1(\Omega);\ v_{/K} \in P_k,\ \forall K \in \mathcal{T}_h\}.$$

Le problème approché s'énonce :

$(FV)_h$*: trouver* $u_h \in V_h$ *tel que :*

$$a(u_h,v_h) = m(1,v_h),\ \forall v_h \in V_h.$$

```
#include "rheolef/rheolef.h"
int main (int argc, char**argv) {
    geo omega (argv[1]);
    space Vh (omega, argv[2]);
    Vh.block ("boundary");
    form a (Vh, Vh, "grad_grad");
    form m (Vh, Vh, "mass");
    field fh (Vh, 1);
    field uh (Vh);
    uh ["boundary"] = 0;
    ssk<Float>fact = ldlt(a.uu);
    uh.u = fact.solve (m.uu*fh.u + m.ub*fh.b - a.ub*uh.b);
    cout << uh;
    return 0;
}
```

FIG. 8 – *Résolution du problème de* POISSON *avec la librairie* `rheolef`.

Le code C++ de la FIG. 8 met en œuvre la résolution du problème de POISSON dans l'environnement `rheolef`. Ce code s'applique pour des maillages en dimension un, deux et trois, et pour des approximations par éléments finis linéaires ou quadratiques par morceaux. La Fig. 9 représente des coupes et isosurfaces de la solution en dimension trois, ainsi que deux rendus volumiques du type lancer de rayon.

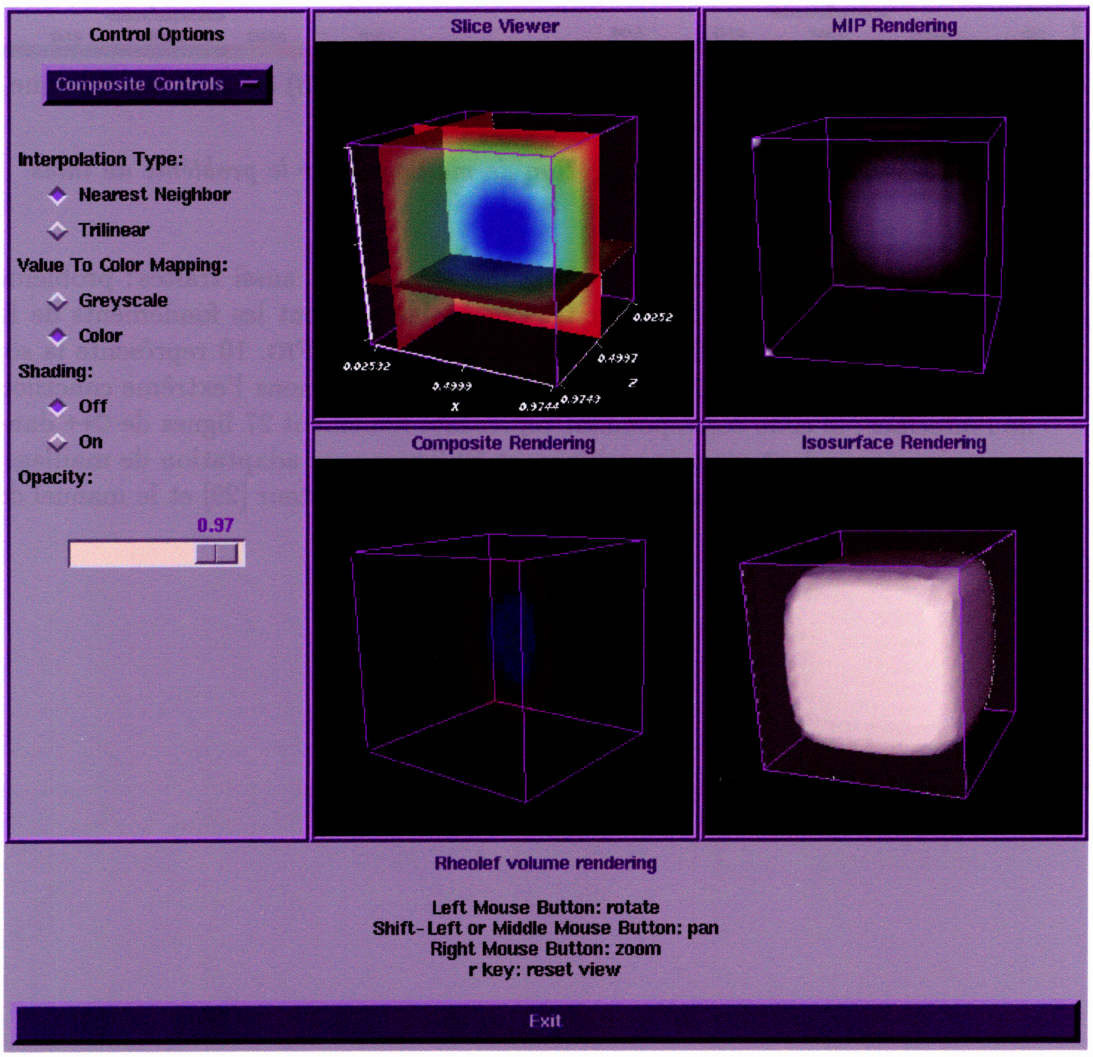

FIG. 9 – *Solution du problème de* POISSON *pour* $N = 3$.

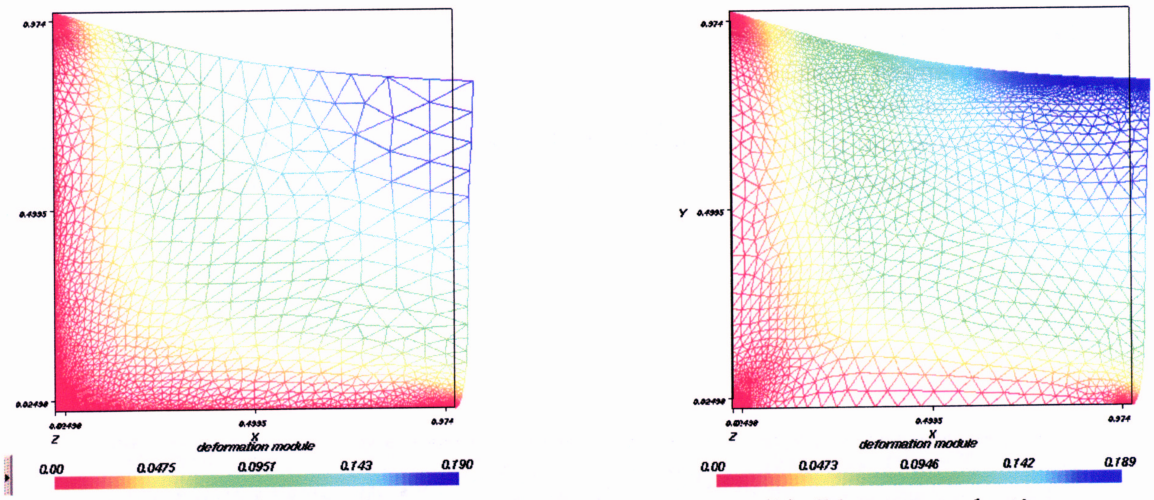

(a) élément linéaire (b) élément quadratique

FIG. 10 – *Résolution avec adaptation de maillage pour le problème du talus.*

Les problèmes linéaires standards de la mécanique sont aussi traités : problème de STOKES et système de l'élasticité. Ces problèmes sont les fondements de la plupart des modèles non-linéaires de la mécanique. La FIG. 10 représente la solution du problème du talus (élasticité linéaire). Soulignons l'extrême concision de l'interface : le code correspondant représente seulement 27 lignes de `C++` dans sa version sans adaptation de maillage, et 52 lignes avec adaptation de maillage. Le lecteur intéressé pourra consulter le guide de l'utilisateur [29] et le manuel de référence [30].

5 Perspectives

5.1 Écoulements à surface libre et phénomènes capillaires

Les forces capillaires interviennent dans un grand nombre de procédés de mise en forme de matériaux : extrusion de fibres, fils et membranes, injection dans des moules, enduction de produits sur des surfaces, jets d'encre, décollement d'adhésifs...

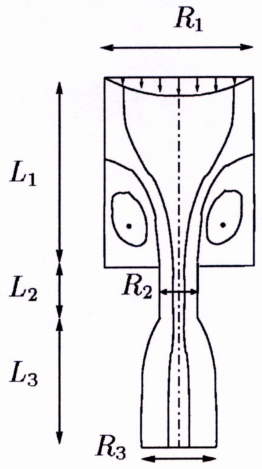

Les matériaux en présence sont fréquemment non-newtoniens et seront décrits par des modèles viscoélastiques. La compétition entre forces capillaires et contraintes viscoélastiques conduit à des phénomènes bien spécifiques. Pour fixer les idées, considérons tout particulièrement le cas du gonflement en sortie de filière et cherchons à répondre à la question suivante :

Comment choisir le rayon de la filière et le débit d'entrée pour obtenir un fil de rayon donné ?

Nous reconnaissons un problème inverse que nous aborderons sous la forme d'un problème de contrôle optimal : il s'agit de contrôler numériquement des écoulements viscoélastiques avec tension de surface. Citons, également, à titre de seconde application possible, le pelage d'un ruban adhésif. Pour une étude théorique et expérimentale, voir [VPB96]. Il s'agit alors d'optimiser les propriétés de l'ahésif afin que le substrat (mur, peau, ...) soit exempt de produit (rupture adhésive). D'autres applications concernent la coalescence, l'enduction, les interfaces fluide-fluide.

Ce thème de recherche, en collaboration avec Jérôme MONNIER, Maître de conférence à l'INPG, a fait l'objet du stage de DEA de Jocelyn ETIENNE [50] dans le cadre du projet INRIA IDOPT. Claude VERDIER, chercheur au CNRS, travaille sur les aspects théoriques et expérimentaux de problèmes avec tension capillaire et de viscoélasticité, et une perspective de collaboration est étudiée. Enfin, je donne un cours sur la modélisation et le calcul des surfaces libres et des interfaces dans le cade du DEA de mathématiques appliquées de Grenoble [59].

5.2 Avalanches et coulées de boue

La prévention des risques en montagne, des avalanches aux coulées de boue, passe par des simulations numériques de plus en plus poussées. Ces dernières mettent en œuvre des lois de comportement de matériaux complexes, comme les fluides à seuil ou les écoulements granulaires, ainsi que des méthodes numériques délicates : volumes finis dans un cadre dynamique, maillages adaptatifs. Les essais peuvent être faits avec la montagne seule, ou en présence d'ouvrages d'art (pare-avalanches, déviateurs, digues) dont on cherche à ajuster la position. Les modèles sont de type visco-plastiques ou granulaires, moyennés dans l'épaisseur (approche du type SAINT-VENANT). Une adaptation du maillage à la topographie sera développée pour rendre les modèles plus précis et plus efficaces. Elle pourra également permettre de concentrer les calculs dans les régions d'intérêt : le front de l'avalanche ou de la coulée, le voisinage des variations brusques du relief, digue ou bien arêtes de rochers.

Ce thème de recherche vient de démarrer et a fait l'objet du stage de DEA de Claire LAUVERNET [51] au Laboratoire de Modélisation et de Calcul, dans le cadre du projet INRIA IDOPT. Une collaboration avec le LEGI (Emil HOPFINGER [Hop83]), le Cemagref (Dominique LAIGLE, Mohamed NAAIM) et le laboratoire GRAVIR (Marie-Paule CANI, Fabrice NEYRET) débute également, avec le soutient financier de l'INRIA (Action de Recherche Coopérative) et de l'INPG (Bonus Qualité Recherche). J'encadre également la thèse de Jocelyn ETIENNE [52] sur ce thème (co-encadrement avec Emil HOPFINGER).

A Liste des travaux

[1] P. Saramito. *Simulation numérique d'écoulements de fluides viscoélastiques par éléments finis incompressibles et une méthode de directions alternées; applications.* Thèse de l'Institut National Polytechnique de Grenoble, mars 1990.

[2] R. Michel and P. Saramito. *Simulation en temps réel de structures vibrantes sur calculateur vectoriel.* DEA de l'Institut National Polytechnique de Grenoble, 1986.

[3] P. Saramito. *Simulation numérique des instabilités lors de l'étirage des fibres de verre.* Stage ENSIMAG, Vetrotex - Saint Gobain, Chambéry, 1985.

Publications dans des revues internationales avec comité de lecture

[4] P. Saramito. Numerical simulation of viscoelastic fluid flows using incompressible finite element method and a θ-method. *Mathematical Modelling and Numerical Analysis*, 28:1–35, 1994.

[5] P. Saramito. Operator splitting for viscoelastic fluid with a differential constitutive law. *C. R. Acad. Sci. Paris, Série II*, t. 319, No. 3:267–270, 1994.

[6] P. Saramito. Efficient simulation of nonlinear viscoelastic fluid flows. *J. Non Newtonian Fluid Mech.*, 60:199–223, 1995.

[7] P. Saramito and J.-M. Piau. Flow characteristics of viscoelastic fluids in an abrupt contraction by using numerical modeling. *J. Non Newtonian Fluid Mech.*, 52:263–288, 1994.

[8] P. Saramito. Operator splitting in viscoelasticity. *Élasticité, Viscoélasticité et Contrôle Optimal, Lyon, décembre 1995, ESAIM: Proceedings*, `http://www.emath.fr/proc/Vol.2/contents.htm`, 2:275–281, 1997.

[9] N. Roquet, R. Michel, and P. Saramito. Errors estimate for a viscoplastic fluid by using P_k finite elements and adaptive meshes. *C. R. Acad. Sci. Paris, Série I, 6 pages*, 331(7):563–568, 2000.

[10] P. Saramito and N. Roquet. An adaptive finite element method for viscoplastic fluid flows in pipes. *Comput. Meth. Applied Mech. Engng*, 190:5391–5412, 2001.

[11] N. Roquet and P. Saramito. An adaptive finite element method for bingham fluid flows around a cylinder. en préparation, *41 pages*, 2001.

[12] N. Roquet and P. Saramito. Friction boundary conditions for the numerical simulation of Bingham fluid. en préparation, 2001.

Colloques avec actes avec comité de lecture

[13] P. Saramito and J.-M. Piau. Characterization of viscoelastic fluids in complex geometries: the numerical approach. *Proceedings of the International Conference on Rheology of Polymers: from the solution to the melt, Abbaye Royale de Fontevraud*, may 1993.

[14] P. Saramito. Why are some operator splitting techniques better than other? *In Ninth International Workshop on Numerical Methods in Non-Newtonian Flows, Llindir Hall, Wales, [1 page]*, april 1995.

[15] P. Saramito and J.-M. Piau. Numerical study of elongational effects and vortex development for viscoelastic fluid in contractions. *Proceedings* XII ^{e} International Congress on Rheology, Quebec (Canada), page 430, August 1996.

[16] B. Nsom, J.-M. Piau, P. Saramito, K. Debiane, and A. Ayadi. Experimental and numerical study of the viscous dam break problem. *Proceedings of the fifth european rheology conference, Portoroż, Slovenia, Springer Verlag*, 6-11 september 1998.

[17] P. Saramito, J.-M. Piau, N. Roquet, and A. Caillaux. Résolution numérique de l'écoulement de Poiseuille établi dans un tuyau de section carrée d'un fluide viscoplastique. *Congrès français de mécanique, Toulouse, [8 pages]*, 1999.

Colloques sans actes ou avec actes à diffusion restreinte

[18] P. Saramito. Une approche comparée par les méthodes BEM et FEM pour la thermorégulation des moules. *Séminaire annuel du Club des Logiciels de l'Industrie Plastique*, page [5 pages], mai 1990.

[19] P. Saramito. Thermique de l'outillage: mise en œuvre d'une stratégie de simulation efficace. *Séminaire annuel du Club des Logiciels de l'Industrie Plastique*, page [6 pages], mai 1991.

[20] P. Saramito. Une méthode de directions alternées pour les lois de type différentiel – application à la contraction 4 à 1. *Colloque-bilan du GDR 901 Rhéologie pour la transformation des polymères fondus*, octobre 1991.

[21] P. Saramito and J.-M. Piau. Approximation mixte du problème de Stokes à trois champs; application au modèle de Phan-Thien et Tanner en contraction brusque. *28 ^{e} colloque annuel du Groupe Français de Rhéologie, Le Mans*, octobre 1993.

Logiciels

[22] P. Saramito. **ariel**: *Résolution des écoulements viscoélastiques en contraction brusque plane et axisymétrique.* Institut de Mécanique de Grenoble, 1990.

[23] P. Saramito. **clip**: *club des logiciels de l'industrie plastique.* société CISI Ingénierie, 1991.

[24] P. Saramito. **mtos**: *A Modgen to Styx translator for integrated circuits at the layout level.* EEC ESPRIT 5075 and JESSI-AC3, société SGS-Thomson Microelectronics, 1993.

[25] P. Saramito. **zebu**: *an environment for the automatic translation between sofware languages.* société SGS-Thomson Microelectronics, 1994.

[26] G. Fourneris and P. Saramito. **ugncheck**: *A toolkit for the validation of integrated circuits.* société SGS-Thomson Microelectronics, 1994.

[27] M. Crastes, O. Lunven, and P. Saramito. **atov**: *simulation, compilation et synthèse des circuits VLSI sous Asyl+ à partir d'une descripton VHDL.* société MINC-IST, 1996.

[28] P. Saramito and N. Roquet. **rheolef**: *A finite element environment, i.e. some* `C++` *classes and unix commands.* `http://www-lmc.imag.fr/lmc-edp/Pierre.Saramito/rheolef`, 2001.

[29] P. Saramito and N. Roquet. **rheolef**: *User's manual,* (64 pages). `http://www-lmc.imag.fr/lmc-edp/Pierre.Saramito/rheolef/usrman.ps.gz`, 2001.

[30] P. Saramito and N. Roquet. **rheolef**: *Reference manual,* (148 pages). `http://www-lmc.imag.fr/lmc-edp/Pierre.Saramito/rheolef/rheolef.ps.gz`, 2001.

Rapport périodique et de fin de contrat

[31] N. Roquet and P. Saramito. *Résultats théoriques sur les modèles de Bingham et de Herschel-Bulckley.* Rapport semestriel d'avancement, société GIST, avril 1997.

[32] P. Saramito, B. Nsom, and J.-M. Piau. *The viscous dam break problem,* 22 pages. projet Européen *Debris flows and risks*, 1998.

Notes internes

[33] P. Saramito. *Note sur la stabilité de mélanges de fluides diffusants à deux et trois composants.* Laboratoire de Rhéologie, *14 pages*, 1998.

Conférences sur invitation

[34] P. Saramito. Efficient numerical simulation of viscoelastic fluid flows. *Department of Aerospace Engineering, University of Minnesota*, august 1996.

[35] P. Saramito. Mixed finite element methods for the direct simulation of viscoelastic fluids. *Department of Aerospace Engineering, University of Minnesota*, `http://www.aem.umn.edu/Solid-Liquid_Flows/`, november 1996.

[36] P. Saramito. Direct simulation of viscoelastic fluids. *University of Pennsylvania*, december 1996.

Séminaires

[37] P. Saramito. Simulation numérique des écoulements de fluides viscoélastiques. *Laboratoire de Rhéologie, Grenoble*, 1995.

[38] P. Saramito. Maillages adaptatifs pour les fluides viscoplastiques. *Laboratoire de Mathématiques, Chambéry*, 1999.

[39] P. Saramito. Maillages adaptatifs pour les fluides viscoplastiques. *Laboratoire de Modélisation et de Calcul, Grenoble*, 1999.

B Formation

Encadrements de thèse, DEA et stage

[40] A. Bellini and D. Dorval. *Mailleur automatique en dimension trois.* DEA mathématiques appliqués, UJF Grenoble et ENSIMAG-INPG, 1991.

[41] W. Choueri. *Maillages adaptatifs et méthodes multigrilles pour la résolution d'une équation de convection-diffusion.* DEA mathématiques appliqués, UJF Grenoble et ENSIMAG-INPG, 1991.

[42] Y. Courtot. *Étude des effets inertiels d'écoulements viscoélastiques dans une contraction brusque.* DEA mécanique, UJF Grenoble, 1996.

[43] N. Roquet. *Simulation numérique d'écoulements de fluides une méthode d'éléments finis incompressibles.* DEA mathématiques appliqués, Université d'Orsay, Paris, pré-publication `http://www.math.u-psud.fr/html/ppo.html`, 1996.

[44] Y. Cornet. *Simulation numérique de rupture de barrage dans le cas de fluides visqueux.* DESS de l'Université de Chambéry, 1997.

[45] A. Caillaux. *Calcul d'un écoulement de Poiseuille pour un fluide de Bingham par lagrangien augmenté et une technique de maillage auto-adaptatif anisotrope.* Stage Ingénieur de L'ENSHMG-INPG, 1997.

[46] A. Caillaux. *Simulation numérique de zones mortes dans un fluide à seuil de contrainte en écoulement établi, par éléments finis et l'utilisation d'un mailleur anisotrope auto-adaptatif.* DEA mécanique, UJF Grenoble et ENSHMG-INPG, 1998.

[47] G. Beltaguy. *Simulation numérique de rupture de barrage pour des fluides à seuil.* DESS de l'Université de Chambéry, 1998.

[48] M. Edwards. *Résolution par éléments finis de la stabilité d'interface.* Stage ENSIMAG-INPG, Grenoble, 1999.

[49] N. Roquet. *Résolution numérique d'écoulements de fluides à effet de seuil par éléments finis mixtes et adaptation de maillage.* Thèse de l'Université Joseph FOURIER, 2000.

[50] J. Etienne. *Simulation numérique d'écoulements à surface libre avec tensions capillaires par une méthode Lagrange-Euler arbitraire.* DEA mathématiques appliqués, UJF Grenoble, 2001.

[51] C. Lauvernet. *Adaptation de maillage pour la modélisation numérique des avalanches par des équations moyennés, dans l'épaisseur.* DEA mathématiques appliqués, UJF Grenoble, 2001.

[52] J. Etienne. *Modélisation et simulation numérique des écoulements à surface libre - application aux avalanches.* Thèse, UJF Grenoble, (**en préparation**), 2001.

Enseignements et formation continue

[53] P. Saramito. *Mécanique générale (40 heures, resp. J. F. Daian).* T.D. IUT de génie énergétique et thermique, Grenoble, 1986-87.

[54] P. Saramito. *Introduction aux outils informatiques (48 heures, resp. Pastor).* T.D. IUT de génie civil, Grenoble, 1987-88.

[55] P. Saramito. *Simulation numérique en mécanique des solides (48 heures, resp. Pastor).* Cours IUT de génie civil, Grenoble, 1987-88.

[56] P. Saramito. *Informatique pour non-voyants (80 heures, resp. Soller).* T.D. ENSIMAG, Grenoble, 1988-89.

[57] P. Saramito. `C++` *et conception orienté objet pour les codes de calcul numérique.* Formation continue au personnel du CEA-CISI, Grenoble, 1992.

[58] P. Saramito. *Méthodes mathématiques pour l'ingénieur.* Cours et T.D., Université Joseph FOURIER, IUP MESSI, Valence (*40 heures*), 2000.

[59] G.-H. Cottet et P. Saramito. *Modélisation et calcul d'interfaces.* Cours, Université Joseph FOURIER, DEA mathématiques appliquées, Grenoble (*24 heures*), 2001.

C Références

[Ala97] P. Alart. Méthode de Newton généralisée en mécanique du contact. *J. Math. Pures Appl.*, 76:83–108, 1997.

[BH82] A. N. Brooks and T. J. R Hughes. Streamline-upwind/Petrov-Galerkin formulation for convection dominated flow with particular emphasis on the incompressible Navier-Stokes equations. *Comp. Meth. in Appl. Mech and Eng.*, 32:199–259, 1982.

[Bin22] E. C. Bingham. *Fluidity and Plasticity.* Mc Graw-Hill, New-York, 1922.

[Bre74] F. Brezzi. On the existence, uniqueness and approximation of saddle point problems arising from Lagrangian multiplier. *RAIRO, série Analyse Numérique*, R2:129–151, 1974.

[BS92] J. Baranger and D. Sandri. A formulation of the Stokes's problem and the linear elasticity equation suggested by the Oldroyd model for viscoelastic flows. *Mathematical Modelling and Numerical Analysis*, 26:331–345, 1992.

[BW69] G. F. Brooks and R. L. Whitmore. Drag forces in Bingham plastics (II). *Rheol. Acta*, 8:472–480, 1969.

[CM87] M. J. Crochet and J. M. Marchal. A new mixed finite element for calculating viscoelastic fluid flows. *J. Non Newtonian Fluid Mech.*, 26:77–114, 1987.

[FF89] M. Fortin and A. Fortin. A new approach for the FEM simulation of viscoelastic flows. *J. Non Newtonian Fluid Mech.*, 32:295–310, 1989.

[FG81] M. Fortin and R. Glowinski. *Lagrangian Augmented Methods.* North Holland, 1981.

[Gie82] H. Giesekus. A simple constitutive equation for polymer fluids based on the concept of deformation dependant tensorial mobility. *J. Non Newtonian Fluid Mech.*, 11:69, 1982.

[GL88] J. B. Goodman and R. J. Leveque. On the accuracy of a stable scheme for two dimensional conservation laws. *Soc. Ind. Appl. Math. Numer. Anal.*, 25:268–284, 1988.

[Glo86] R. Glowinski. Numerical methods for the numerical solution of the incompressible Navier-Sokes equations. In *Vistas in Applied Mathematics, Optimization Software*, pages 57–95, New York 1986.

[GLT81] R. Glowinski, J. L. Lions, and R. Trémolières. *Numerical analysis of variational inequalities.* North Holland, Amsterdam, 1981.

[GR86] V. Girault and P. A. Raviart. *Finite Element Methods for Navier-Stokes Equations - Theory and Algorithms.* Springer-Verlag, 1986.

[GS87] C. Guillopé and J. C. Saut. Résultat d'existence pour les fluides viscoélastiques à loi de comportement de type différentiel. *C. R. Acad. Sci. Paris*, t.305, série I:489–492, 1987.

[GT89] R. Glowinski and P. Le Tallec. *Augmented Lagrangian and Operator Splitting Method in Non-Linear Mechanics.* SIAM Studies in Applied Mathematics, 1989.

[Hec97] F. Hecht. *Bidimensional anisotropic mesh generator.* INRIA, `http://www-rocq.inria.fr/gamma/cdrom/www/bamg/eng.htm`, 1997.

[Hop83] E. J. Hopfinger. Snow avalanche motion and related phenomena. *Ann. Rev. Fluid Mech.*, 15:47–76, 1983.

[KO88] N. Kikuchi and J. T. Oden. *Contact problems in elasticity: A study of variational inequalities and finite element methods.* SIAM Studies in Applied Mathematics, 1988.

[Lar88] R. G. Larson. *Constitutive Equations for Polymer Melts and Solutions.* Butterworths series in Chemical Engineering, H. Brenner,mit edition, 1988.

[Leo92] A. I. Leonov. Analysis of simple constitutive equations for viscoelastic liquids. *J. of Non Newtonian Fluid Mech.*, 42:323–350, 1992.

[LR74] P. Lesaint and P. A. Raviart. *On Finite Element Methods For Solving the Neutron Transport Equation.* Academic Press, Carl de Boor edition, 1974.

[Old50] J. G. Oldroyd. On the formulation of rheological equations of states. *Proc. Roy. Soc, London*, A 200:523–541, 1950.

[PHBO01] O. Pironneau, F. Hecht, D. Bernardi, and K. Ohtsuka. FREEFREM+: an implementation of a language dedicated to the finite element method. `http://www-rocq.inria.fr/Frederic.Hecht/FreeFemPlus.htm`, 2001.

[PTT77] N. Phan-Thien and R. I. Tanner. A new constitutive equation derived from network theory. *J. Non Newtonian Fluid Mech.*, 2:353–365, 1977.

[Ren85] M. Renardy. Existence of slow flows of viscoelastic fluids with differential constitutive equations. *Z. Angew. Math. u Mech.*, 65:449–451, 1985.

[Ren88] M. Renardy. Recent advances in the mathematical theory of steady flows of viscoelastic fluids. *J. Non Newtonian Fluid Mech.*, 29:11–24, 1988.

[Tou01] R. Touzani. OFELI: an object finite element library. `http://wwwlma.univ-bpclermont.fr/~touzani/ofeli.html`, 2001.

[VPB96] C. Verdier, J.-M. Piau, and L. Benyahia. Influence des propriétés élongationnelles dans le pelage des polymères. *C. R. Acad. Sci. Paris, Série IIb*, 323:739–746, 1996.

[YA73] N. Yoshioka and K. Adachi. On creeping flow of a viscoplastic fluid past a cylinder. *Chem. Eng. Sci.*, 28:215–226, 1973.

D Curriculum vitæ

LMC-IMAG
équipe EDP

Pierre.Saramito@imag.fr
http://www-lmc.imag.fr/lmc-edp/Pierre.Saramito

né le 14 septembre 1963 (37 ans), nationalité française, célibataire.

Expériences Professionnelles

95-01 **Chargé de Recherche** au CNRS (CR1, section 9) : simulation numérique en matériaux non-newtoniens.
- Encadrements de thèse, DEA, DESS, stage ingénieurs, ...
- Enseigement à Université Joseph FOURIER
- Séjour de quatre mois en 1996 aux USA (collaboration D. D. JOSEPH, R. GLOWINSKI).
- Consultant à MINC-IST (microélectronique).

93-94 **Ingénieur** R & D à ST microelectronics.
- Conception et développement d'outils de vérification de circuits intégrés.
- Collaboration aux projets européens ESPRIT 5075 (Philips, ST) et JESSI-AC3 (Bosch, CNET, ST).

90-92 **Chef de projet** à CISI.
- Club des Logiciels de l'Industrie Plastique (consortium Atochem - Peugeot SA - Renault - Rhône Poulenc)
- Enseigement : formation continue pour le CEA

86-89 **Allocataire de recherche** MRT
- Enseigements : Université Joseph FOURIER, ENSIMAG, IUT, formation continue, ...
- Membre du groupement de recherche 901 du CNRS sur la rhéologie pour la transformation des polymères fondus.

Diplômes

86-89 **Thèse** de doctorat de l'INPG : simulation numérique par éléments finis des écoulements de fluides viscoélastiques.

1986 **DEA** : Simulation en temps réel sur calculateur vectoriel.

1986 **Ingénieur ENSIMAG.**

MATHEMATICAL MODELLING AND NUMERICAL ANALYSIS
MODELISATION MATHEMATIQUE ET ANALYSE NUMERIQUE
(Vol. 28, n° 1, 1994, p. 1 à 34)

A NEW θ-SCHEME ALGORITHM AND INCOMPRESSIBLE FEM FOR VISCOELASTIC FLUID FLOWS (*)

by P. SARAMITO (1)

Communicated by R. TEMAM

Abstract. — *This paper presents a new mixed finite element method for the computation of incompressible viscoelastic fluids flows. The decoupled computation of stresses and velocities is performed with an algorithm which involves a time approximation by alternating direction implicit algorithms. The method is of order two in time and allows fast calculation of stationary solutions. As finite elements, we have used the zero divergence Raviart-Thomas element for approximating the velocities, and the Lesaint-Raviart element for the stresses. Application of the Oldroyd-B fluid in an abrupt contraction is given. The numerical results show that no upper limit of the Weissenberg number is encountered.*

Résumé. — *Nous présentons une nouvelle formulation mixte pour le calcul d'écoulements de fluides viscoélastiques incompressibles. L'approximation en temps du problème est effectuée à l'aide d'une méthode de directions alternées. Ceci nous conduit à un algorithme permettant de découpler le calcul des vitesses de celui des contraintes. D'ordre deux en temps, cette méthode permet de plus le calcul rapide de solutions stationnaires. L'élément à divergence nulle de Raviart-Thomas est utilisé pour les vitesses, et celui de Lesaint-Raviart pour les contraintes. La méthode est appliquée au problème de l'écoulement d'un fluide d'Oldroyd dans une contraction brusque. Les résultats numériques ont été effectués sans rencontrer de nombre de Weissenberg limite.*

1. INTRODUCTION

The spectacular effects occurring in viscoelastic fluid flows have been extensively described in many books and papers (for example [1, 5]) and cannot be predicted by Navier-Stokes equations. These phenomena are

(*) Manuscript received January, 31, 1991 and revised September, 12, 1991.

(1) Correspondence to : Laboratoire de Rhéologie, BP 53X, 38041 Grenoble Cedex.
Present address : Institut National polytechnique, 46, avenue Félix Viallet, 38031 Grenoble Cedex, France.

M² AN Modélisation mathématique et Analyse numérique 0764-583X/94/01/$ 4.00

mainly related to memory and elongational effects of the material, which can be represented by a suitable rheological model. In this context, numerical simulation may be considered as an important tool for prediction of phenomena, as vortex flows which are of interest in polymer processing. In the isothermal case, the basic equations of the problem are mass and momentum equations to be solved together with a rheological constitutive equation. The relevant set of equations is generally non-linear.

In relation to numerous applications and fundamental problems arising in the field of non-Newtonian flows, intensive research has revealed the main problems and theoretical difficulties for solving the large systems obtained from the discretisation of the non-linear boundary value problems. We may refer to Keunigs's book [16] as an exhaustive historical document on the considerable work performed in viscoelastic flow calculations. We now briefly recall and comment the main features of previous work reported before 1987, and the more recent theoretical and numerical results beyond this date. As many authors, we still find that it is convenient to define two simple non-dimensional numbers Re and We to characterize the viscoelastic fluid flows. The Reynolds number Re is given by

$$Re = \rho \frac{UL}{\eta_n} \tag{1.1}$$

where η_n is the (constant) viscosity, ρ is the density, U is the characteristic velocity and L is a characteristic length. The elastic number, We, generally called the Weissenberg number (or Deborah number) is expressed by :

$$We = \frac{\lambda U}{L} \tag{1.2}$$

where λ is an average characteristic time of the fluid.

1.1. Main results before 1987

The numerical results have indicated a divergence of the algorithms beyond $We = 4$. At that time, research has more investigated the problem of computational « unstabilities » than realistic physical features. Although the failure of the algorithms can be related to the theoretical foundations of the constitutive models, we may generally question on flow problems occurring close to singularities of complex geometries and theoretical problems due to prescription of boundary conditions. Those numerical methods also lead losses of convergence, which may explained as follows :

(i) non-compatibility between the approximating spaces for the stresses and the velocities ;

(ii) the non-consideration of the hyperbolicity [15] of equations in relation

to boundary conditions to be involved, and the approximating schemes for the derivatives leading to wiggles for the solutions ;

(iii) the non-efficiency of the algorithms : the computing times are enormous and even macro-computers might be saturated.

1.2. In 1987 : Marchal and Crochet

In 1987, Marchal and Crochet [4] have presented the streamline upwind technique introduced by Hughes and Brooks [3] for convection problems. Using particular elements for approximating the velocities and stresses, numerical results were obtained for high We. The authors have adopted a continuous finite element approximation for the stresses.

To obtain a *well-posed* problem [9], as well as acceptable solutions in the Stokes problem (at $We = 0$), these authors used meshes involving sub-elements.

Then, the resulting high order matrices arising from the discretized system of equations had to be solved by use of a CRAY-XMP, with an important computing time.

1.3. The recent work of M. Fortin and A. Fortin

The recent work of M. Fortin and A. Fortin [7] is also to be underlined. By developing a non-continuous finite element approximation for the stresses, the authors have proved that the problem is well-posed for $We = 0$ and have used a discontinuous method proposed by Lesaint and Raviart [17].

However, when using high-order finite elements, the corresponding scheme does not verify the TVD (Total Variation Decreasing) condition [12], and oscillating approximate solutions are obtained. The method still involves large degrees of freedom, and the decoupled technique leads to high computing times (on work stations), which prevents from further numerical experiments.

1.4. The present work

In the present work, we develop a finite element method applied to the Oldroyd-B constitutive model. The basic equations and the related mathematical problems are presented in section 2. Taking into account the incompressibility condition for the fluid (which implies the zero divergence for the velocity vector), we consider the incompressible finite elements of Raviart and Thomas [10, 23].

In section 3, some original approximations of the stresses are proposed, and are shown to correspond to a well-posed problem at $We = 0$. In particular, for elements of lower degree, a minimum size of the discretized

problem is obtained (asymptotically, one degree-of-freedom by scalar function and by element).

In section 4, on the basis of the work of Glowinski and Périaux [11] on Navier-Stokes equations, we present a new algorithm using the alternating directions implicit method. This enables us to decouple the difficulties involved by the non-linearity of the equations. The non-stationary approach is used to obtain solutions in steady flow situations.

2. FORMULATION OF THE PROBLEM

In this section, we consider the general laws of conservation of the incompressible isothermal flow and the rheological constitutive equation of the fluid. The boundary condition equations to be prescribed are also given.

2.1. The Oldroyd-B constitutive equation

The Cauchy stress tensor may be expressed as :

$$\sigma = -pI + 2\,\eta_n D(\mathbf{u}) + \tau \tag{2.1}$$

where p is the hydrostatic pressure, $\mathbf{u}$ is the velocity vector, $D(\mathbf{u}) = \frac{1}{2}(\nabla\mathbf{u} + \nabla\mathbf{u}')$ the rate-of-deformation tensor, τ the extra-stress and $\eta_n > 0$ denotes the « solvent viscosity ». For the extra-stress tensor, we consider the differential Oldroyd-B model [1, 19] of equation :

$$\lambda \overset{\square}{\tau} + \tau = 2\,\eta_p D(\mathbf{u}) \tag{2.2}$$

where $\lambda > 0$ is the relaxation time, $\eta_p > 0$ is the « elastic » viscosity. The symbol $(\overset{\square}{\ })$ is related to the objective derivation of a symmetric tensor [12, 2] :

$$\overset{\square}{\tau} = \frac{\partial \tau}{\partial t} + (\mathbf{u}\cdot\nabla)\tau + \tau W(\mathbf{u}) - W(\mathbf{u})\tau - a(D(\mathbf{u})\tau + \tau D(\mathbf{u})) \tag{2.3}$$

with $a \in [-1, 1]$ and $W(\mathbf{u}) = \frac{1}{2}(\nabla\mathbf{u} - \nabla\mathbf{u}')$ denote the vorticity tensor.

2.2. Conservation laws

The mass conservation equation may be written as :

$$\operatorname{div}\mathbf{u} = 0 \tag{2.4}$$

for a fluid of constant specific mass $\rho > 0$.

The momentum equation is :

$$\rho \left(\frac{\partial \mathbf{u}}{\partial t} + (\mathbf{u} \,.\, \nabla)\, \mathbf{u} \right) - \mathbf{div}\, \tau - \eta_n \, \Delta \mathbf{u} + \nabla p = 0 \,. \tag{2.5}$$

In the following, we investigate the case of slow flows. Thus, the inertia term $(\mathbf{u} \,.\, \nabla)\, \mathbf{u}$ may be ignored.

The conservation of moments leads to symmetry properties of the tensor σ : $\sigma = \sigma^t$. Then, from (2.1) :

$$\tau = \tau^t \,. \tag{2.6}$$

2.3. Boundary conditions

The conservation laws (2.4)-(2.5) and the Oldroyd constitutive equation (2.2) have to be used together with initial and boundary conditions. For $a = 1$ in (2.3) and $\eta_n > 0$, the set of equations (2.2), (2.4)-(2.5) is found to be of mixed parabolic-hyperbolic type [14, 15]. The characteristic lines are the streamlines, and the components of the stress tensor τ may be considered as quantities conveyed on these characteristics.

Let Ω be a finite connected flow domain of $\mathbb{R}^2$ or $\mathbb{R}^3$. The required boundary and initial conditions are the following :

(i) a condition of Dirichlet type for the velocities, on the boundary $\Gamma = \partial\Omega$:

$$\mathbf{u} = \mathbf{u}_\Gamma \quad \text{on} \quad \Gamma \tag{2.7}$$

(ii) a condition for the stresses on the upstream boundary section

$\Gamma_- = \{x \in \Gamma \,;\, (\mathbf{u} \,.\, \mathbf{n})(x) < 0\}$:

$$\tau = \tau_\Gamma \quad \text{on} \quad \Gamma_- \tag{2.8}$$

where $\mathbf{n}$ is the outward unit normal vector to Ω at the boundary Γ.

(iii) At time $t = 0$, the initial conditions are :

$$\mathbf{u}(0) = \mathbf{u}_0 \,; \quad \tau(0) = \tau_0 \quad \text{in} \quad \Omega \,. \tag{2.9}$$

The incompressibility equation (2.4) requires the following compatibility condition :

$$\int_\Gamma \mathbf{u}_\Gamma \,.\, \mathbf{n} \, ds = 0 \tag{2.10}$$

where ds is the measure on the boundary Γ.

2.4. Non-dimensional numbers and governing equations

In the present paper, added to the non-dimensional Re and We numbers, we use a retardation parameter α [14] given by :

$$\alpha = \frac{\eta_v}{\eta_n + \eta_v}. \tag{2.11}$$

Referring to the basic equations (2.2), (2.4)-(2.5) of the problem, we may now consider the following problem :

(P) : Find the non-dimensional quantities, still noted τ, $\mathbf{u}$ and p, defined in Ω, which verify the following equations :

$$We\left(\frac{\partial \tau}{\partial t} + (\mathbf{u} \cdot \nabla)\tau + \beta_\alpha(\tau, \nabla \mathbf{u})\right) + \tau - 2\alpha D(\mathbf{u}) = 0 \quad \text{in} \quad \Omega \tag{2.12}$$

$$Re\left(\frac{\partial \mathbf{u}}{\partial t} + (\mathbf{u} \cdot \nabla)\mathbf{u}\right) - \operatorname{div} \tau - (1-\alpha)\Delta \mathbf{u} + \nabla p = 0 \quad \text{in} \quad \Omega \tag{2.13}$$

$$\operatorname{div} \mathbf{u} = 0 \quad \text{in} \quad \Omega \tag{2.14}$$

subjected to boundary and initial conditions (2.7)-(2.9). The function β_α involved in equation (2.12) is given by :

$$\beta_\alpha(\tau, \nabla \mathbf{u}) = \tau \cdot W(\mathbf{u}) - W(\mathbf{u}) \cdot \tau - \alpha(D(\mathbf{u}) \cdot \tau + \tau \cdot D(\mathbf{u})). \tag{2.15}$$

2.5. Existence results

Some results concerning the existence of solutions of problem (P) (equations (2.12)-(2.14) and boundary condition (2.7)-(2.9)) are known. There results are obtained upon the assumptions made for the boundary Γ, the values τ_Γ, $\mathbf{u}_\Gamma$, τ_0 and $\mathbf{u}_0$ and data of the parameters Re, We and α :

i) Renardy [21, 22] has obtained, using a fixed-point method, existence of stationary solutions for any value of α, the other parameters being small.

ii) Guillopé and Saut [13, 14] have proved a global existence result of the solution of problem (P), in the unsteady case, for small values of α.

3. SEMI-APPROXIMATION OF THE EVOLUTION USING A θ-SCHEME

We now consider the problem (P) where the inertia term of equation (2.13) is ignored, since only slow flows are investigated. We present in this section a new method for solving problem (P) by the steps related to the alternating

direction implicit technique [20] for decoupling the two main difficulties, e.g., the non-linearity of equation (2.12) and the incompressibility equation (2.14). It will be shown that the corresponding algorithm enables to solve the problem under consideration in a reliable and efficient way.

3.1. The θ-scheme

Let H be a Hilbert space on $\mathbb{R}$. Consider a continuous operator A on H and the following problem :

Find $U \in L^{\infty}(H, \mathbb{R})$ such that :

$$m \frac{dU}{dt} + A(U) = 0 \tag{3.1}$$

$$U(0) = U_0 \tag{3.2}$$

given $U_0 \in H$ and $m \in \mathbb{R}$.

Using a decomposition of A on the form :

$$A = A_1 + A_2 \tag{3.3}$$

we may associate the sequence $(U^n)_{n \geq 0}$, $U^n \in H$, defined by the following relations :

$$U(0) = U_0 \tag{3.4}$$

and, for $n \geq 0$, an implicit definition of U^{n+1} according to the three-step following procedure :

$$m \frac{U^{n+\theta} - U^n}{\theta \, \Delta t} + A_1 U^{n+\theta} = - A_2 U^n \tag{3.5}$$

$$m \frac{U^{n+1-\theta} - U^{n+\theta}}{(1 - 2\theta) \Delta t} + A_2 U^{n+1-\theta} = - A_1 U^{n+\theta} \tag{3.6}$$

$$m \frac{U^{n+1} - U^{n+1-\theta}}{\theta \, \Delta t} + A_1 U^{n+1} = - A_2 U^{n+1-\theta} \tag{3.7}$$

where $\theta \in]0, 1/2[$ and $\Delta t > 0$.

It should be pointed out that equation (3.7) corresponds to a symmetrization step, which allows us to ensure the stability of the θ-scheme [11].

When A_1 and A_2 are linear operators, the scheme defined by equations (3.5)-(3.7) is unconditionally stable and has a error of $O(\Delta t^2)$.

3.2. Application to the solution of problem (P)

The relevant equations (2.12)-(2.14) of the slow flow of an Oldroyd-B fluid enable us to introduce two operators A_1 and A_2 related to the original

operator A by (3.3) which may be defined as follows :

$$A_1(\tau, \mathbf{u}, p) = \begin{pmatrix} \dfrac{\omega}{2\alpha}\tau - D(\mathbf{u}) \\ \operatorname{div}\tau + (1-\alpha)\Delta\mathbf{u} - \nabla p \\ \operatorname{div}\mathbf{u} \end{pmatrix} \tag{3.8}$$

where Δ denotes the Laplace operator corresponding to a boundary condition of Dirichlet type (2.7), $\omega \in]0, 1[$, and :

$$A_2(\tau, \mathbf{u}, p) = \begin{pmatrix} \dfrac{We}{2\alpha}((\mathbf{u}\cdot\nabla)\tau + \beta_a(\tau, \nabla\mathbf{u})) + \dfrac{1-\omega}{2\alpha}\tau \\ 0 \\ 0 \end{pmatrix}. \tag{3.9}$$

The diagonal matrix involving real elements is :

$$m = \operatorname{diag}\left(\frac{We}{2\alpha}, -Re, 0\right). \tag{3.10}$$

Application of the procedure defined by equations (3.5)-(3.7) to operator (3.8) and (3.9) gives a new algorithm [24] which allows us to decouple of the computation of stresses and pressure-velocity (we have used the relations $\operatorname{div}\mathbf{u}^{n+\theta} = 0$ and $2\operatorname{div}D(\mathbf{u}^{n+\theta}) = \Delta\mathbf{u}^{n+\theta}$ in step 1). This algorithm is described below.

Algorithm 3.1 alternating direction method ($We > 0$)

step 1 : τ^n and $\mathbf{u}^n$ being known, determine successively in an explicit way :

$$\gamma^n = (\mathbf{u}^n\cdot\nabla)\tau^n + \beta_a(\tau^n, \nabla\mathbf{u}^n) \tag{3.11}$$

$$f_1 = \lambda\mathbf{u}^n + c_1\operatorname{div}\tau^n + c_2\operatorname{div}\gamma^n \tag{3.12}$$

then determine $(\mathbf{u}^{n+\theta}, p^{n+\theta})$ solution of (S) :

$$\lambda\mathbf{u}^{n+\theta} - \eta\Delta\mathbf{u}^{n+\theta} + \nabla p^{n+\theta} = f_1 \quad \text{in} \quad \Omega \tag{3.13}$$

$$\operatorname{div}\mathbf{u}^{n+\theta} = 0 \quad \text{in} \quad \Omega \tag{3.14}$$

$$\mathbf{u}^{n+\theta} = u_f((n+\theta)\Delta t) \quad \text{on} \quad \Gamma \tag{3.15}$$

and compute :

$$\tau^{n+\theta} = c_1\tau^n + c_2\gamma^n + c_3 D(\mathbf{u}^{n+\theta}) \tag{3.16}$$

step 2 : $\tau^{n+\theta}$, $\mathbf{u}^{n+\theta}$ and $\mathbf{u}^n$ being known, compute explicitly :

$$g^{n+1-\theta} = c_4\tau^{n+\theta} + c_5 D(\mathbf{u}^{n+\theta}) \tag{3.17}$$

$$\mathbf{u}^{n+1-\theta} = \frac{1-\theta}{\theta}\mathbf{u}^{n+\theta} - \frac{1-2\theta}{\theta}\mathbf{u}^n \tag{3.18}$$

then find $\tau^{n+1-\theta}$ solution of (T) :

$$(\mathbf{u}^{n+1-\theta} \cdot \nabla)\,\tau^{n+1-\theta} + \beta_a(\tau^{n+1-\theta}, \nabla\mathbf{u}^{n+1-\theta}) + \nu\tau^{n+1-\theta} = g^{n+1-\theta} \tag{3.19}$$

$$\tau^{n+1-\theta} = \tau_\Gamma((n+1-\theta)\,\Delta t) \quad \text{on} \quad \Gamma_- \tag{3.20}$$

step 3 is obtained by replacing $(n+\theta)$ by $n+1$, and n by $(n+1-\theta)$ in step 1.

The different coefficients λ, η, ν, c_1, c_2, c_3, c_4 and c_5 are obtained from We, Re, α, θ, Δt and ω according to the following equations :

$$\lambda = \frac{Re}{\theta\,\Delta t} \tag{3.21}$$

$$\eta = 1 - \alpha\,\frac{We - (1-\omega)\,\theta\,\Delta t}{We + \omega\,\theta\,\Delta t} \tag{3.22}$$

$$\nu = \frac{1}{(1-2\,\theta)\,\Delta t} + \frac{1-\omega}{We} \tag{3.23}$$

$$c_1 = \frac{We - (1-\omega)\,\theta\,\Delta t}{We + \omega\,\theta\,\Delta t} \tag{3.24}$$

$$c_2 = -\frac{We\,\theta\,\Delta t}{We + \omega\,\theta\,\Delta t} \tag{3.25}$$

$$c_3 = \frac{2\,\alpha\,\theta\,\Delta t}{We + \omega\,\theta\,\Delta t} \tag{3.26}$$

$$c_4 = \frac{1}{(1-2\,\theta)\,\Delta t} - \frac{\omega}{We} \tag{3.27}$$

$$c_5 = \frac{2\,\alpha}{We}\,. \tag{3.28}$$

The algorithm 3.1 involves sub-problems (S) of Stokes type and sub-problems (T) of transport type. The steps 1 and 3 require the solving of sub-problems (S), and remain well-posed [10] because $\eta > 0$ for all $\alpha \in [0, 1[$, $We > 0$ and $\Delta t > 0$. Especially for high Weissenberg numbers :

$$\lim_{We \to +\infty} \eta = 1 - \alpha > 0 \tag{3.29}$$

for all $\alpha \in [0, 1[$.

A sufficient condition of well-posedness of the sub-problem (T) of transport type will be presented in section 5. Considering the choice of θ, we have followed Glowinski [11] using $\theta = 1 - \frac{1}{\sqrt{2}}$.

4. APPROXIMATION WITH RESPECT TO SPACE

We now consider the steady flow problem $\left(\frac{\partial}{\partial t} = 0 \right)$ of the Oldroyd-B fluid. This problem can be regarded as a singular perturbation of the Stokes problem (P_α), obtained with $We = 0$ [22] :

(P_α) : find τ, $\mathbf{u}$ and p, defined in Ω, and such that :

$$\tau - 2\,\alpha D(\mathbf{u}) = 0 \quad \text{in} \quad \Omega \tag{4.1}$$

$$\mathbf{div}\,\tau + (1-\alpha)\,\Delta\mathbf{u} - \nabla p = -\mathbf{f} \quad \text{in} \quad H^{-1}(\Omega)^2 \tag{4.2}$$

$$\operatorname{div}\mathbf{u} = 0 \quad \text{in} \quad \Omega \tag{4.3}$$

$$\mathbf{u} = \mathbf{u}_\Gamma \quad \text{on} \quad \Gamma \tag{4.4}$$

where Ω is convex, $\alpha \in [0, 1]$, $\mathbf{f} \in H^{-1}(\Omega)^2$, $\mathbf{u}_\Gamma \in H^{1/2}(\Gamma)$ are given, and $\mathbf{u}_\Gamma$ verify (2.10).

The problem (P_α) is effectively equivalent to the Stokes problem (P_0), of solution $(\mathbf{u}, p)$ independent of α :

(P_0) : Find $\mathbf{u}$ and p, defined in Ω, such that :

$$-\Delta\mathbf{u} + \nabla p = \mathbf{f} \quad \text{in} \quad H^{-1}(\Omega)^2 \tag{4.5}$$

$$\operatorname{div}\mathbf{u} = 0 \quad \text{in} \quad \Omega \tag{4.6}$$

$$\mathbf{u} = \mathbf{u}_\Gamma \quad \text{on} \quad \Gamma\,. \tag{4.7}$$

Although equations (4.1)-(4.4) are still linear, it should be pointed out that great care is to be taken with the incompressibility condition (4.3). In the finite-element context, the use of classical approximation methods for the velocity field requires sophisticated elements, leading to more or less good approximation of equation (4.3). This is all the more troublesome as the velocity fiel $\mathbf{u}$ is likely to transport the stress tensor, for example in sub-problem (T).

As the starting point of our analysis, we shall consider here the incompressible finite element of Thomas-Raviart [10, 23] for the velocities. Then, we shall list here the basic properties of this element. Finally, two possible approximations for the tensors which will assure the well-posedness of the related approximate problems are considered.

4.1. Approximation of vectors

We consider now a two-dimensional flow situation in a convex polygonal domain Ω. In order to approximate the Stokes problem (P_0), we introduce the (scalar) vorticity field ω as :

$$\omega = \operatorname{curl}\mathbf{u} = \partial_1 u_2 - \partial_2 u_1 \tag{4.8}$$

related to a vector field $\mathbf{u} = (u_1, u_2)$.

Using the notation :

$$\mathbf{curl}\ \omega = (\partial_2 \omega\ ;\ -\partial_1 \omega) \tag{4.9}$$

we may write the following equation :

$$\mathbf{curl}\ \mathbf{curl}\ \mathbf{u} = -\Delta \mathbf{u} + \nabla\ \mathrm{div}\ \mathbf{u} \tag{4.10}$$

Let Θ_h, V_h and P_h be finite dimensional vector spaces such that :

$$\begin{aligned} &\Theta_h \subset H^1(\Omega) \\ &V_h \subset H(\mathrm{div}\ ;\ \Omega) \\ &P_h \subset L^2(\Omega)\ . \end{aligned} \tag{4.11}$$

We also consider the spaces :

$$V_{0h} = \{\mathbf{v} \in V_h\ ;\ \mathbf{v}\ .\ \mathbf{n} = 0 \quad \text{on} \quad \Gamma\} \tag{4.12}$$

and

$$P_{0h} = \left\{q \in L^2(\Omega)\ ;\ \int_\Omega q\ dx = 0\right\}\ . \tag{4.13}$$

An approximating variational formulation of problem (P_0) involved by equations (4.5)-(4.7) is :

$(P_0)_h$: Find $(\omega_h, \mathbf{u}_h, p_h) \in \Theta_h \times V_h \times P_{0h}$ such that $\mathbf{u}\ .\ \mathbf{n} = \mathbf{u}_\Gamma\ .\ \mathbf{n}$ on Γ and :

$$(\omega_h, \theta) - (\mathbf{curl}\ \theta, \mathbf{u}_h) = \langle \mathbf{u}_\Gamma\ .\ \mathrm{t}, \theta \rangle \tag{4.14}$$

$$-(\mathbf{curl}\ \omega_h, \mathbf{v}) + (\mathrm{div}\ \mathbf{v}, p_h) = -(\mathrm{f}, \mathbf{v}) \tag{4.15}$$

$$(\mathrm{div}\ \mathbf{u}_h, q) = 0 \tag{4.16}$$

for any $(\theta, \mathbf{v}, q) \in \Theta_h \times V_{0h} \times P_h$. We suppose here $\mathrm{f} \in L^2(\Omega)^2$. The symbols $(\ .\ ,\ .\ )$ and $\langle\ .\ ,\ .\ \rangle$ denote the scalar product of spaces $L^2(\Omega)$ and $L^2(\Gamma)$ respectively. The vector t is written as : $\mathrm{t} = (-n_2, n_1)$ if $\mathbf{n} = (n_1, n_2)$.

Lastly, we define the spaces X_h and X_{0h} by the following expressions :

$$X_h = \{\mathbf{v} \in V_h\ ;\ (\mathrm{div}\ \mathbf{v}, q) = 0,\ \text{for all}\ q \in P_h\} \tag{4.17}$$

$$X_{0h} = \{\mathbf{v} \in X_h\ ;\ \mathbf{v}\ .\ \mathbf{n} = 0 \quad \mathbf{on} \quad \Gamma\}\ . \tag{4.18}$$

On the basis on [10], if the spaces Θ_h, V_h and P_h satisfy the following compatibility conditions :

$$X_h \subset \mathbf{curl}\ \Theta_h \tag{4.19}$$

$$(q_h \in P_h \text{ and } (\mathrm{div}\ \mathbf{v}_h, q_h) = 0, \text{ for all } \mathbf{v}_h \in X_{0h}) \Rightarrow q_h = 0 \tag{4.20}$$

then the problem $(P_0)_h$ (equations (4.14)-(4.16)) has a unique solution.

Practically, following [10, chap. 3] and [23], we adopt the following spaces :

$$\Theta_h = \left\{\theta \in H^1(\Omega) \cap C^0(\Omega) ; \theta_{|K} \in P_k(K), \text{ for all } K \in T_h\right\} \quad (4.21)$$

$$V_h = \left\{\mathrm{v} \in H(\mathrm{div} ; \Omega) ; \mathrm{v}_{|K} \in RT_k(K), \text{ for all } K \in T_h\right\} \quad (4.22)$$

$$P_h = \left\{q \in L^2(\Omega) ; q_{|K} \in P_{k-1}(K), \text{ for all } K \in T_h\right\} \quad (4.23)$$

which satisfy the conditions (4.19)-(4.20). The subspace $RT_k(K)$ is defined hereafter. $(T_h)_{h>0}$ denotes a family of regular triangulations of $\bar{\Omega}$ indexed by a parameter $h > 0$. T_h is a triangulation composed of triangles or convex quadrilaterals of diameter majored by h. $k \geq 1$ denotes an integer which is used to define the level of the finite element method. $P_l(K)$, $l \geq 0$, denotes the subspace of dimension $\frac{1}{2}(l+1)(l+2)$ related to polynomials defined on a triangle K (respectively $(l+1)^2$ for a convex quadrilateral) of degree lower or equal than l with respect to the two variables (respectively, to each variable).

These definitions imply that elements of Θ_h are continuous at the interfaces of the elements, which is not verified, in general, for elements of P_h. According to the definition (4.22) of V_h, the assumption $\mathrm{v} \in H(\mathrm{div} ; \Omega)$ is equivalent to verify the continuity of normal components of $\mathrm{v} \in V_h$ through the interfaces of the elements.

We define the subspace $RT_k(K)$ by :

$$RT_k(K) = \left\{\mathrm{v} \in H(\mathrm{div} ; K) ; J_K^{-1} . DF_K'(\mathrm{v}) \in RT_k(\hat{K})\right\} \quad (4.24)$$

where F_K is the invertible application which maps the triangle (respectively square) $\hat{K}$ of reference into a triangle (respectively convex quadrilateral) K. DF_K denotes the Jacobian matrix of K and J_K its determinant.

When $\hat{K}$ is the reference triangle, $RT_k(\hat{K})$ is found to be the space of dimension $k(k+2)$ of vectors $\hat{\mathrm{v}} = (\hat{v}_1, \hat{v}_2)$ of the form :

$$\hat{v}_1(\xi_1, \xi_2) = \hat{p}_1(\xi_1, \xi_2) + \left(\sum_{i=0}^{k-1} \alpha_i \xi_1^{k-i-1} \xi_2^i\right) \cdot \xi_1 \quad (4.25)$$

$$\hat{v}_2(\xi_1, \xi_2) = \hat{p}_2(\xi_1, \xi_2) + \left(\sum_{i=0}^{k-1} \alpha_i \xi_1^{k-i-1} \xi_2^i\right) \cdot \xi_2 \quad (4.26)$$

where $\hat{p}_1, \hat{p}_2 \in P_{k-1}(\hat{K})$ and $\alpha_i \in \mathbb{R}$, $0 \leq i \leq k-1$. We also get :

$$\mathrm{div}\ \hat{\mathrm{v}} = 0 \quad \text{if and only if} \quad \alpha_i = 0, \text{ for all } i,\ 0 \leq i \leq k-1 . \quad (4.27)$$

In the case where $\hat{K}$ is the reference square $[-1, 1]^2$, it can be shown that $RT_k(\hat{K})$ is the space of dimension $2k(k+1)$ of vectors $\hat{v} = (\hat{v}_1, \hat{v}_2)$ of the form :

$$\hat{v}_1 = \hat{p}_1(\xi_2) + \hat{q}_1(\xi_1, \xi_2) \cdot \xi_1 \tag{4.28}$$

$$\hat{v}_2 = \hat{p}_2(\xi_1) + \hat{q}_2(\xi_1, \xi_2) \cdot \xi_2 \tag{4.29}$$

where $\hat{p}_1, \hat{p}_2 \in P_{k-1}([0, 1])$ and $\hat{q}_1, \hat{q}_2 \in P_{k-1}(\hat{K})$. It is immediately seen that :

$$\text{div } \hat{v} = 0 \text{ if and only if } \partial_1(\xi_1 \cdot \hat{q}_1) + \partial_2(\xi_2 \cdot \hat{q}_2) = 0 . \tag{4.30}$$

Remark 4.1 : If T_h involves only triangles, the property (4.27) may be concisely written as :

$$X_h = P_h^2 . \tag{4.31}$$

Remark 4.2 : If T_h involves only rectangles, the sides of which are parallel to the reference axes, we obtain the interesting following property : for each $v = (v_1, v_2) \in X_{0h}$, there exists $\psi_1, \psi_2 \in P_h$ such that :

$$v_1(x_1, x_2) = x_1 \cdot \psi_1(x_1, x_2) \quad \text{and} \quad v_2(x_1, x_2) = x_2 \cdot \psi_2(x_1, x_2) \tag{4.32}$$

and

$$\partial_1(x_1 \cdot \psi_{1|K}) + \partial_2(x_2 \cdot \psi_{2|K}) = 0 \text{ in } K , \quad \text{for all} \quad K \in T_h . \tag{4.33}$$

4.2. Approximation of tensors

We now consider the problem (P_1) resulting from equations (4.1)-(4.4) for $\alpha = 1$. By relaxing the symmetry constraint $\tau = \tau'$ of the stress tensor, we define a family of finite elements which leads to a well-posed problem. Then, introducing a family of triangulations constituted by rectangles the sides of which are parallel to the axes, we propose a symmetric approximation of the tensors that generalizes the « Marker-and-Cell » [25] technique.

4.2.1. *Relaxation of the symmetry constraint*

Let T_h be a finite-dimensional subspace which verifies :

$$T_h \subset \{\gamma = (\gamma_{ij}) ; (\gamma_{i1}, \gamma_{i2}) \in H(\text{div} ; \Omega), i = 1, 2\} . \tag{4.34}$$

We now introduce a Lagrange multiplier λ, which belongs to a finite-dimensional space $M_h \subset L^2(\Omega)$ and define the space S_h by :

$$S_h = \{\gamma \in T_h ; (\gamma_{12} - \gamma_{21}, \mu) = 0 , \quad \text{for all} \quad \mu \in M_h\} . \tag{4.35}$$

An approximate variational formulation of the problem (P_1) may be expressed as follows :

$(P_1)_h$: find $(\tau_h, \mathbf{u}_h, \lambda_h, p_h) \in T_h \times V_h \times M_h \times P_{0h}$, $\mathbf{u} \cdot \mathbf{n} = \mathbf{u}_\Gamma \cdot \mathbf{n}$ on Γ, such that :

$$\frac{1}{2}(\tau_h, \gamma) + (\mathbf{div}\ \gamma, \mathbf{u}_h) + (\gamma_{12} - \gamma_{21}, \lambda_h) = \langle \mathbf{u}_\Gamma, \gamma \cdot \mathbf{n} \rangle \quad (4.36)$$

$$(\mathbf{div}\ \tau_h, \mathbf{v}) + (\operatorname{div} \mathbf{v}, p_h) = -(\mathbf{f}, \mathbf{v}) \quad (4.37)$$

$$(\tau_{h;12} - \tau_{h;21}, \mu) = 0 \quad (4.38)$$

$$(\operatorname{div} \mathbf{u}_h, q) = 0 \quad (4.39)$$

for any $(\gamma, \mathbf{v}, \mu, q)$ in $T_h \times V_{0h} \times M_h \times P_h$.

PROPOSITION 4.1 : *If the spaces T_h, V_h, M_h and P_h verify the compatibility conditions* (4.20) *and :*

if $(\mathbf{v}_h, \mu_h) \in X_{0h} \times M_h$,

$$(\mathbf{div}\ \gamma, \mathbf{v}_h) + (\gamma_{12} - \gamma_{21}, \mu_h) = 0\ , \quad \text{for all} \quad \gamma \in T_h \quad (4.40)$$

then $\mathbf{v}_h = 0$ *and* $\mu_h = 0$.

Then, the problem $(P_1)_h$ admits a unique solution.

Proof : Equations (4.36)-(4.39) of $(P_1)_h$ define a closed linear system, it is sufficient to prove the uniqueness property.

Suppose $\mathbf{f} = 0$ and $\mathbf{u}_\Gamma = 0$, and let $(\tau_h, \mathbf{u}_h, \lambda_h, p_h)$ a solution of the problem under consideration. Putting (4.39) with $q = p_h$ in equation (4.37) with $\mathbf{v} = \mathbf{u}_h$, we get $(\mathbf{u}_h, \mathbf{div}\ \tau_h) = 0$. Similarly, using equation (4.38) with $\mu = \lambda_h$ in equation (4.36) with $\gamma = \tau_h$, leads to $\tau_h = 0$. Thus, equation (4.36) may be written as :

$$(\mathbf{div}\ \gamma, \mathbf{u}_h) + (\gamma_{12} - \gamma_{21}, \lambda_h) = 0$$

for all $\gamma \in T_h$, that means, according to (4.40) : $\mathbf{u}_k = 0$ and $\lambda_h = 0$. In that case, with the help of (4.20), equation (4.37) implies that $p_h = 0$. □

We now select the following spaces :

$$T_h^{(1)} = \left\{ \gamma = (\gamma_{ij}) \in H(\operatorname{div} ; \Omega) ; (\gamma_{i1}, \gamma_{i2}) \in V_h,\ i = 1, 2 \right\} \quad (4.41)$$

$$M_h^{(1)} = P_h \quad (4.42)$$

and $S_h^{(1)}$, related to definition (4.35).

THEOREM 4.1 : *When the subspaces $T_h^{(1)}$ (equation* (4.41)*), V_h* (4.22)*, $M_h^{(1)}$* (4.42) *and P_h* (4.23) *are selected as spaces T_h, V_h, M_h, P_h, respectively, the problem $(P_1)_h$ admits a unique solution.*

Proof : It is sufficient to verify condition (4.40). For purpose of simplification, let us suppose that the triangulation T_h involves only triangles.

First, we consider $\gamma \in T_h^{(1)}$ such that **div** $\gamma = 0$. According to (4.31), we have $\gamma \in P_h^4$. With $\gamma_{11} = \gamma_{22} = 0$ and $\gamma_{12} = -\gamma_{21} = \frac{1}{2}\mu_h \in P_h$, we get $\mu_h = 0$.

Secondly, using (4.40) for every component of $\mathbf{v}_h$, we obtain, from (4.20) : $\mathbf{v}_h = 0$. □

Remark 4.3 : The element of lowest order $k = 1$ and the nodal localization of degrees of freedom are shown on figure 1.

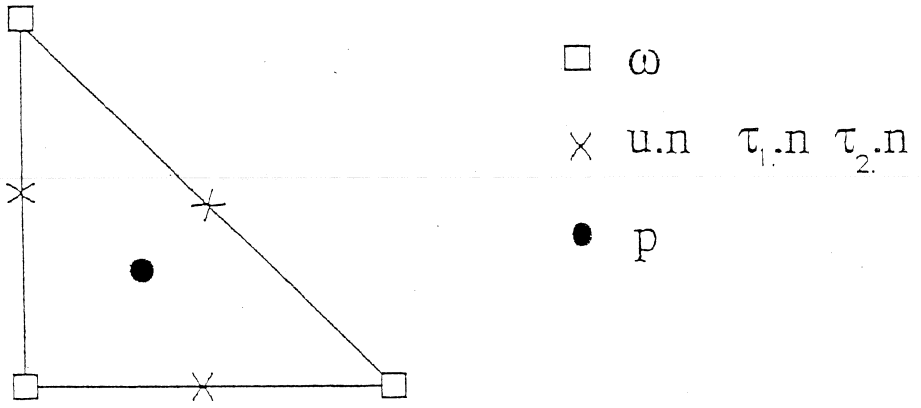

Figure 1. — Triangular element ($k = 1, 2$).

4.2.2. *Symmetric approximation of the tensors*

When the triangulation T_h only involves rectangles the sides of which are parallel to the reference axes, it is possible to define the derivatives $\partial_i \nu_i$, $i = 1, 2$ as elements of P_h, for a given element $\mathbf{v} = (\nu_1, \nu_2) \in V_h$. The main idea consists in considering separately the normal components τ_{ii}, $i = 1, 2$ and the shearing components $\tau_{ij} = \tau_{ji}$, $i \neq j$ of the stress tensor $\tau = (\tau_{ij})$.

Let S_h be a finite-dimensional subspace defined as :

$$S_h \subset \left\{ \gamma = (\gamma_{ij}) ;\ \gamma_{ii} \in L^2(\Omega) ;\ \gamma_{ij} = \gamma_{ji} \in H^1(\Omega) \cap \bar{C}^0(\bar{\Omega}),\ i \neq j \right\} . \tag{4.43}$$

An approximate variational formulation of problem (P_1) may be expressed as :

$(\tilde{P}_1)_h$: find $(\tau_h, \mathbf{u}_h, p_h) \in S_h \times V_h \times P_{0h}$, $\mathbf{u} = \mathbf{u}_\Gamma$ on Γ, such that

$$\frac{1}{2}(\tau_h, \gamma) - \sum_{i=1}^{2} (\gamma_{ii}, \partial_i \nu_i) + \sum_{i \neq j} (\partial_j \gamma_{ij}, u_{h;i}) = \sum_{i \neq j} \langle \gamma_{ij} \cdot n_j, u_{\Gamma;i} \rangle \tag{4.44}$$

$$- \sum_{i=1}^{2} (\tau_{h;ii}, \partial_i \nu_i) + \sum_{i \neq j} (\partial_j \tau_{h;ij}, \nu_i) +$$

$$+ (\text{div } \mathbf{v}, p_h) = - (\mathbf{f}, \mathbf{v}) - \sum_{i=1}^{2} \langle \tau_{\Gamma;ii} \cdot n_i, \nu_i \rangle \quad (4.45)$$

$$(\text{div } \mathbf{u}_h, q) = 0 \quad (4.46)$$

for any $(\gamma, \mathbf{v}, q) \in S_h \times V_{0h} \times P_h$, where $\tau_{\Gamma;ii} = 2\, \partial_i \mathbf{u}_{\Gamma;i}$ on Γ.

PROPOSITION 4.2 : *If the spaces S_h, V_h and P_h verify the compatibility condition* (4.20) *and :*

if $\mathbf{v}_h \in X_{0h}$,

$$- \sum_{i=1}^{2} (\gamma_{ii}, \partial_i \nu_{i;h}) + \sum_{i \neq j} (\partial_j \gamma_{ij}, \nu_{i;h}) = 0\,, \quad \text{for all} \quad \gamma \in S_h \quad (4.47)$$

then $\mathbf{v}_h = 0$

then a unique solution for problem $(\tilde{P}_1)_h$ *exists.*

Proof : The proof is similar to that given for proposition 4.1. □

We now consider the space :

$$S_h^{(2)} = \left\{ \gamma = (\gamma_{ij})\,;\ \gamma_{ii} \in P_h\,;\ \gamma_{ij} = \gamma_{ji} \in \Theta_h \right\}\,. \quad (4.48)$$

THEOREM 4.2 : *If $S_h^{(2)}$ is considered as space S_h, and V_h and P_h are given by* (4.22) *and* (4.23), *then the problem $(P_1)_h$ admits a unique solution.*

Proof : We only have to verify the compatibility condition (4.47). Let $\mathbf{v}_h \in X_{0h}$. From remark 4.2, there exist ψ_1, $\psi_2 \in P_h$ such that $\mathbf{v}_h = (x_1\, \psi_1, x_2\, \psi_1)$. A choice of $\gamma \in S_h$ which satisfy $\gamma_{11|K} = \partial_1 (x_1 \cdot \psi_{1|K})$ and $\gamma_{22|K} = \partial_2 (x_2 \cdot \psi_{2|K})$ for all $K \in T_h$, $\gamma_{12} = \gamma_{21} = 0$ leads to $\partial_1 (x_1 \cdot \psi_{1|K}) = \partial_2 (x_2 \cdot \psi_{2|K}) = 0$ in K, for all $K \in T_h$. Hence $\psi_1 = \psi_2 = 0$: $\mathbf{v}_h = 0$. □

Remark 4.4 : In figure 2, we present a rectangular element the sides of which are parallel to the axes. The element of lowest order $k = 1$ may be considered as an extension of the « Marker and Cell » scheme [25].

4.3. Approximation of the Stokes problem

From the elements presented in previous sections we propose a variational approximation of problem (4.1)-(4.4) :

$(P_\alpha)_h$: Find $(\tau_h, \omega_h, \mathbf{u}_h, p_h) \in S_h \times \Theta_h \times V_h \times P_{0h}$, $\mathbf{u}_h \cdot \mathbf{n} = \mathbf{u}_\Gamma \cdot \mathbf{n}$ on Γ, such that :

$$(\tau_h, \gamma) + 2\, \alpha\, (\text{div } \gamma, \mathbf{u}_h) = 2\, \alpha\, \langle \mathbf{u}_\Gamma, \gamma \cdot \mathbf{n} \rangle \quad (4.49)$$

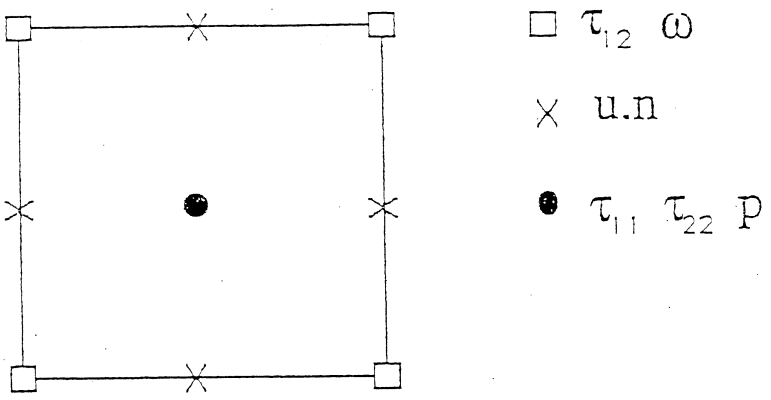

Figure 2. — Rectangular element ($k = 1, 2$).

$$(\omega, \theta) - (1 - \alpha)(\mathbf{curl}\ \theta, \mathbf{u}_h) = (1 - \alpha)\langle \mathbf{u}_\Gamma . \mathbf{t}, \theta \rangle \tag{4.50}$$

$$(\mathbf{div}\ \tau_h, \mathbf{v}) - (\mathbf{curl}\ \omega_h, \mathbf{v}) + (p_h, \mathrm{div}\ \mathbf{v}) = -(\mathbf{f}, \mathbf{v}) \tag{4.51}$$

$$(\mathrm{div}\ \mathbf{u}_h, q) = 0 \tag{4.52}$$

for each $(\gamma, \theta, \mathbf{v}, q) \in T_h \times \Theta_h \times V_{0h} \times P_h$.

Moreover, when the finite spaces are expressed by (4.21)-(4.23) and (4.41) or (4.48), it can be readily proved from the previous results that the problem $(P_\alpha)_h$ admits a unique solution, for all $\alpha \in [0, 1]$. When S_h is given by (4.48), $(\mathbf{u}_h, p_h)$ is independent of α.

The algebraic equations involved by equations (4.49)-(4.52) may be written as :

$$\begin{pmatrix} M_\tau & 0 & 2\alpha B' & 0 \\ 0 & M_\omega & (1-\alpha)R' & 0 \\ B & R & 0 & D' \\ 0 & 0 & D & 0 \end{pmatrix} \begin{pmatrix} T \\ W \\ U \\ P \end{pmatrix} = \begin{pmatrix} G_1 \\ G_2 \\ G_3 \\ G_4 \end{pmatrix} \tag{4.53}$$

where T, W, U, P denote the vectors of degrees of freedom related to τ_h, ω_h, $\mathbf{u}_h$ and p_h, respectively.

Using appropriate quadrature formulas for the evaluation of the coefficients of M_τ and M_ω, the matrices may be diagonalized. Then, the vector W can be easily eliminated from the system, by defining :

$$C = -(1 - \alpha) R . M_\omega^{-1} . R' . \tag{4.54}$$

Hence, we obtain :

$$\begin{pmatrix} M_\tau & 2\alpha B' & 0 \\ B & C & D' \\ 0 & D & 0 \end{pmatrix} \begin{pmatrix} T \\ U \\ P \end{pmatrix} = \begin{pmatrix} F_1 \\ F_2 \\ F_3 \end{pmatrix} . \tag{4.55}$$

By introducing the transport terms for the stresses, in order to involve the viscoelastic effects, the relevant system is written as :

$$\begin{pmatrix} A(U) & 2\alpha B^t & 0 \\ B & C & D^t \\ 0 & D & 0 \end{pmatrix} \begin{pmatrix} T \\ U \\ P \end{pmatrix} = \begin{pmatrix} \bar{F}_1 \\ F_2 \\ F_3 \end{pmatrix} \tag{4.56}$$

where $A(U) = M_\tau + We \, . \, T(U)$ and the « perturbation » matrix $T(U)$ is obtained from approximation of the transport term $(\mathbf{u} \, . \, \nabla)$. The approximating techniques are considered in the following section.

5. APPROXIMATION FOR THE TRANSPORT OF STRESSES

In this section, we present the analysis for approximation of sub-problems (T) related to algorithm 3.1 :

(T) : Given $\nu > 0$, $\mathbf{u} \in W^{1,\infty}(\Omega)^2$ and $g \in L^2(\Omega)^{4_s}$, find τ, defined in Ω, which verify :

$$(\mathbf{u} \, . \, \nabla)\tau + \beta_a(\tau, \nabla u) + \nu\tau = g \quad \text{in} \quad \Omega \tag{5.1}$$

$$\tau = \tau_\Gamma \quad \text{on} \quad \Gamma_- \, . \tag{5.2}$$

The bilinear form β_a is given by equation (2.15).

In order to avoid numerical oscillating solutions which may appear despite the existence of a regular exact solution, we have selected methods which permit to approximate the transport operator $(\mathbf{u} \, . \, \nabla)$ by a monotonous (or total variation decreasing) operator.

A sufficient condition to existence of weak solutions to problem (5.1)-(5.2) is given in [24] :

$$\nu - 2|a| \, \|D(\mathbf{u})\|_\infty > 0 \tag{5.3}$$

where a denotes the parameter involved in the objective derivation operator, and $\| \, . \, \|_\infty$ the norm of $L^\infty(\Omega)^4$.

For $a \neq 0$, and ν given by (3.23), a sufficient condition is :

$$\Delta t < \frac{1}{2|a|(1 - 2\theta)\|D(\mathbf{u})\|_\infty} \, . \tag{5.4}$$

In the following, upwind schemes for the approximating spaces will be examined.

5.1. Non-symmetric tensors

To simplify the notation, we will consider the approximation of the transport term for a general second-order tensor. The reader has to take care to introduce the symmetry constraint and the corresponding Lagrange multiplier for the problem under consideration.

Components of a tensor $\tau_h \in T_h^{(1)}$ are generally discontinuous at interfaces between elements (more precisely, the tangential components $\tau_i \,.\, t_K$, $i = 1, 2$ are discontinuous through the elements interfaces). Non-centered techniques are possible in schemes involving right-side or left-side values, according to the direction of the flow [17]. Then, the approximate problem may be written as follows :

$(T)_h$: find $\tau_h \in T_h^{(1)}$, $\tau_h = \tau_\Gamma$ on Γ_- such that

$$\sum_{K \in T_h} \left(- \int_{\partial K_-} (\mathbf{u} \,.\, \mathbf{n}_K)[\tau_h] \,.\, \gamma \, ds + \int_K (\mathbf{u} \,.\, \nabla)\, \tau_h \,.\, \gamma \, dx \right) + \int_\Omega (\beta_a(\tau_h, \nabla \mathbf{u}) + \nu \tau_h) \,.\, \gamma \, dx = \int_\Omega g \,.\, \gamma \, dx \quad (5.5)$$

for each $\gamma \in T_h^{(1)}$, $\gamma = 0$ on Γ_-.

We note $[\tau_h] = \tau_h^{\text{int}} - \tau_h^{\text{ext}}$ the step of τ_h at the separating line between one element to another in the direction of the outer unit normal vector $\mathbf{n}_K$ to the element K. We define :

$$\partial K_- = \{ x \in \partial K \,;\, (\mathbf{u} \,.\, \mathbf{n}_K)(x) < 0 \} \,. \quad (5.6)$$

The numerical analysis of this scheme has been extensively described by Girault and Raviart [10] for Navier-Stokes equations.

5.2. Symmetric tensors

In problem (T), a scalar transport problem may be considered for each component of tensor τ.

The normal component $\tau_{h\,;\,ii}$ are generally discontinuous and the method previously presented in section 5.1 can be applied in order to obtain the non-centered corresponding scheme.

The shear components $\tau_{h\,;\,ij}$, $i \neq j$ are continuous. In that case, the streamline upwind scheme as proposed by Hughes and Brooks [3] may be considered. The « non-consistent » formulation of the streamline upwind technique for the shear components is considered here. (See [18] for a comparison of efficiency with the Petrov-Galerkin formulation).

It should be pointed out that :

- The discontinuous method leads to monotonous schemes [12] only for element whose degree is equal or lower than 1 ;
- Although the streamline upwinding technique is not monotonous, the corresponding numerical results are generally found to be acceptable in many cases of practical interest.

6. NUMERICAL EXPERIMENTS

We now describe the application of the ADI method (already presented in 3.1) to the computation of the flow in a plane or axisymmetric contraction, subjected to specified boundary conditions. The results were obtained for different meshes, at various Weissenberg numbers.

6.1. General features of the flow in an abrupt contraction

6.1.1. *Introduction*

Such a flow is of interest from both theoretical and practical points of view (e.g., in relation to polymer processing problems), and has been investigated in numerous experimental works (see for example [2] and [6]). In the entry flow region, before the contraction, the fluid particles are accelerated close to the central region of the duct, while vortices appear close to the edges (see *fig.* 3). This flow may be considered a complex one, because it appears to be practically a shear flow close to the solid wall, and becomes rather elongational at the vicinity of the center. Experiments reported in the literature have shown increasing recirculating zones when the value of the Weissenberg number We increases.

6.1.2. *Boundary conditions*

In our numerical experiments, the abrupt contraction was considered as plane (plane flow, with cartesian coordinates $x_1 = x$, $x_2 = y$), with a plane of symmetry for $x = 0$, or axisymmetrical (we use cylindrical coordinates $x_1 = z$, $x_2 = r$, $x_3 = \theta$), involving an axis of symmetry $r = 0$. In both situations, we may consider a half-domain Ω corresponding to $x_2 > 0$, as shown in figure 4.

The rheological model of equation (1.3) involves the upper convected derivative for $a = 1$. The computational domain is assumed to be long enough to verify Poiseuille velocity profiles at upstream and downstream sections $x_1 = s_1$ and $x_2 = s_2$ of respective widths r_1 and r_2. Then we have :

$$u_{f:1}(s_i, x_2) = \frac{f_i}{2}\left(1 - \left(\frac{x_2}{r_i}\right)^2\right), \quad 0 \leq x_2 \leq r_i, \quad i = 1, 2 \qquad (6.1)$$

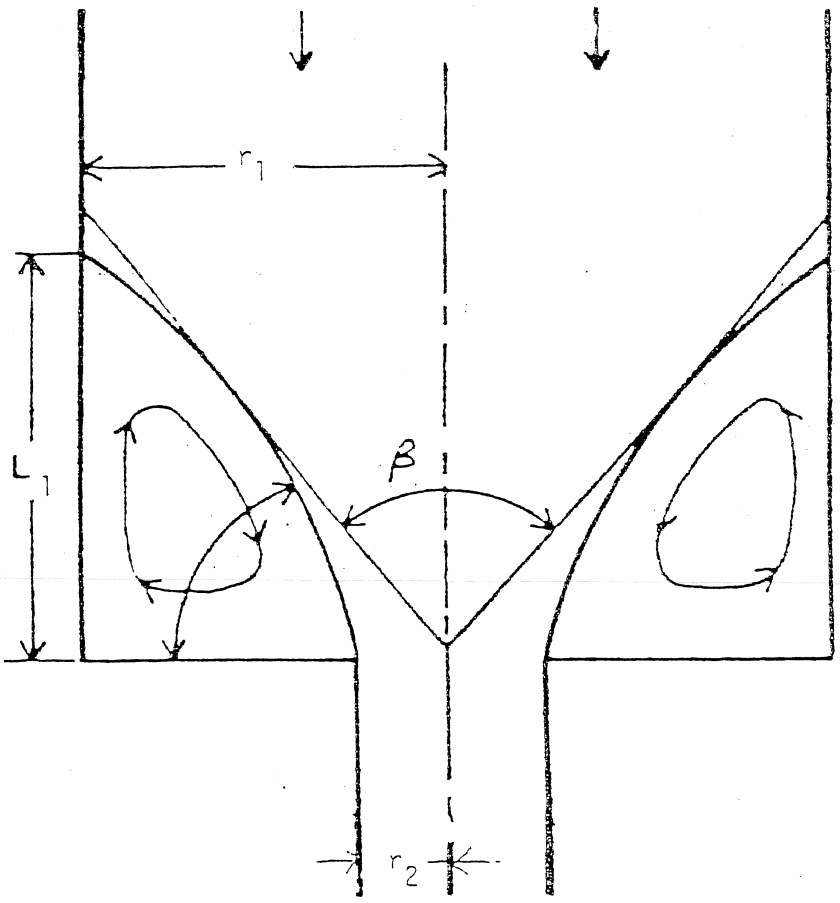

Figure 3. — Flow description in an abrupt contraction.

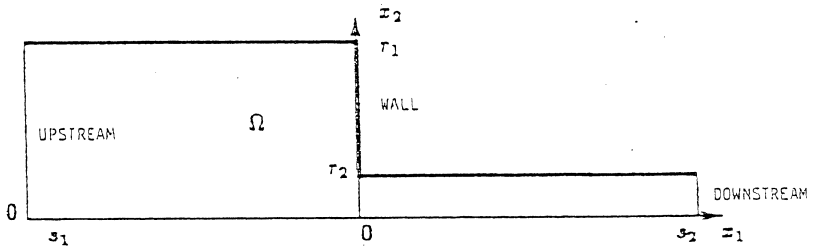

Figure 4. — Domain Ω for an abrupt contraction ($C = 4$).

$$u_{\Gamma;2}(s_i, x_2) = 0\,, \quad 0 \leq x_2 \leq r_i, \quad i = 1, 2 \tag{6.2}$$

where $f_i \in \mathbb{R}$, $i = 1, 2$.

For points in the plane or the axis of symmetry, we may write the following symmetry equation :

$$\frac{\partial u_{\Gamma;1}}{\partial x_2}(x_1, 0) = u_{\Gamma;2}(x_1, 0) = 0\,, \quad s_1 \leq x_1 \leq s_2 \tag{6.3}$$

and the boundary condition for the velocity :

$$\mathbf{u}_\Gamma = 0 \quad \text{at the wall}\,. \tag{6.4}$$

From the compatibility equation (2.10) related to the mass conservation, we get :

$$f_1 = \begin{cases} C^{-1} f_2 & \text{for a plane domain} \\ C^{-2} f_2 & \text{for an axisymmetric domain} \end{cases} \tag{6.5}$$

where $C = r_1/r_2$ denotes the contraction ratio.

The stresses at the upstream section are given by :

$$\tau_{11}(s_1, x_2) = 2\,\alpha We\,\frac{f_1^2\, x_2^2}{r_1^4}\,, \quad 0 \leq x_2 \leq r_1 \tag{6.6}$$

$$\tau_{22}(s_1, x_2) = 0\,, \quad 0 \leq x_2 \leq r_1 \tag{6.7}$$

$$\tau_{12}(s_1, x_2) = -\,\alpha\,\frac{f_1\, x_2}{r_1^2}\,, \quad 0 \leq x_2 \leq r_1\,. \tag{6.8}$$

In the axisymmetric case, the component τ_{33} (related to the coordinate θ) may be computed, and verify at the upstream section the following equation :

$$\tau_{33}(s_1, x_2) = 0\,, \quad 0 \leq x_2 \leq r_1\,. \tag{6.9}$$

The choice :

$$f_2 = r_2 \tag{6.10}$$

led us to fix the shear component σ_{12} of the Cauchy stress tensor σ (equation (2.1)) at the wall, in the downstream fully developed flow : $|\sigma_{12}| \to 1$ when $s_2 \to +\infty$. This choice allows us to fix the average velocity at the downstream to 1/3 (resp. 1/8) for a plane (resp. axisymmetric) domain.

6.2. Triangulation and finite elements

6.2.1. *Choice of parameters*

In our numerical investigations, we have chosen $C = 4$ and $r_2 = 1$. This corresponds to the classical four-to-one abrupt contraction generally investigated in numerical works. The values $s_1 = -64$ and $s_2 = 200$, related to positioning the upstream and downstream sections have proved to be satisfactory for obtaining accurate Poiseuille velocity profiles. The parameter α of the Oldroyd-B model was taken to be $\alpha = 8/9$, as usually done in calculations. The range of the Weissenberg numbers was : $0 \leq We \leq 90$. The tests were run on a Appolo DN 4000 workstation.

6.2.2. *Mesh and elements*

The choice of rectangular finite elements has proved to be well-adapted to the shape of the computational flow domain. We have retained the elements of lower degree ($k = 1$) with a symmetric approximation for the stresses (see section 4.2.2).

Starting from a rough triangulation $T^{(0)}$, a family $(T^{(i)})_{i \geq 0}$ was constructed by using a refining procedure of $T^{(0)}$ near the re-entrant corner (*fig.* 5). On $T^{(i)}$, the length of the elements close to the re-entrant corner is given by :

$$h_i = \frac{1}{3 \times 2^i} . \tag{6.11}$$

The length of elements quite distant from the corner is given by a geometric progression of constant factor. NE_i and NS_i denote the number of elements and vertices, respectively, such that :

$$N_i = \dim\,(S_h \times V_h \times P_h) = 4\,NE_i + 2\,NS_i - 1 . \tag{6.12}$$

It can be noticed that $NE_i \approx NS_i$ asymptotically, which leads to the approximation $N_i/NE_i \approx 6$ (see table 1).

Table 1. — Number of elements of the triangulations.

i	h_i	NF_i	NS_i	N_i	N_i/NF_i
0	0.3333	144	184	945	6.56
1	0.1667	299	356	1 909	6.38
2	0.0833	576	655	3 615	6.27
3	0.0416	1 196	1 309	7 403	6.18

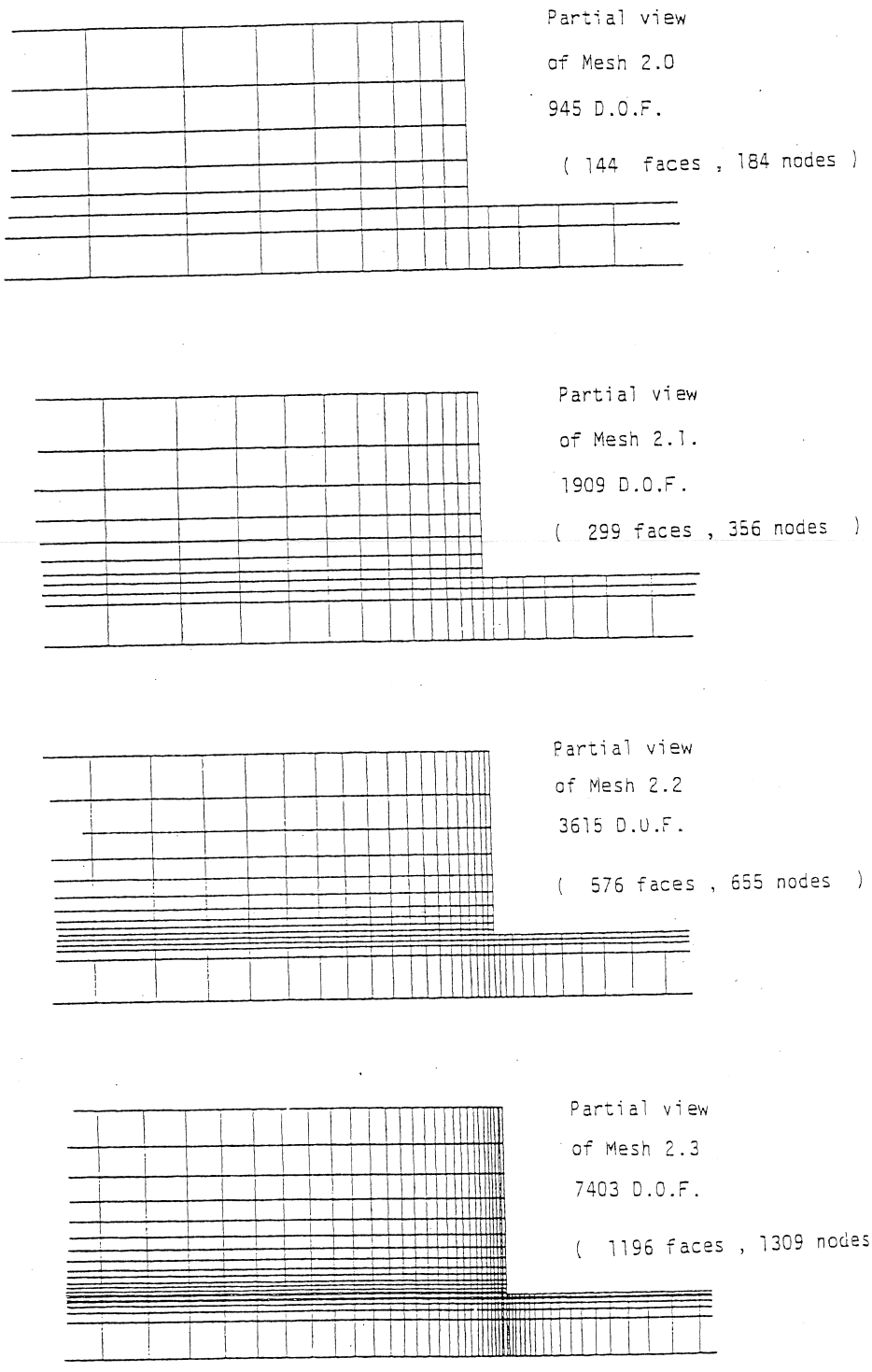

Figure 5. — Mesh family of the domain Ω (partial views).

Consequently, the method uses asymptotically a degree of freedom by element and by (one of the 6) scalar fields τ_{11}, τ_{12}, τ_{22}, u_1, u_2, and p, which appear to be an optimal number of unknowns.

6.3. Resolution of the sub-problems

The sub-problems (S) of the Stokes-type are solved using a conjugate-gradient method. The preconditioning is obtained by means of augmented Lagrangian methods [8]. The efficiency of this method was particularly spectacular, as the initial problem is ill-conditioned, due to the domain length and the presence of the re-entrant corner.

The transport sub-problems (T) are solved by using SSOR with block symmetrization [24]. All the elements are numbered in the direction of the main flow. Numerical tests of this procedure have shown fast convergence (in iteration number and time) of the residual terms.

6.4. Results for a four-to-one abrupt contraction

We now consider the numerical results obtained for the plane or axisymmetric contraction, in relation to the presence of the corner, which is expected to generate important vortices near the salient corner, and modifications on the evolution of stresses and velocities.

6.4.1. *Normal stress component τ_{11} at the vicinity of the corner*

We first observe on figure 6 the influence of the Weissenberg number on the first normal stress τ_{11} along the straight line $x_2 = 1$ close to the re-entrant corner. We notice that :

(i) the peak (theoretically infinite at the corner singularity) becomes sharper and higher as the Weissenberg number increases. Similar examples could be also presented for the other stress components τ_{12} and τ_{22}.

(ii) the accuracy of our computations can be asserted by considering the fully-developed Poiseuille profiles (for velocity and stress) at the downstream section. The shortest downstream section length such that the Poiseuille profiles are fully-developed increases as the Weissenberg number becomes greater (see also [4, 7]).

The stress at the downstream section tends to $2\,\alpha We\,\dfrac{f_2^2}{r_2^2}$.

6.4.2. *Recirculating zones*

In order to comment the numerical results for the vortices, we have computed the stream function ψ, which is characterized as the unique solution of the following variational problem :

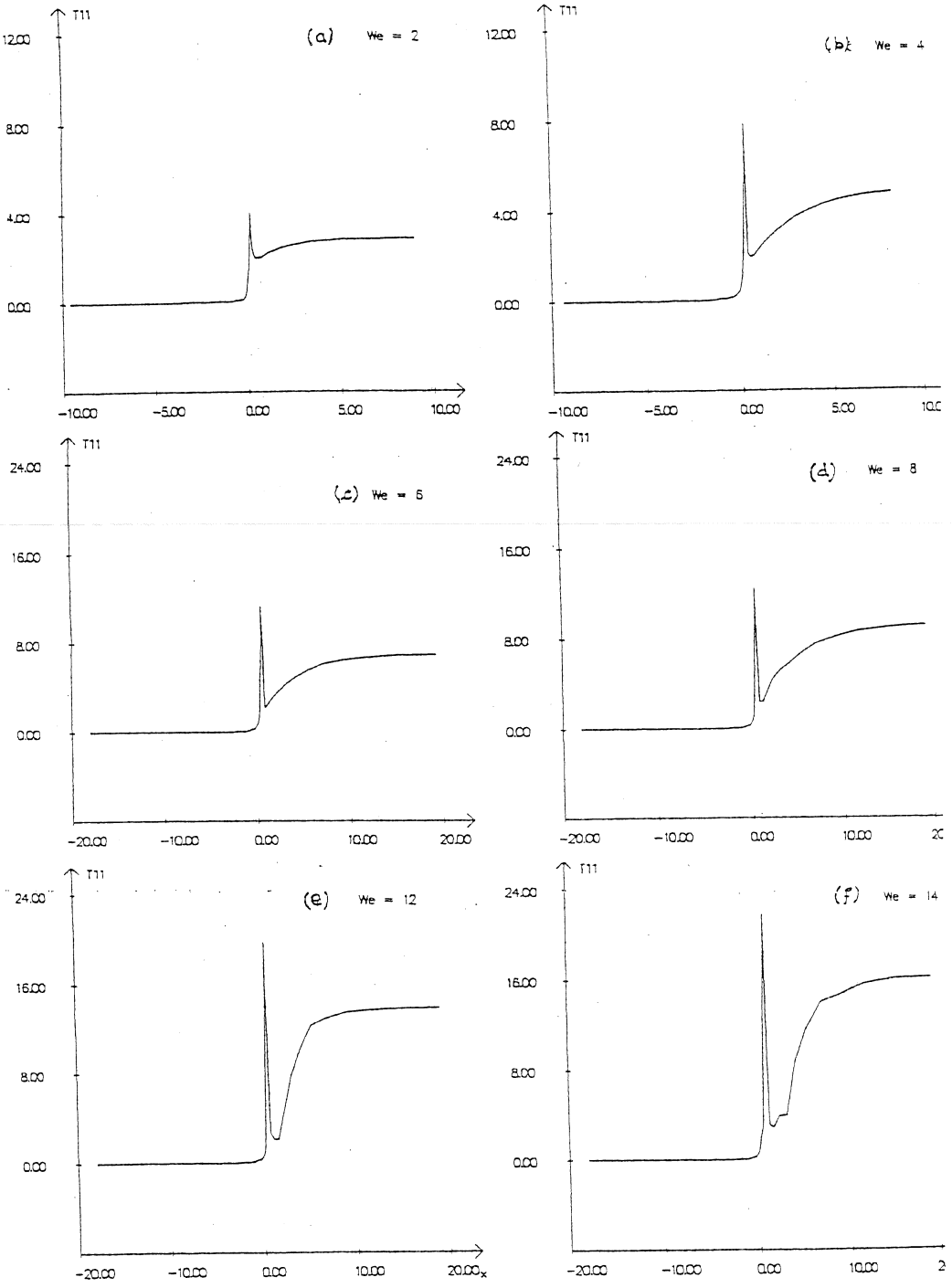

Figure 6. — Stress component τ_{11} at the corner singularity.

(F) find $\psi \in H^1(\Omega)$, $\psi = \psi_\Gamma$ on Γ, such that :

$$(\mathbf{curl}\ \psi,\ \mathbf{curl}\ \xi) = (\mathbf{u},\ \mathbf{curl}\ \xi), \quad \text{for all} \quad \xi \in H_0^1(\Omega) \tag{6.13}$$

where $\mathbf{u}$ denotes the velocity field, and ψ_Γ the boundary condition given at the upstream and downstream section by :

$$\psi_\Gamma = \psi_0 \cdot \Phi\left(\frac{x_2}{r_i}\right), \quad 0 \leq x_2 \leq r_i, \quad i = 1, 2 \tag{6.14}$$

where

$$\Phi(x) = \begin{cases} 1/2\,(x-1)^2\,(x+2) & \text{for a plane domain} \\ (x-1)^2\,(x+1)^2 & \text{for an axisymmetric domain} \end{cases} \tag{6.15}$$

and

$$\psi_0 = \begin{cases} f_2\, r_2/3 & \text{for a plane domain} \\ f_2\, r_2^2/8 & \text{for an axisymmetric domain .} \end{cases} \tag{6.16}$$

On the axis, we may write :

$$\psi_\Gamma(x_1, 0) = \psi_0, \quad s_1 \leq x_1 \leq s_2 \tag{6.17}$$

and $\psi_\Gamma = 0$ on the wall.

The flow will be represented by the sketch of the computed streamlines, which are lines of ψ/ψ_0. The main flow in the central region corresponds to the case $\psi > 0$, since the recirculating zone is characterized by $\psi < 0$. The separating line between the two regions is determined by the condition $\psi = 0$.

The intensity of the recirculations is determined by the quantity

$$\min_{x \in \Omega} (\psi/\psi_0).$$

When the velocity field is approximated by $\mathbf{u}_h \in V_h$, it is possible to approximate ψ, the unique solution of (F), by $\psi_h \in \Theta_h$.

Figure 7 shows the sketch of streamlines in a plane (7*a*) and an axisymmetric (7*b*) contractions, for the triangulation $T^{(3)}$. It can be seen in figure 8 that for the case of plane symmetry, the intensity and the length of the circulating zones appear to increase moderately when the Weissenberg number grows. This result confirms those given in the literature [4, 7].

Conversely, in the case of the axisymmetric contraction, it is well-known that viscoelastic liquids exhibit important vortex zones, which notably differ from the Newtonian behavior in such geometry. From our own results, we observe that, when the Weissenberg *We* increase, the center of the circulating zone moves from the re-entrant corner to the salient edge

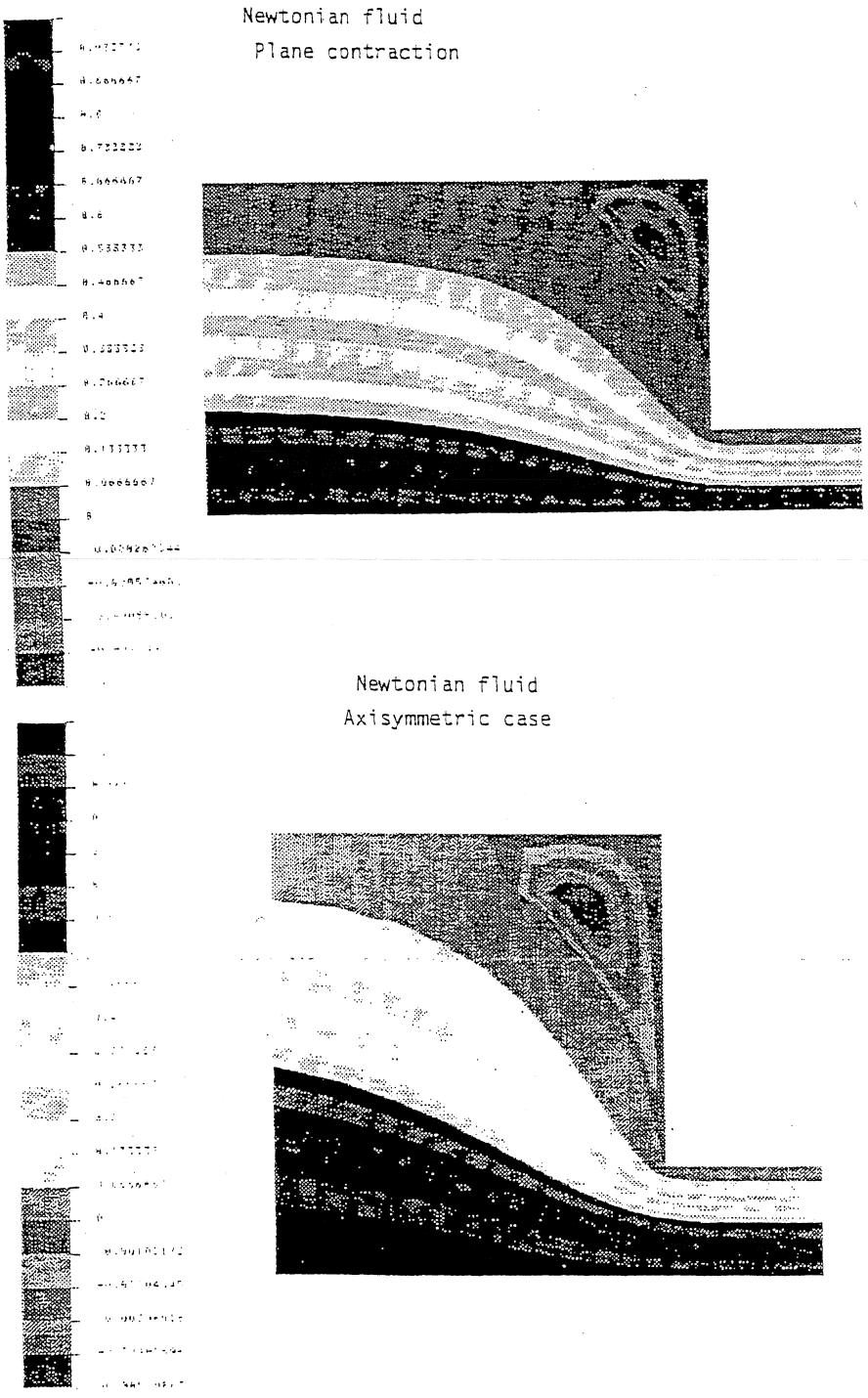

Figure 7. — Streamlines for a slow Newtonian flow in a plane (a) and axisymmetric (b) abrupt contraction.

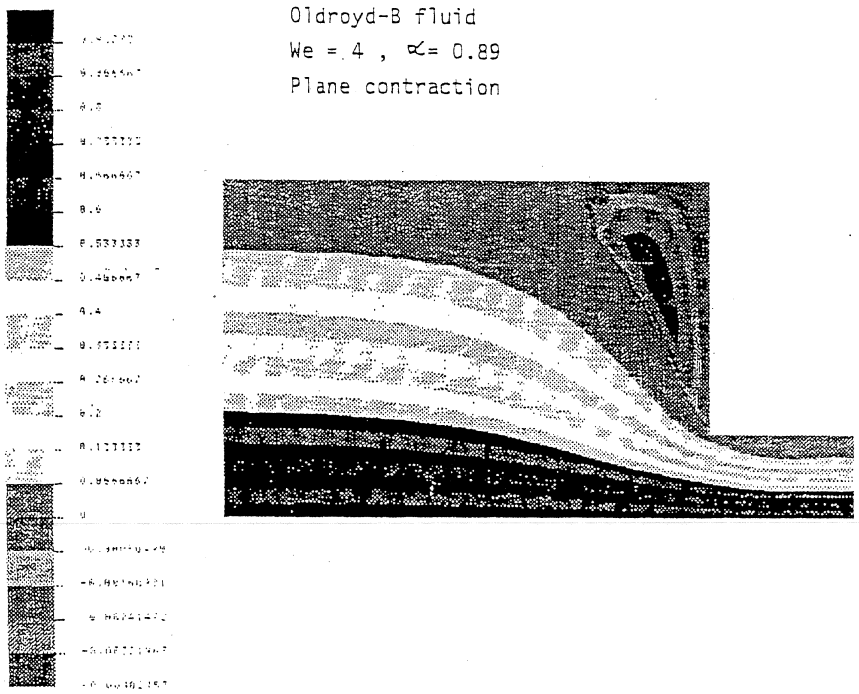

Figure 8. — Streamline in plane contraction ($We = 4$).

($We = 20$, *fig.* 9) and the intensity of the recirculation is increasing. The focus zone then moves towards the upstream section and enlarges near the separating line, as can be seen in figure 10, at $We = 60$. It can finally be observed that the secondary flow zone leaves the re-entrant corner towards the salient edge with an axial increase of size in direction to the upstream section (*fig.* 11, $We = 90$).

Beyond the value of $We = 100$, the width $s_2 = 200$ does not permit the fully developed Poiseuille flow to be obtained at the limiting downstream section. Although no convergence problems were encountered for $We > 100$, the numerical experiments were not pursued beyond this value, mainly because of the necessity to extend the downstream flow zone. It should be outlined that, up to $We = 100$, stationary numerical solutions were still obtained by the algorithm.

6.4.3. *Velocity profiles on the axis*

A velocity overshoot for the first velocity component $u_1(x_1, 0)$, $s_1 \leq x_1 \leq s_2$ may be observed, in comparison with the downstream Poiseuille velocity profile. This overshoot phenomenon, which is not clearly apparent

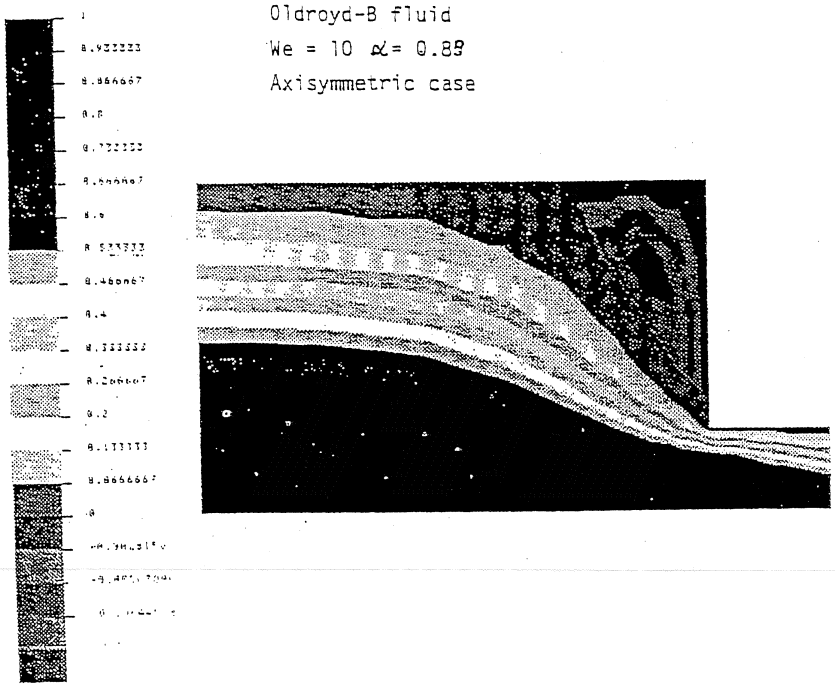

Figure 9. — Streamline in axisymmetric contraction ($We = 10$).

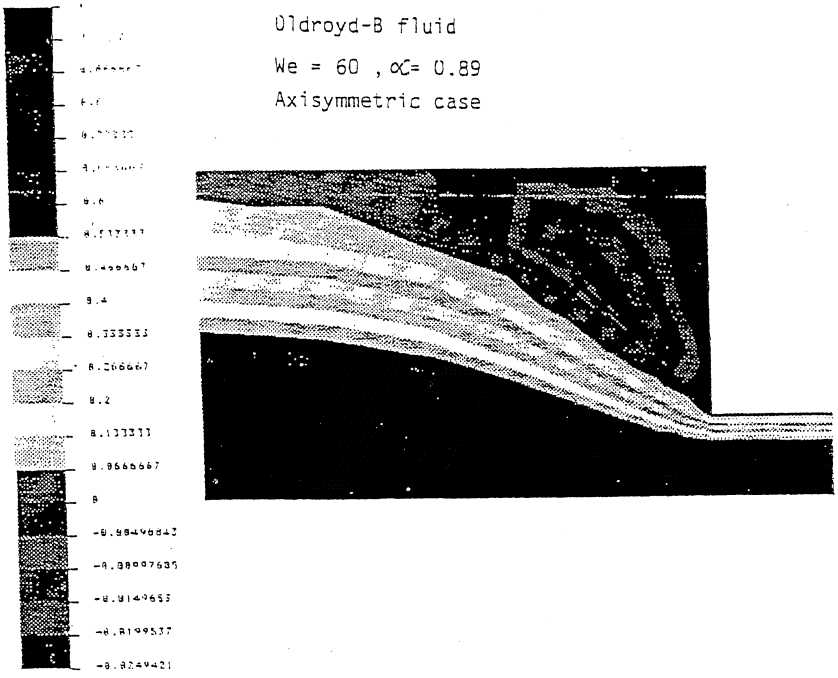

Figure 10. — Streamline in axisymmetric contraction ($We = 60$).

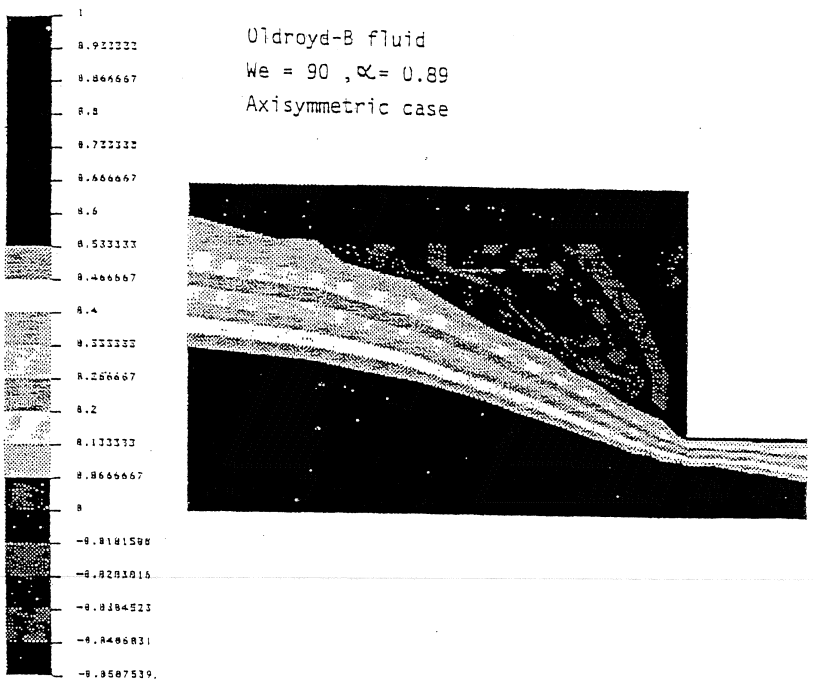

Figure 11. — Streamline in axisymmetric contraction ($We = 90$).

for a Newtonian fluid (*fig.* 12*a*) is found to increase fastly *versus* *We*. According to our results, the abscissa of the maximum value of u_1 moves towards the downstream section when the Weissenberg number increases (*figs.* 12*b* and 12*c*).

6.4.4. *Computing time*

On table 2, we have reported the CPU times for the converged solution at $We = 4$, as a function of the triangulation which has been used.

The low cost of our numerical procedure makes it practical for a workstation (e.g., Apollo DN 4000). The use of the C language allowed us to manage the storage area efficiently (by performing dynamic memory allocation and reclamation) : compacting procedures for the storage of the matrix resulting from the finite element method were used. The storage area cost was found to be linear in term of the size N.

7. CONCLUSION

In this paper, the major problems related to the numerical simulation of the flow of certain classes of constitutive equations have been considered. A

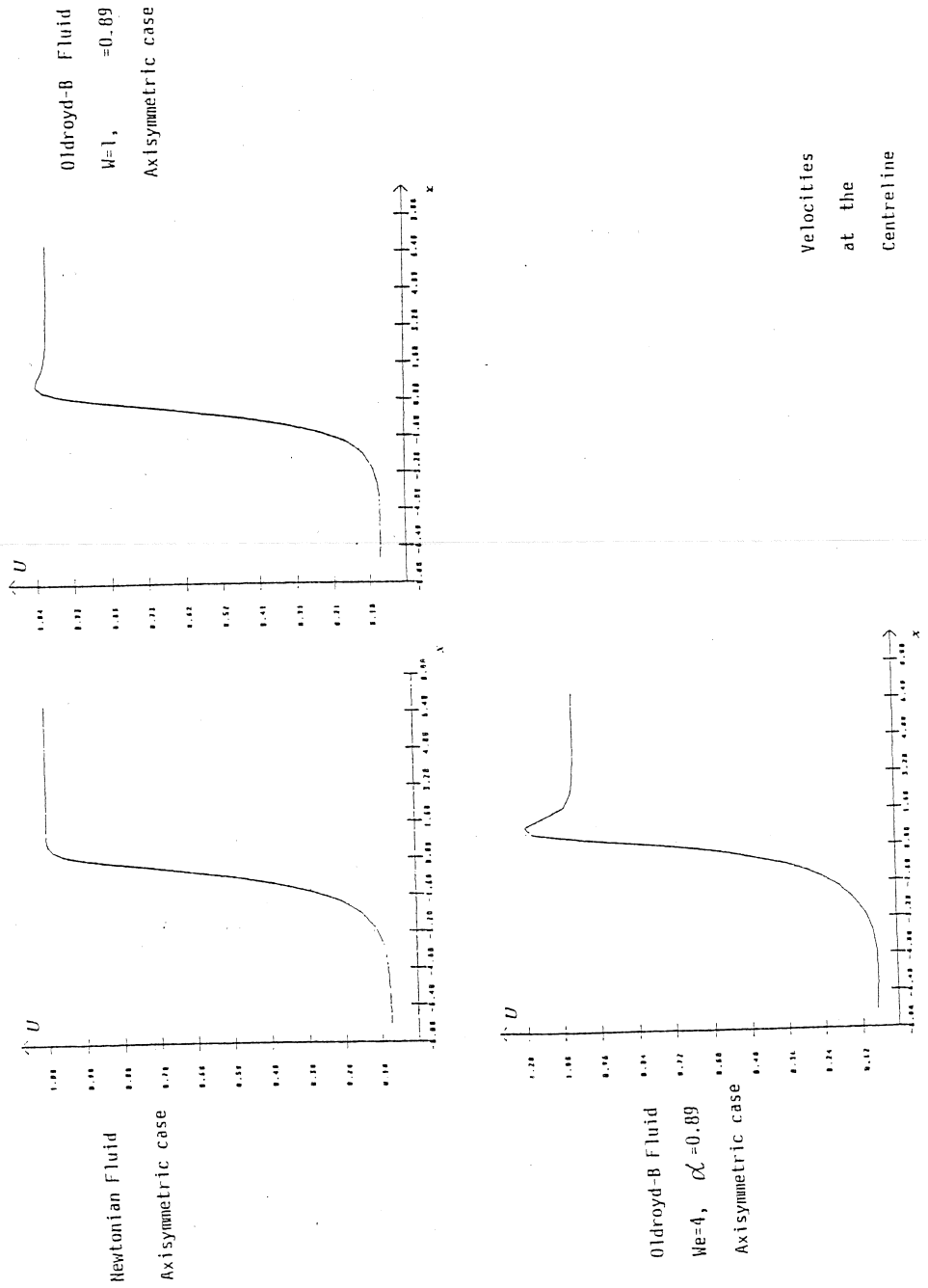

Figure 12. — Velocity profile on the axis.

Table 2. — Cost in computing time and storage area.

Mesh	N	CPU time
0	945	55 s
1	1 909	3 mm 28 s
2	3 615	10 mm 16 s
3	7 403	28 mm 32 s

resolution procedure has been proposed, which enables to overcome the difficulties detailed at the beginning of the paper. The distinguishing features of the method may be summarized as follows :

i) The retained approximation for the unknowns verifies the compatibility conditions, leading to a well-posed problem when the Weissenberg number is zero. The elements chosen for the computation are robust : the incompressibility condition is verified exactly. Moreover, the particular element defined in section 4.2.2 is inexpensive, and may be interpreted in the context of finite difference schemes : this element is easy to use and could be inserted in existing codes.

ii) The approximate transport sub-problem related to the Oldroyd-B equations has been solved with appropriate schemes, giving stationary solutions at high Weissenberg numbers.

iii) Spectacular reduction of the CPU time has been obtained. The algorithm involving an ADI procedure appears to be robust and efficient : the computational steps are decoupled into standard sub-problems which can be solved in optimal conditions. Moreover, the space-time solution procedure enables us to consider in the next future time-dependent viscoelastic problems.

The method presented in this paper has been applied (and validated) to a difficult problem. Since the solution is singular due to the re-entrant corner of the contraction, we have had to generate meshes involving a high number of elements : our method made it practically tractable.

Our results have been found to be quantitatively consistent with those given by Marchal and Crochet [4]. Moreover, it has proved possible to compute on a workstation, for the first time to our knowledge, stationary solution of the flows of an Oldroyd-B fluid, at high Weissenberg numbers in the 4/1 axisymmetric contraction.

ACKNOWLEDGMENT

It is a pleasure to acknowledge J. Baranger, C. Guillopé, J. M. Piau and J. C. Saut for helpful discussions. I wish to thank gratefully my thesis adviser, J. R. Clermont, for his help and comments all along this work.

REFERENCES

[1] R. B. BIRD, R. C. AMSTRONG and O. HASSAGER, *Dynamics of Polymeric Liquid*, vol. 1, Fluid Mechanics, 2nd ed. (1987) Wiley, New York.

[2] D. V. BOGER, *Annu. Rev. Fluid Mech.*, 19 (1987) 157 : 182.

[3] A. N. BROOKS and T. J. R. HUGHES, Streamline-Upwind/Petrov-Galerkin Formulation for Convection Dominated Flow with Particular Emphasis on the Incompressible Navier-Stokes Equations, *Comp. Meth. in Appl. Mech. and Eng.*, 32 (1982) pp. 199-259.

[4] M. J. CROCHET and J. M. MARCHAL, A new mixed Finite Eleement for calculating Viscoelastic Flow, *Journal of Non-Newtonian Fluid Mechanics*, 26 (1987) pp. 77-114.

[5] N. El KISSI, J. M. PIAU and B. TREMBLAY, Low Reynolds number flow visualisation of linear and branched silicones upstream of orifices dies, *Journal of Non-Newtonian Fluid Mechanics* (1988).

[6] R. E. EVANS and K. WALTERS, Flow characteristics associated with abrupt changes in geometry in the case of highly elastic liquid, *Journal of Non-Newtonian Fluid Mechanics*, 20 (1986) pp. 11-29.

[7] M. FORTIN and A. FORTIN, A new approach for the FEM simulation of viscoelastic flow, *Journal of Non-Newtonian Fluid Mechanics*, 32 (1989) pp. 295-310.

[8] M. FORTIN and R. GLOWINSKI, *Lagrangian Augmented Methods*, (1981) North Holland.

[9] M. FORTIN and R. PIERRE, On the convergence of the mixed method of Crochet and Marchal for viscoelastic flow, (1989) *Comput. Meth. in Appl. Mech. Eng.*

[10] V. GIRAULT and P. A. RAVIART, Finite Element Approximation of the Navier-Stokes Equations, *Lecture Notes in Mathematics*, 749, (1979) Springer Verlag.

[11] R. GLOWINSKI and J. PÉRIAUX, *Numerical Methods for Nonlinear Problems in Fluid Dynamics*, Proceeding of the International Seminar on Scientific Supercomputer, (1987) Feb 2-6.

[12] J. B. GOODMAN and R. J. LEVEQUE, On the accuracy of stable scheme for two dimensional conservation laws, *Soc. Ind. Appl. Math. Numer. anal.*, 25 (1988) pp. 268-284.

[13] C. GUILLOPÉ and J. C. SAUT, Global existence and one-dimensional non-linear stability of shearing motions of viscoelastic fluids of Oldroyd type, *Modélisation Mathématique et Analyse Numérique*, 24 (1990) pp. 369-401.

[14] C. GUILLOPÉ et J. C. SAUT, Résultat d'existence pour les fluides viscoélastiques à loi de comportement de type différentiel, *Compte-rendu de l'Académie des Sciences de Paris*, 305, série I (1987) pp. 489-492.

[15] D. D. JOSEPH, M. RENARDY and J. C. SAUT, Hyperbolicity and Change of Type in the Flow of Viscoelastic Fluids, *Arch. Ration. Mech. Anal.*, 87 (1985) pp. 213-251.

[16] R. KEUNIGS, Simulation of Viscoelastic Flow, in *Fundamentals of Computer Modeling for Polymer Processing*, C. L. Tucker III, Carl Hanser Verlag.

[17] P. LESAINT and P. A. RAVIART, *On finite element methods for solving the neutron transport equation* (1974) Carl de Boor, Academic Press.

[18] X. L. LUO and R. I. TANNER, A Decoupled Finite Element Streamline-Upwind Scheme for Viscoelastic Flow Problems, *J. of Non-Newtonian Fluid Mechanics*, 31 (1989) pp. 143-162.

[19] J. G. OLDROYD, On the formulation of Rheological equation of states, *Proc. Roy. Soc. London*, A200 (1950) pp. 523-541.

[20] D. W. PEACEMAN and H. H. RACHFORD, The numerical solution of parabolic and elliptic differential equations, *J. Soc. Ind. Appl. Math.*, 3 (1955) pp. 28-41.

[21] M. RENARDY, Existence of Slow Steady Flows of Viscoelastic Fluids with Differential Constitutive Equations, *Z. Angew. Math. u Mech.*, 65 (1985) pp. 449-451.

[22] M. RENARDY, Recent advances in the mathematical theory of steady flow of viscoelastic fluids, *J. of Non-Newtonian Fluid Mechanics*, 9 (1988) pp. 11-24.

[23] J. E. ROBERTS and J. M. THOMAS, Mixed and hybrid methods, in *Handbook of Numerical Analysis*, vol. 3, P. G. Ciarlet and J. L. Lions, North Holland, Amsterdam (Rapport de Recherche 737, INRIA 1987).

[24] P. SARAMITO, *Simulation numérique d'écoulements de fluides viscoélastiques par éléments finis incompressibles et une méthode de directions alternées ; applications*, thèse de l'INPG (1990) Grenoble.

[25] J. E. WELCH, F. H. HARLOW, J. P. SHANNON and B. J. DALY, *The M.A.C. method*, LASL report LA3425, Los Alamos Scientific Laboratory, 1965.

C. R. Acad. Sci. Paris, t. 319, Série II, p. 267-270, 1994

Méthodes numériques appliquées à la mécanique/*Computational Mechanics*
(Analyse numérique/*Numerical Analysis*)

Décomposition d'opérateurs pour des fluides à loi de comportement de type différentiel

Pierre SARAMITO

Résumé – On étudie une application du θ-schéma au calcul d'écoulements de fluides viscoélastiques. La décomposition vise à séparer les termes de viscosité des termes de transport. On se ramène ainsi à résoudre deux sous-problèmes plus simples, l'un de type Stokes, l'autre de type transport du tenseur des contraintes. De plus, en présence de singularités, ce schéma permet de contourner les difficultés rencontrées par la plupart des méthodes itératives dans ce type de simulation. En conclusion, on présente des résultats d'expériences numériques qui, de notre point de vue, justifient pleinement la méthodologie numérique qui y est décrite.

Operator splitting for viscoelastic fluid with a differential constitutive law

Abstract – *We study a θ-scheme applied to the computation of viscoelastic fluid flows. The splitting technique leads to two problems, the first a Stokes-like one, and the second, a stress tensor transport problem. Furthermore, when the solution is singular, this scheme overcomes difficulties appearing when using other classical interative procedures for this kind of simulation. To conclude, we present the result of numerical experiments which in our opinion fully validate the numerical methodology described here.*

1. PRÉSENTATION DU PROBLÈME. – Considérons les fluides viscoélastiques à loi de comportement de type Oldroyd (Oldroyd, 1950), gouvernés par les équations suivantes :

$$\text{We}\left(\frac{\partial \tau}{\partial t} + \mathbf{u}\,.\,\nabla\tau + \beta_a(\tau,\ \nabla\mathbf{u})\right) + \tau - 2\alpha\,\mathrm{D}(\mathbf{u}) = 0 \quad \text{dans } \Omega \tag{1}$$

$$\text{Re}\left(\frac{\partial \mathbf{u}}{\partial t} + \mathbf{u}\,.\,\nabla\mathbf{u}\right) - \operatorname{div}\tau - (1-\alpha)\,\Delta\mathbf{u} + \nabla p = f \quad \text{dans } \Omega \tag{2}$$

$$\operatorname{div}\mathbf{u} = 0 \quad \text{dans } \Omega \tag{3}$$

où Ω est un ouvert régulier de $\mathbb{R}^N$, $N = 2, 3$, τ est le tenseur des extra-contraintes, les contraintes totales étant données par $\sigma = -p\,\mathrm{I} + (1-\alpha)\,\mathrm{D}(u) + \tau$, $\mathbf{u}$ est le champ des vitesses, et p est la pression hydrostatique ; $\beta_a(\tau,\ \nabla\mathbf{u}) = \mathrm{W}\tau - \tau\mathrm{W} - a(\mathrm{D}\tau + \tau\mathrm{D})$, où $a \in [-1,\ 1]$, $\mathrm{D} = (1/2)(\nabla\mathbf{u} + \nabla\mathbf{u}^t)$ est le tenseur des taux de déformation et $\mathrm{W} = (1/2)(\nabla\mathbf{u} - \nabla\mathbf{u}^t)$ est le tenseur de vorticité ; enfin, $f \in (\mathrm{L}^2(\Omega))^N$ est une donnée, We est le nombre sans dimension de Weissenberg, Re le nombre de Reynolds, et $\alpha \in]0,\ 1]$ un paramètre de retard.

Le cas limite $\text{We} = 0$ correspond à un fluide newtonien, tandis que $\text{We} > 0$ décrit des solutions de polymères dans un solvant newtonien. Ces équations peuvent être complétées par des conditions initiales $\tau(0) = \tau_0$ et $\mathbf{u}(0) = \mathbf{u}_0$, ainsi qu'une condition aux bords $\mathbf{u} = 0$ sur $\Gamma = \partial\Omega$. Lorsque la frontière Γ est régulière, et $\mathbf{u}_0$, τ_0 et f sont suffisamment petits, on montre dans Guillopé et Saut (1987) l'existence globale de solutions.

Note présentée par Roland GLOWINSKI.

1251-8069/94/03190267 $ 2.00

2. Décomposition du problème. – Afin de simplifier l'analyse qui suit, supposons le fluide lent, et négligeons le terme d'inertie $\mathbf{u} \cdot \nabla \mathbf{u}$ dans (2). Il s'agit d'une hypothèse classique dans ce type de simulation ; la difficulté du problème est désormais portée par la non-linéarité de l'équation (1). Introduisons les espaces classiques :

$$\mathrm{T} = \{ \tau \in \mathrm{L}^2(\Omega)^{\mathrm{N}\times\mathrm{N}} ;\ \tau = \tau^t \} \quad \text{de norme } |.|$$
$$\mathrm{V} = \{ \mathbf{u} \in \mathrm{H}_0^1(\Omega)^{\mathrm{N}} ;\ \operatorname{div} \mathbf{u} = 0 \} \text{ de norme } \|.\|$$

Le problème peut se mettre sous la forme :
(P) : trouver $\mathcal{U} = (\tau, \mathbf{u}) \in \mathrm{L}^\infty(\mathbb{R}^+ ; \mathrm{T} \times \mathrm{V})$ tel que :

$$\mathrm{S}\frac{d\mathcal{U}}{dt} + \mathrm{A}(\mathcal{U}) = \mathcal{F} \qquad \text{et} \qquad \mathcal{U}(0) = \mathcal{U}_0 \tag{4}$$

où $\mathrm{S} = \operatorname{diag}(\mathrm{We}, \mathrm{Re})$, $\mathcal{F} = (0, f)^t$, $\mathcal{U}_0 = (\tau_0, \mathbf{u}_0)^t$ et $\mathrm{A}(\mathcal{U}) = \mathrm{A}_1(\mathcal{U}) + \mathrm{A}_2(\mathcal{U} ; \mathcal{U})$, défini de $\mathrm{T} \times \mathrm{V}$ dans $\mathrm{T}' \times \mathrm{V}'$, est donné par la décomposition suivante :

$$\mathrm{A}_1(\tau, \mathbf{u}) = \begin{bmatrix} \nu\tau - 2\alpha \mathrm{D}(\mathbf{u}) \\ -\mathbf{div}\,\tau - (1-\alpha)\Delta \mathbf{u} \end{bmatrix} ; \quad \mathrm{A}_2(\sigma, \mathbf{v} ; \tau, \mathbf{u}) = \begin{bmatrix} \nu'\tau + \mathrm{We}\,\mathrm{T}(\mathbf{v})\tau \\ 0 \end{bmatrix} \tag{5}$$

où $\nu' = 1 - \nu$ et $\nu \in [0, 1]$ est un paramètre de la décomposition. Dans (5), $\mathrm{T}(\mathbf{v})$ désigne l'opérateur de transport des contraintes : $\mathrm{T}(\mathbf{v})\tau = \mathbf{v} \cdot \nabla \tau + \beta_a(\tau, \nabla \mathbf{v})$.

Introduisons à présent la semi-approximation de (P). Soit $\Delta t > 0$ un pas de temps et θ un paramètre, $\theta \in]0, 1/2[$. Considérons les notations $\theta' = 1 - 2\theta$, $\mathcal{U}^0 = \mathcal{U}_0$ et $\mathcal{U}^{n+\delta} \approx \mathcal{U}((n+\delta)\Delta t)$. Puisque A_1 et A_2 sont plus simples que A, utilisons cette décomposition pour résoudre (P) par le θ-schéma (Glowinski, 1986 ; Saramito, 1994) :

$$\frac{\mathrm{S}\mathcal{U}^{n+\theta} - \mathrm{S}\mathcal{U}^n}{\theta \Delta t} + \mathrm{A}_1(\mathcal{U}^{n+\theta}) + \mathrm{A}_2(\mathcal{U}^n ; \mathcal{U}^n) = \mathcal{F}^{n+\theta} \tag{6}$$

$$\frac{\mathrm{S}\mathcal{U}^{n+1-\theta} - \mathrm{S}\mathcal{U}^{n+\theta}}{\theta' \Delta t} + \mathrm{A}_1(\mathcal{U}^{n+\theta}) + \mathrm{A}_2(\mathcal{U}^n ; \mathcal{U}^{n+1-\theta}) = \mathcal{F}^{n+1-\theta} \tag{7}$$

$$\frac{\mathrm{S}\mathcal{U}^{n+1} - \mathrm{S}\mathcal{U}^{n+1-\theta}}{\theta \Delta t} + \mathrm{A}_1(\mathcal{U}^{n+1}) + \mathrm{A}_2(\mathcal{U}^n ; \mathcal{U}^{n+1-\theta}) = \mathcal{F}^{n+1} \tag{8}$$

Proposition 1 (cas newtonien). – *Pour* $\mathrm{We} = 0$, *le schéma (6)-(8) est inconditionnellement stable et du premier ordre en temps. De plus, la méthode est d'ordre deux en temps pour* $\theta = 1 - 1/\sqrt{2}$.

Indication sur la démonstration. – Par décomposition spectrale. Voir aussi Glowinski et Périaux (1987). □

Remarque 1. – La résolution de (6) et (8) se réduit à celle d'un problème de type Stokes, et la résolution de (7), à celle d'un problème de type transport pour l'opérateur $\mathrm{I} + \varepsilon \mathrm{T}(\mathbf{v})$, avec $\varepsilon > 0$.

Remarque 2. – Aucun résultat n'a été établi à présent dans le cas viscoélastique ($\mathrm{We} > 0$). Numériquement, l'algorithme (6)-(8) est bien adapté à la recherche des solutions stationnaires, la vitesse de converge dépend alors de θ et Δt. Les exemples qui suivent abordent le cas viscoélastique.

3. ÉLONGATION UNIAXIALE. – Le tenseur gradient de vitesse est donné par $\nabla \mathbf{u} = \mathrm{diag}\,(\dot{\varepsilon},\ -\dot{\varepsilon}/2,\ -\dot{\varepsilon}/2)$, où $\dot{\varepsilon} > 0$ est le taux d'élongation (sans dimension). Le problème se ramène à trouver τ_{11}, τ_{22} et τ_{33} dans $\mathrm{L}^\infty(\mathbb{R}^+)$ satisfaisant trois équations différentielles découplées. Les valeurs propres du problème sont $\lambda_1 = 1/\mathrm{We} - 2\,a\,\dot{\varepsilon}$ et $\lambda_2 = \lambda_3 = 1/\mathrm{We} + a\,\dot{\varepsilon}$.

PROPOSITION 2 (élongation). – *Si* $a\,\dot{\varepsilon}\,\mathrm{We} < 1/2$, *alors le problème admet une solution unique dans* $\mathrm{L}^\infty(\Omega)$. *Le schéma* (6)-(8) *pour* $\nu = 0$, *est précis au premier ordre, et au second ordre pour* $\theta = 1 - 1/\sqrt{2}$. *Il est stable sous la condition*

$$\Delta t < \frac{\mathrm{We}}{\theta^2\,(1 - 2\,a\,\dot{\varepsilon}\,\mathrm{We})} \tag{9}$$

Enfin, un cycle de deux pas de temps $\Delta t_1 = \mathrm{We}/\theta\,(1 - 2\,a\,\dot{\varepsilon}\,\mathrm{We}))$ *et* $\Delta t_2 = \mathrm{We}/(\theta\,(1 + a\,\dot{\varepsilon}\,\mathrm{We}))$ *permet d'obtenir exactement la solution stationnaire.*

4. CISAILLEMENT SIMPLE. – L'écoulement est bidimensionnel, et le tenseur gradient des vitesses est donné par :

$$\nabla \mathbf{u} = \begin{pmatrix} 0 & \dot{\gamma}/2 \\ \dot{\gamma}/2 & 0 \end{pmatrix}$$

où $\dot{\gamma} > 0$ est le taux de cisaillement (sans dimension). Le problème se ramène à trouver τ_{11}, τ_{22} et τ_{12} dans $\mathrm{L}^\infty(\mathbb{R}^+)$ satisfaisant à trois équations différentielles découplées. Les valeurs propres du problème sont $\lambda_1 = 1/\mathrm{We}$, $\lambda_2 = 1/\mathrm{We} + i\,\dot{\gamma}\,\sqrt{1 - a^2}$ et $\lambda_3 = \bar{\lambda}_2$.

PROPOSITION 3 (cisaillement). – *Le problème admet toujours une solution dans* $\mathrm{L}^\infty(\mathbb{R}^+)$. *Le schéma* (6)-(8) *pour* $\nu = 0$, *est précis au premier ordre, et au second ordre pour* $\theta = 1 - 1/\sqrt{2}$. *La stabilité est conditionnelle. Enfin, pour* $|a| = 1$, *il est possible de converger en un pas de temps* $\Delta t = \mathrm{We}/\theta$ *vers la solution stationnaire.*

ÉCOULEMENTS COMPLEXES ET SINGULARITÉS. – On considère le schéma (6)-(8), ayant en vue de remplacer T et V par des espaces de dimension finie T_h et V_h, et de rechercher la solution stationnaire approchée $\mathcal{U}_h^* = (\tau_h^*,\ \mathbf{u}_h^*)$ correspondante.

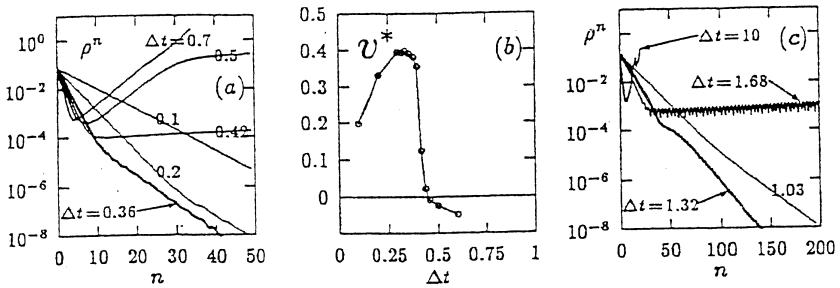

Écoulement à singularité ($a = 1$, $\alpha = 8/9$) : (*a*) résidu selon l'itéré ($\mathrm{We} = 0.5$) ; (*b*) vitesse de convergence selon Δt ($\mathrm{We} = 0.5$) ; (*c*) résidu selon l'itéré ($\mathrm{We} = 11$).

Flow with a singularity ($a = 1$, $\alpha = 8/9$) : (*a*) *residual term versus n* ($\mathrm{We} = 0.5$) ; (*b*) *convergence velocity versus* Δt ($\mathrm{We} = 0.5$) ; (*c*) *residual term versus n* ($\mathrm{We} = 11$).

Observons les résultats rassemblés dans la figure. L'écoulement a lieu dans une géométrie plane à contraction brusque de rapport 4 à 1 [*voir* Saramito (1990) pour une présentation détaillée des éléments finis et des formes matricielles correspondantes]. La solution stationnaire approchée $\mathcal{U}_h^*$ n'étant pas connue *a priori*, nous mesurons la convergence de

l'itéré $\mathcal{U}_h^n$ vers $\mathcal{U}_h^*$ à l'aide de ρ^n, la norme du résidu $\mathrm{A}(\mathcal{U}_h^n) - \mathcal{F}$ du problème stationnaire. Le schéma (6)-(8) apparaît comme une méthode itérative découplée pour la résolution du problème stationnaire $\mathrm{A}(\mathcal{U}_h^*) = \mathcal{F}$, le résidu convergeant vers zéro pour Δt assez petit.

La figure (*a*) met en évidence des changements de pente durant les itérations. La deuxième partie de la courbe exprime la convergence plus lente d'un groupe spécifique de composantes du résidu. On peut conjecturer que ces composantes sont dues à la présence de grandes valeurs propres de l'opérateur A_2. En effet, A_2 fait intervenir le terme $\beta_a(.\,, \nabla \mathbf{u}_h^*)$, et $\nabla \mathbf{u}_h^*$ devient grand au voisinage de la singularité. D'où la nécessité de réduire Δt afin de maîtriser les valeurs propres de $(\mathrm{I} - \theta\,\Delta t\,\mathrm{S}^{-1}\,\mathrm{A}_2)$ et $(\mathrm{I} + \theta'\,\Delta t\,\mathrm{S}^{-1}\,\mathrm{A}_2)^{-1}$ apparaissant dans l'opérateur d'itération du schéma. On pourra aussi faire l'analogie avec une CFL, remarquant cependant qu'ici la condition de stabilité dépend de la nature de la singularité et du maillage au voisinage de cette singularité.

Par un choix particulier de Δt, on annule la vitesse asymptotique de convergence $v^* = \lim_{n\to\infty} (-\log|\rho^n|)/n$ [*fig.* (*b*)] ; le résidu se stabilise [*fig.* (*a*), $\Delta t = 0.42$, et *fig.* (*c*), $\Delta t = 1.68$]. On ne manquera pas de faire le rapprochement avec la méthode de la puissance itérée pour les problèmes de valeurs propres [*cf.* Chatelain (1988), par exemple]. Pour des pas de temps plus élevés, ces composantes vont aller en amplitude croissante, d'où l'aspect particulier, en « V », des courbes obtenues [*fig.* (*a*), $\Delta t = 0,6$ et *fig.* (*c*), $\Delta t = 10$].

Signalons enfin que schéma a été étendu au cas du modèle de Phan-Thien et Tanner (1977). Dans Saramito et Piau (1994), sur une géométrie complexe, et dans le cas $|a| < 1$, on construit par un procédé de cheminement des branches de solutions stationnaires, et on met en évidence les propriétés asymptotiques des écoulements pour les grandes valeurs de We, ceci pour différents paramètres du modèle. Ces résultats de propriétés asymptotiques sont, à notre connaissance, les premiers relatifs à ce type de simulation pour les modèles viscoélastiques à loi de comportement de type différentiel.

Note remise le 10 mai 1994, acceptée le 14 juin 1994.

RÉFÉRENCES BIBLIOGRAPHIQUES

F. CHATELAIN, *Valeurs propres de matrices*, Masson, 1988.

R. GLOWINSKI, Numerical methods for the numerical solution of the incompressible Navier-Stockes equations. In *Vistas in Applied Mathematics, Optimization Software*, New York, 1986, p. 57-95.

R. GLOWINSKI et J. PÉRIAUX, Numerical methods for nonlinear problems in fluid dynamics. In *Proceeding of the International Seminar on Scientific Super-Computer*, Feb. 1987.

C. GUILLOPÉ et J. C. SAUT, Résultat d'existence pour les fluides viscoélastiques à loi de comportement de type différentiel, *C. R. Acad. Sci. Paris*, 305, série I, 1987, p. 489-492.

J. G. OLDROYD, On the formulation of rheological equations of states, *Proc. Roy. Soc., London A*, 200, 1950, p. 523-541.

N. PHAN-THIEN et R. I. TANNER, A new constitutive equation derived from network theory, *J. Non Newtonian Fluid Mech.*, 2, 1977, p. 353-365.

P. SARAMITO, Simulation numérique d'écoulements de fluides viscoélastiques par éléments finis incompressibles et une méthode de directions alternées ; applications, *Thèse*, Institut national Polytechnique, Grenoble, 1990.

P. SARAMITO, Numerical simulation of viscoelastic fluid flows using incompressible finite element method and a θ-method, *Mathematical Modelling and Numerical Analysis*, 28, 1994, p. 1-34.

P. SARAMITO et J. M. PIAU, Flow characteristics of viscoelastic fluids in an abrupt contraction by using numerical modeling, under press, *J. Non Newtonian Fluid Mech.*, 1994.

Université de Grenoble, Laboratoire de Rhéologie, BP n° 53 X, *38041 Grenoble, France.*

Journal of Non-Newtonian Fluid Mechanics, 52 (1994) 263–288
Elsevier Science B.V.

Flow characteristics of viscoelastic fluids in an abrupt contraction by using numerical modeling

P. Saramito [1] and J. M. Piau *

Laboratoire de Rhéologie [2], *B.P. 53, 38041 Grenoble Cedex 9, France*

(Received September 26, 1993; in revised form February 7, 1994)

Abstract

Consideration is given to the influence of elongational properties on flow characteristics in the case of shear-thinning highly elastic fluids in an abrupt contraction. Sufficient data has been published to demonstrate that viscoelasticity can have a significant effect on flow characteristics in abrupt contractions. This paper reports on numerical experiments with four representative test-fluids of Phan-Thien–Tanner models. Furthermore, a new dimensionless number that takes into account elongational properties is proposed.

Of major importance is the observation that the vortex enhancement and the energy loss in the entrance region both vary strongly with the elongational properties of Phan-Thien–Tanner models. Numerical results are qualitatively in good agreement with experimental measurements on polymer solutions and melts.

Finally, this numerical study provides a fundamental basis, which may be quite useful for the prediction of viscoelastic fluid flows by using numerical modeling, and for the calculation of rheometrical properties of viscoelastic fluids through constitutive equation parameter adjustment.

Keywords: abrupt contraction; elongational properties; energy losses; numerical modeling; viscoelasticity; vortex enhancement

---

* Corresponding author.

[1] Present address: Institut National Polytechnique, 46 avenue F. Viallet, 38000 Grenoble, France.

[2] Université Joseph Fourier Grenoble I, et Institut National Polytechnique de Grenoble, Associé an CNRS (URA 1510).

SSDI 0377-0257(94)01246-E

1. Introduction

One of the difficult problems in viscoelastic fluid mechanics is to analyze the relationship between macroscopic features of complex flows in an abrupt contraction, such as vortex pattern, energy loss, ... and its viscous behaviour in simple shear and extensional flows.

Understanding entry flow of viscoelastic fluids is of importance in fundamental flow-property measurement and in extrusion of polymer melts and solutions. Furthermore, the characteristics of vortices and flow curves are of particular interest in the design of extrusion dies.

In a number of cases, numerical simulations of complex flows predict a correct qualitative behavior but fail to produce quantitative agreement on the value of the Weissenberg number. In a recent paper, Boger, Crochet and Keiller [1] have proposed a definition of the Weissenberg number in abrupt contraction flow problems. By using the White–Metzner model, that predicts a finite time relaxation parameter for high shear rate, they obtain finite values of the Weissenberg number for high flow rates. Nevertheless, this definition is not completely satisfying: it does not apply successfully to other models, such as the Phan-Thien–Tanner model. Furthermore, it does not take into account the elongational properties of viscoelastic flows in abrupt contractions. However, experimental results show that elongational properties in the entrance region appear as a major factor for the vortex enhancement [2,3]. It was also shown on the basis of numerical simulation that the elongational viscosity leads to an increase of the vortex activity and pressure drop (see [4–7] and related works).

In this paper, four shear thinning fluids in a circular 8 to 1 abrupt contraction are considered. The first fluid presents a monotonically decreasing elongational viscosity versus the elongation rate. The second one develops an elongational viscosity that reaches a maximum and then decays. The third and the fourth have monotonically increasing elongational viscosities that reach plateaus.

The second section presents the Phan-Thien–Tanner models [8,9], which make relatively good predictions for shear and elongational material properties, and allows one to cover expected properties both for polymer solutions and melts for the full range of molecular weight variations. A preselection of models based on simple kinematics like uniaxial elongation and shear flows will be considered. The Weissenberg number defined in [1] and a dimensionless number that takes into account elongational properties of such models will be introduced.

The third section gives an overview of the numerical method: a time-dependent approach and a finite element method [10,11]. This numerical strategy will allow us to obtain in an efficient way stationary solutions for complex flows of viscoelastic fluids.

The fourth section presents numerical results for a circular abrupt 8 to 1 contraction. Flow patterns and vortex activity are exhibited for a large range of flow rates. The computation of the energy loss in the entrance region is also provided. A careful analysis of the flow curves and the Couette correction is also given in this section. This analysis points out the effect of the elongational properties upon the energy loss in the entrance region. Section 4 finishes with a study of the elongation rate and first normal stress difference along the axis of symmetry.

2. Phan-Thien–Tanner models

We split the Cauchy stress tensor into a spherical part pI, a Newtonian contribution, with a first viscosity η_n, and an extra-stress component τ:

$$\sigma = -pI + 2\eta_n D(\boldsymbol{u}) + \tau, \tag{1}$$

where $D(\boldsymbol{u}) = (1/2)(\nabla \boldsymbol{u} + \nabla \boldsymbol{u}^t)$ denotes the rate-of-deformation tensor. The extra-stress component τ satisfies a constitutive equation. In the exponential version of the Phan-Thien–Tanner model, a material parameter ϵ of the model is introduced:

$$\lambda \overset{\square}{\tau} + \exp\left(\frac{\epsilon\lambda}{\eta_v} \operatorname{tr} \tau\right)\tau = 2\eta_v D(\boldsymbol{u}), \tag{2}$$

where λ is the time-relaxation parameter and η_v is a second viscosity. The linear version introduces a linear term instead of the exponential one:

$$\lambda \overset{\square}{\tau} + \left(1 + \frac{\epsilon\lambda}{\eta_v} \operatorname{tr} \tau\right)\tau = 2\eta_v D(\boldsymbol{u}). \tag{3}$$

The material derivative $\overset{\square}{(\cdot)}$ in (2) and (3) is defined by

$$\overset{\square}{\tau} = \frac{\partial \tau}{\partial t} + \boldsymbol{u} \cdot \nabla \tau + \beta_a(\tau, \nabla \boldsymbol{u}), \tag{4}$$

where the bilinear form $\beta_a(.,.)$ is given by

$$\beta_a(\tau, \nabla \boldsymbol{u}) = -W(\boldsymbol{u}) \cdot \tau + \tau \cdot W(\boldsymbol{u}) - a(D(\boldsymbol{u}) \cdot \tau + \tau \cdot D(\boldsymbol{u})). \tag{5}$$

$a \in [-1, 1]$ is a material parameter and $W = (1/2)(\nabla \boldsymbol{u} - \nabla \boldsymbol{u}^t)$ is the vorticity tensor.

2.1 Shear and elongational viscosities

The present section shows the sensitivity of steady shear and elongational viscosities to the variations of the material parameters ϵ, a, and $\alpha = \eta_v/\eta_0$, where $\eta_0 = \eta_n + \eta_v$.

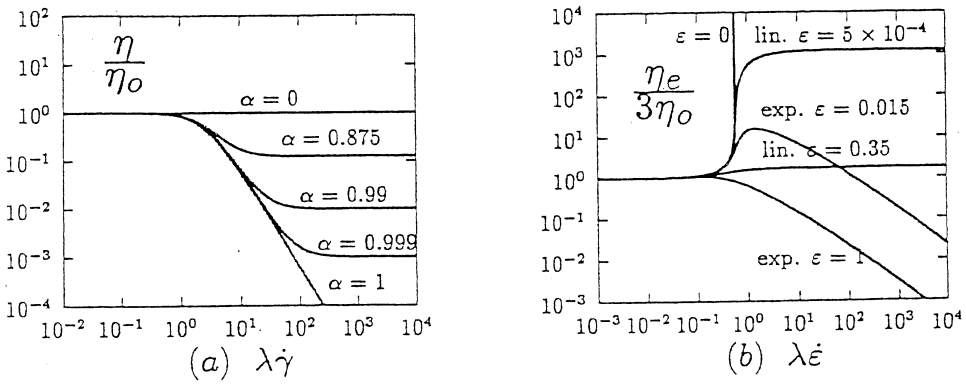

Fig. 1. Simple flows: (a) shear viscosity ($\epsilon = 0.015$, $a = 0.9$, exponential version); (b) elongational viscosity ($\alpha = 0.875$, $a = 0.9$).

The shear viscosity η is a decreasing function of the shear rate $\dot{\gamma}$ (Fig. 1(a)). For high values of shear rate, the steady shear viscosity is mainly governed by α. When α vanishes, $\eta = \eta_0$, and the behavior is Newtonian. When $0 < \alpha < 1$, η tends to a plateau. The asymptotical value of the plateau depends strongly upon α. A large amount of shear-thinning appears at the vicinity of $\alpha = 1$. For $\alpha = 1$, η tends to zero for high values of $\dot{\gamma}$, and the model is Maxwell-like. The material parameters a and ϵ and the model family (exponential or linear) have little impact upon η outside the vicinity of the Oldroyd-B model ($a = 1$ and $\epsilon = 0$).

In the case of the exponential Phan-Thien–Tanner model, the elongational viscosity η_e, as a function of the elongational rate $\dot{\epsilon}$, reaches a maximum, and decreases for high values of $\dot{\epsilon}$ (Fig. 1(b)). For the linear version, η_e increases monotonically with $\dot{\epsilon}$, and tends to a plateau. When ϵ vanishes, the Johnson–Segalman model is obtained: η_e becomes infinite for a finite value of $\dot{\epsilon}$. The material parameters a and α have very little impact upon η_e outside the vicinity of the Oldroyd-B model.

2.2 Dimensionless numbers

Since the shear rate at the downstream wall $\dot{\gamma}_w$ takes large values for shear-thinning fluid models in contractions, we introduce an average value $\overline{\dot{\gamma}_w}$ (overlined), defined by

$$\overline{\dot{\gamma}_w} = \frac{4Q}{\pi r_0^3}.$$

Q is the flow rate, and r_0 is the downstream channel radius.

The Weissenberg number We is defined in an abrupt contraction by [1]

$$We = \frac{N_{1|\dot{\gamma}=\overline{\dot{\gamma}_w}}}{\sigma_{rz|\dot{\gamma}=\overline{\dot{\gamma}_w}}}, \tag{6}$$

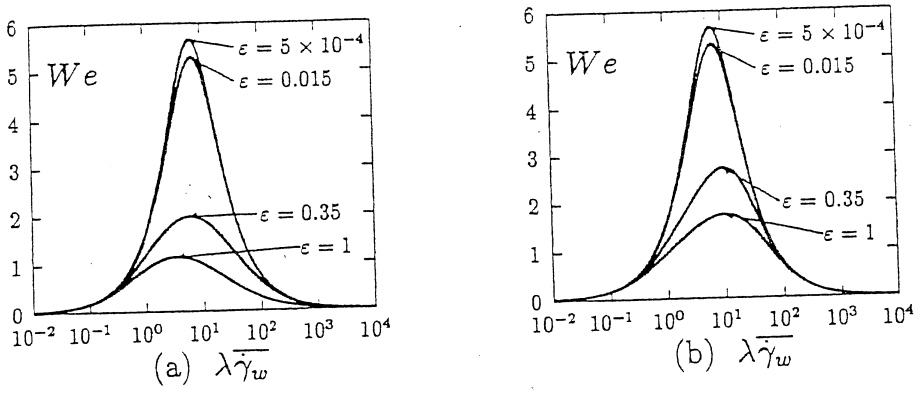

Fig. 2. Weissenberg number: (a) exponential version, and (b) linear version ($\alpha = 0.875$, $a = 0.9$).

where N_1 is the first normal stress difference in shear, σ_{rz} the total shear stress in shear. Figure 2 shows the variations of We versus $\lambda\dot{\gamma}_w$. For both the exponential and the linear versions, We presents a maximum and decreases for high values of $\lambda\dot{\gamma}_w$. We will see in section 4 that these variation are not correlated to vortex enhancements.

Let X_E be the following dimensionless number:

$$X_E = \log_{10}\left(\frac{\sigma_{E|e=\dot{\gamma}_w}}{3\sigma_{rz|\dot{\gamma}=\dot{\gamma}_w}}\right), \tag{7}$$

where σ_E is the first normal stress difference in uniaxial extension. Figure 3 shows the variations of X_E versus $\lambda\dot{\gamma}_w$. For the exponential version (Fig. 3(a)), X_E shows a maximum, and decreases for high values of $\lambda\dot{\gamma}_w$. For the linear version (Fig. 3(b), X_E increases with $\lambda\dot{\gamma}_w$, and tends to a plateau. We

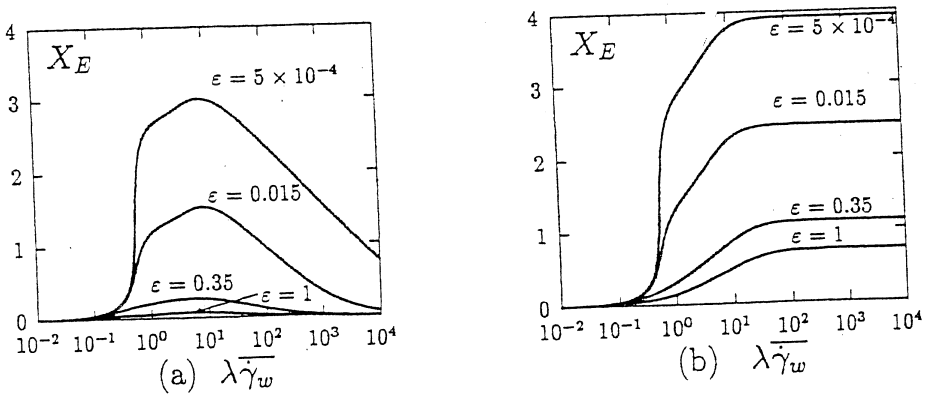

Fig. 3. Dimensionless X_E number: (a) exponential version and, (b) linear version ($\alpha = 0.875$, $a = 0.9$).

will see in section 4 that the variations of X_E correspond to the vortex developments. For the exponential version, vortex size and intensity as a function of $\lambda\dot{\gamma}_w$, increase, reach a maximum, and then decrease. For the linear version, vortex size and intensity reach a plateau for high values of $\lambda\dot{\gamma}_w$.

In fact, definition (7) takes into account the elongational properties of the models, while the expression (6) for *We* only contains shear properties. Note that X_E can be expressed by using the Trouton ratio $X_E = \log_{10}(\eta_e/3\eta)$ and takes advantage of the $\log_{10}$ function to reduce the range of $\eta_e/3\eta$.

3. Numerical method

We introduce in this paragraph the partial derivative formulation of the problem and the numerical strategy. The set of equations contains the constitutive eqn. (8), the conservation of momentum (9), and the conservation of mass (10):

$$\frac{\lambda}{2\eta_v}\overset{\square}{\tau} + \frac{f(\tau)}{2\eta_v}\tau - D(\boldsymbol{u}) = 0, \tag{8}$$

$$-\rho\left(\frac{\partial \mathbf{u}}{\partial t} + \boldsymbol{u}\cdot\nabla\boldsymbol{u}\right) + \operatorname{div}\tau + \eta_n\,\Delta\boldsymbol{u} - \nabla p = 0, \tag{9}$$

$$\operatorname{div}\boldsymbol{u} = 0. \tag{10}$$

We add initial conditions for τ and $\boldsymbol{u}$, boundary conditions for $\boldsymbol{u}$, and upstream boundary conditions for τ. The inertia term $\boldsymbol{u}\cdot\nabla\boldsymbol{u}$ is neglected in (9), since only slow flows are investigated. The material function $f(\tau)$ switches between the two versions of the Phan-Thien–Tanner model:

$$f(\tau) = \begin{cases} \exp\left(\dfrac{\epsilon\lambda}{\eta_v}\operatorname{tr}\tau\right) \\ \text{or} \\ 1 + \dfrac{\epsilon\lambda}{\eta_v}\operatorname{tr}\tau. \end{cases}$$

3.1 Operator splitting

Let $T(\boldsymbol{u})$ be the stress transport operator: $T(\boldsymbol{u})\tau = \boldsymbol{u}\cdot\nabla\tau + \beta_a(\tau, \nabla\boldsymbol{u})$.

Let A be the following operator:

$$A(\tau, \boldsymbol{u}, p) = \begin{bmatrix} \dfrac{\lambda}{2\eta_v}T(\boldsymbol{u})\tau + \dfrac{f(\tau)}{2\eta_v}\tau - D(\boldsymbol{u}) \\ \operatorname{div}\tau + \eta_n\Delta\boldsymbol{u} - \nabla p \\ \operatorname{div}\boldsymbol{u} \end{bmatrix} \tag{11}$$

associated with the boundary conditions for τ and $\boldsymbol{u}$. As mentioned above, the inertia term $\boldsymbol{u}.\nabla\boldsymbol{u}$ is neglected in (11).

Let m be the constant diagonal matrix: $m = \mathrm{diag}(\lambda/2\eta_v, -\rho, 0)$.

The problem can be rewritten in a more compact way:

(P): Find $\mathcal{U} = (\tau, \boldsymbol{u}, p)$ such that

$$m\frac{\partial \mathcal{U}}{\partial t} + A(\mathcal{U}) = 0 \tag{12}$$

We propose a time-approximation of problem (P). Our goal is here to obtain fast convergence to stationary solutions. We use an operator splitting procedure [12, 13]:

$$A = A_1 + A_2, \tag{13}$$

where A_1 contains the elliptic part of the operator A, and A_2 the hyperbolic non-linear part [10, 11, 14].

3.2 Time approximation

Using results of operator splitting procedure, we solve problem (P) by a three-step algorithm:

$(P)_{\Delta t}$: $\mathcal{U}_0$ given;

$n \geq 0$, $\mathcal{U}^n$ being known, find $\mathcal{U}^{n+1}$ such that

$$m\frac{\mathcal{U}^{n+\theta} - \mathcal{U}^n}{\theta\,\Delta t} + A_1(\mathcal{U}^{n+\theta}) = -A_2(\mathcal{U}^n), \tag{14}$$

$$m\frac{\mathcal{U}^{n+1-\theta} - \mathcal{U}^{n+\theta}}{(1-2\theta)\,\Delta t} + A_2(\mathcal{U}^{n+1-\theta}) = -A_1(\mathcal{U}^{n+\theta}), \tag{15}$$

$$m\frac{\mathcal{U}^{n+1} - \mathcal{U}^{n+1-\theta}}{\theta\,\Delta t} + A_1(\mathcal{U}^{n+1}) = -A_2(\mathcal{U}^{n+1-\theta}), \tag{16}$$

where Δt is the time step and θ is a parameter of the method (see Fig. 4).

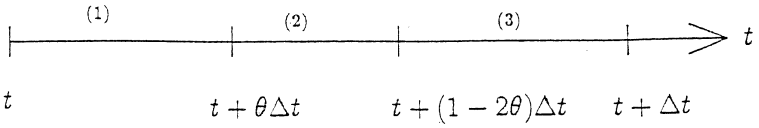

Fig. 4. Time-approximation by using a θ-method.

This algorithm enables us to split up the two main difficulties of the problem, i.e. the non-linearity of the constitutive equation (8) and the incompressibility relation (10). The choice of the time-step Δt is related to a conditional stability condition [11,15].

Furthermore, this time-approximation leads to fast convergence to stationary solutions [10,14]. The critera for determining that a steady state solution is reached, is related to the discrete L^2-norm of the stationary solution $A(\mathscr{U}) = 0$.

3.3 Finite element method

We use here the light element proposed in [10,11] (see also Fig. 5). This element leads to roughly ten times smaller non-linear systems than the other elements [16, 17]. It is a combination of the Raviart–Thomas [18] element for the velocity–pressure field, a P_0 discontinuous element for normal stress components, and a linear continuous element for the shear stress components (see Fig. 5). Note that this finite element method appears as an extension of a Marker and Cell finite difference scheme.

We use an upwinding scheme for the stress transport term $\boldsymbol{u} \cdot \nabla \tau$ in (8). We develop the Lesaint–Raviart scheme [19] for the normal stress components, and the Baba–Tabata scheme [20] for the shear stress components. These two schemes are Total Variation Decreasing. This property guarantees non-artificial oscillating solutions, as shown in paragraph 3.5 for profile along the axis of symmetry. We refer also to [14] for a study of this numerical technique and related results for stresses at the vicinity of the reentrant corner.

Note that the SUPG and the SU methods [11,16,21] do not guarantee this property (see also Ref. 22).

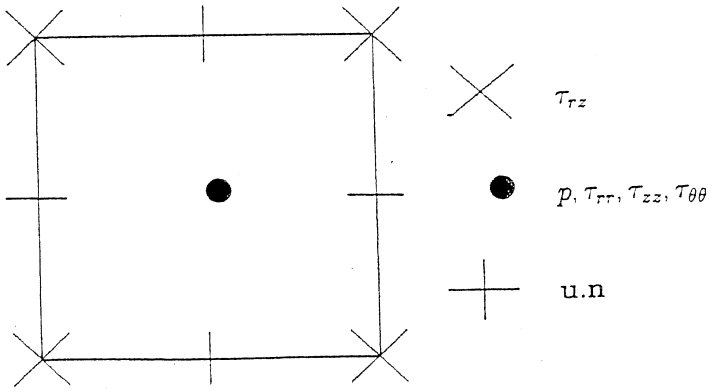

Fig. 5. Finite element method.

4. Numerical experiments in an 8:1 abrupt contraction

In the present section, we wish to investigate the linear and the exponential version of the Phan–Thien–Tanner model. An axisymmetric 8:1 abrupt contraction is considered. The material parameters are $\eta_v/\eta_0 = 0.875$ and $a = 0.9$. For the exponential version, we choose $\epsilon = 1$ (tiny elongational effects) and $\epsilon = 0.015$ (large effects), and for the linear version $\epsilon = 0.35$ (tiny effects). $\epsilon = 5 \times 10^{-4}$ (large effects).

As the boundary condition are concerned, we consider Poiseuille flows at upstream and downstream sections, a symmetry condition along the axis, and $\mathbf{u} = 0$ at the wall.

Starting from a Newtonian solution, a branch of viscoelastic solutions is computed by using a continuation process. The parameter of command is $\lambda\dot{\gamma}_w$ during the computation. This parameter increases with the flow rate Q and with the time relaxation parameter λ.

4.1 Finite element meshes

Two finite element meshes (Fig. 6) of domain Ω are considered for the study of this section. They have in common entry and exit lengths respec-

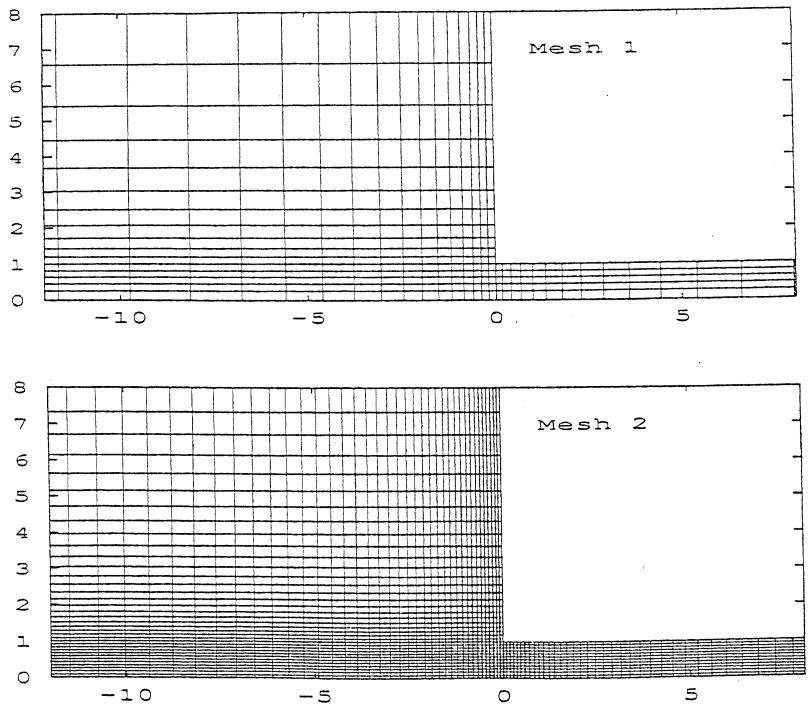

Fig. 6. Partial view of the finite element meshes.

Table 1
Relevant data for the finite element meshes

Mesh	Number of elements	Number of nodes	Number of degrees of freedom	Size of the corner element
1	525	592	3810	0.16
2	3264	3445	23211	0.08

tively equal to 64 and 150 radii. Both upstream and downstream lengths are sufficiently long so that fully developed conditions can exist. Mesh 1 is coarse and is useful to experiment models and test convergence with mesh refinement. Mesh 2 present a quasi-regular spacing in the entry region (axial and radial directions). Relevant data about these meshes are summarized in Table 1.

4.2 Flow Patterns

Let us observe the flow pattern versus the command parameter $\lambda\dot{\gamma}_w$. Figure 7(a) shows the Newtonian behavior. A small vortex is present in the salient corner of the contraction.

The set of pictures in Fig. 7 shows the evolution of the exponential model with $\epsilon = 0.015$. The elongational viscosity reaches a maximum and tends to zero for high ratios of the elongational rate (see Fig. 1(b)). For small values of $\lambda\dot{\gamma}_w$, the vortex develops from the salient corner to the reentrant corner (Fig. 7(b)). When $\lambda\dot{\gamma}_w$ increases, the vortex grows in intensity, and the borderline separating the main flow from the vortices goes from concave to convex (Fig. 7(c)). For higher values of $\lambda\dot{\gamma}_w$, the vortex size increases rapidly and the vortex develops in the upstream domain. The maximum vortex intensity, i.e. the ratio of the recirculating flow rate to the main flow rate, reaches a maximum for $\lambda\dot{\gamma}_w = 42$ (Fig. 7(d)) while its maximum size is reached for $\lambda\dot{\gamma}_w = 206$ (Fig. 7(e). For higher values of $\lambda\dot{\gamma}_w$, the vortex decreases slowly in size and intensity (Fig. 7(f)). We refer also to [14, 23] for numerical experiments of the exponential Phan-Thien–Tanner model in a 4:1 abrupt contraction.

Let us now consider the exponential model with $\epsilon = 1$. We get a monotonically decreasing elongational and shear viscosity (see Fig. 1(a) and 1(b). Figure 8 show that the vortex decreases in size and intensity for high values of $\lambda\dot{\gamma}_w$, and becomes smaller than for a Newtonian fluid.

A second approach to elongational effects can be obtained by using the linear model with $\epsilon = 5 \times 10^{-4}$. The elongational viscosity is an mono-

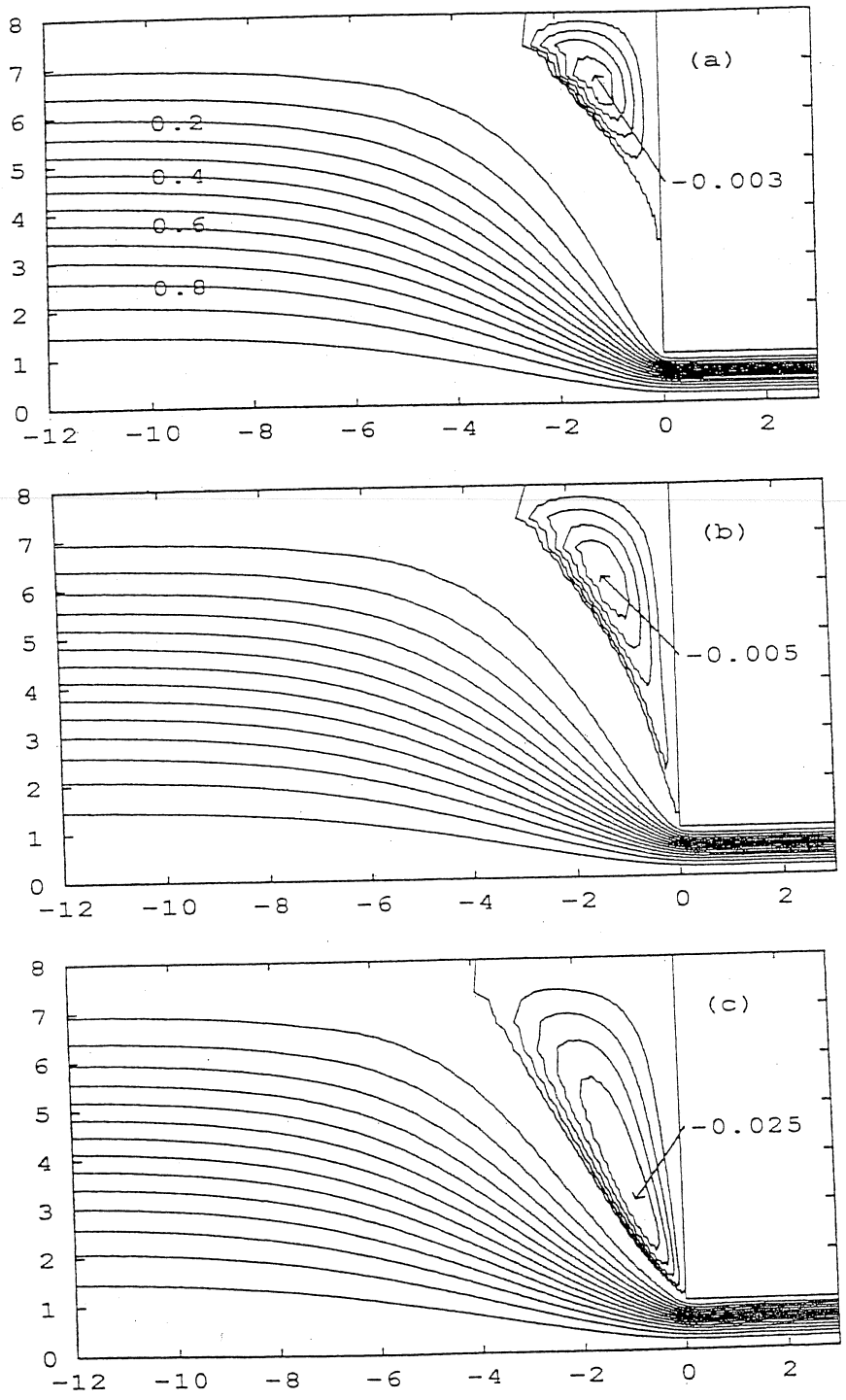

Fig. 7 (a–c).

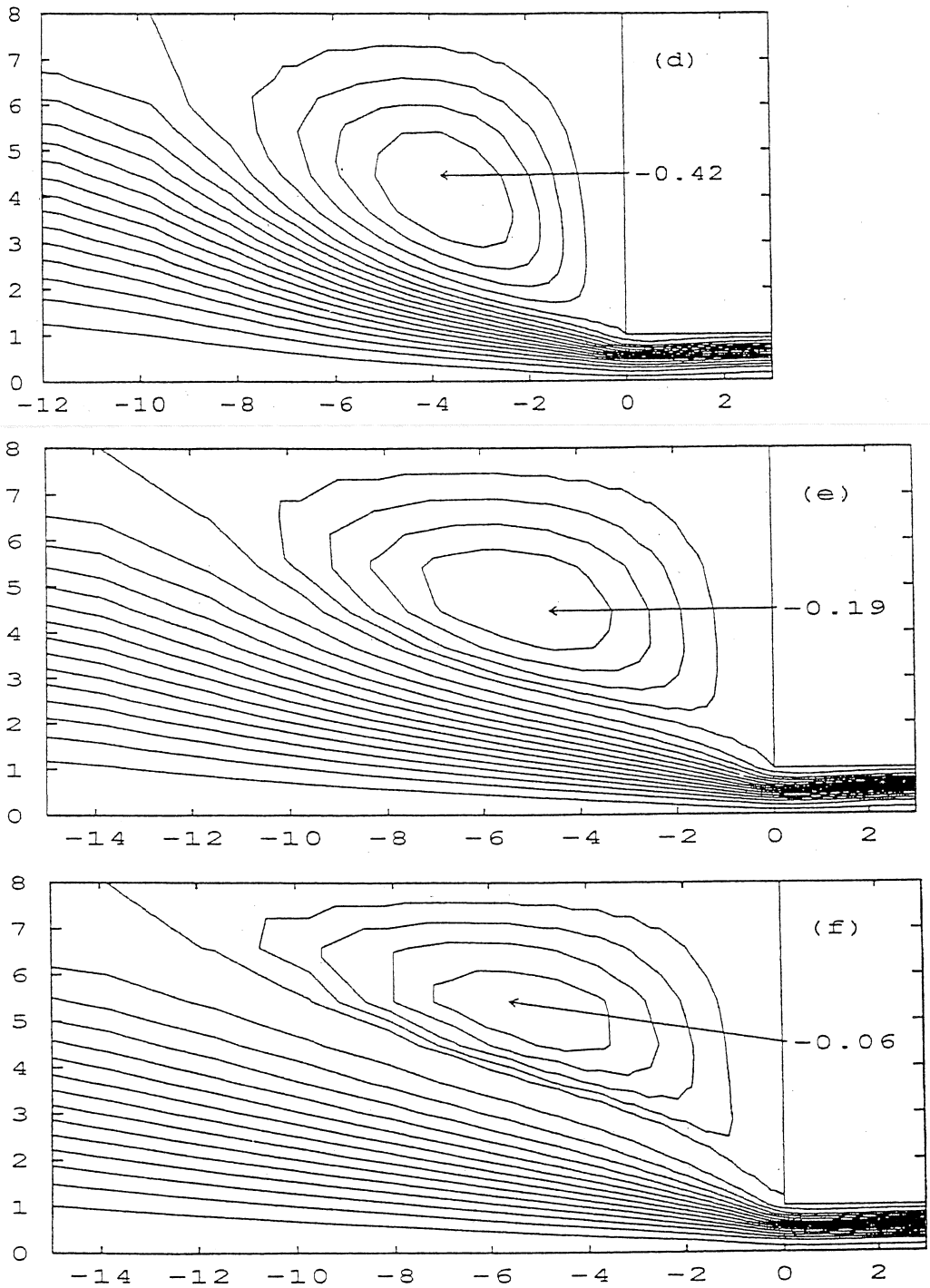

Fig. 7. Exponential version ($\epsilon = 0.015$): vortex developments: (a) $\lambda\dot{\bar{\gamma}}_w = 0$; (b) $\lambda\dot{\bar{\gamma}}_w = 1.5$; (c) $\lambda\dot{\bar{\gamma}}_w = 4.5$; (d) $\lambda\dot{\bar{\gamma}}_w = 42$; (e) $\lambda\dot{\bar{\gamma}}_w = 206$; (f) $\lambda\dot{\bar{\gamma}}_w = 626$.

tonically increasing function of $\lambda\overline{\dot{\gamma}_w}$ (see Fig. 1(b)). For small values of $\lambda\overline{\dot{\gamma}_w}$, the situation is comparable with the previous one (exponential version, $\epsilon = 0.015$). When $\lambda\overline{\dot{\gamma}_w}$ increases, the vortex grows in intensity (Fig. 9(a)), and we observe also the change of the borderline concavity (Fig. 9(b)). For higher values of $\lambda\overline{\dot{\gamma}_w}$, the vortex develops rapidly in the upstream channel (Fig. 9(c)). The vortex size and activity is a monotonically increasing function of $\lambda\overline{\dot{\gamma}_w}$, and tends slowly to an asymptotical behavior (Fig. 9(d)). Note also the movement of the vortex center from the salient corner region (Fig. 9(a)) to the vicinity of the reentrant corner (Fig. 9(b)) and then upstream (Fig. 9(c)) and 9(d)). See Refs. 2, 24–26 for related experiments with real fluids.

Finally, the linear model with $\epsilon = 0.35$ is considered. The vortex develops from the salient corner to the reentrant corner of the contraction (Fig. 10(a)). The vortex intensity reaches a maximum for $\lambda\overline{\dot{\gamma}_w} = 77$ (Fig. 10(b)). For higher values of $\lambda\overline{\dot{\gamma}_w}$, the vortex size continues to increase, and tends slowly to asymptotical behavior (Fig. 10(c) and 10(d)).

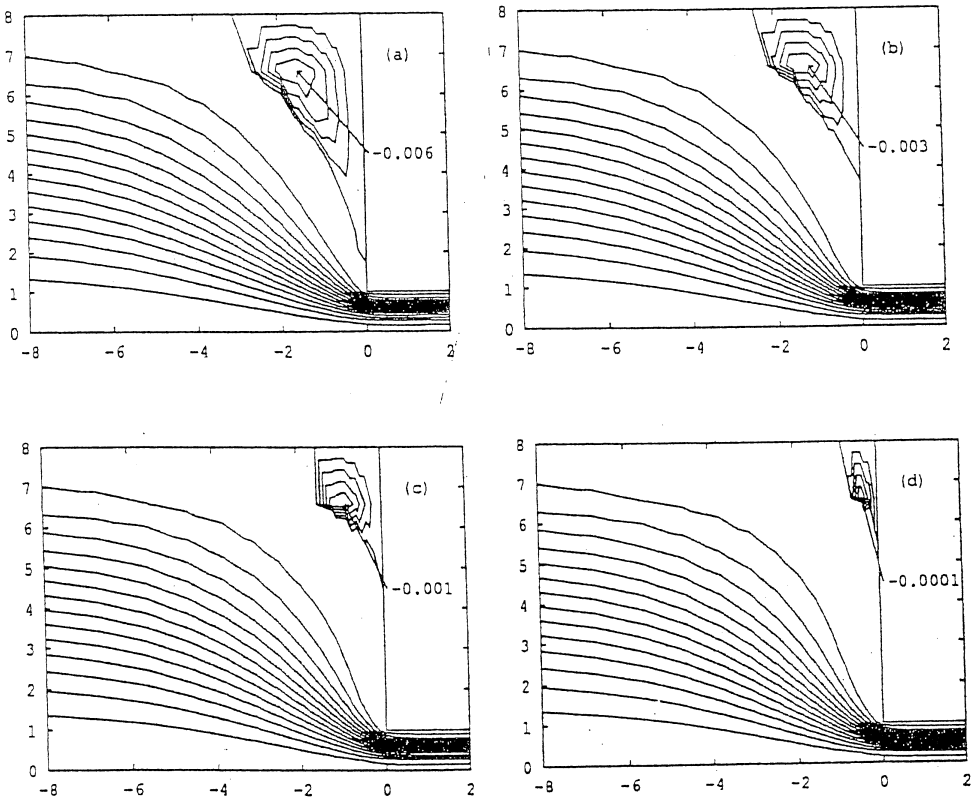

Fig. 8. Exponential version ($\epsilon = 1$): vortex developments: (a) $\lambda\overline{\dot{\gamma}_w} = 4$; (b) $\lambda\overline{\dot{\gamma}_w} = 19$; (c) $\lambda\overline{\dot{\gamma}_w} = 52$; (d) $\lambda\overline{\dot{\gamma}_w} = 182$.

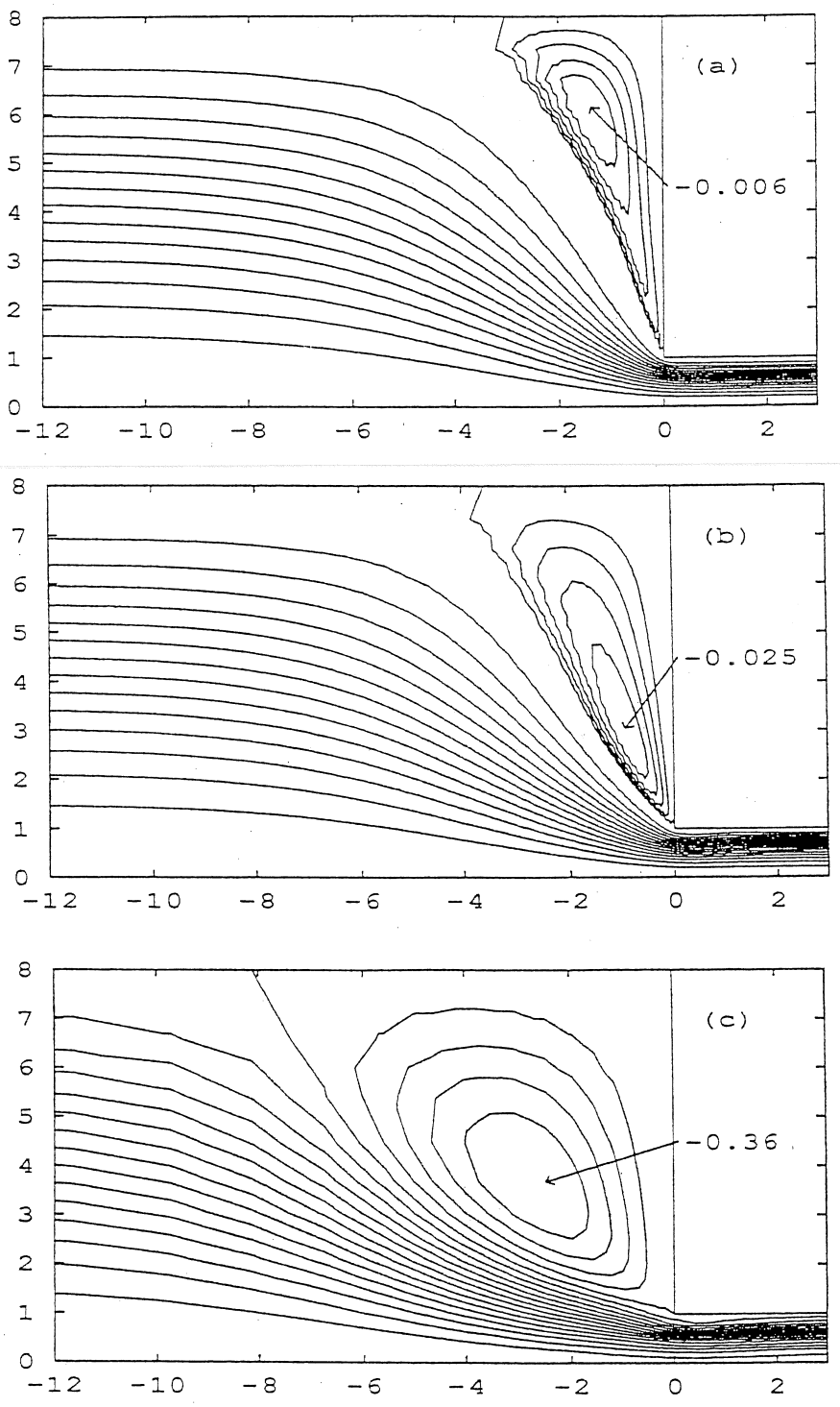

Fig. 9(a–c).

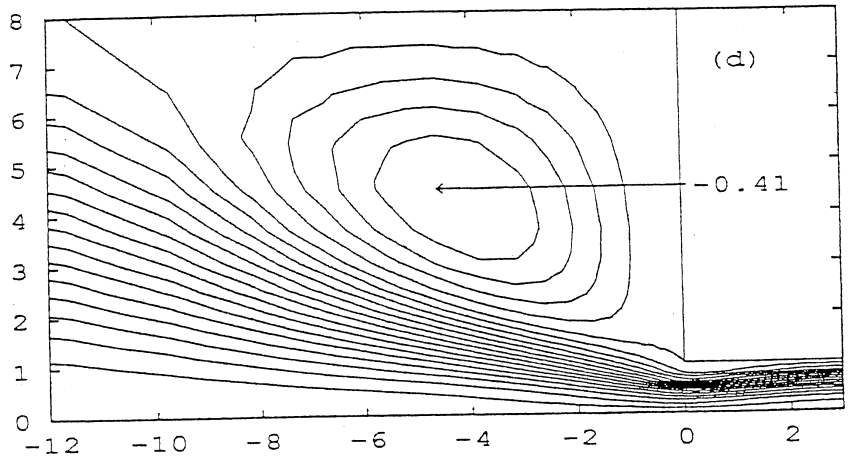

Fig. 9. Linear version ($\epsilon = 5 \times 10^{-4}$): vortex developments: (a) $\lambda\dot{\gamma}_w = 2.0$; (b) $\lambda\dot{\gamma}_w = 4.6$; (c) $\lambda\dot{\gamma}_w = 14$; (d) $\lambda\dot{\gamma}_w = 69$.

4.3 *Vortex activity and reattachment length*

Figure 11 shows the vortex activity for the various fluids under consideration. Vortex activity is considered as a function of both $\lambda\dot{\gamma}_w$ and X_E. For small values of $\dot{\gamma}_w$, the vortex activity is an increasing function of $\dot{\gamma}_w$ (Fig. 11, first column). For large values of $\dot{\gamma}_w$, exponential and linear versions exhibit different asymptotical behaviors. In the exponential case (Fig. 11(a) and 11(b)), the vortex activity decreases. This is not surprising, since η_e asymptotically decreases too. In the linear case (Fig. 11(c) and 11(d), as expected, the vortex activity tends to an asymptotical value, while η_e reaches

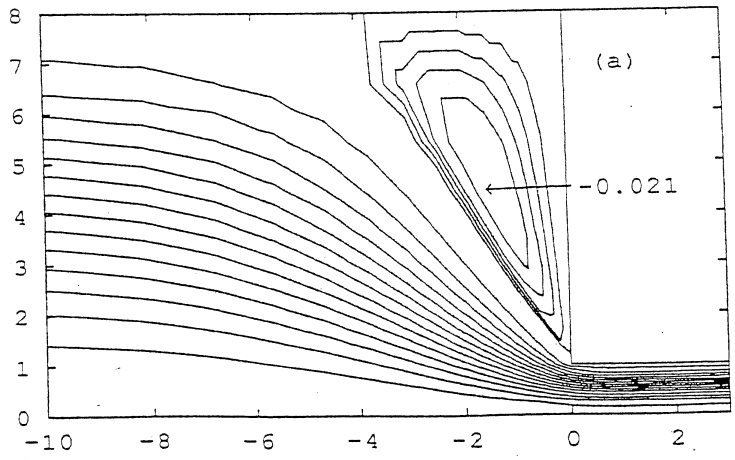

Fig. 10(a).

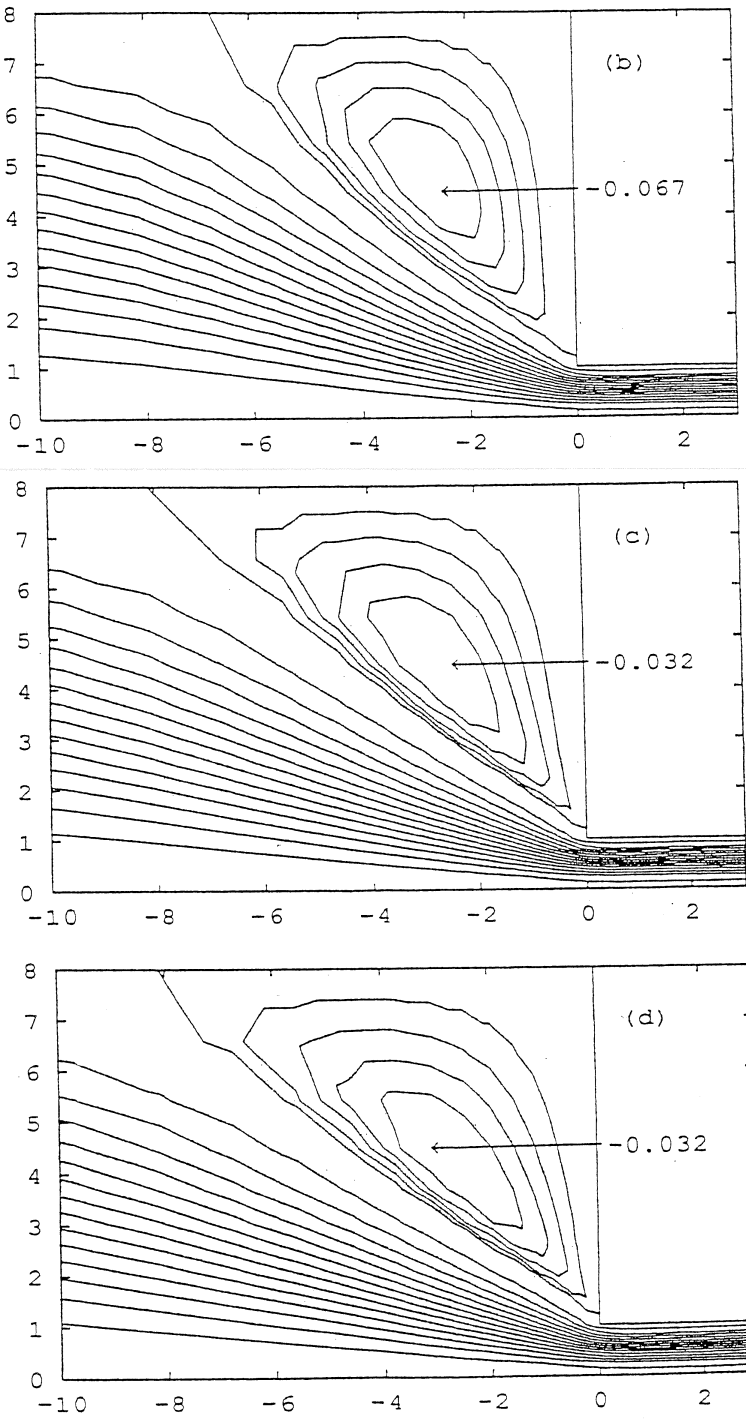

Fig. 10. Linear version ($\epsilon = 0.35$): vortex developments. (a) $\lambda\overline{\dot{\gamma}_w} = 7$; (b) $\lambda\overline{\dot{\gamma}_w} = 77$; (c) $\lambda\overline{\dot{\gamma}_w} = 768$; (d) $\lambda\overline{\dot{\gamma}_w} = 1667$.

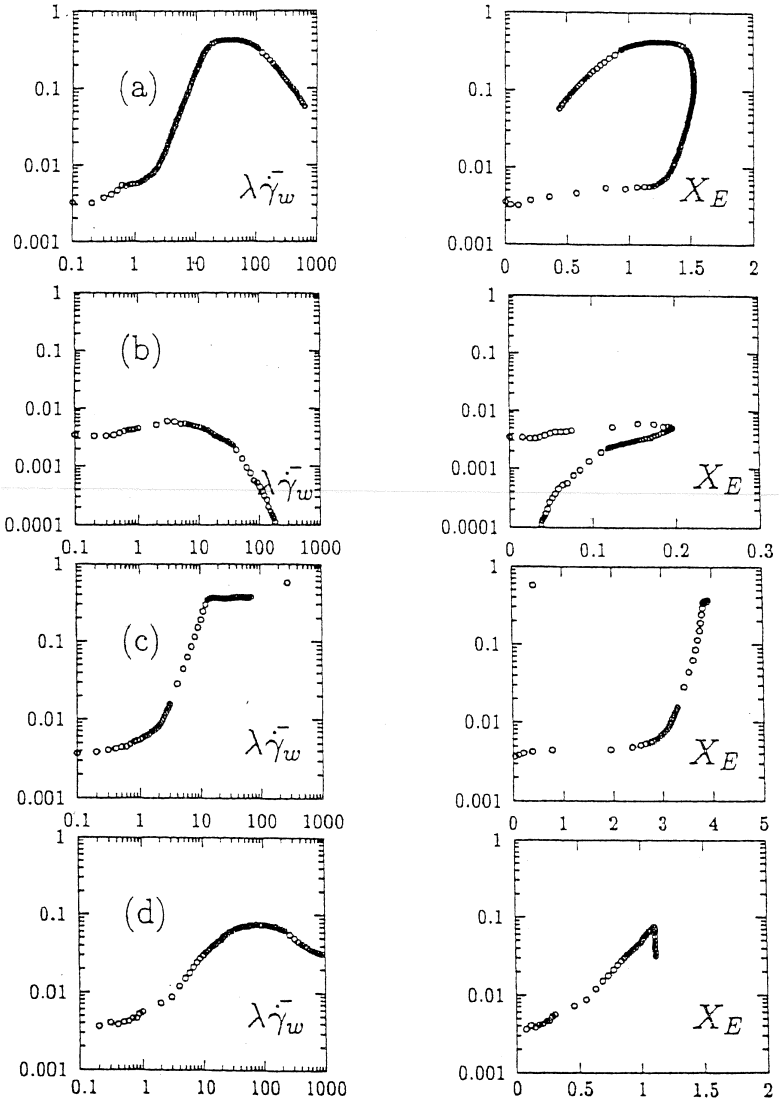

Fig. 11. Vortex activity: exponential version: (a) $\epsilon = 0.015$, (b) $\epsilon = 1$; linear version: (c) $\epsilon = 5 \times 10^{-4}$, (d) $\epsilon = 0.35$.

a plateau. Note the logarithmic scale used for $\dot{\bar{\gamma}}_w$. The second column of Fig. 11 uses X_E to show in a dimensionless way the correlation between the variations of the vortex activity and the elongational effects. In the exponential case, the curves go back to the origin, and in the linear case, a fixed point is reached. While elongational effects and vortex activity are clearly correlated, no simple analytic law can yet be deduced. The vortex development phenomena appears as a complex one.

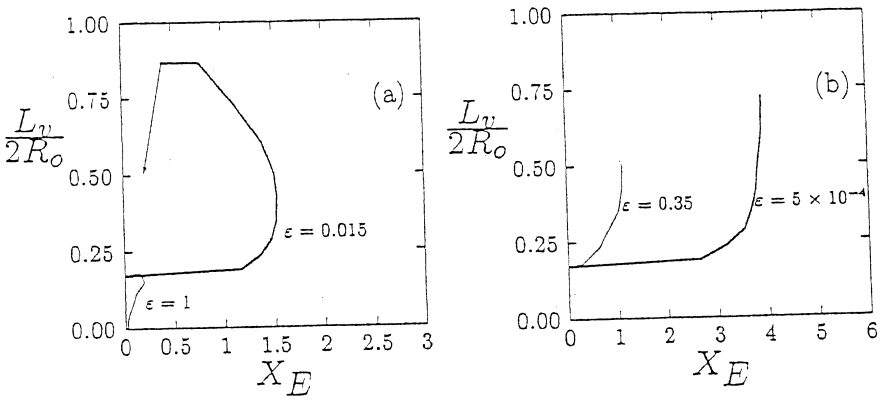

Fig. 12. Reattachment length: (a) exponential version; (b) linear verions

Let L_v be the reattachment length and R_0 the upstream channel radius. The dimensionless quantity $L_v/2R_0$ as a function of X_E is reproduced in Fig. 12. Significant vortex growth is generated for the exponential and linear version both for small values of ϵ (exponential version $\epsilon = 0.015$ (Fig. 12(a)), and linear version $\epsilon = 5 \times 10^{-4}$ (Fig. 12(b)). The linear version with $\epsilon = 0.35$ shows moderate vortex growth (Fig. 12(b)). We refer to Ref. 24, p. 173 for related results with polymer solutions. The exponential model with $\epsilon = 1$ point out shear-thinning eflects. As expected, the vortex reattachment length is decreasing.

Note that the ratio $L_v/2R_0$ takes the Newtonian value 0.17 associated with $X_E = 0$. For the exponential model at high values of $\lambda\dot{\gamma}_w$, the elongational properties become negligible, and the shear properties are predominant (see also Fig. 1). As a consequence, the ratio η_e/η and X_E decrease when $\lambda\dot{\gamma}_w$ becomes large. As expected, the vortex size reaches a maximum and start to decrease, according to the variation of X_E (Fig. 12(a)). For the linear model, the elongational and shear viscosities tend to constant values when $\lambda\dot{\gamma}_w$ becomes large. Thus, X_E tends to a constant. According to this prediction, the vortex reattachment length tends to a constant at high values of $\lambda\dot{\gamma}_w$ (Fig. 12(b)).

4.4 Pressure drop in the entrance

The total pressure drop in the flow domain Ω is given by

$$\Delta p(\Omega; \tau, \boldsymbol{u}) = -\frac{2\pi}{Q} \int_\Gamma (\boldsymbol{u} \cdot \boldsymbol{n}) p \, ds, \tag{17}$$

where Q is the flow rate, and $\boldsymbol{n}$ the outward unit normal onto the boundary $\Gamma = \partial\Omega$ of Ω. According to Green's formula, the sum over Γ in (17) can be

also expressed as

$$\int_\Gamma (\boldsymbol{u}\cdot\boldsymbol{n})p\ \mathrm{d}s = \int_\Omega \boldsymbol{u}\cdot\nabla p\ \mathrm{d}x,$$

since $\operatorname{div}\boldsymbol{u} = 0$.

The solution is assumed to be stationary ($\partial\boldsymbol{u}/\partial t = 0$). The conversion of momentum (9) leads to $\nabla p = \operatorname{div}(2\eta_n D(\boldsymbol{u}) + \tau)$ since only slow flows are considered (the inertia term $\boldsymbol{u}\cdot\nabla\boldsymbol{u}$ is neglected).

By using a second integration by part, (17) becomes

$$\Delta p(\Omega;\tau,\boldsymbol{u}) = \frac{2\pi}{Q}\int_\Omega D(\boldsymbol{u}):(2\eta_n D(\boldsymbol{u})+\tau)\ \mathrm{d}x$$
$$-\frac{2\pi}{Q}\int_\Gamma (2\eta_n D(\boldsymbol{u})+\tau):(\boldsymbol{u}\otimes\boldsymbol{n})\ \mathrm{d}s, \tag{18}$$

where $\boldsymbol{u}\otimes\boldsymbol{n} = (u_i n_j)_{i,j}$ denotes the tensorial product of the two vectors $\boldsymbol{u}$ and $\boldsymbol{n}$.

The pressure drop associated with the fully developed Poiseuille flow is defined by

$$\Delta p_i = \Delta p(\Omega_i;\tau_i,\boldsymbol{u}_i),\quad 1\le i\le 2,$$

where Ω_1 (resp. Ω_2) is the upstream (resp. downstream) channel, and $\tau_1, \boldsymbol{u}_1$ (resp. $\tau_1, \boldsymbol{u}_2$) the fully developed Poiseuille flow at upstream (resp. downstream).

Following Ref. 24, we define the energy loss in the entrance region of the contraction by taking away the energy loss caused by the Poiseuille flow from the total energy loss in the contraction:

$$\Delta p_{\mathrm{en}} = \Delta p(\Omega;\tau,\boldsymbol{u}) - \sum_{i=1}^{2}\Delta p_i.$$

As specified in paragraph 4.1, both upstream and downstream lengths are sufficiently long so that fully developed conditions can exist. This property guarantees that Δp_{en} is independent of the length of both upstream and downstream domains.

The Couette correction (C) is given by

$$C = \frac{\Delta p_{\mathrm{en}}}{2\eta_0\dot{\gamma}_{\mathrm{w}}}. \tag{19}$$

The Couette correction expresses (in a dimensionless way) the energy loss in the entrance region.

Since Δp_{en} depends on the dimension of our system, a dimensionless version of this quantity is introduced:

$$\delta p_{\mathrm{en}} = \frac{\lambda}{2\eta_0}\Delta p_{\mathrm{en}} = \lambda\overline{\dot{\gamma}_{\mathrm{w}}}C. \tag{20}$$

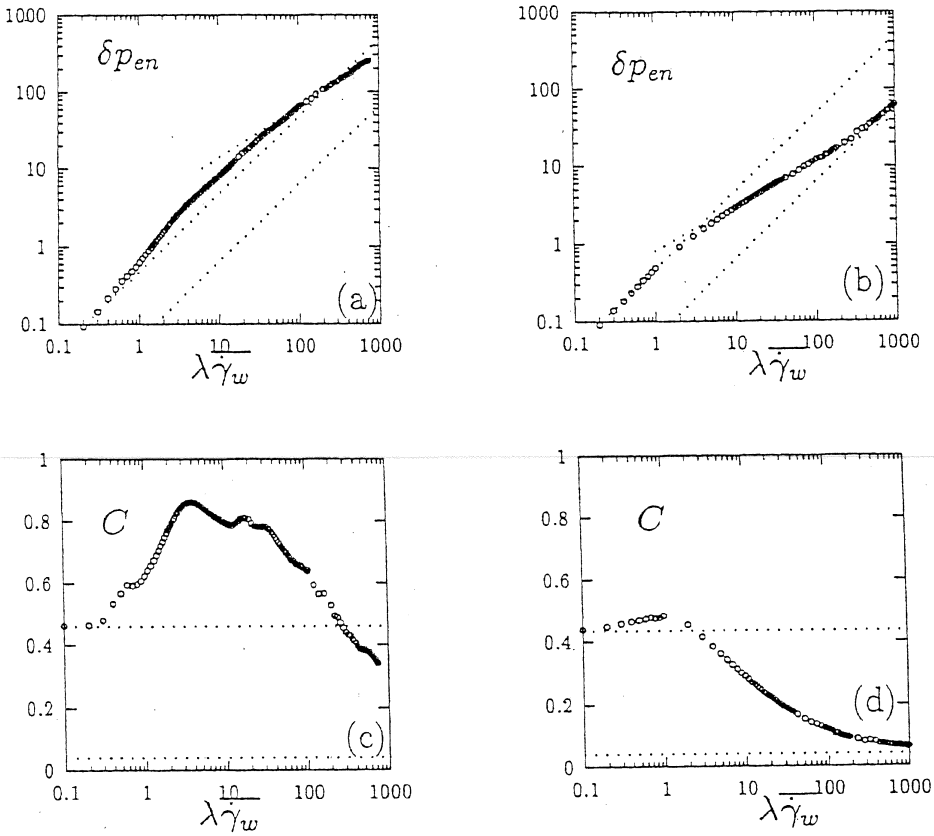

Fig. 13. Exponential version: pressure drop: (a) $\epsilon = 0.015$, (b) $\epsilon = 1$; Couette correction: (c) $\epsilon = 0.015$, (d) $\epsilon = 1$.

Figures 13 and 14 plot δp_{en} and C versus $\lambda\dot{\gamma}_w$. For both the exponential version (Fig. 13) and the linear version (Fig. 14), different flow regimes can be observed. The first flow regime is Newtonian-like. The flow curves on Figs. 13(a), 13(b), 14(a), and 14(b) exhibit a slope of 1, and $\delta p_{en} = C_o \lambda\dot{\gamma}_w$ for small values of $\lambda\dot{\gamma}_w$, where $C_0 = 0.46$.

For high values of $\lambda\dot{\gamma}_w$, the flow curves also show a slope of 1, and $\delta p_{en} = C_\infty \lambda\dot{\gamma}_w$, except on Fig. 13(a), where the asymptotical behavior is still not reached. In this case, the expected asymptote for very high values of $\lambda\dot{\gamma}_w$ is indicated by a dotted line. Note that C_∞ depends on the material parameters of the model, while C_0 is constant.

The intermediate flow regime presents roughly a power law character: δp_{en} is proportional to $(\lambda\dot{\gamma}_w)^k$. The linear case with $\epsilon = 5 \times 10^{-4}$ shows $k > 1$. We refer to Refs 26, 27 for the experimental study and the modeling of the pressure drop associated with solutions in thick solvents. We point

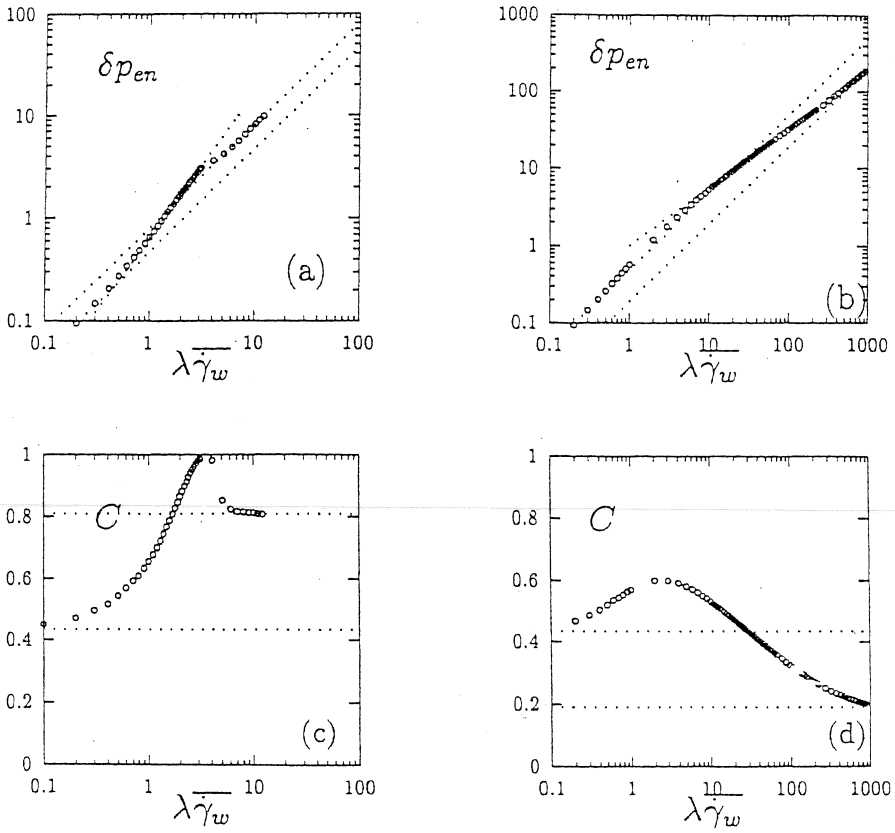

Fig. 14. Linear version: pressure drop: (a) $\epsilon = 5 \times 10^{-4}$, (b) $\epsilon = 0.35$; Couette correction: (c) $\epsilon = 5 \times 10^{-4}$, (d) $\epsilon = 0.35$.

out that the behaviors of Phan-Thien–Tanner fluids are qualitatively in good agreement with experimental measurements. The linear version can be associated with polymer solutions, while the exponential one reflects more polymer melt-like behavior.

The Couette correction on Figs. 13 and 14 presents some details of the pressure drop in the entrance region. For the exponential version $\epsilon = 0.015$, the dependence of C on $\lambda\dot{\gamma}_w$ is complex (Fig. 13(c)). Asymptotically, for very high values of $\lambda\dot{\gamma}_w$, we expect an asymptotical value of C (in dotted lines). Using the exponential Phan-Thien–Tanner model in a 4:1 circular abrupt contraction, Debbaut et al. [23] report the C decreases very slightly before increasing to a maximum of approximately 3.75 at $\lambda\dot{\gamma}_w \approx 2.5$ before decreasing again. Note that the "Weissenberg number" introduced in [23], denoted here We^*, is given by $We^* = \lambda\dot{\gamma}_w/4$.

Table 2 gives a summary for the values of C_∞ and k, depending on the fluid under consideration. These values are computed by using mesh 1.

Table 2
Flow regimes: Phan-Thien–Tanner models

C_∞	k	Model version	ϵ
0.04?	0.67	exponential	0.015
0.04	0.58	exponential	1
0.81	1.40	linear	5×10^{-4}
0.19	0.75	linear	0.35

Calculations with mesh 2 show that the behavior of C as a function of $\lambda\overline{\dot{\gamma}_w}$ remains the same (see Fig. 15). Values differ by about 11% of the maximum value, and $C_o = 0.51$ on mesh 2. These values are in semi-quantitative agreement with the results of Coates et al. [28, p. 183], where $C_0 \approx 0.57$ with two different meshes on a 8:1 abrupt contraction. Finally, using two meshes of a 4:1 contraction, Debbaut et al. [23] report a 10% change in the maximum value of C.

4.5 *Profiles along the axis of symmetry*

The profile along the axis of symmetry are presented in this paragraph for both the exponential ($\epsilon = 0.015$) and the linear ($\epsilon = 5 \times 10^{-4}$) versions. The velocity profile is reproduced in Figs 16(a) and 16(d), where $\bar{U}$ is the average velocity downstream. Note the overshoot of the velocity in the entrance region. The velocity reaches a maximum in the downstream domain.

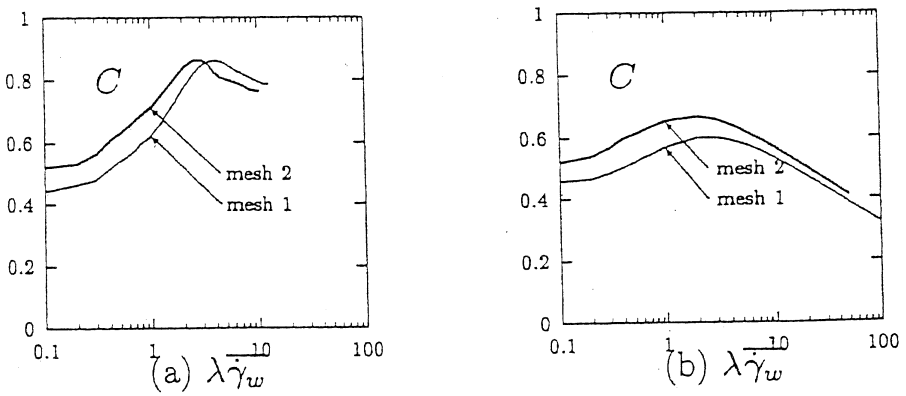

Fig. 15. Mesh sensitivity for the Couette correction: (a) exponential version ($\epsilon = 0.015$); (b) linear version ($\epsilon = 0.35$).

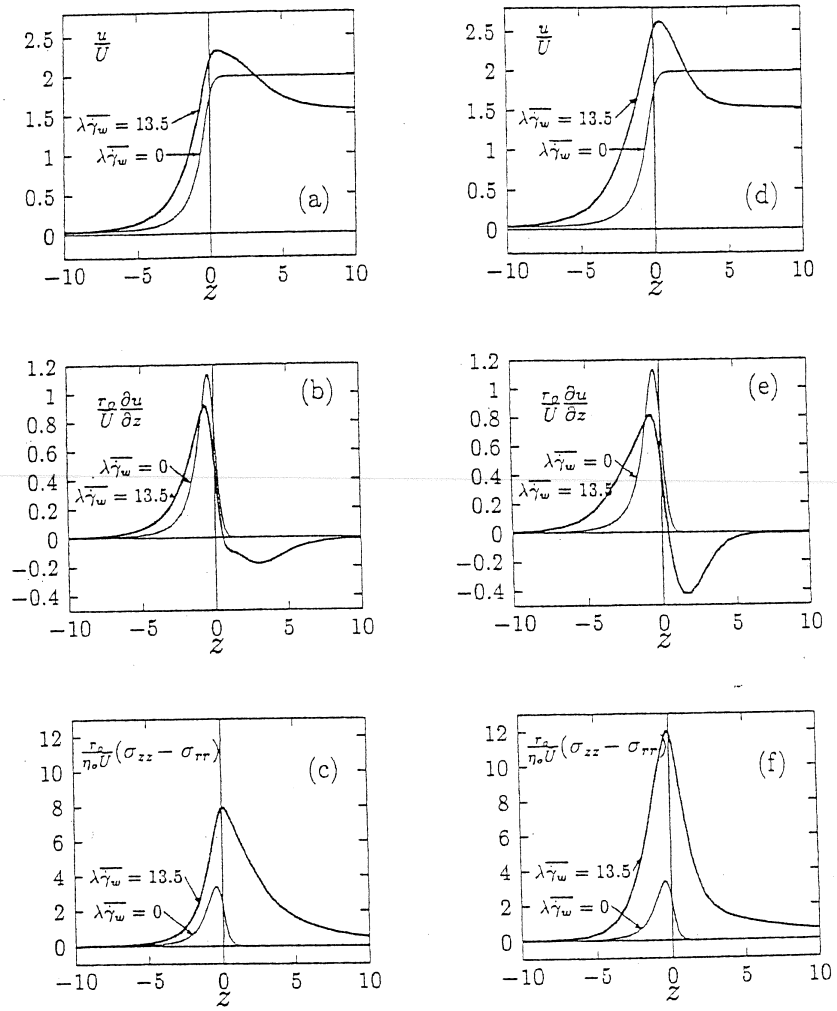

Fig. 16. Profiles along the axis: exponential version $\epsilon = 0.015$, $\lambda\dot{\bar{\gamma}}_w = 13.5$: (a) velocity; (b) elongational rate; (c) first normal stress difference; linear version $\epsilon = 5 \times 10^{-4}$, $\lambda\dot{\bar{\gamma}}_w = 13.5$: (d) velocity; (e) elongational rate; (f) first normal stress difference.

Figures 16(b) and 16(e) show the elongational rate along the axis of symmetry ($r = 0$), where r_0 is the downstream channel radius. The Newtonian behavior presents a maximum in the upstream domain near the entry. In the downstream channel, the elongational rate quickly reaches the asymptotical zero value. For the viscoelastic fluid, the maximum goes slightly upstream. The upstream elongation rate is reduced. The elongational rate takes negative values in the downstream channel and slowly reaches the zero value. The change of sign is associated with the overshoot of the velocity.

Figures 16(c) and 16(f) represent the first normal stress difference along the axis of symmetry. The change of scale between the Newtonian and the viscoelastic behavior is here spectacular. The maximum goes slightly downstream, and the relaxation is slower in the viscoelastic case.

5. Conclusions

The objective of this work was to examine the relation between macroscopic features of complex flows in an circular abrupt contraction, such as vortex enhancement, flow curves, velocity gradient, and normal stress difference along the flow axis, and its viscous behavior is simple extensional flows. Since the elongational viscosity of the Phan-Thien–Tanner model is mainly governed by one material parameter, four representative test-fluids have been studied. This model leads to numerical results, such as vortex development and flow curves, that are qualitatively in good agreement with experimental measurements. As previously observed [26,27] with solutions in thick solvents, flow curves here show three flow regimes, and the second one develops a power law character. Moreover, the numerical approach allows a direct access to flow properties, such as elongational rate and first normal stress difference along the axis of symmetry.

The results of the present paper confirm the robustness and the efficiency of the numerical strategy introduced in Refs. 10, 11 and 14. The time dependent approach has allowed us to obtain rapidly stationary solutions of the Phan-Thien–Tanner models. Moreover, the conservative finite element approximation guarantees non-artificial oscillating solutions. An important property of our result is the convergence with the mesh refinement. Macroscopy quantities such as vortex intensity and velocity overshoot (see Ref. 14) show a fast convergence with mesh refinement. The Couette correction reflects some variations between the two meshes of the present study. Values differ by about 11% of the maximum value.

As pointed out by Boger [24], viscoelastic fluid entry flows are not only of interest as an appropriate test problem for developing the fluid mechanics of viscoelastic fluids, but they are also of practical interest and great importance in polymer processing. The ultimate aim is to predict the influence of the entry flow geometry on the kinematics and pressure drop in order both to minimize the latter and optimize the former. Optimization tends to eliminate secondary flows and regions of high stress. Thus, the robustness and efficiency of our approach opens new paths for this prediction of flow phenomena. In addition, complex entry flows appear to be potentially important for viscoelastic fluids rheometrical properties calculations, through the use of appropriate constitutive equations and numerical models.

References

1 D.V. Boger, M.J. Crochet, and R.A. Keiller, On viscoelastic flows through abrupt contractions. J. Non-Newtonian Fluid Mech., 44 (1992) 267–279.
2 J.M. Piau, N. El Kissi, and B. Tremblay, Low Reynolds number flow visualisation of linear and branched silicones upstream of orifice dies. J. Non-Newtonian Fluid Mech., 30 (1988) 197–232.
3 J.M. Piau, N. El Kissi, and B. Tremblay, Influence of upstream instabilities and wall slip on melt fracture and sharkskin phenomena during silicones extrusion through orifice dies, J. Non-Newtonian Fluid Mech., 34 (1990) 145–180.
4 R. Keunings and M.J. Crochet, J. Non-Newtonian Fluid Mech., 14 (1984) 279–299.
5 S.A. White, A.D. Gotsis, and D.G. Baird, J. Non-Newtonian Fluid Mech., 24 (1987) 121–160.
6 B. Debbaut and M.J. Crochet, J. Non-Newtonian Fluid Mech., 30 (1988) 169–184.
7 B. Debbaut, J. Non-Newtonian Fluid Mech., 37 (1990) 281–296.
8 R.G. Larson, Constitutive Equations for Polymer Melts and Solutions., Butterworths series in Chemical Engineering, Boston, 1988.
9 N. Phan-Thien and R.I. Tanner, A new constitutive equation derived from network theory, J. Non-Newtonian Fluid Mech., 2 (1977) 353–365.
10 P. Saramito, Numerical simulation of viscoelastic fluid flows using incompressible finite element method and a θ-method. Mathematical Modelling and Numerical Analysis, 28 (1994) 1–35.
11 P. Saramito, Simulation numérique d'écoulements de fluides viscoélastiques par éléments finis incompressibles at une méthode de directions alternées; applications, thèse de l'Institut National Polytechnique de Grenoble, 1990.
12 R. Glowinski and J. Périaux, Numerical methods for nonlinear problems in fluid dynamics. In: Proceeding of the International Seminar on Scientific Super-Computer, Feb. 1987.
13 R. Glowinski and P. Le Tallec, Augmented Lagrangian and Operator Splitting Method in Non-linear Mechanics, SIAM Studies in Applied Mathematics, 1989.
14 P. Saramito, Efficient simulation of nonlinear viscoelastic fluid flows. J. Non-Newtonian Fluid Mech., (1993) submitted.
15 P. Saramito, Operator splitting for viscoelastic fluid with a differential constitutive law. C. R. Acad. Sci. Paris, (1994) submitted.
16 M.J. Crochet and J.M. Marchal, A new mixed finite element for calculating viscoelastic fluid flows. J. Non-Newtonian Fluid Mech., 26 (1987) 77–114.
17 A. Fortin and A. Zine, An improved GMRES method for solving viscoelastic fluid flow problems, J. Non-Newtonian Fluid Mech., 42 (1992) 1–18.
18 V. Girault and P.A. Raviart, Finite Element Methods for Navier–Stokes Equations—Theory and Algorithms, Springer-Verlag, 1986.
19 P. Lesaint and P.A. Raviart, On Finite Element Methods for Solving the Neutron Transport Equation, Academic Press, Carl de Boor edition, 1974.
20 K. Baba and M. Tabata, On a conservative upwind finite element scheme for convection diffusion equations. RAIRO Numer. Anal., 15 (1981) 3–25.
21 A.N. Brooks and T.R.J. Hughes, Streamline-Upwind/Petrov–Galerkin formulation for convection dominated flow with particular emphasis on the incompressible Navier–Stokes equations. Comp. Meth. Appl. Mech. Eng., 32 (1982) 199–259.
22 J. B. Goodman and R.L. Leveque, A geometric approach to high resolution TVD schemes, SIAM J. Numer. Anal. 25 (1988) 268–284.

23 B. Debaut, J.M. Marchal, and M.J. Crochet, Numerical simulation of highly viscoelasti flows though an abrupt contraction, J. Non-Newtonian Fluid Mech., 29 (1988) 119–14
24 D.V. Boger, Viscoelastic flows through contractions. Ann. Rev. Fluid Mech., 19 (198 57–182.
25 R.E. Evans and K. Walters. Flow characteristics associated with abrupt change i geometry in the case of highly elastic liquids, J. Non-Newtonian Fluid Mech., 20 (198 11–29.
26 U. Cartalos and J.M. Piau, Creeping flow regimes of low concentration polymer solutio in thick solvents though an orifice die. J. Non-Newtonian Fluid Mech., 45 (199 231–285.
27 U. Cartalos and J.M. Piau, Pressure drop scaling law and structural stress contributio for complex flow of flexible polymer solutions in thick solvents. J. Non-Newtonian Flu Mech., 44: (1992) 55–93.
28 P.J. Coates, R.C. Armstrong, and R.A. Brown, Calculation of steady-state viscoelast flow through axisymmetric contractions with the EEME formulation, J. Non-Newtonia Fluid Mech., 42: (1992) 141–188.

ELSEVIER

J. Non-Newtonian Fluid Mech., 60 (1995) 199–223

Journal of Non-Newtonian Fluid Mechanics

Efficient simulation of nonlinear viscoelastic fluid flows

P. Saramito

Laboratoire de Rhéologie, BP53, 38041, Grenoble cedex, France

Received 22 March 1993; in revised form 13 June 1995

Abstract

This paper presents a new and efficient method for computing the flow of a non-Newtonian fluid. The approach is based on two independent concepts:

Time-dependent simulation of viscoelastic flow: A new decoupled algorithm, presented in P. Saramito, Simulation numérique d'ecoulements de fluides viscoélastiques par éléments finis incompressibles et une méthode de directions alternées; applications, Thèse de l'Institut National Polytechnique de Grenoble, 1990 and P. Saramito, Numerical simulation of viscoelastic fluid flows using incompressible finite element method and a θ-method, Math. Modelling Num. Anal., 35 (1994) 1–35, enables us to split the major difficulties of this problem, and to solve it more efficiently. Moreover, this scheme is of order two in time, and can be used to obtain stationary flows in an efficient way.

Conservative finite element method: this method combines the incompressible Raviart–Thomas element, the discontinuous Lesaint–Raviart element, and a finite volume element method. It satisfies exactly the mass conservation law, and leads to an optimal size for the nonlinear system in terms of the total degree of freedom versus the mesh size.

We apply our numerical procedure to the Phan-Thien–Tanner model with a classical benchmark: the four to one abrupt contraction. The numerical solutions exhibit good behavior, especially near the singularity, in the vicinity of the re-entrant corner. The numerical experiments present the main features of such flows: vortex development and overshooting of the velocity profile along the axis of symmetry in the entry region.

Keywords: Viscoelastic fluids; Viscoelastic flow

1. Introduction

The numerical simulation of viscoelastic fluid flows is a major challenge: it appears as both a test for assessing the robustness and efficiency of numerical methods, and a qualification of models for complex flow geometries.

SSDI 0377-0257(95)01380-6

Intensive research has pointed out the theoretical difficulties in solving the large nonlinear system obtained from the approximation of the boundary value problem. Keunings [23] provides an exhaustive survey of the considerable work performed in this domain. There are three main difficulties in the previous approaches:

- The so-called *high Weissenberg number problem*: simulations were stopping before a limit value (approximately 4) of this dimensionless parameter, which expresses the memory effect of the material. It is now well accepted that the reasons for this difficulty are numerical: the use of inappropriate boundary conditions and numerical schemes associated with the type of governing equations [22].
- The *approximation strategy*: finite element spaces have to satisfy compatibility conditions (i.e. the well-known inf–sup conditions [2,5,13]). These conditions guarantee that the approximate problem is well-posed and that convergence occurs with mesh refinement.
- The tremendous amount of computation needed, thus limiting the size of the system that can be simulated.

In 1987, Crochet and Marchal [7] presented the first result above the "critical" Weissenberg number. They solved the stationary problem by using Newton's algorithm and a global Gaussian inversion of the Jacobian matrix. This direct method allowed them to reach numerical results using the Oldroyd model for Weissenberg numbers (We) up to 14 for a plane contraction, and $We = 20.8$ in the axisymmetric case, using two meshes ($We = 64$ for the lower mesh). The authors presented a subelement approximation strategy for stress tensor components. In this approach the number of degrees of freedom of the system was large, therefore requiring considerable computing time on a supercomputer.

In 1989, Fortin and Fortin [11] proposed a decoupled algorithm, based on the GMRES method, for solving the stationary problem of an Oldroyd fluid. They developed discontinuous approximation of the stress tensor. Using this approach, they obtained up to $We = 8$, with the Oldroyd model and for a plane contraction. However, their solutions present oscillations: the authors pointed out that stress schemes were not strictly TVD (total variation diminishing) and that computing time was important on a workstation.

We propose here an efficient method for computing flows of non-Newtonian fluids. Moreover, we apply this method by using a realistic viscoelastic model: the Phan-Thien–Tanner model. Section 2 develops constitutive and conservation laws of viscoelastic fluids of the Phan-Thien–Tanner type. Section 3 presents the study of viscometric properties and one-dimensional Poiseuille fluid flow, using Phan-Thien–Tanner model.

In Sections 4 and 5 we develop our numerical approach. On the one hand, we use a time-dependent decoupled algorithm [36,35]. As shown in Section 4, this algorithm enables us to split the major difficulties of this problem, and to solve it more efficiently. Moreover, this scheme is of order two in time, and can be used to obtain stationary flows in an efficient way. On the other hand, we develop an original conservative finite element approximation of the problem in Section 5. This element is based on a combination of the incompressible Raviart–Thomas element, the discontinuous Lesaint–Raviart element, and a finite volume element method. It

satisfies exactly the mass conservation law, and leads to an optimal size for the nonlinear system, in terms of the total degree of freedom versus mesh size.

We apply our numerical procedure to the Phan-Thien–Tanner model with a classical benchmark: the four to one abrupt contraction (Sections 6 and 7). By drawing a first normal extra-stress component near the re-entrant corner, we can check the high quality of the numerical approximation. Then, we point out vortex development, and overshooting of the velocity profile along the axis of symmetry in the entry region.

2. The governing equations

In this section we present the formulation of constitutive and conservative laws, and the mathematical formulation of the problem.

2.1. Constitutive laws

The Cauchy stress tensor is given by the relation:

$$\sigma = -pI + 2\eta_n D(\boldsymbol{u}) + \tau. \tag{1}$$

We use the following notations: p is the pressure field, $\boldsymbol{u}$ is the velocity field, τ is an extra-stress tensor. In addition, $D(\boldsymbol{u}) = (\nabla \boldsymbol{u} + \nabla \boldsymbol{u}^t)/2$ denotes the rate-of-deformation tensor, and η_n represents the Newtonian viscosity of the fluid. The extra-stress τ satisfies a constitutive law. First, we consider the Oldroyd model [30],

$$\lambda \overset{\square}{\tau} + \tau - 2\eta_v D(\boldsymbol{u}) = 0, \tag{2}$$

where λ is the relaxation time of the fluid memory, η_v a second viscosity, and $(\overset{\square}{\cdot})$ represents a material derivation of a tensor [30,26]

$$\overset{\square}{\tau} = \frac{\partial \tau}{\partial t} + \boldsymbol{u} \cdot \nabla \tau - W(\boldsymbol{u}) \cdot \tau + \tau \cdot W(\boldsymbol{u}) - a(D(\boldsymbol{u}) \cdot \tau + \tau \cdot D(\boldsymbol{u})). \tag{3}$$

In the last relation, a is related to a material parameter: $a \in [-1,1]$, and $W(\boldsymbol{u}) = (\nabla \boldsymbol{u} - \nabla \boldsymbol{u}^t)/2$ is the vorticity tensor.

This model includes a retardation time $\mu = \alpha\lambda$, where $\alpha = \eta_v/(\eta_n + \eta_v)$ is a retardation parameter. Let us denote by $\eta = \eta_n + \eta_v$ the total viscosity. For $|a| < 1$ in (2), we obtain the Johnson–Segalman model, and for $\eta_n = 0$, the Maxwell model.

Some extra properties can be obtained by modifying the Oldroyd model (2): the Phan-Thien–Tanner model [38,27] is given by the following constitutive equation:

$$\lambda \overset{\square}{\tau} + \exp\left(\frac{\epsilon\lambda}{\eta_v} \operatorname{tr}(\tau)\right) - 2\eta_v D(\boldsymbol{u}) = 0, \tag{4}$$

where $\operatorname{tr}(\cdot)$ is the trace of a tensor, and ϵ is a parameter of the model. This gives rise to the following properties:

– the shear viscosity $\eta_s(\dot{\gamma})$ decreases with the shear rate $\dot{\gamma}$ (for $|a| < 1$), and

– the elongational viscosity $\eta_e(\dot{\epsilon})$ reaches a maximum (for $\epsilon > 0$).

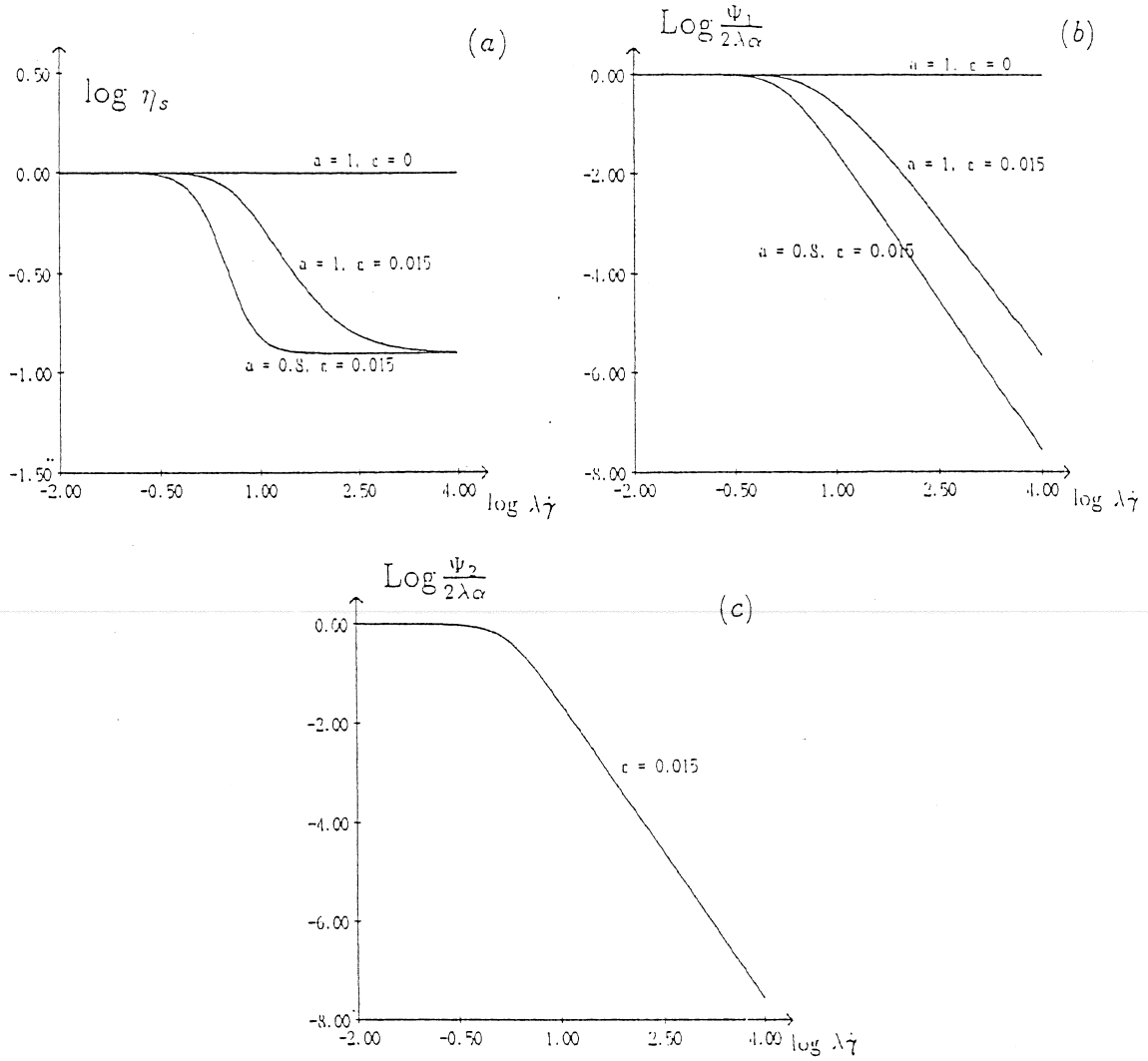

Fig. 2. Phan-Thien–Tanner model ($\alpha = 0.875$): Normalized shear viscosity (a), first normal stress difference (b), and second normal stress difference (c).

agreement with experimental data for polymer melts [26, p. 204] than the version with a linear coefficient (Fig. 1b). Note that the Johnson–Segalman model ($\varepsilon = 0$) predicts an infinite value for the steady state elongational viscosity.

3.2. Simple shear flows

The Phan-Thien–Tanner model shows shear thinning and a non-constant first normal stress coefficient (Fig. 2a). Let $f_s(\lambda\dot{\gamma})$ be the unique value satisfying

$$f_s(\lambda\dot{\gamma}) = \exp\left(\frac{2\varepsilon a(\lambda\dot{\gamma})^2}{f_s(\lambda\dot{\gamma})^2 + (1-a^2)(\lambda\dot{\gamma})^2}\right). \tag{15}$$

Then, the shear viscosity is given by

$$\eta_s \overset{\text{def}}{=} \frac{\sigma_{12}}{\eta\dot{\gamma}} = 1 - \alpha + \alpha \frac{f_s(\lambda\dot{\gamma})}{f_s(\lambda\dot{\gamma})^2 + (1-a^2)(\lambda\dot{\gamma})^2} . \tag{16}$$

The model predicts first and second normalized stress difference, ψ_1 and ψ_2, respectively (see also Figs. 2b,c):

$$\frac{\psi_1}{2\alpha\lambda} \overset{\text{def}}{=} \frac{\sigma_{11} - \sigma_{22}}{2\alpha\lambda\dot{\gamma}^2} = \frac{1}{f_s(\lambda\dot{\gamma})^2 + (1-a^2)(\lambda\dot{\gamma})^2} , \tag{17}$$

and $\psi_2 \overset{\text{def}}{=} (\sigma_{22} - \sigma_{33})/\dot{\gamma}^2 = (1-a)\psi_1$. Therefore, the second normal stress difference vanishes for $a = 1$ (upper-convected derivative).

Nevertheless, for $|a| < 1$ and up to a critical value $\alpha_c(\varepsilon)$ of α, the model predicts an excessive shear thinning; in this case, the shear stress $\sigma_{12} = \eta_s\dot{\gamma}$ becomes non-monotonic (Fig. 3). Conversely, when $0 \le \alpha \le \alpha_c(\varepsilon)$, the shear stress is always monotonic. For the Johnson–Segalman model, we have $\alpha_c(0) = 8/9$.

3.3. Poiseuille flows

We find in Refs. [21,29] an analytical resolution and stability study for Poiseuille flows of Oldroyd fluids. We need here a numerical approach to solve the Poiseuille flow of a Phan-Thien–Tanner fluid. Both analytical and numerical approaches start by reducing the one-dimensional Poiseuille problem to a scalar nonlinear characteristic equation. We solve the characteristic equation and obtain numerical solutions by a continuation algorithm.

Such solutions can exhibit pathological cases depending on material parameter values: we point out loss of existence or unicity of solutions, and existence of non-regular solutions.

Let g and $2g$ be the constant pressure gradients driving the plane and axisymmetric Poiseuille flows, respectively. By integration of the momentum conservation law, we obtain the characteristic equation

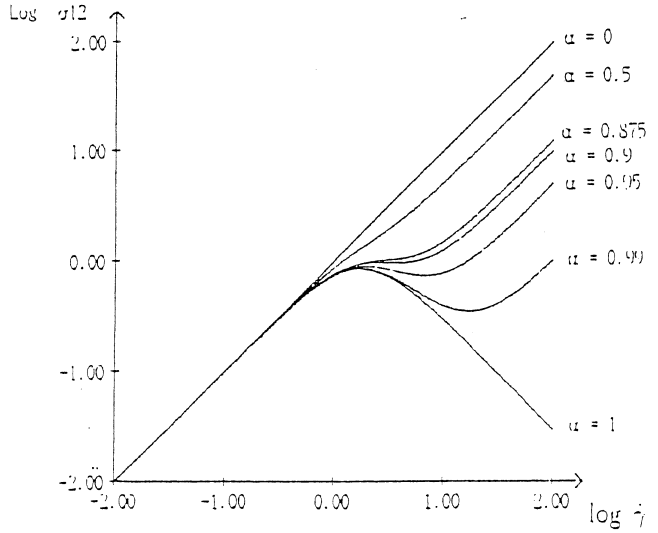

Fig. 3. Shear stress as predicted by the Phan-Thien–Tanner model: $\lambda = 1$, $a = 0.8$ and $\varepsilon = 0.015$.

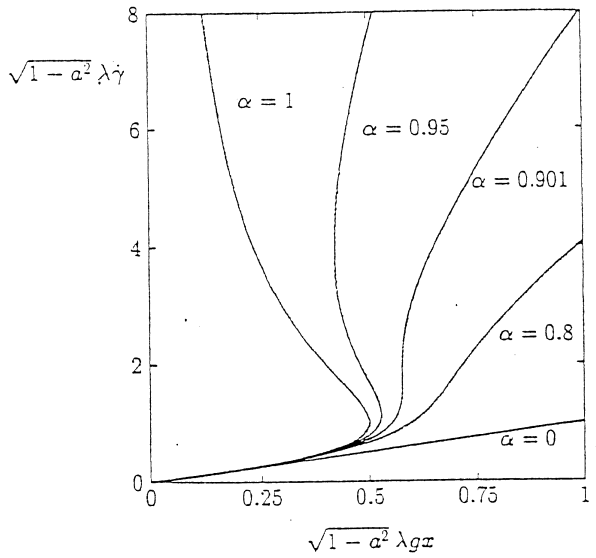

Fig. 4. Characteristic curves for the Phan-Thien–Tanner model: $\varepsilon = 0.015$.

$$gx = \eta_s \dot{\gamma}, \quad 0 \le x \le r, \tag{18}$$

where r is the radius of the section. Fig. 4 shows the characteristic curves of the fluid: $\sqrt{1-a^2}\lambda\dot{\gamma}$ versus $\sqrt{1-a^2}\lambda gx$. Up to the critical value $\alpha_c(\varepsilon)$ of α, the characteristic curve admits two turning-back points denoted by χ^- and χ^+, $0 \le \chi^- \le \chi^+$. The situation is characterized as follows:

- For $0 < \alpha < \alpha_c(\varepsilon)$, we obtain one regular solution (Figs. 5a–c).
- For $\alpha = \alpha_c(\varepsilon)$, $\chi^+ = \chi^-$, this solution remains regular if $\sqrt{1-a^2}\lambda gr \le \chi^-$ (Fig. 5d), and becomes singular otherwise (Figs. 5e,f).
- For $\alpha_c(\varepsilon) < \alpha < 1$, we have one regular solution if $\sqrt{1-a^2}\lambda gr \le \chi^-$ (Fig. 5g), or a continuum of solutions if $\sqrt{1-a^2}\lambda gr > \chi^-$. Moreover, one of these solutions remains regular for $\sqrt{1-a^2}\lambda gr \le \chi^+$ (Fig. 5h). When $\sqrt{1-a^2}\lambda gr > \chi^+$ all solutions are singular (Fig. 5i), and present discontinuous rates of deformation.
- For $\alpha = 1$ (Maxwell-like model), we have only one solution for $\sqrt{1-a^2}\lambda gr \le \chi^+$ (Fig. 5j), and no more solution otherwise.

There are different opinions in the literature about the interpretation of such solutions (i.e. when $\alpha > \alpha_c(\varepsilon)$ and high values of the rate of deformation appear near the wall). Malkus and co-workers [29] developed a description of a *spurt* flow as a trigger mechanism for the melt instabilities: they referred to this as an *apparent slip*, despite the fact that there is no actual slip, due to the relative thinness of the wall layer. However, as the pressure gradient increases, this wall layer thickens. Schowalter [9] proposes sharp velocity gradients near the wall as a possible model for fluid slip in the context of continuous velocity profile.

This model is not completely satisfactory: discontinuous rates of deformation have not been observed in the flow domain by experimenters, when macroscopic slip phenomena appear [39,25,24]. This leads us to argue that we have reached a possible limit of such differential models when a discontinuous rate of deformation appears.

Nevertheless, this "rheological artifact" [27] is of great interest from mathematical and numerical points of view; it is helpful in understanding and writing constitutive equations. Moreover, the critical case before the appearance of a discontinuous rate of deformation can be viewed as a significant benchmark for testing the robustness and the efficiency of algorithms for viscoelastic flow problems. This last point is discussed in the following sections.

3.4. Definition of the Weissenberg number

We consider here the Poiseuille flow, which will be treated in the next paragraph. The shear-thinning character of the Phan-Thien–Tanner fluid makes it difficult to define We using directly $\dot{\gamma}$ at the wall. Instead, we use an *average* value $\overline{\dot{\gamma}_w}$ defined by $\overline{\dot{\gamma}_w} = 4\bar{U}/r$ for axisymmetric flow, and $\overline{\dot{\gamma}_w} = 3\bar{U}/r$ for plane flow where $\bar{U}$ denotes the average velocity. Let We be the Weissenberg number, as introduced in ref. [4] for the White–Metzner fluid:

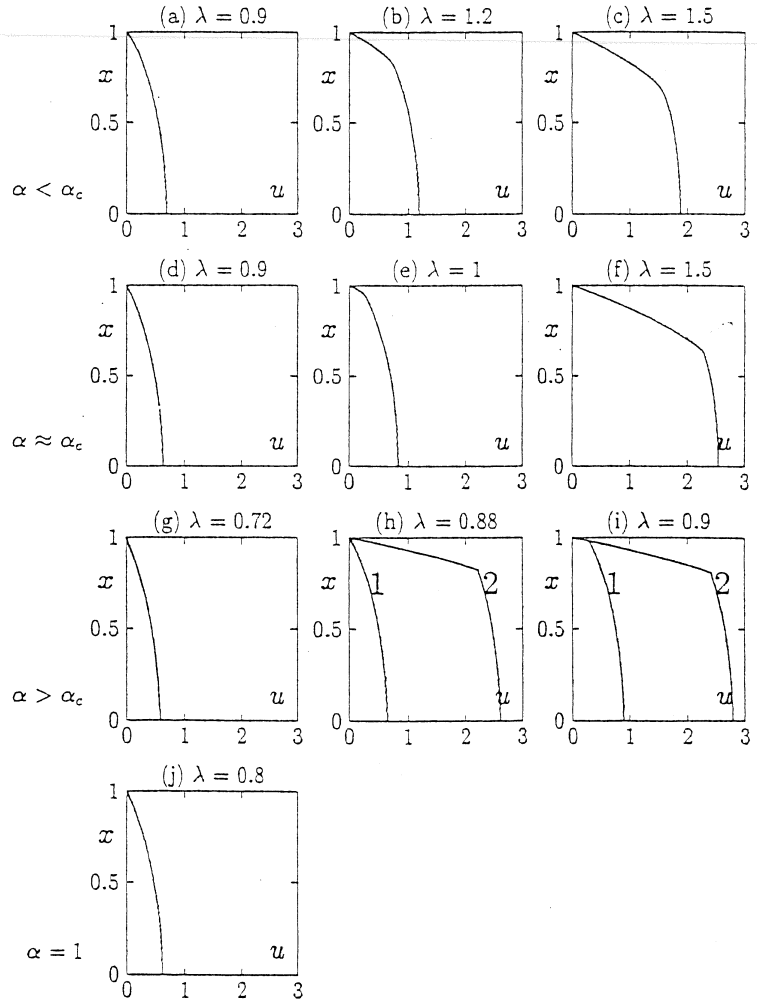

Fig. 5. Solutions of Poiseuille flow ($\varepsilon = 0.015$, $g = 1$): $\alpha = 0.875 < \alpha_c$: $\lambda = 0.9$ (a); $\lambda = 1.2$ (b); $\lambda = 1.5$ (c); $\alpha = 0.901 \approx \alpha_c$: $\lambda = 0.9$ (d); $\lambda = 1$ (e); $\lambda = 1.5$ (f); $\alpha = 0.95 > \alpha_c$: $\lambda = 0.72$ (g); $\lambda = 0.8$ (h); $\lambda = 0.9$ (i); $\alpha = 1$: $\lambda = 0.8$ (j).

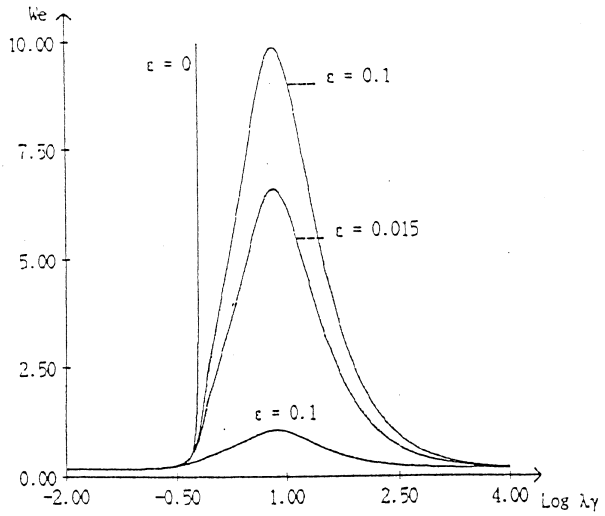

Fig. 6. Weissenberg number versus $\lambda\overline{\dot{\gamma}_w}$; $a = 0.8$, $\varepsilon = 0.015$.

$$We = \lambda_n \overline{\dot{\gamma}_w}, \tag{19}$$

where λ_n is the *natural* time of the fluid:

$$\lambda_n = \sigma_{E|\dot{\varepsilon}=\overline{\dot{\gamma}_w}} / 6\sigma_{12}\overline{\dot{\gamma}_w}. \tag{20}$$

Note that the definition (20) of the natural time λ_n uses the first normal stress difference σ_E in uniaxial extension $\dot{\varepsilon} = \overline{\dot{\gamma}_w}$. A representative rate of elongation $\dot{\varepsilon}$ is given by: $\dot{\varepsilon} = \overline{\dot{\gamma}_w}$. Thus the definition given in Ref. [4] for the White–Metzner fluid has been modified in order to include elongational properties. Moreover, Section 7 shows that this definition of *We* corresponds to vortex development.

Therefore, when $\varepsilon > 0$, the Phan-Thien–Tanner model predicts bounded values of the Weissenberg number (Fig. 6). Conversely, with $\varepsilon = 0$ (Johnson–Segalman and Oldroyd models), the Weissenberg number is not bounded for high values of $\lambda\overline{\dot{\gamma}_w}$. As pointed out in Ref. [4], the prediction of bounded values of *We* is in better agreement with experimental data.

Definition (19) of *We* applies to flow in contractions, by considering Poiseuille flow at the downstream section.

4. Time approximation using a θ-scheme

We shall now restrict our study to the problem (8)–(10), (12)–(14), where the inertia term $(\boldsymbol{u} \cdot \nabla)\boldsymbol{u}$ in (9) is neglected, since only slow flows are investigated.

In this section, we present a new method for solving unsteady viscoelastic problems. This method is related to the alternating direction implicit technique [31,17,16] for decoupling the main two difficulties: the nonlinearities of Eq. (8), and the incompressibility relation (10).

4.1. Splitting the problem

We consider the following two operators:

$$A_1(\tau,\boldsymbol{u},p) = \begin{bmatrix} \dfrac{w}{2\alpha}\tau - D(\boldsymbol{u}) \\ \operatorname{div}\tau + (1-\alpha)\Delta\boldsymbol{u} - \nabla p \\ \operatorname{div}\boldsymbol{u} \end{bmatrix}, \tag{21}$$

$$A_2(\tau,\boldsymbol{u},p) = \begin{bmatrix} \dfrac{We}{2\alpha}T(\boldsymbol{u})\tau + \dfrac{f(\tau)-\dot{w}}{2\alpha}\tau \\ 0 \\ 0 \end{bmatrix}. \tag{22}$$

As mentioned above, the advective part of the momentum equation $(\boldsymbol{u}\cdot\nabla)\boldsymbol{u}$ is neglected, since only slow flows are investigated.

In (21)–(22), we introduce $w \in]0,1[$, a parameter associated with the splitting. The Laplace operator Δ in (21) is related to the boundary conditions (12) for $\boldsymbol{u}$, and the transport operator $T(\boldsymbol{u}) \overset{\text{def}}{=} (\boldsymbol{u}\cdot\nabla) + \beta_a(\cdot,\nabla\boldsymbol{u})$ in (22) is related to the inflow boundary condition (13) for τ. The bilinear form $\beta_a(\cdot,\cdot)$ is defined by

$$\beta_a(\tau,\nabla\boldsymbol{u}) = \tau\cdot W(\boldsymbol{u}) - W(\boldsymbol{u})\cdot\tau - a(D(\boldsymbol{u})\cdot\tau + \tau\cdot D(\boldsymbol{u})). \tag{23}$$

Let us consider the following problem:

find $\mathcal{U} = (\tau,\boldsymbol{u},p)$ defined in Ω, such that

$$m\frac{\mathrm{d}\mathcal{U}}{\mathrm{d}t} + A_1(\mathcal{U}) + A_2(\mathcal{U}) = 0, \tag{24}$$

and satisfying the initial condition (14). The diagonal matrix in (24) is defined by $m = \operatorname{diag}(We/2\alpha, -Re, 0)$. The parameter w is related to a numerical relaxation parameter of the splitting.

4.2. Time approximation

Using these definitions, we build a time approximation sequence $\mathcal{U}^n = (\tau^n,\boldsymbol{u}^n,p^n)$ of a solution $\mathcal{U}(t) = (\tau(t),\boldsymbol{u}(t),p(t))$ of (24). For a given $\mathcal{U}^0$, the sequence $(\mathcal{U}^n)_{n>0}$ is defined by the following three-step procedure [15]:

$$m\frac{\mathcal{U}^{n+\theta}-\mathcal{U}^n}{\theta\Delta t} + A_1(\mathcal{U}^{n+\theta}) = -A_2(\mathcal{U}^n), \tag{25}$$

$$m\frac{\mathcal{U}^{n+1-\theta}-\mathcal{U}^{n+\theta}}{(1-2\theta)\Delta t} + A_2(\mathcal{U}^{n+1-\theta}) = -A_1(\mathcal{U}^{n+\theta}), \tag{26}$$

$$m\frac{\mathcal{U}^{n+1}-\mathcal{U}^{n+1-\theta}}{\theta\Delta t} + A_1(\mathcal{U}^{n+1}) = -A_2(\mathcal{U}^{n+1-\theta}), \tag{27}$$

where Δt is the total time step, and $\theta \in]0,\frac{1}{2}[$ is the parameter of the time scheme.

4.3. The θ-method

The definitions of Section 4.1 and the time scheme of Section 4.2 lead to our new algorithm [35,36] for solving unsteady flows of viscoelasticity fluids. This scheme is of order two in time, and allows us to compute steady solutions efficiently. We can also decouple the computation of stress and velocity–pressure; we get two standard sub-problems: Stokes-type, from steps (25) and (27), and transport type, from step (26).

First, let us study step 1. For τ^n, $\boldsymbol{u}^n$ given, we search $(\tau^{n+\theta},\boldsymbol{u}^{n+\theta},p^{n+\theta})$ such that

$$\frac{We}{2\alpha}\frac{\tau^{n+\theta}-\tau^n}{\theta\Delta t}+\frac{w}{2\alpha}\tau^{n+\theta}-D(\boldsymbol{u}^{n+\theta})=-\frac{We}{2\alpha}T(\boldsymbol{u}^n)\tau^n-\frac{f(\tau^n)-w}{2\alpha}\tau^n, \tag{28}$$

$$-Re\frac{\boldsymbol{u}^{n+\theta}-\boldsymbol{u}^n}{\theta\Delta t}+\operatorname{div}\tau^{n+\theta}+(1-\alpha)\Delta\boldsymbol{u}^{n+\theta}-\nabla p^{n+\theta}=0, \tag{29}$$

$$\operatorname{div}\boldsymbol{u}^{n+\theta}=0, \tag{30}$$

$$\boldsymbol{u}^{n+\theta}=\boldsymbol{u}_\Gamma((n+\theta)\Delta t)\ \text{on}\ \Gamma. \tag{31}$$

We set

$$\gamma^n=(We-(f(\tau^n)-w)\theta\Delta t)\tau^n-(We\theta\Delta t)T(\boldsymbol{u}^n)\tau^n. \tag{32}$$

From (28), we get

$$\tau^{n+\theta}=\frac{1}{We+w\theta\Delta t}(\gamma^n+2\theta\Delta tD(\boldsymbol{u}^{n+\theta})). \tag{33}$$

Since $\operatorname{div}\boldsymbol{u}^{n+\theta}=0$, we have $2\operatorname{div}D(\boldsymbol{u}^{n+\theta})=\Delta\boldsymbol{u}^{n+\theta}$, and Eq. (29) becomes

$$k\boldsymbol{u}^{n+\theta}-s\Delta\boldsymbol{u}^{n+\theta}=f^n, \tag{34}$$

with

$$k=Re/(\theta\Delta t), \tag{35}$$

$$s=1-\alpha\frac{We-(1-w)\theta\Delta t}{We+w\theta\Delta t} \tag{36}$$

and

$$f^n=k\boldsymbol{u}^n+\frac{1}{We+w\theta\Delta t}\operatorname{div}\gamma^n. \tag{37}$$

Step 1 can be solved as follows:

- $-\tau^n$ and $\boldsymbol{u}^n$ being known, compute successively γ^n and f^n using (32) and (37), respectively;
- $-f^n$ being known, compute $(\boldsymbol{u}^{n+\theta},p^{n+\theta})$ as the solution of the Stokes-type problem (34) and (30) with the boundary condition (31);
- $-\gamma^n$ and $\boldsymbol{u}^{n+\theta}$ being known, compute $\tau^{n+\theta}$ in an explicit way, using (33).

Now, we can study the second step. We search $(\tau^{n+1-\theta},\boldsymbol{u}^{n+1-\theta})$ such that

$$\frac{We}{2\alpha}\frac{\tau^{n+1-\theta}-\tau^{n+\theta}}{(1-2\theta)\Delta t}+\frac{We}{2\alpha}T(\boldsymbol{u}^{n+1-\theta})\tau^{n+1-\theta}+\frac{f(\tau^{n+1-\theta})-w}{2\alpha}\tau^{n+1-\theta}$$

$$=-\frac{w}{2\alpha}\tau^{n+\theta}+D(\boldsymbol{u}^{n+\theta}), \tag{38}$$

$$-Re\frac{\boldsymbol{u}^{n+1-\theta}-\boldsymbol{u}^{n+\theta}}{(1-2\theta)\Delta t}=-\operatorname{div}\tau^{n+\theta}-(1-\alpha)\Delta\boldsymbol{u}^{n+\theta}+\nabla p^{n+\theta}, \tag{39}$$

$$\tau^{n+1-\theta}=\tau_\Gamma((n+1)\Delta t)\text{ on }\Gamma. \tag{40}$$

From (29) and (39), we obtain

$$\boldsymbol{u}^{n+1-\theta}=\frac{1-\theta}{\theta}\boldsymbol{u}^{n+\theta}-\frac{1-2\theta}{\theta}\boldsymbol{u}^{n}. \tag{41}$$

Step 2 reduces to the transport-type problem (38) with the boundary condition (40). Moreover, using Oldroyd or Maxwell models ($f\equiv 1$), this problem becomes linear in τ. The resolution of step 3 can be deduced from (32)–(37) by substituting n, $(n+\theta)$ by $(n+1-\theta)$, $(n+1)$, respectively. Finally, we can solve the time-dependent problem using a θ-method. We obtain a succession of Stokes-type and transport-type problems.

The choice $\theta=1/\sqrt{2}$ presents some good convergence properties, as shown in Ref. [37]. Since our numerical experiments on the Phan-Thien–Tanner model, and previously [35] on an Oldroyd-B model, are concerned, the parameter w of the splitting has no influence on the convergence rate of the θ-schema towards the stationary solution. The convergence rate is related to the residual term $A_1(\mathcal{U})+A_2(\mathcal{U})$ of the stationary problem. The time step Δt is automatically adjusted during iterations, in order to optimize the convergence rate.

We point out that the θ-method is independent of the approximation with respect to space: as a consequence, this method is worth using for other space-approximations than the one presented in the following section.

4.4. *Resolution of the sub-problems*

The sub-problems of Stokes-type are solved using a conjugate gradient method. The preconditioning is obtained by means of the augmented Lagrangian method [12]. The efficiency of this method is particularly spectacular for the test problem of Section 6, as the initial problem is ill-conditioned due to the domain length and the presence of the re-entrant corner.

The transport sub-problems are solved by using a symmetrized successive over-relaxation method (SSOR, see Ref. [18]). Numerical tests of this procedure have shown fast convergence of the residual terms.

5. Approximation with respect to space

In the finite element approach, the use of classical approximation methods for the velocity (for example, the P_2-P_1 element) leads to a questionable approximation

of conservation properties, especially the incompressibility relation (10). This is all the more troublesome as the velocity field $\boldsymbol{u}$ is likely to transport the stress tensor τ in relation (8).

We present in this section an original mixed finite element method for the approximation of the viscoelastic fluid flow problems. This approximation is based on a combination of Thomas–Raviart element [14, ch. 3] for velocity–pressure fields, piecewise constant functions for normal stress components, and linear continuous functions for the shear stress components (see Fig. 7). We have shown in Ref. [36] that this method leads to a well-posed problem for $We = 0$.

For $We \neq 0$, a scalar transport term $(\boldsymbol{u} \cdot \nabla)\tau_{ij}$ appears for each component τ_{ij} of the extra-stress tensor τ. We use the Lesaint–Raviart scheme [28] for the transport term of the normal stress components τ_{11} and τ_{22} (τ_{rr}, τ_{zz} and $\tau_{\theta\theta}$ in the axisymmetric case). These approximations are generally discontinuous at interfaces between elements. Upwinding techniques are possible in schemes involving right-side or left-side values, according to the direction of the flow. We use the Bab–Tabata scheme [1,34], based on a finite volume element formulation on an approximate Riemann solver, for the shear component τ_{12} (τ_{rz} in the axisymmetric case). This approximation of $(\boldsymbol{u} \cdot \nabla)\tau$ is used for all three steps of the θ-method.

It should be pointed out that the incompressibility relation is exactly satisfied when using the Thomas–Raviart element, and both Lesaint–Raviart and Baba–Tabata schemes are TVD (total variation diminishing), so no artificial numerical oscillations can occur. This is an improvement on the previous method [35], where the SUPG method [6] was used for approximation of the transport term of shear stress component. In fact, the SUPG scheme is not TVD [19], and numerical oscillations can occur near singularities, associated with strong effects at high Weissenberg numbers.

Moreover, this finite element method was found to be of optimal cost in terms of the total number of degrees of freedom versus the number of element of mesh: six or seven degrees of freedom per element, for six or seven scalar fields, in plane or axisymmetric geometry, respectively.

Table 1 gives a comparative synthesis of this cost with other authors. The test value $(N_{\text{dof}}/6N_{\text{elem}})_\infty$ is the asymptotic value of the number of degrees of freedom N_{dof} versus the number of elements N_{elem} and the number of scalar fields: (six, for

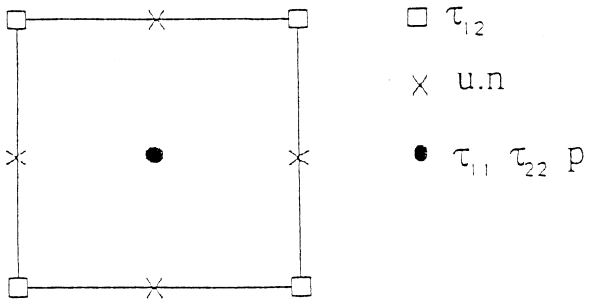

Fig. 7. Incompressible finite element.

Table 1
Comparative cost of three finite element methods

N_{elem}	N_{dof}	$(N_{dof}/6N_{elem})_{\infty}$	Ref.
210	16 719	9.5 (57/6)	[7]
326	19 532	9.83 (59/6)	[10]
1 144	23 645	3.33 (20/6)	[11]
1 196	7 403	1	This work

planar geometry): τ_{11}, τ_{12}, τ_{22}, u_1, u_2, and p. We use the Euler relation $N_{edge} + 1 = N_{elem} + N_{node}$ and suppose that the mesh is regular, made only of quadrangles, and satisfies $N_{node} = \mathcal{O}(N_{elem})$.

Finally, this element can be easily extended to approach three-dimensional problems, always with an optimal cost.

6. Numerical experiments in an abrupt contraction

We now describe the application of both the θ-method and the incompressible finite element method to the computation of viscoelastic flows in an axisymmetric contraction. We recall briefly the main features of such flows, and give the conditions of our numerical experiments on the Phan-Thien–Tanner model.

6.1. General features of the flow in an abrupt contraction

Such a flow is of greatest interest from both theoretical and practical points of view (e.g. in relation to polymer processing problems) and has been investigated in numerous experimental works. In the entry flow region, before the contraction, the fluid particles are accelerated close to the central part of the duct, while vortices appear close to the edges (see Fig. 8).

This flow can be considered as a complex one, because it is roughly a shear flow close to the solid wall, and becomes rather elongational at the vicinity of the centre. Experiments related to the axisymmetric contraction have shown increasing recirculating zones when the Weissenberg number *We* increases. We refer to the recent paper of Binding [3] for a review and an analysis of such intriguing flow behaviours.

6.2. Numerical and geometrical conditions

In our numerical experiments, the abrupt contraction was considered to be axisymmetrical ($x_1 = z$, $x_2 = r$, $x_3 = \theta$), involving an axis of symmetry $r = 0$. We may consider a half-flow domain Ω, as shown in Fig. 9.

We have chosen the upstream radius $R = 4$, and the downstream radius $r = 1$. This corresponds to the classical four-to-one contraction generally investigated in numerical works. Both upstream and downstream lengths are assumed to be

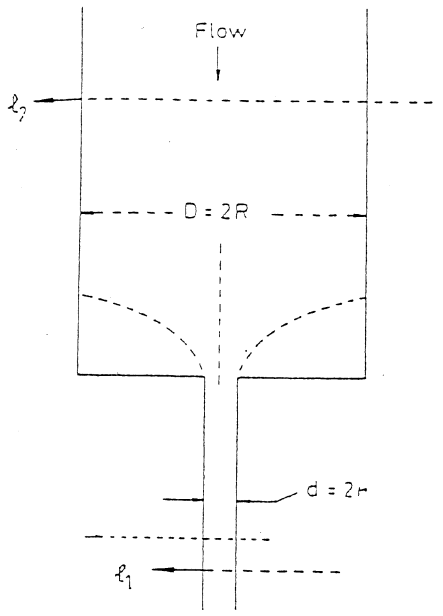

Fig. 8. Description of the 4:1 abrupt contraction (from Ref. [3], p. 29).

sufficiently long so that fully developed conditions can exist; we have chosen $l_1 = 64$ and $l_2 = 200$.

6.3. Choice of material parameters

The Phan-Thien–Tanner model predicts realistic elongational viscosity, which reaches a maximum (see also Section 3.1). Furthermore, the choice $\varepsilon = 0.015$ with an exponential coefficient is consistent with data for polymer melts [26, p. 205]. Moreover, this choice, also used in Ref. [8], is convenient for a cross-checked approach.

The use of the derivative parameter a allows us to control the level of shear thinning (see Section 3.2): $a \neq 0$ and $|a| < 1$ lead to non-vanishing second normal stress difference and bounded values of We at high shear rates; $0.8 \leq a < 1$ is consistent with the experimental data. The results of Section 7 use $a = 0.8$.

The choice $0 < \alpha < \alpha_c(\varepsilon)$ guarantees a strictly monotonically increasing shear stress, and the existence of one unique regular solution of the Poiseuille flow

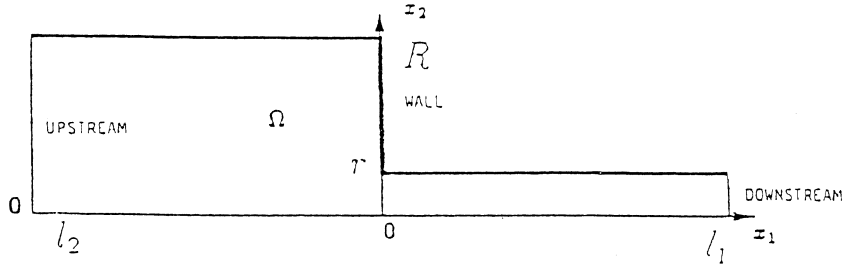

Fig. 9. Specification of the domain of computation.

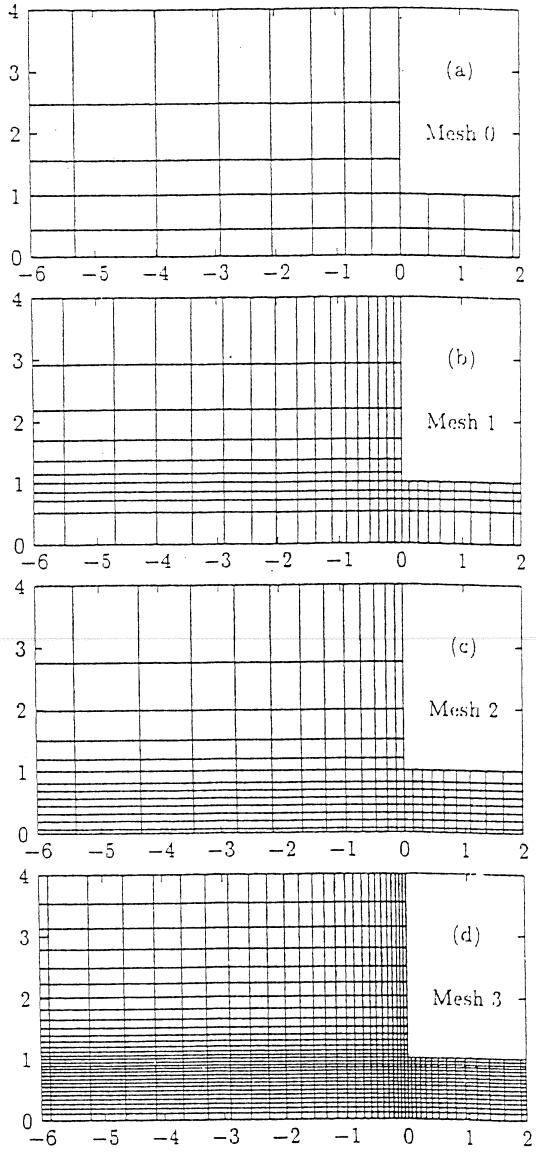

Fig. 10. The finite element mesh family.

problem (see Section 3.3). The choice $\alpha = 7/8$, near the critical value, satisfies those properties, and allows important viscoelastic effects.

The Weissenberg number is defined by (19), considering the downstream Poiseuille flow. Here, the Reynolds number has no influence on the stationary solution, since only slow flows are investigated; the inertia term $(\boldsymbol{u} \cdot \nabla)\boldsymbol{u}$ in (9) is neglected.

6.4. *Mesh family*

Starting from a rough mesh $\mathscr{T}^{(0)}$, we build a family $(\mathscr{T}^{(i)})_{i \geq 0}$ by using a refining procedure of $\mathscr{T}^{(0)}$ near the re-entrant corner (see Fig. 10).

On $\mathcal{T}^{(i)}$, the length of the element close to the re-entrant corner is given by

$$h_i \approx \frac{r}{3 \times 2^i}. \tag{42}$$

The sizes of the elements are given by a geometric progression of constant factor, starting from the re-entrant corner.

7. Phan-Thien–Tanner fluid in an axisymmetric contraction

We present the computation of the flow through a four-to-one axisymmetric contraction of a Phan-Thien–Tanner fluid with a constitutive equation given by (4). Section 6.3 develops the main motivation for this choice.

7.1. Convergence tests

The velocity and stress profiles are given by reference to the average velocity $\bar{U}$ at the downstream section. The mesh convergence properties can be observed by drawing velocity profiles along the axis of symmetry for the meshes 1, 2 and 3 (Fig. 11). We notice an important overshoot near the entry section. We also notice that the mesh convergence of the solution is remarkable for fine meshes 2 and 3, while the rough mesh 1 gives only qualitative results; the convergence velocity of the mesh family is considerable.

Fig. 12 presents the first normal component of the extra-stress tensor along the line $r = 1$ close to the re-entrant corner, for the three meshes 1, 2 and 3. In the vicinity of the re-entrant corner, stresses become singular, and the theoretical value is infinite at the corner. As expected, the peak of the stress approximation becomes sharper with the mesh refinement near the singularity. Nevertheless, we can check that convergence occurs outside the vicinity of the re-entrant corner.

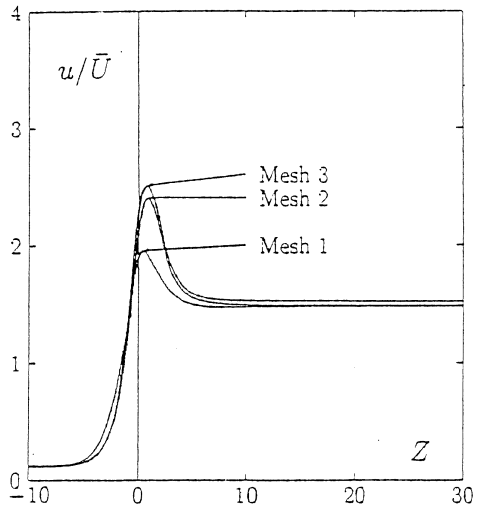

Fig. 11. Mesh convergence of the velocity profile along the axis of symmetry at $\lambda\overline{\dot{\gamma}_w} = 9.30$: meshes 1, 2 and 3.

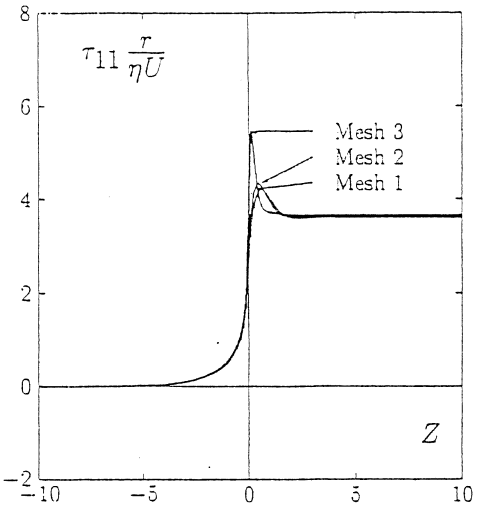

Fig. 12. Mesh convergence of the first normal stress component along the line $r = 1$ close to the re-entrant corner at $\lambda\dot{\bar{\gamma}}_w = 4.50$: meshes 1, 2 and 3.

7.2. Velocity and stress profiles

Let us observe in Fig. 13 the velocity profile along the axis of symmetry as a function of $\lambda\dot{\bar{\gamma}}_w$. At $We = 0$, a tiny overshoot of the velocity profile theoretically exists, but is not perceptible in Fig. 13(a). From small values of $\lambda\dot{\bar{\gamma}}_w > 0$ (Fig. 13b), an overshoot of the velocity clearly appears near the entry section. This overshoot increases with $\lambda\dot{\bar{\gamma}}_w$ (Fig. 13c).

Fig. 14 presents the first normal component profile of the extra-stress tensor along the line $r = 1$ close to the re-entrant corner, as a function of We. At $We = 0$ (Fig. 14a), the peak of the Newtonian extra-stress takes negative values, but from small values of $We > 0$, the extra-stress profile changes type, and the peak becomes positive (Figs. 14b,c). As expected, the relaxation process of the stresses along the

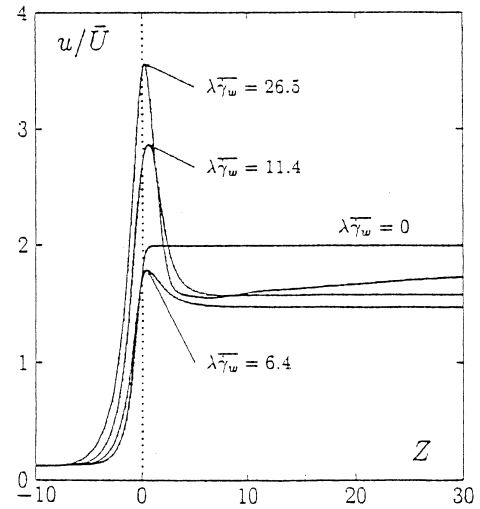

Fig. 13. Velocity profile along the axis of symmetry, as a function of $\lambda\dot{\bar{\gamma}}_w$ (mesh 3).

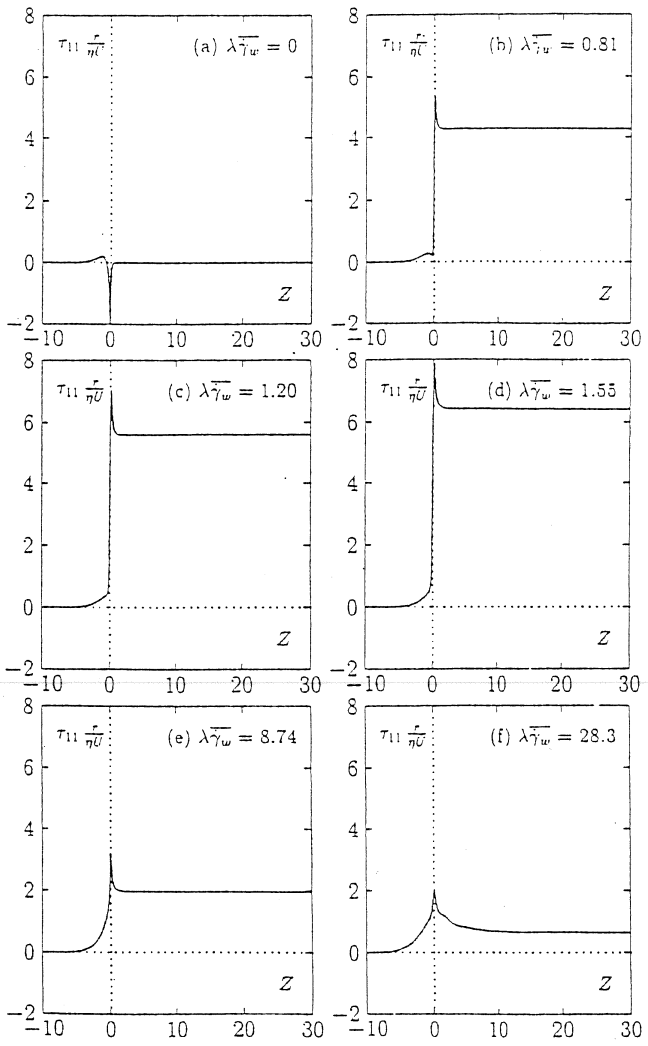

Fig. 14. First normal stress component along the line $r = 1$ close to the re-entrant corner, as a function of We (mesh 3).

wall after the re-entrant corner becomes slower as We increases; the downstream length must be sufficiently long for fully developed stress conditions to exist.

Note that the dimensionless first normal component of the extra-stress tensor $\tau_{11} \cdot r/\eta\bar U$ at upstream grows to a maximum value (Fig. 14d), and starts to decrease for higher values of $\lambda\overline{\dot\gamma_w}$ (Fig. 14e). For high values of the flow rate (see Fig. 14f) this quantity tends to zero, as predicted by relation (17); the lack of interest of the branch of solutions for large values of $\lambda\overline{\dot\gamma_w}$ could define a limit of the Phan-Thien–Tanner model for high flow rates.

7.3. *Vortex development and intensity*

Fig. 15 shows the vortex development as a function of We and $\lambda\overline{\dot\gamma_w}$. For $We = 0$ (Newtonian fluid), we observe a small vortex close to the salient corner of the contraction. The change in concavity can be observed between Figs. 15(b) and (c). We notice in Figs. 15(c) and (d) the growth of the vortex size. The development of

the vortex reaches a maximum (nearly Fig. 15d) and is followed by a slow decrease for high values of the flow rate.

Figs. 16(a) and (b) present the vortex instensity as functions of $\lambda\dot{\bar{\gamma}}_w$ and We, respectively. The vortex intensity is defined by the ratio of the recirculating flow rate in the vortex to the flow rate through the contraction. Vortex intensity grows, reaching a maximum value for $\lambda\dot{\bar{\gamma}}_w \approx 13.8$ ($We = 6.60$), and then slowly decreases to the asymptotic Newtonian value. When $\lambda\dot{\bar{\gamma}}_w \approx 13.8$, the vortex intensity reaches nearly 10% of the main flow rate; the corresponding Newtonian value is nearly 0.2%. Note that in Fig. 15(b) the variations of We fits the variations of the vortex

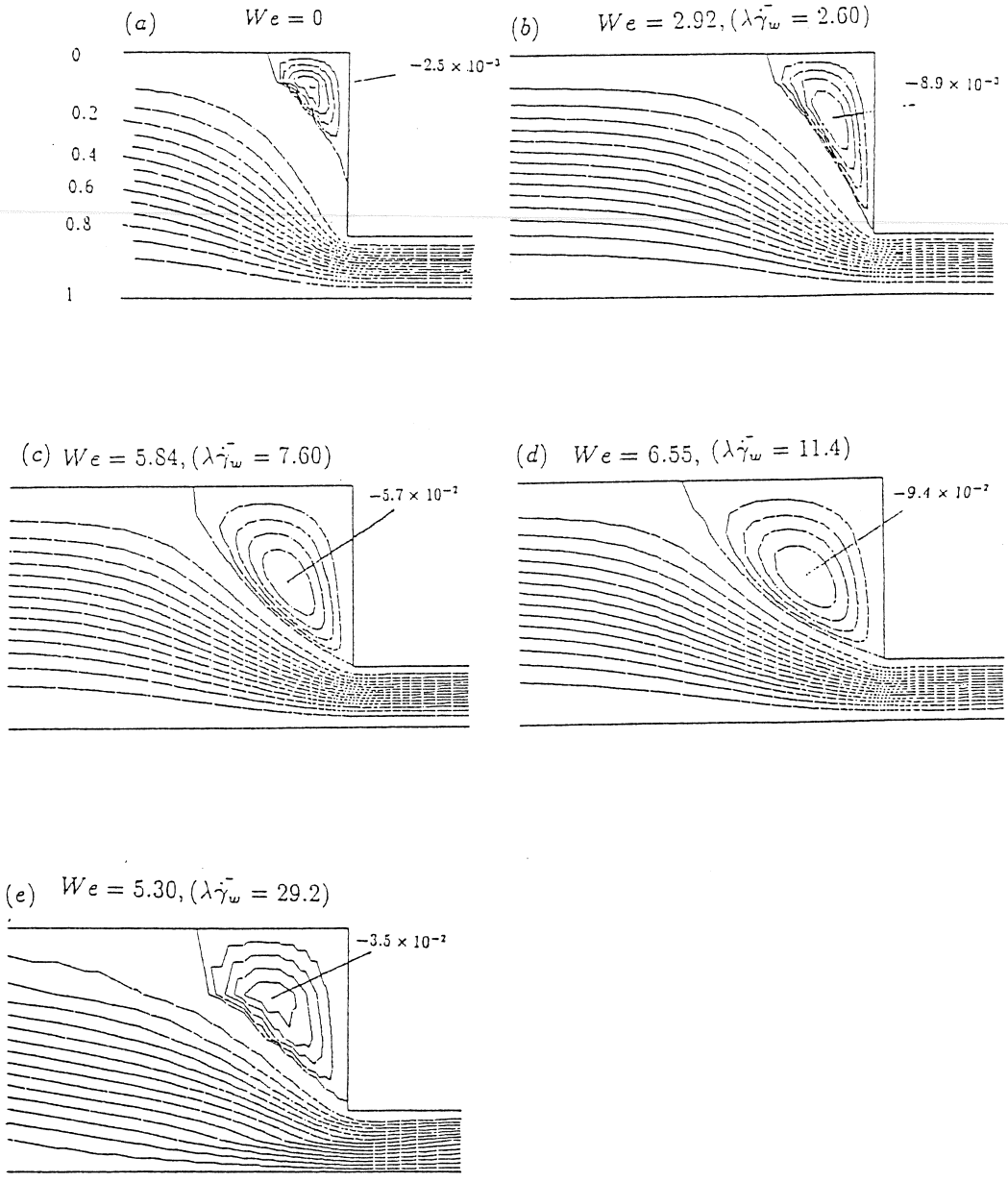

Fig. 15. Vortex developments as a function of We.

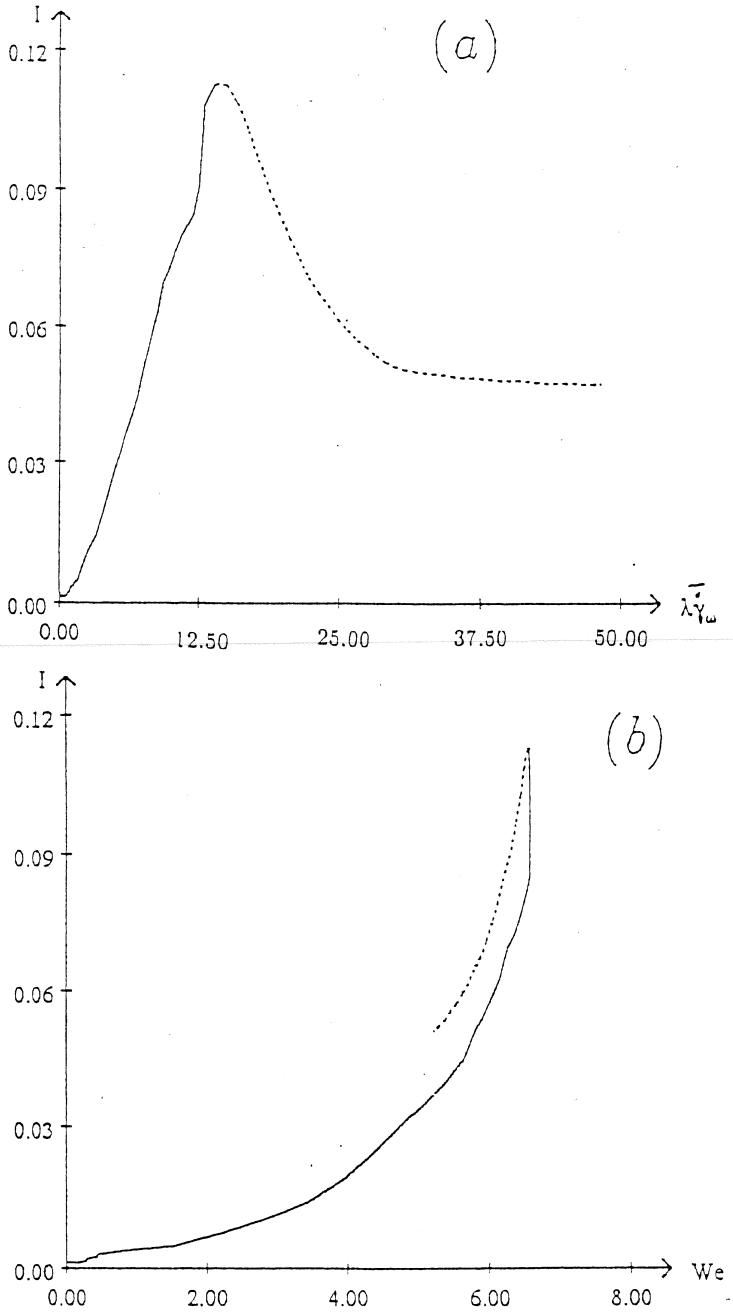

Fig. 16. Vortex intensity as a function of $\lambda\overline{\dot{\gamma}_w}$ (a) and We (b).

development (see also Fig. 6). This leads to argue that both the Weissenberg number (defined by relation 19) and the vortex activity of converging flows are related to the elongational properties of Phan-Thien–Tanner fluids.

These numerical results have been found to be qualitatively and quantitatively consistent with those of ref. [8]. Note that in Ref. [8] the authors used $We^* \overset{\text{def}}{=} \lambda\bar{U}/r$ as a definition of the Weissenberg number, where $\bar{U}$ is the average velocity at the downstream section, and r is the radius of the downstream section ($We^* = \lambda\overline{\dot{\gamma}_w}/4$ for an axisymmetric contraction, and $We^* = \lambda\overline{\dot{\gamma}_w}/3$ for a plane contraction). As a

Table 2
Comparative efficiency of three decoupled algorithms

Algorithm	No. of iterations
Picard method	2100
GMRES method	210 (7×30)
θ-method	42 (21×2)

consequence, the Weissenberg number, as defined in Ref. [8], is a linear function of the flow rate.

8. Conclusions

The efficiency of our time-dependent decoupled approach (θ-method) is confirmed by the numerical results of this paper. The θ-method is used here as a fast algorithm for reaching stationary solutions.

However, in Ref. [8], Debbaut et al. used a coupled Newtonian method. This approach, combined with a sub-element approximation of stress components, requires long computation times on a supercomputer. Following Fortin et al. [10], we point out that decoupled methods seem to be the only realistic alternative for three-dimensional flow problems.

Combining the θ-method with the finite element approximation presented in Section 5, we obtain a fast solver for viscoelastic fluid flow problems. This method is shown to be much more efficient than the Picard or the GMRES method [10]. Using the plane four-to-one abrupt contraction, the Oldroyd-B model and starting with stationary solution at $\lambda = 2.5$ as in Ref. [10], the θ-method converges in just 21 time steps to the stationary solution at $\lambda = 2.75$. After 21 time steps the L^2 norm of the residual term of the approximate stationary system takes the value of 9.1×10^{-4}. One time step is roughly equivalent, from a computational point of view, to two Picard iterations. Table 2 gives comparative test results of these three decoupled algorithms. We can conclude that the θ-method is five times faster than GMRES method, and 50 times faster than the Picard method.

The good quality of numerical solutions given by TVD schemes for the stress transport term is exhibited: in particular, we observe no numerical oscillations near the re-entrant corner at high values of the flow rate, which is not the case in previous works [7,11,35].

Finally, the main flow features of the Phan-Thien–Tanner fluid are presented. This model allows realistic predictions of elongational properties and shear thinning. We have introduced a new definition of the Weissenberg number in converging flows. This definition takes into account the elongational properties of the flow. Moreover, we have shown that this dimensionless number fits the vortex activity in an axisymmetric abrupt contraction.

Acknowledgements

J.M. Piau helped me greatly in preparing and reviewing this paper. The author would like to thank C. Guillopé and J.C. Saut for fruitful discussions, and H. Garavel and R. Michel for their careful reading of the paper.

References

[1] K. Baba and M. Tabata, On a conservative upwind finite element scheme for convection diffusion equations. RAIRO Numer. Anal., 15 (1981) 3–25.
[2] J. Baranger and D. Sandri, A formulation of the Stokes problem and the linear elasticity equation suggested by the Oldroyd model for viscoelastic flows, Math. Modelling Num. Anal., 26 (1992) 331–345.
[3] D.M. Binding, Further considerations of the axisymmetric contraction, J. Non-Newtonian Fluid Mech., 41 (1991) 27–42.
[4] D.V. Boger, M.J. Crochet and R.A. Keiller, On viscoelastic flows though abrupt contractions, J. Non-Newtonian Fluid Mech., 44 (1992) 257–279.
[5] F. Brezzi, On the existence, uniqueness and approximation of saddle point problems arising from Lagrangian multiplier, RAIRO, série Analyse Numérique, R2 (1974) 129–151.
[6] A.N. Brooks and T.R.J. Hughes, Streamline-upwind/Petrov–Galerkin formulation for convection dominated flow with particular emphasis on the incompressible Navier–Stokes equations, Comp. Meth. Appl. Mech. Eng., 32 (1982) 199–259.
[7] M.J. Crochet and J.M. Marchal, A new mixed finite element for calculating viscoelastic fluid flows, J. Non-Newtonian Fluid Mech., 26 (1987) 77–114.
[8] B. Debbaut, J.M. Marchal and M.J. Crochet, Numerical simulation of highly viscoelastic flows though an abrupt contraction, J. Non-Newtonian Fluid Mech., 29 (1988) 119–146.
[9] J.A. Deiber and W.R. Schowalter, On the comparison of simple non-monotonic constitutive equations with data showing slip of well-characterized polybutadienes, J. Non-Newtonian Fluid Mech., 40 (1991) 141–150.
[10] A. Fortin and A. Zine, An improved GMRES method for solving viscoelastic fluid flow problems, J. Non-Newtonian Fluid Mech., 42 (1992) 1–18.
[11] M. Fortin and A. Fortin, A new approach for the FEM simulation of viscoelastic flows, J. Non-Newtonian Fluid Mech., 32 (1989) 295–310.
[12] M. Fortin and R. Glowinski, Lagrangian Augmented Methods, North-Holland, Amsterdam, 1981.
[13] M. Fortin and R. Pierre, On the convergence of a mixed method of Crochet and Marchal for viscoelastic flows, Comp. Meth. Appl. Mech. Eng., 73 (1989) 341.
[14] V. Girault and P.A. Raviart, Finite Element Approximation of the Navier–Stokes Equations, Lecture Notes in Mathematics, 1979.
[15] R. Glowinski and J. Périaux, Numerical methods for nonlinear problems in fluid dynamics, in: Proc. Int. Seminar on Scientific Super-Computers, Feb. 1987.
[16] R. Glowinski and O. Pironeau, Ann. Rev. Fluid Mech., 24 (1992) 167–204.
[17] R. Glowinski and P. Le Tallec, Augmented Lagrangian and Operator Splitting Method in Non-Linear Mechanics, SIAM Studies in Applied Methematics, 1989.
[18] G.H. Golub and A. Meurant, Résolution numérique des grandes systèmes linéaires, CEA-EDF-INRIA, 1983.
[19] J.B. Goodman and R.L. Leveque, A geometric approach to high resolution TVD schemes, SIAM J. Numer. Anal., 25 (1988).
[20] C. Guillopé and J.C. Saut, Résultat d'existence pour les fluides viscoélastiques à loi de comportement de type différentiel, C. R. Acad. Sci. Paris, I, 305 (1987) 489–492.
[21] C. Guillopé and J.C. Saut, Global existence and one-dimensional non-linear stability of shearing motions of viscoelastic fluids of Oldroyd type. Math. Modelling Num. Anal., 24 (1990) 369–401.

[22] D.D. Joseph, M. Renardy and J.C. Saut, Hyperbolicity and change of type in the flow of viscoelastic fluids, Arch. Ration. Mech. Anal., (1985) 213–251.
[23] R. Keunings, Fundamentals of Computer Modeling for Polymer Processing, ed. C.L. Tucker III, Carl Hanser Verlag, 1988.
[24] N. El Kissi and J.M. Piau, Ecoulement de fluides polymères enchevêtrés dans un capillaire. modélisation du glissement macroscopique à la paroi, C. R. Acad. Sci. Paris, 309 (1989) 7–9.
[25] N. El Kissi and J.M. Piau, The different capillary flow regimes of entangled polydimethylsiloxane polymers: macroscopic slip at the wall, hysteresis and cork flow. J. Non-Newtonian Fluid Mech., 37 (1990) 55–94.
[26] R.G. Larson, Constitutive Equations for Polymer Melts and Solutions, Butterworths Ser. Chem. Eng. H. Brenner, 1988.
[27] A.I. Leonov, Analysis of simple constitutive equations for viscoelastic liquids, J. Non-Newtonian Fluid Mech., 42 (1992) 323–350.
[28] P. Lesaint and P.A. Raviart, On Finite Element Methods for Solving the Neutron Transport Equation, Academic Press, 1974.
[29] D.S. Malkus, M.G. Hansen, G.R. Ierley and R.A. Worthing, Spurt phenomena of the Johnson–Segalman fluid and related models, J. Non-Newtonian Fluid Mech., 29 (1988) 303–335.
[30] J.G. Oldroyd, On the formulation of rheological equations of states, Proc. R. Soc, London, A, 200 (1950) 523–541.
[31] D.W. Peaceman and H.H. Rachford, The numerical solution of parabolic and elliptic differential equations, J. Soc. Ind. Appl. Math., 3 (1955) 28–41.
[32] M. Renardy, Existence of slow flows of viscoelastic fluids with differential constitutive equations, Z. Angew. Math. Mech., 65 (1985) 449–451.
[33] M. Renardy, Recent advances in the mathematieal theory of steady flows of viscoelastic fluids, J. Non-Newtonian Fluid Mech., 29 (1988) 11–24.
[34] P. Rostand and B. Stoufflet, Finite volume Galerkin methods for viscous gas dynamics, RR INRIA (1988) 863.
[35] P. Saramito, Simulation numérique d'écoulements de fluides viscoélastiques par éléments finis incompressibles et une méthode de directions alternées; applications, Thèse de l'Institut National Polytechnique de Grenoble, 1990.
[36] P. Saramito, Numerical simulation of viscoelastic fluid flows using incompressible finite element method and a θ-method, Math. Modelling Num. Anal., 35 (1994) 1–35.
[37] P. Saramito, Operator splitting for viscoelastic fluid with a differential constitutive law, C. R. Acad. Sci. Paris, II (1994) 267–270.
[38] N. Phan-Thien and R.I. Tanner, A new constitutive equation derived from network theory, J. Non-Newtonian Fluid Mech., 2 (1977) 353–365.
[39] G.V. Vinogradov, V.P. Protasov and V.E. Dreval, The rheological behavior of flexible-chain polymers in the region of high shear rates and stresses, the critical process of spurting, and supercritical conditions of their movement at $T > T_g$. Rheol. Acta, 23 (1984) 46–61.

ESAIM PROCEEDINGS
ÉLASTICITÉ, VISCOÉLASTICITÉ ET CONTRÔLE OPTIMAL
HUITIÈMES ENTRETIENS DU CENTRE JACQUES CARTIER
URL: http://www.emath.fr/Maths/Proc/Vol.2/

ESAIM: PROC., VOL. 2, 1997, 275–281

DÉCOMPOSITION D'OPÉRATEURS EN FLUIDES VISCOÉLASTIQUES

PIERRE SARAMITO

RÉSUMÉ. On étudie une application du θ-schéma au calcul d'écoulements de fluides viscoélastiques. La décomposition vise à séparer les termes de viscosité des termes de transport. On se ramène ainsi à résoudre deux sous-problèmes plus simples, l'un de type Stokes, l'autre de type transport du tenseur des contraintes. De plus, en présence de singularités, ce schéma permet de contourner les difficultés rencontrées par la plupart des méthodes itératives dans ce type de simulation. En conclusion, on présente des résultats d'expériences numériques qui, de notre point de vue, justifient pleinement la méthodologie numérique qui y est décrite.

ABSTRACT. We study a θ-scheme applied to the computation of viscoelastic fluid flows. The splitting technique leads to two problems, the first one, a Stokes-like, and the second, a stress tensor transport problem. Furthermore, when the solution is singular, this scheme allows to overcome difficulties appearing when using other classical iterative procedures for this kind of simulation. To conclude, we present the result of numerical experiments which in our opinion fully validate the numerical methodology described here.

1. LOIS DE COMPORTEMENT

Considérons les fluides viscoélastiques à loi de comportement de type Oldroyd [5], gouvernés par les équations suivantes :

$$We\left(\frac{\partial \tau}{\partial t} + \mathbf{u}.\nabla\tau + \beta_a(\tau, \nabla\mathbf{u})\right) + \tau - 2\alpha D(\mathbf{u}) = 0 \quad (1)$$

$$Re\left(\frac{\partial \mathbf{u}}{\partial t} + \mathbf{u}.\nabla\mathbf{u}\right) - \operatorname{div}\tau - (1-\alpha)\Delta\mathbf{u} + \nabla p = f \quad (2)$$

$$\operatorname{div}\mathbf{u} = 0 \quad (3)$$

où Ω est un domaine régulier de $\mathbb{R}^N$, $N = 2, 3$, τ est le tenseur des extra-contraintes, les contraintes totales étant données par

$$\sigma = -pI + 2(1-\alpha)D(u) + \tau$$

$\mathbf{u}$ est le champ des vitesses, et p est la pression hydrostatique. D'autre part,

$$\beta_a(\tau, \nabla\mathbf{u}) = W\tau - \tau W - a(D\tau + \tau D)$$

où $a \in [-1, 1]$, $D = (1/2)(\nabla\mathbf{u} + \nabla\mathbf{u}^t)$ est le tenseur des taux de déformation et $W = (1/2)(\nabla\mathbf{u} - \nabla\mathbf{u}^t)$ est le tenseur de vorticité; enfin, $f \in (L^2(\Omega))^N$ est une donnée, We est le nombre sans dimension de Weissenberg, Re le nombre de Reynolds, et $\alpha \in]0, 1]$ un paramètre de retard.

Remarquons que le cas limite $We = 0$ correspond à un fluide newtonien. Pour $We > 0$, ce modèle permet de décrire des solutions de polymères dans un solvant newtonien. Cette loi peut s'étendre aux modèles différentiels,

Ces équations peuvent être complétées par des conditions initiales $\tau(0) = \tau_0$ et $\mathbf{u}(0) = \mathbf{u}_0$, ainsi qu'une condition aux bords $\mathbf{u} = 0$ sur $\Gamma = \partial\Omega$. Lorsque la frontière Γ est régulière, et $\mathbf{u}_0$, τ_0 et f sont suffisamment petits, on montre alors dans [4] l'existence globale de solutions.

2. Décomposition du problème

Afin de simplifier l'analyse des méthodes numériques proposées, nous supposerons le fluide lent, et négligerons dans la suite le terme d'inertie $\mathbf{u}.\nabla\mathbf{u}$ dans (2). Il s'agit d'une hypothèse classique dans ce type de simulation; la difficulté du problème est désormais portée par la non-linéarité de l'équation (1).

Soit $\mathbf{n}$ la normale unitaire extérieure à Γ. Introduisons les espaces classiques :

$$\begin{aligned} T &= \{\tau \in L^2(\Omega)^{N\times N};\ \tau = \tau^t\} \\ V &= \{\mathbf{u} \in H_0^1(\Omega)^N;\ \operatorname{div}\mathbf{u} = 0\},\ \text{ de norme } \|.\| \\ H &= \{\mathbf{u} \in \dot{L}^2(\Omega)^N;\ \operatorname{div}\mathbf{u} = 0,\ \mathbf{u}.\mathbf{n}_\Gamma = 0\} \end{aligned}$$

où T et H sont munis de la norme $|.|$. Nous noterons indifféremment $(.,.)$ et $|.|$ les normes et produits scalaires de $L^2(\Omega)^{N\times N}$ et $L^2(\Omega)^N$. Le problème précédent peut alors se mettre sous la forme :

(P): trouver $\mathbf{U} = (\tau, \mathbf{u}) \in L^\infty(\mathbb{R}^+; T \times V)$ tel que :

$$\left\{ \begin{array}{rl} S\dfrac{d\mathbf{U}}{dt} + A(\mathbf{U}) &= \mathbf{F} \\ \mathbf{U}(0) &= \mathbf{U}_0 \end{array} \right. \tag{4}$$

où $S = \operatorname{diag}(We, Re)$, $\mathbf{F} = (0, f)^t$, $\mathbf{U}_0 = (\tau_0, \mathbf{u}_0)^t$ et $A(\mathbf{U}) = A_1(\mathbf{U}) + A_2(\mathbf{U}; \mathbf{U})$, défini de $T \times V$ dans $T' \times V'$, est donné par la décomposition suivante :

$$A_1(\tau, \mathbf{u}) = \begin{bmatrix} \nu\tau & - & 2\alpha D(\mathbf{u}) \\ -\mathbf{div}\,\tau & - & (1-\alpha)\Delta\mathbf{u} \end{bmatrix} \tag{5}$$

$$A_2(\sigma, \mathbf{v};\ \tau, \mathbf{u}) = \begin{bmatrix} \nu'\tau + We\mathrm{T}(\mathbf{v})\tau \\ 0 \end{bmatrix} \tag{6}$$

où $\nu' = 1 - \nu$ et $\nu \in [0, 1]$ est un paramètre de la décomposition. Dans (6), $\mathrm{T}(\mathbf{v})$ désigne l'opérateur de transport des contraintes : $\mathrm{T}(\mathbf{v})\tau = \mathbf{v}.\nabla\tau + \beta_a(\tau, \nabla\mathbf{v})$. Remarquons que l'équation (2) prend ici un sens faible, dans V'. Cette formulation permet aussi de réduire le problème à la recherche de τ et $\mathbf{u}$.

Introduisons à présent la semi-approximation de (P). Soit $\Delta t > 0$ un pas de temps et θ un paramètre, $\theta \in]0, \frac{1}{2}[$. Introduisons les notations $\mathbf{U}^0 = \mathbf{U}_0$ et $\mathbf{U}^{n+\delta} \approx \mathbf{U}((n+\delta)\Delta t)$. Puisque A_1 et A_2 sont plus simples que A, utilisons cette décomposition pour résoudre (P) par le θ-schéma suivant (voir [3], par exemple) :

$$\frac{S\mathbf{U}^{n+\theta} - S\mathbf{U}^n}{\theta\Delta t} + A_1(\mathbf{U}^{n+\theta}) + A_2(\mathbf{U}^n;\ \mathbf{U}^n) = \mathbf{F}^{n+\theta} \tag{7}$$

$$\frac{S\mathbf{U}^{n+1-\theta} - S\mathbf{U}^{n+\theta}}{\theta'\Delta t} + A_1(\mathbf{U}^{n+\theta}) + A_2(\mathbf{U}^n;\ \mathbf{U}^{n+1-\theta}) = \mathbf{F}^{n+1-\theta} \tag{8}$$

$$\frac{S\mathbf{U}^{n+1} - S\mathbf{U}^{n+1-\theta}}{\theta\Delta t} + A_1(\mathbf{U}^{n+1}) + A_2(\mathbf{U}^{n+1-\theta};\ \mathbf{U}^{n+1-\theta}) = \mathbf{F}^{n+1} \tag{9}$$

PROPOSITION 1. *(cas newtonien)*
Pour $We = 0$, le schéma (7)-(9) est inconditionnellement stable et du premier ordre en temps. De plus, la méthode est d'ordre deux en temps pour $\theta = 1 - 1/\sqrt{2}$.

Indication sur la démonstration. Étudions le cas $\nu = 1$. Le problème étant linéaire, on se ramène au cas $f = 0$. Soit $(\mathbf{w}_m, \lambda_m)_{m\geq 0}$, le couple d'éléments propres associée à l'opérateur de Stokes : $(\nabla \mathbf{w}_m, \nabla \mathbf{v}) = \lambda_m (\mathbf{w}_m, \mathbf{v})$, $\forall \mathbf{v} \in V$; $(\mathbf{w}_m)$ est une base de V, orthonormale dans H. Introduisons la décomposition $\mathbf{u}^{n+\delta} = \sum_{m=0}^{\infty} u_m^{n+\delta} \mathbf{w}_m$. De (7)-(9), il vient : $u_m^{n+1} = r(\lambda_m \Delta t/Re)\, u_m^n$, où on a posé :

$$r(x) = \frac{1 - \theta' x}{(1 + \theta x)^2}$$

La solution exacte du problème se décompose selon : $\mathbf{u}(t) = \sum_{m=0}^{\infty} u_m(t) \mathbf{w}_m$, où $u_m(t) = u_m(0) \exp(-\lambda_m t/Re)$. Le développement limité :

$$e^x - r(x) = (2\theta^2 - 4\theta + 1)\, \frac{x^2}{2} \; + \; x^2\, \eta(x)$$

avec $\lim_{x\to 0} \eta(x) = 0$ permet d'obtenir le résultat de convergence au premier ordre, et au second ordre pour $\theta = 1 - 1/\sqrt{2}$. La stabilité découle de $|r(x)| < 1$, $\forall x \in \mathbb{R}^+$. La démonstration pour $\nu \neq 1$ est semblable, en introduisant $\gamma_m = D(\mathbf{w}_m)$. Remarquons que $\lim_{x\to\infty} r(x) = 0$, ce qui assure la décroissance rapide de la contribution haute fréquence à l'erreur, et la convergence rapide vers la solution stationnaire pour les grands pas de temps. □

REMARQUE 1. La résolution de (7) et (9) se réduit à celle d'un problème de type Stokes pour l'opérateur $\epsilon I - P\Delta$, avec $\epsilon > 0$, et la résolution de (8), à celle d'un problème de type transport pour l'opérateur $\epsilon' I + \mathrm{T}(\mathbf{v})$, avec $\epsilon' > 0$. □

REMARQUE 2. Aucun résultat n'a été établi à présent dans le cas viscoélastique ($We > 0$). Numériquement, l'algorithme (7)-(9) est bien adapté à la recherche des solutions stationnaire, la vitesse de converge dépend alors de θ et Δt. Les exemples qui suivent abordent le cas viscoélastique. □

3. EXEMPLES

3.1. ÉLONGATION UNIAXIALE

Le tenseur gradient de vitesse est donné par $\nabla \mathbf{u} = \mathrm{diag}(\dot\varepsilon, -\dot\varepsilon/2, -\dot\varepsilon/2)$, où $\dot\varepsilon > 0$ est le taux d'élongation (sans dimension). Le problème se ramène à trouver τ_{11}, τ_{22} et τ_{33} dans $L^\infty(\mathbb{R}^+)$ satisfaisant à :

$$\begin{aligned}
We\frac{d\tau_{11}}{dt} \; &+ (1 - 2a\dot\varepsilon We)\, \tau_{11} - 2\alpha\dot\varepsilon \;\; = 0 \\
We\frac{d\tau_{22}}{dt} \; &+ (1 + \; a\dot\varepsilon We)\, \tau_{22} + \alpha\dot\varepsilon \;\; = 0 \\
We\frac{d\tau_{33}}{dt} \; &+ (1 + \; a\dot\varepsilon We)\, \tau_{33} + \alpha\dot\varepsilon \;\; = 0
\end{aligned}$$

avec $\tau(0) = 0$, par exemple, pour un démarrage en élongation. Les valeurs propres du problème sont $\lambda_1 = 1/We - 2a\dot\varepsilon$ et $\lambda_2 = \lambda_3 = 1/We + a\dot\varepsilon$, et la

pour $a\dot{\varepsilon}We < \frac{1}{2}$. Posant $e_i^n = \tau_{ii}^n - \tau_{ii}^*$, $1 \le i \le 3$, l'algorithme (7)-(9) pour $\nu = 0$ conduit à $e_i^{n+1} = r(\lambda_i \Delta t)\, e_i^n$, avec :

$$r(x) = \frac{(1-\theta x)^2}{1+\theta' x}$$

Un développement limité à l'ordre deux montre que :

$$e^{-x} - r(x) = -(2\theta^2 - 4\theta + 1)\, x^2 + x^2\, \varphi(x)$$

avec $\lim_{x\to 0} \varphi(x) = 0$. Le schéma est donc précis au second ordre pour $\theta = 1 - 1/\sqrt{2}$. L'algorithme est stable ($|r| < 1$) si et seulement si :

$$\Delta t < \Delta t_{crit} \overset{\text{déf}}{=} \frac{We}{\theta^2(1 - 2a\dot{\varepsilon}We)} \tag{10}$$

Enfin, l'élimination des modes 1 et 2 à l'erreur peut être réalisée en deux itérations de pas Δt_1 et Δt_2 tels que $r(\lambda_1 \Delta t_1) = r(\lambda_2 \Delta t_2) = 0$, soit encore :

$$\Delta t_1 = \frac{We}{\theta(1 - 2a\dot{\varepsilon}We)} \quad ; \quad \Delta t_2 = \frac{We}{\theta(1 + a\dot{\varepsilon}We)} \tag{11}$$

Ainsi, un cycle de deux pas de temps donnés par (11) permet d'obtenir exactement τ^*.

3.2. Cisaillement simple

L'écoulement est bidimensionnel, et le tenseur gradient des vitesses est donné par :

$$\nabla \mathbf{u} = \begin{pmatrix} 0 & \dot{\gamma}/2 \\ \dot{\gamma}/2 & 0 \end{pmatrix}$$

où $\dot{\gamma} > 0$ est le taux de cisaillement (sans dimension). Le problème se ramène à trouver τ_{11}, τ_{22} et τ_{12} dans $L^\infty(\mathbb{R}^+)$ satisfaisant à :

$$\begin{array}{lllllllll}
We\dfrac{d\tau_{11}}{dt} & + & \tau_{11} & & & - & (1+a)\dot{\gamma}We\tau_{12} & = & 0 \\
We\dfrac{d\tau_{22}}{dt} & & & + & \tau_{22} & + & (1-a)\dot{\gamma}We\tau_{12} & = & 0 \\
2We\dfrac{d\tau_{12}}{dt} & + & (1-a)\dot{\gamma}We\tau_{11} & - & (1+a)\dot{\gamma}We\tau_{22} & + & 2\tau_{12} & = & 2\alpha\dot{\gamma}
\end{array}$$

avec $\tau(0) = 0$ pour un démarrage en cisaillement (figure 1.a).

$$\Delta t_1 = \frac{We}{\theta} \tag{12}$$

Les valeurs propres du problème sont $\lambda_1 = 1/We$, $\lambda_2 = 1/We + i\dot{\gamma}\sqrt{1-a^2}$ et $\lambda_3 = \bar{\lambda}_2$. La solution τ^* obtenue pour $\partial/\partial t = 0$ est toujours stable. En conséquence, la solution du problème instationnaire est toujours dans $L^\infty(\mathbb{R}^+)$. Posant $\hat{e}_{ij}^n = \hat{\tau}_{ij}^n - \hat{\tau}_{ij}^*$, où $\hat{(.)}$ désigne la transformation dans la base propre associée aux valeurs propres $(\lambda_i)_{1\le i\le 3}$, l'algorithme (7)-(9) pour $\nu = 0$ conduit à $\hat{e}_{ij}^{n+1} = r(\lambda_i \Delta t)\, \hat{e}_{ij}^n$, avec :

$$r(z) = \frac{(1-\theta z)^2}{1+\theta' z}$$

Le schéma est ici aussi précis au second ordre pour $\theta = 1 - 1/\sqrt{2}$, et la stabilité est conditionnelle. Enfin, l'annulation de la contribution du premier mode à l'erreur peut être réalisée avec : Dans le cas $|a| = 1$, la solution τ^* est

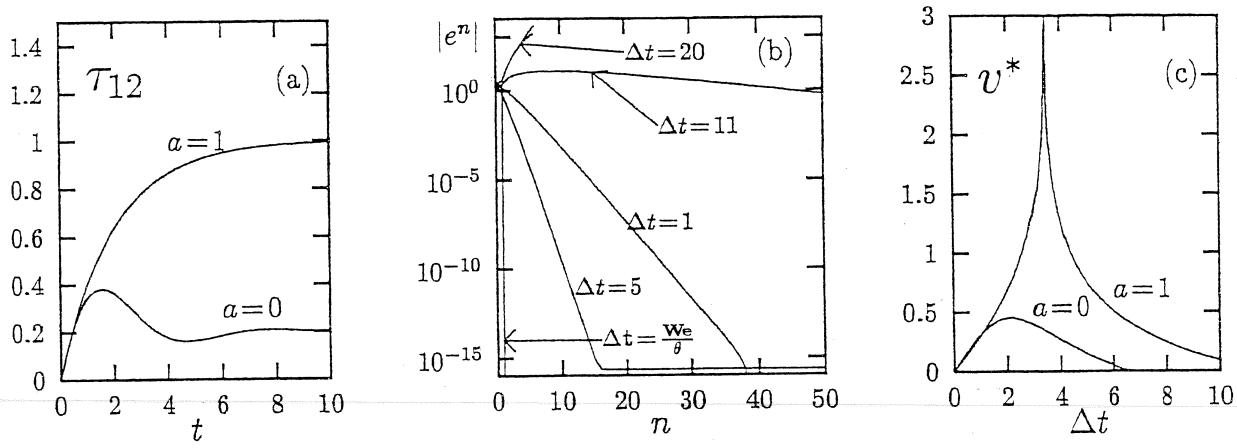

FIGURE 1. Cisaillement ($\alpha = 1$) : (a) démarrage en cisaillement ($\dot{\gamma}We = 2$; $\Delta t = 0.1$); (b) erreur $|e^n|$ selon l'itéré n ($\dot{\gamma}We = 1$); (c) vitesse de convergence v selon Δt ($\dot{\gamma}We = 1$).

La quantité $1/v^*$ est alors le nombre moyen d'itérations asymptotiquement nécessairement à une réduction de la norme de l'erreur d'un facteur égal au nombre e. Lorsque $|a| < 1$, la convergence ne peut plus être obtenue en une itération, et est alors généralement plus lente.

3.3. ÉCOULEMENTS COMPLEXES ET SINGULARITÉS

On considère le schéma (7)-(9), ayant en vue de remplacer T et V par des espaces de dimension finie T_h et V_h, et de rechercher la solution stationnaire approchée $(\tau_h^*, \mathbf{u}_h^*)$ correspondante (voir [7] pour une présentation détaillée des formes matricielles correspondantes).

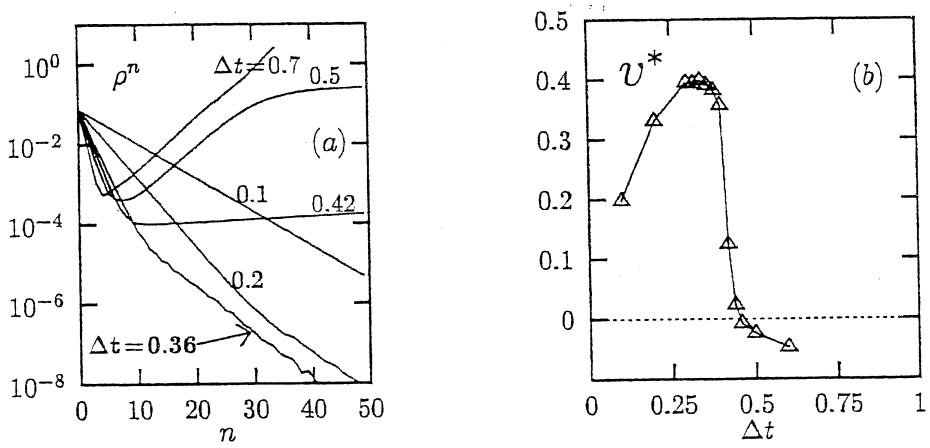

FIGURE 2. Écoulement bidimensionnel en contraction brusque 4:1 ($a = 1$, $\alpha = 8/9$, $We = 0.5$) : (a) résidu ρ^n selon l'itéré n; (b) vitesse de convergence v^* selon Δt.

Observons les résultats rassemblés dans les figures 2 et 3. L'écoulement

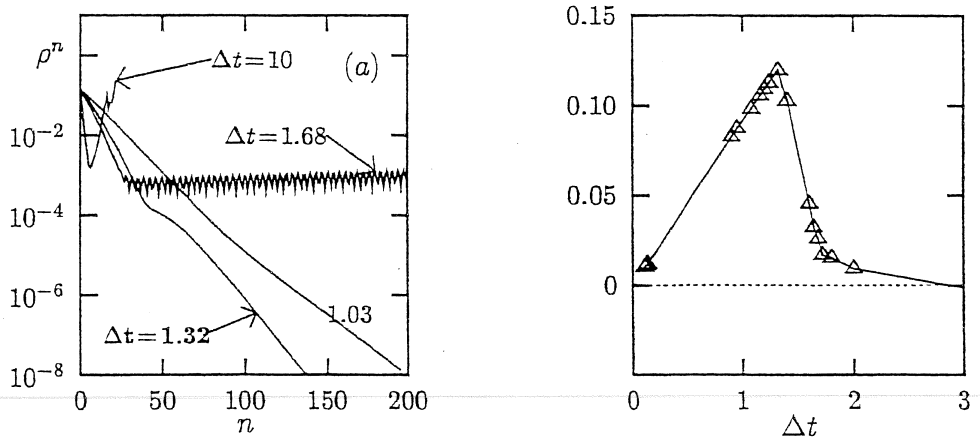

FIGURE 3. Écoulement bidimensionnel en contraction brusque 4:1 ($a = 1$, $\alpha = 8/9$, $We = 11$) : (a) résidu ρ^n selon l'itéré n; (b) vitesse de convergence v^* selon Δt.

mesurons la convergence de l'itéré $\mathbf{U}_h^n$ vers $\mathbf{U}_h^*$ à l'aide de ρ^n, la norme du résidu $A(\mathbf{U}_h^n) - \mathbf{F}$ du problème stationnaire. Pour un pas de temps choisis assez petit, le résidu $A(\mathbf{U}_h^*) - \mathbf{F}$ tend zéro. Par conséquent, le schéma (7)-(9) apparaît comme une méthode itérative découplée pour la résolution du problème stationnaire $A(\mathbf{U}_h^*) = \mathbf{F}$. Le problème résolu n'est pas plus *diffusif* (ou plus régulier), comme ce peut être le cas dans certaines approches itératives pour ce type de simulation, mais bien $A(\mathbf{U}_h^*) = \mathbf{F}$.

La figure 2.a met en évidence des changement de pente durant les itérations. La deuxième partie de la courbe exprime la convergence plus lente d'un groupe spécifique de composantes du résidu. Nous conjecturons que ces composantes sont dues à la présence de grandes valeurs propres de l'opérateur A_2. En effet, A_2 fait intervenir le terme $\beta_a(., \nabla \mathbf{u}_h^*)$, et $\nabla \mathbf{u}_h^*$ devient grand au voisinage de la singularité. D'où la nécessité de réduire Δt afin de maîtriser les valeurs propres de $(I - \theta \Delta t S^{-1} A_2)$ et $(I + \theta' \Delta t S^{-1} A_2)^{-1}$ apparaîssant dans l'opérateur d'itération du schéma.

Par un choix particulier de Δt, on annule la vitesse asymptotique de convergence $v^* = \lim_{n \to \infty} (-\log |\rho^n|)/n$ (figure 2.b); le résidu se stabilise (figure 2.a, $\Delta t = 0.42$, et figure 3.a, $\Delta t = 1.68$). On ne manquera pas de faire le rapprochement avec la méthode de la puissance itérée pour les problèmes de valeurs propres (c.f. [1], par exemple). En particulier, les pulsations du résidu, au voisinage du pas de temps critique (figure 3.a, $\Delta t = 1.68$), expriment la présence de valeurs propres complexes conjuguées. Pour des pas de temps plus élevés, ces composantes vont aller en amplitude croissante, d'où l'aspect particulier, en 'V', des courbes obtenues (figure 2.a, $\Delta t = 0.6$ et figure 3.a, $\Delta t = 10$). On pourra aussi faire l'analogie avec une condition de type Courant-Friedrichs-Lévy, remarquant cependant qu'ici la condition de stabilité dépend de plus de la nature de la singularité et du maillage au voisinage de cette singularité.

Signalons enfin que schéma a été étendu au cas du modèle de Phan-Thien et Tanner mentionné au paragraphe 1. Dans [8], sur une géométrie

asymptotiques des écoulements pour les grandes valeurs de We, ceci pour différents paramètres du modèle. Ces résultats de propriétés asymptotiques sont, à notre connaissance, les premiers relatifs à ce type de simulation pour les modèles viscoélastiques à loi de comportement de type différentiel.

Nous pouvons résumer les principales conclusion comme suit :

- La résolution du problème (1)-(3) par le schéma (7)-(9) se ramène à résoudre une succession de problèmes plus simple, de type Stokes et de type transport du tenseur des extra-contraintes.
- $\theta = 1 - 1/\sqrt{2}$ est un choix intéressant dans le cas newtonien ($We = 0$, c.f. proprosition 1), et dans le cas viscoélastique (c.f. paragraphes 3.1 et 3.2), la méthode étant alors d'ordre deux en temps.
- Le schéma (7)-(9) est conditionnellement stable dès que $We > 0$.
- Lors de la recherche de la solution stationnaire, le pas de temps Δt apparaît comme un paramètre de commande sur la vitesse de convergence de la méthode. La vitesse maximum de convergence dépend aussi des paramètres a et We du modèle.
- Dans le cas particulier de l'approximation de la solution stationnaire d'un écoulement présentant une singularité, la vitesse maximum de convergence dépend principalement de l'aspect de la solution approchée dans un voisinage de la singularité. En particulier, elle va alors dépendre fortement du maillage dans ce voisinage. Le pas de temps doit alors être choisi d'autant plus petit que les éléments sont petits dans ce voisinage (on pourra penser à une condition de type CFL mais locale à la singularité, et dépendante de la nature de cette singularité).

REFERENCES

[1] F. CHATELIN. Valeurs propres de matrices. Masson (1988).

[2] H. GIESEKUS. *A simple constitutive equation for polymer fluids based on the concept of deformation dependant tensorial mobility. J. Non Newtonian Fluid Mech.*, 11:69 (1982).

[3] R. GLOWINSKI. *Numerical Methods for the Numerical Solution of the incompressible Navier-Sokes Equations.* In *Vistas in Applied Mathematics, Optimization Software*, pp. 57–95 (New York 1986).

[4] C. GUILLOPÉ AND J. C. SAUT. *Résultat d'existence pour les fluides viscoélastiques à loi de comportement de type différentiel. C. R. Acad. Sci. Paris*, t.305, série I:489–492 (1987).

[5] J. G. OLDROYD. *On the Formulation of Rheological Equations of States. Proc. Roy. Soc, London*, A 200:523–541 (1950).

[6] N. PHAN-THIEN AND R. I. TANNER. *A new constitutive equation derived from network theory. J. Non Newtonian Fluid Mech.*, 2:353–365 (1977).

[7] P. SARAMITO. Simulation numérique d'écoulements de fluides viscoélastiques par éléments finis incompressibles et une méthode de directions alternées; applications. thèse de l'Institut National Polytechnique, Grenoble (1990).

[8] P. SARAMITO AND J. M. PIAU. *Flow Characteristics of Viscoelastic Fluids in an Abrupt Contraction by Using Numerical Modeling. In International Conference on Rheology of Polymers, may 1993,* submitted to *J. Non Newtonian Fluid Mech.* (1993).

Pierre.Saramito@ujf-grenoble.fr, LABORATOIRE DE RHÉOLOGIE, 38041 GRENOBLE CEDEX 9, FRANCE.

C. R. Acad. Sci. Paris, t. 331, Série I, p. 563–568, 2000
Analyse numérique/*Numerical Analysis*

Estimations d'erreur pour un fluide viscoplastique par éléments finis P_k et maillages adaptés

Nicolas ROQUET [a], Richard MICHEL [b], Pierre SARAMITO [a]

[a] LMC-Imag, B.P. 53, 38041 Grenoble cedex 9, France
Courriel : Nicolas.Roquet@imag.fr, Pierre.Saramito@imag.fr

[b] CNRS–Lepmi, B.P. 75, 38402 Saint-Martin-d'Hères cedex, France
Courriel : Richard.Michel@inpg.fr

(Reçu le 2 avril 2000, accepté le 19 juin 2000)

Résumé. Nous montrons une estimation a priori de l'erreur en $\mathcal{O}(h^k\sqrt{|\ln h|})$, en utilisant des maillages adaptés et des méthodes d'éléments finis de type P_k, lors de l'approximation de l'écoulement d'un fluide de Bingham dans une conduite cylindrique avec adhérence à la paroi. D'autre part, l'utilisation de maillages uniformes conduit à une estimation en $\mathcal{O}(h)$, ce qui met en évidence l'intérêt de l'adaptation de maillages. En conclusion, des tests numériques viennent confirmer les résultats annoncés. © 2000 Académie des sciences/Éditions scientifiques et médicales Elsevier SAS

Errors estimate for a viscoplastic fluid by using P_k finite elements and adaptive meshes

Abstract. *An a priori error estimate $\mathcal{O}(h^k\sqrt{|\ln h|})$ result is presented when using a suitable adaptive mesh approach and P_k finite element approximation for the simulation of the flow of a Bingham fluid in a pipe with no-slip at the wall. Moreover, we show that the use of an uniform mesh family leads to a $\mathcal{O}(h)$ estimate for all $k \geqslant 1$. This result points out the efficiency of the adaptive mesh approach. To conclude, we present results of numerical tests which confirm the previous estimates.* © 2000 Académie des sciences/Éditions scientifiques et médicales Elsevier SAS

Abridged English version

The flow of a Bingham fluid in a pipe of polygonal cross-section $\Omega \subset \mathbb{R}^2$ with no-slip at the wall (*see* [1,8,3]) is described by the so-called Mosolov problem:

$$\begin{cases} \sigma = \nabla u + \mathrm{Bi}\,\dfrac{\nabla u}{|\nabla u|} & \text{when } \nabla u \neq 0, \\ |\sigma| \leqslant Bi & \text{otherwise,} \end{cases} \tag{1}$$

$$\operatorname{div}\sigma = -f \quad \text{in } \Omega, \tag{2}$$

$$u = 0 \quad \text{on } \partial\Omega, \tag{3}$$

Note présentée par Roland GLOWINSKI.

S0764-4442(00)01619-0/FLA

where u is the axial component of the velocity and σ is a vector whose components are the shear stress; Bi is the Bingham dimensionless number and f is the constant linear pressure drop. The limit case $\mathrm{Bi} = 0$ is related to a Newtonian fluid while $\mathrm{Bi} > 0$ describe a yield stress fluid. The problem (1)–(3) can be expressed by using the variational framework:

$$u \in \mathrm{H}_0^1(\Omega), \big(\nabla u, \nabla(v-u)\big) + \mathrm{Bi}\big(|\nabla v|_{0,1;\Omega} - |\nabla u|_{0,1;\Omega}\big) \geqslant (f, v-u), \quad \forall v \in \mathrm{H}_0^1(\Omega). \tag{4}$$

Subsequently, a general assumption is made: $f \in \mathrm{L}^2(\Omega)$. The notations $(\cdot,\cdot)$ and $|\cdot|_{m,p;\Omega}$ denote respectively the $\mathrm{L}^2(\Omega)$ scalar product and the $\mathrm{W}^{m,p}(\Omega)$ semi-norm, for all $m \geqslant 0$ and $p \in [1,\infty]$. Let $V_h = \big\{v \in \mathrm{C}^0(\overline{\Omega});\ v|_K \in P_k, \forall K \in \mathcal{T}_h \text{ and } v|_{\partial\Omega} = 0\big\}$ be a finite dimensional space, where $k \geqslant 1$ denotes the order of the polynomials and $(\mathcal{T}_h)_{h>0}$ is a regular family of triangulations. The finite dimensional problem writes:

$$u_h \in V_h, \quad \big(\nabla u_h, \nabla(v_h - u_h)\big) + \mathrm{Bi}\big(|\nabla v_h|_{0,1;\Omega} - |\nabla u_h|_{0,1;\Omega}\big) \geqslant (f, v_h - u_h), \tag{5}$$

for all $v_h \in V_h$. The solutions of (4) and (5) exist and are unique [7].

The problem of the error estimate $\|u - u_h\|$ in the H^1 semi-norm (i.e. $\|v\| = |v|_{1,2;\Omega}$) is addressed in this paper. In 1976, Glowinski [5] showed for $k = 1$ a $\mathcal{O}(h^{1/2})$ estimate and noticed that when Ω is a disk, the solution u satisfies, for all $\varepsilon > 0$:

$$\int_{\Omega_\varepsilon} \frac{\mathrm{d}x}{|\nabla u|} = \mathcal{O}(-\ln\varepsilon), \quad \text{where } \Omega_\varepsilon = \big\{x \in \Omega;\ \|\nabla u| > \varepsilon\big\}, \tag{6}$$

$$\mathrm{meas}(\Omega_{0,\varepsilon}) = \mathcal{O}(\varepsilon), \qquad \text{where } \Omega_{0,\varepsilon} = \{x \in \Omega;\ 0 < |\nabla u| < \varepsilon\}. \tag{7}$$

This author showed for $k = 1$ a quasi-optimal $\mathcal{O}\big(h\sqrt{|\ln h|}\big)$ error estimate on an quasi-uniform triangulation of the disk. In 1977, Falk and Mercier [4] introduced a formulation equivalent to (4) and showed an optimal $\mathrm{O}(h)$ estimate for the vorticity in L^2 norm (*see* also [7], App. 5, for nice developments). Finally, many authors [7,6] suggested that the convergence is not faster for $k = 2$ than for $k = 1$.

Using a new mesh partitioning argument, the (6)–(7) hypothesis, and extending the framework introduced by [6], we show a $\mathcal{O}\big(h^k\sqrt{|\ln h|}\big)$ estimate for $k \geqslant 2$ and a suitable family of regular triangulations. Moreover, when Ω is a disk and $k = 2$, this estimation becomes $\mathcal{O}\big(N^{-1}\sqrt{\ln N}\big)$ in term of $N = \dim V_h$, the number of degrees of freedom.

---

1. Estimation abstraite

Les relations (6)–(7) suggèrent l'introduction de l'ensemble $\Omega_0 = \{x \in \Omega;\ |\nabla u| = 0\}$, appelé ensemble des zones rigides (*voir* figure 1 (a)), et par commodité, nous noterons Ω_+ l'intérieur du complémentaire de Ω_0 dans Ω, appelé ensemble des zones cisaillées, ainsi que $\Gamma_0 = \partial\Omega_0 \setminus \partial\Omega$ l'interface entre ces deux zones. Définissons $\Omega_{0,+}^h$ (*voir* figure 1 (c)) à partir des éléments de $\mathcal{T}_h$ rencontrant Γ_0 :

$$\Omega_{0,+}^h = \mathrm{int}\Big(\bigcup\{K;\ K \in \mathcal{T}_h \text{ et } K \cap \Gamma_0 \neq \varnothing\}\Big).$$

Notons $h = \max\{h_K;\ K \in \mathcal{T}_h\}$ ainsi que $h_0 = \max\{h_K;\ K \in \mathcal{T}_h \text{ et } K \cap \Gamma_0 \neq \varnothing\}$ la taille du plus grand élément K inclus dans $\Omega_{0,+}^h$. Par commodité, nous noterons aussi $\Omega_0^h = \mathrm{int}(\Omega_0 \setminus \Omega_{0,+}^h)$ et $\Omega_+^h = \mathrm{int}(\Omega_+ \setminus \Omega_{0,+}^h)$. Nous supposerons Γ_0 assez régulière et $(\mathcal{T}_h)_{h>0}$ quasi uniforme dans $\Omega_{0,+}^h$, de sorte que $\mathrm{mes}(\Omega_{0,+}^h) = \mathcal{O}(h_0)$.

LEMME 1 (Estimation abstraite). – *Supposons que la solution u de* (4) *soit dans* $\mathrm{W}_0^{1,\infty}(\Omega)$. *Alors, la solution u_h de* (5) *vérifie l'estimation* :

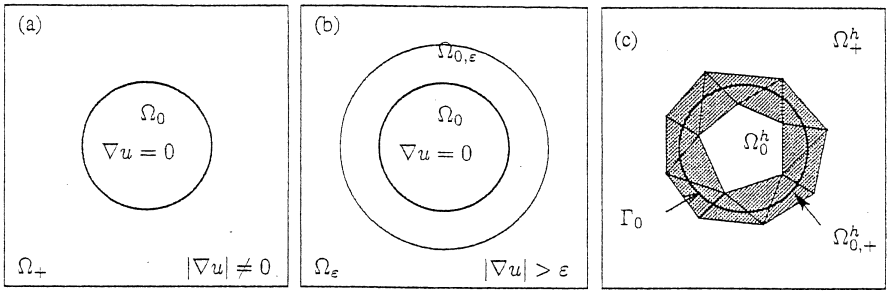

Figure 1. – Trois partitions de Ω.

Figure 1. – Three partitions of Ω.

$$\|u-u_h\|^2 \leqslant C\Big(\|v_h-u\|^2 + \mathrm{Bi}\,|v_h|_{1,1;\Omega_0^h} + \mathrm{Bi}\,\mathrm{mes}\big(\Omega_{0,+}^h\big)\,|v_h-u|_{1,\infty;\Omega_{0,+}^h} + \mathrm{Bi}\,\mathrm{mes}(\Omega_{0,\varepsilon})\,|v_h-u|_{1,\infty;(\Omega_+^h\cap\Omega_{0,\varepsilon})} + \mathrm{Bi}\,|v_h-u|^2_{1,\infty;(\Omega_+^h\cap\Omega_\varepsilon)} \int_{\Omega_\varepsilon} \frac{\mathrm{d}x}{|\nabla u|} \Big)$$

pour tout $v_h \in V_h$, *où* $C > 0$ *est une constante indépendante de* h *et de* u.

Démonstration. – Soit $\Lambda = \big\{\tau \in \mathrm{L}^2(\Omega)^2;\ |\tau| \leqslant 1 \text{ p.p. dans } \Omega\big\}$. Il existe $\lambda \in \Lambda$ tel que (*voir* [6], chap. 2, théorème 6.3) :

$$(\nabla u, \nabla v) + \mathrm{Bi}(\lambda, \nabla v) = (f, v), \quad \forall v \in \mathrm{H}_0^1(\Omega) \quad \text{et} \quad \lambda \cdot \nabla u = |\nabla u| \quad \text{p.p. dans } \Omega,$$

et de plus, l'estimation suivante est satisfaite :

$$\|u_h - u\|^2 \leqslant \big(\nabla(u_h-u), \nabla(v_h-u)\big) + \mathrm{Bi}\big(\mu_h - \lambda, \nabla(v_h-u)\big) \tag{8}$$

ceci pour tout $\mu_h \in \Lambda$ tel que $\mu_h \cdot \nabla v_h = |\nabla v_h|$. Après application des inégalités de Cauchy–Schwarz puis de Young au premier terme du membre de droite, la relation (8) devient :

$$\|u_h - u\|^2 \leqslant \|v_h - u\|^2 + 2\,\mathrm{Bi}\big(\mu_h - \lambda, \nabla(v_h-u)\big). \tag{9}$$

Le dernier terme du membre de droite de (9) se décompose selon $\overline{\Omega} = \overline{\Omega_0^h} \cup \overline{\Omega_{0,+}^h} \cup \overline{\Omega_+^h}$.

– Dans Ω_0^h, par définition $\nabla u = 0$ et, de plus $|\lambda| \leqslant 1$ et $|\mu_h| \leqslant 1$:

$$\int_{\Omega_0^h} (\mu_h - \lambda) \cdot \nabla(v_h - u)\,\mathrm{d}x \leqslant 2\,|v_h|_{1,1;\Omega_0^h}. \tag{10}$$

– Dans la fine couche $\Omega_{0,+}^h$, utilisons $|\lambda| \leqslant 1$ et $|\mu_h| \leqslant 1$:

$$\int_{\Omega_{0,+}^h} (\mu_h - \lambda) \cdot \nabla(v_h - u)\,\mathrm{d}x \leqslant 2\,\mathrm{mes}\big(\Omega_{0,+}^h\big)\,|v_h-u|_{1,\infty;\Omega_{0,+}^h}. \tag{11}$$

– Dans Ω_+^h, utilisons à présent la partition $\overline{\Omega} = \overline{\Omega_0} \cup \overline{\Omega_{0,\varepsilon}} \cup \overline{\Omega_\varepsilon}$. Puisque $\Omega_+^h \cap \Omega_0 = \varnothing$, la somme sur Ω_+^h se décompose en deux termes, l'un sur $\Omega_{0,\varepsilon} \cap \Omega_+^h$, l'autre sur $\Omega_\varepsilon \cap \Omega_+^h$. Dans $\Omega_+^h \cap \Omega_{0,\varepsilon}$, reprenons la

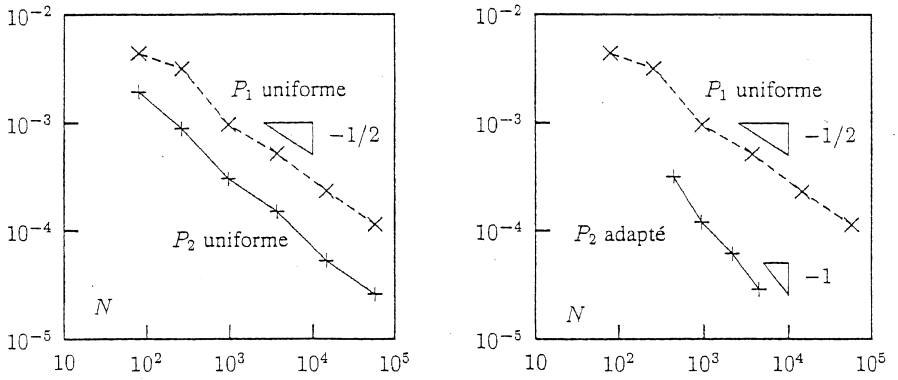

Figure 2. – Comparaison pour Bi $= 0,3$ de l'élément P_1 en maillages uniformes avec l'élément P_2 en maillages (a) uniformes ; (b) adaptés.

Figure 2. – Comparison for Bi $= 0.3$ *of the* P_1 *element and uniform meshes with the* P_2 *element and* (a) *uniform meshes ;* (b) *adaptive meshes.*

même idée que dans $\Omega^h_{0,+}$:

$$\int_{\Omega^h_+\cap\Omega_{0,\varepsilon}} (\mu_h-\lambda)\cdot\nabla(v_h-u)\,\mathrm{d}x \leqslant 2\,\mathrm{mes}(\Omega_{0,\varepsilon})|v_h-u|_{1,\infty;\Omega^h_+\cap\Omega_{0,\varepsilon}}. \tag{12}$$

Dans $\Omega^h_+\cap\Omega_\varepsilon$ nous rendons à présent explicite λ et μ_h :

$$\lambda=\frac{\nabla u}{|\nabla u|}\quad\text{et}\quad \mu_h=\begin{cases}\nabla v_h/|\nabla v_h| & \text{si } \nabla v_h\neq 0,\\ 0 & \text{sinon.}\end{cases}$$

Remarquant ensuite l'inégalité (*voir* [6], chap. 2, lemme 6.1) : $|\xi/|\xi|-\eta/|\eta||\leqslant 2\,|\xi-\eta|/(|\xi|+|\eta|)$, $\forall\,\xi,\eta\in(\mathbb{R}\setminus\{0\})^2$, il vient successivement :

$$\begin{aligned}\int_{\Omega^h_+\cap\Omega_\varepsilon}(\mu_h-\lambda)\cdot\nabla(v_h-u)\,\mathrm{d}x &\leqslant \int_{\Omega^h_+\cap\Omega_\varepsilon}|\mu_h-\lambda|\,|\nabla(v_h-u)|\,\mathrm{d}x\\ &\leqslant 2\int_{\Omega^h_+\cap\Omega_\varepsilon}\frac{|\nabla(v_h-u)|^2}{|\nabla v_h|+|\nabla u|}\,\mathrm{d}x \leqslant 2\,|v_h-u|^2_{1,\infty;\Omega^h_+\cap\Omega_\varepsilon}\int_{\Omega_\varepsilon}\frac{\mathrm{d}x}{|\nabla u|}.\end{aligned} \tag{13}$$

Pour conclure, il suffit de sommer les estimations (10)–(13) et de reporter dans (9).

2. Application aux éléments P_k

THÉORÈME 1 (estimation concrète). – *Soient* $k\geqslant 1$ *et* $s\in[1,k]$. *Si* $u\in \mathrm{W}^{2,\infty}(\Omega)\cap\mathrm{W}^{s+1,\infty}(\Omega_+)$ *et vérifie les hypothèses* (6)–(7), *alors* $\|u-u_h\|=\mathcal{O}\big(\max\big(h_0,h^s\sqrt{|\ln h|}\big)\big)$.

Indication sur la démonstration. – Choisissons pour v_h l'interpolé de Lagrange $\pi_h u$ de u. Nous avons alors $\nabla(\pi_h u)=0$ dans Ω^h_0 ce qui a deux conséquences ; d'une part, $|\pi_h u|_{1,1;\Omega^h_0}=0$ et d'autre part, avec la partition $\overline{\Omega}=\overline{\Omega^h_0}\cup\overline{\Omega^h_{0,+}}\cup\overline{\Omega^h_+}$,

$$\|\pi_h u-u\|^2=|\pi_h u-u|^2_{1,2;\Omega^h_{0,+}}+|\pi_h u-u|^2_{1,2;\Omega^h_+}\leqslant \mathrm{mes}\big(\Omega^h_{0,+}\big)|\pi_h u-u|^2_{1,\infty;\Omega^h_{0,+}}+|\pi_h u-u|^2_{1,2;\Omega^h_+}.$$

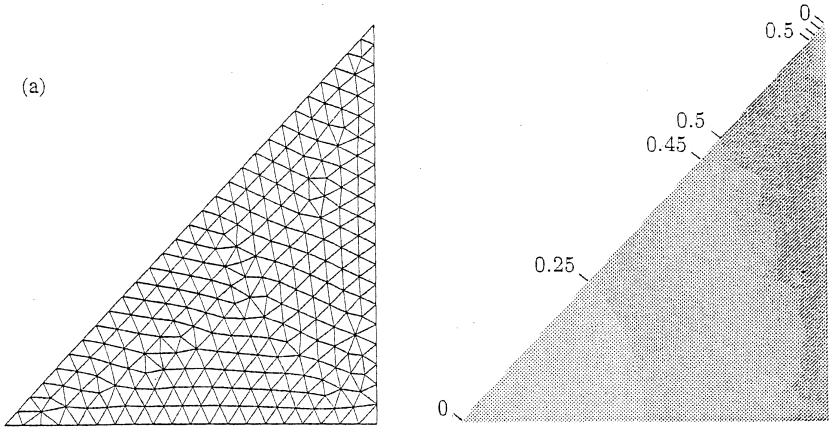

Figure 3. – Isovaleurs de $|\sigma|$ pour $\mathrm{Bi} = 0,5$ et $k = 2$. Maillage uniforme (256 sommets).
Figure 3. – Contours of $|\sigma|$ *for* $\mathrm{Bi} = 0.5$ *and* $k = 2$. *Uniform mesh* (256 *vertices*).

En outre, classiquement [2], nous avons :

$$|\pi_h u - u|_{1,\infty;\Omega^h_{0,+}} \leqslant C h_0 |u|_{2,\infty;\Omega^h_{0,+}} \leqslant C h_0 |u|_{2,\infty;\Omega},$$
$$|\pi_h u - u|_{1,\infty;\Omega^h_{+}} \leqslant C\, h^s |u|_{s+1,\infty;\Omega^h_{+}} \leqslant C\, h^s |u|_{s+1,\infty;\Omega_+},$$
$$|\pi_h u - u|_{1,2;\Omega^h_{+}} \leqslant C\, h^s |u|_{s+1,2;\Omega^h_{+}} \leqslant C\, h^s |u|_{s+1,2;\Omega_+},$$

où $C > 0$ désigne une constante indépendante de h. Le résultat découle ensuite du lemme 1, en rappelant que $\mathrm{mes}(\Omega^h_{0,+}) = \mathcal{O}(h_0)$ et en choisissant $\varepsilon = h^s$ dans (6)–(7). □

Signalons que lorsque Ω est un disque, la frontière Γ_0 de la zone rigide est un cercle, et l'hypothèse de régularité $u \in \mathrm{W}^{2,\infty}(\Omega) \cap \mathrm{W}^{s+1,\infty}(\Omega_+)$ est satisfaite pour tout $s > 0$.

COROLLAIRE 1 (maillages uniformes). – *Soient* $k \geqslant 1$ *et* $s \in [1, k]$. *Soit* $(\mathcal{T}_h)_{h>0}$ *une famille quasi uniforme de triangulations. Si* $u \in \mathrm{W}^{2,\infty}(\Omega) \cap \mathrm{W}^{s+1,\infty}(\Omega_+)$ *et vérifie les hypothèses* (6)–(7), *alors*

$$\|u - u_h\| = \begin{cases} \mathcal{O}\big(h\sqrt{|\ln h|}\big) & \text{pour } k = 1, \\ \mathcal{O}(h) & \text{pour } k \geqslant 2 \text{ et } s > 1. \end{cases}$$

COROLLAIRE 2 (maillages adaptés). – *Soient* $k \geqslant 2$ *et* $s \in]1, k]$. *Soit* $(\mathcal{T}_h)_{h>0}$ *une famille régulière de triangulations vérifiant* $h_0 = \mathcal{O}(h^s)$. *Si* $u \in \mathrm{W}^{2,\infty}(\Omega) \cap \mathrm{W}^{s+1,\infty}(\Omega_+)$ *et vérifie les hypothèses* (6)–(7), *alors* $\|u - u_h\| = \mathcal{O}\big(h^s\sqrt{|\ln h|}\big)$.

Pour $k \geqslant 2$, le corollaire 1 a pu être nettement amélioré. Dans la mesure où les triangulations ne sont plus quasi uniformes, il paraît judicieux d'exprimer l'erreur en fonction du nombre $N = \dim V_h$ de degrés de liberté.

PROPRIÉTÉ 1 (estimation en taille). – *Supposons que* Ω *soit un disque,* $f = 1$ *et* $k = 2$.
(i) *Si* $(\mathcal{T}_h)_{h>0}$ *est une famille uniforme de triangulations, alors* $\|u - u_h\| = \mathcal{O}(N^{-1/2})$.
(ii) *Il existe* $(\mathcal{T}_h)_{h>0}$ *une famille régulière de triangulations et vérifiant* $h_0 = h^2$ *telle que* $\|u - u_h\| = \mathcal{O}\big(N^{-1}\sqrt{\ln N}\big)$.

Indication sur la démonstration. – Nous avons étendu les résultats précédents au cas d'un ouvert non polygonal (en utilisant les techniques de [2], chap. 8), et donc au cas d'un disque. Pour (i), d'après le

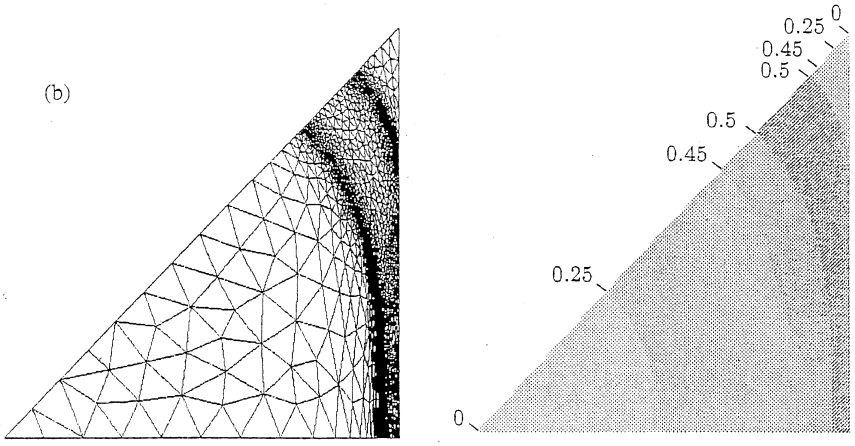

Figure 4. – Isovaleurs de $|\sigma|$ pour $\mathrm{Bi} = 0,5$ et $k = 2$. Maillage adapté (1944 sommets).

Figure 4. – Contours of $|\sigma|$ *for* $\mathrm{Bi} = 0.5$ *and* $k = 2$. *Adaptive mesh* (1944 *vertices*).

corollaire 1 et en remarquant que $h = \mathcal{O}\left(N^{-1/2}\right)$. Pour (ii), d'après le corollaire 2 et par construction d'une famille de triangulation en progression géométrique de $h_0 = h^2$ à h et telle que $N = \mathcal{O}\left(h^{-2}\right)$. □

3. Tests numériques

La résolution du problème (5) par une méthode de Lagrangien augmenté et une procédure auto-adaptative de maillages est décrite en détails dans [9]. L'erreur lorsque Ω est le disque unité est présenté sur la figure 2 pour une famille quasi uniforme de triangulations. Observons, figure 2 (a), que l'utilisation de l'élément P_2 n'apporte pas de gain asymptotique, par comparaison avec l'élément P_1. La figure 2 (b) met en évidence le gain obtenu par l'élément P_2 combiné avec une adaptation de maillage.

Enfin, les figures 3 et 4 présentent les isovaleurs de $|\sigma|$ lorsque Ω est une section carrée, $k = 2$ et $\mathrm{Bi} = 0,5$. Par symétrie par rapport aux deux axes de coordonnées et à la première bissectrice, nous pouvons nous ramener à un domaine triangulaire. La frontière Γ_0 des deux zones rigides correspond à l'isovaleur $|\sigma| = \mathrm{Bi} = 0,5$. Nous observons une nette amélioration de cette isovaleur lors de l'utilisation d'un maillage adapté.

Références bibliographiques

[1] Bingham E.C., Fluidity and Plasticity, Mc Graw-Hill, New York, 1922.
[2] Brenner S., Scott R., The Mathematical Theory of Finite Element Methods, Springer-Verlag, 1991.
[3] Duvaut G., Lions J.-L., Les inéquations en mécanique et en physique, Dunod, Paris, 1972.
[4] Falk R.S., Mercier B., Error estimates for elastoplastic problems, RAIRO, Anal. Numér. 11 (1977) 135–144.
[5] Glowinski R., Sur l'approximation d'une inéquation variationnelle elliptique de type Bingham, RAIRO, Anal. Numér. 10 (12) (1976) 13–30.
[6] Glowinski R., Numerical Methods for Non-Linear Variational Problems, Springer-Verlag, New York, 1984.
[7] Glowinski R., Lions J.-L., Trémolières R., Numerical Analysis of Variational Inequalities, North-Holland, Amsterdam, 1981.
[8] Mosolov P.P., Mjasnikov V.P., Variational methods in the theory of the fluidity of a viscous-plastic medium, PMM, J. Appl. Math. Mech. 29 (1965) 545–577.
[9] Saramito P., Roquet N., An adaptive finite element method for viscoplastic fluid flows in pipes, Comput. Meth. Appl. Mech. Engrg. (2000) (submitted).

ELSEVIER

Comput. Methods Appl. Mech. Engrg. 190 (2001) 5391–5412

Computer methods in applied mechanics and engineering

www.elsevier.com/locate/cma

An adaptive finite element method for viscoplastic fluid flows in pipes

Pierre Saramito *, Nicolas Roquet

LMC-IMAG, B.P. 53, 38041 Grenoble Cedex 9, France

Received 2 June 2000

Abstract

The numerical modelling of the fully developed Poiseuille flow of a yield stress fluid in a square section is presented. The dead regions in outer corners and the plug region in the center are exhibited. Numerical computations cover the complete range of the dimensionless number describing the yield stress effect, from a Newtonian flow to a fully stopped flow. The resolution of variational inequalities describing the flow is based on the augmented Lagrangian method and a specific mixed finite element method. The localization of yield surfaces is approximated by an anisotropic auto-adaptive mesh procedure. The limit load analysis and the associated limit yield surface are obtained by an extrapolation procedure. © 2001 Elsevier Science B.V. All rights reserved.

Keywords: Yield stress fluids; Bingham model; Variational inequalities; Limit load analysis; Adaptive mesh; Mixed finite element methods

1. Introduction

One of the difficult problems in viscoplastic fluid mechanics is to predict the appearance and development of dead regions with the variation of material properties and flow parameters. Understanding yield stress mechanisms is of major importance in petroleum industry (pipe-line), food industry, ceramics extrusion, bricks, debris flows, and semi-solid materials. Furthermore, the characteristics of dead regions and flow curves are of particular interest in the design of extrusion geometries.

The fully developed flow of a Bingham fluid in a tube with a square cross-section (see Fig. 1(a)), contains most of the features of viscoplastic flows. In a *plug region*, located in the center of the section (see Fig. 1(b)), the material translates with a constant velocity, while four *dead regions* are located in the outer corners. In contrast, the flow in a circular tube does not exhibit dead regions. Plug and dead regions are characterized by a rigid body motion of the material, and are related to *rigid zones*, by contrast to *shear zones*, where the material deforms. The separation surfaces between rigid and shear zones are related to the *yield surfaces*.

By using variational methods, Mosolov and Mjasnikov [1] showed the existence and uniqueness of the plug region. The existence of dead regions and the fact that dead regions always present a concavity turned towards the inside of the section is also showed in [2]. Accurate exhibition of such flow patterns represents a challenge for numerical methods.

The pour accuracy of most numerical simulations can be explained in part by the replacement of the viscoplastic model by more regular ones, such as non-linear biviscous laws (see [3–5]). These biviscous laws introduce an additional regularization parameter. The practical difficulty to solve the regularized model

* Corresponding author. Tel.: +33-4-76-51-46-10; fax: +33-4-76-63-12-63.
E-mail address: pierre.saramito@imag.fr (P. Saramito).

0045-7825/01/$ - see front matter
PII: S0045-7825(01)00175-X

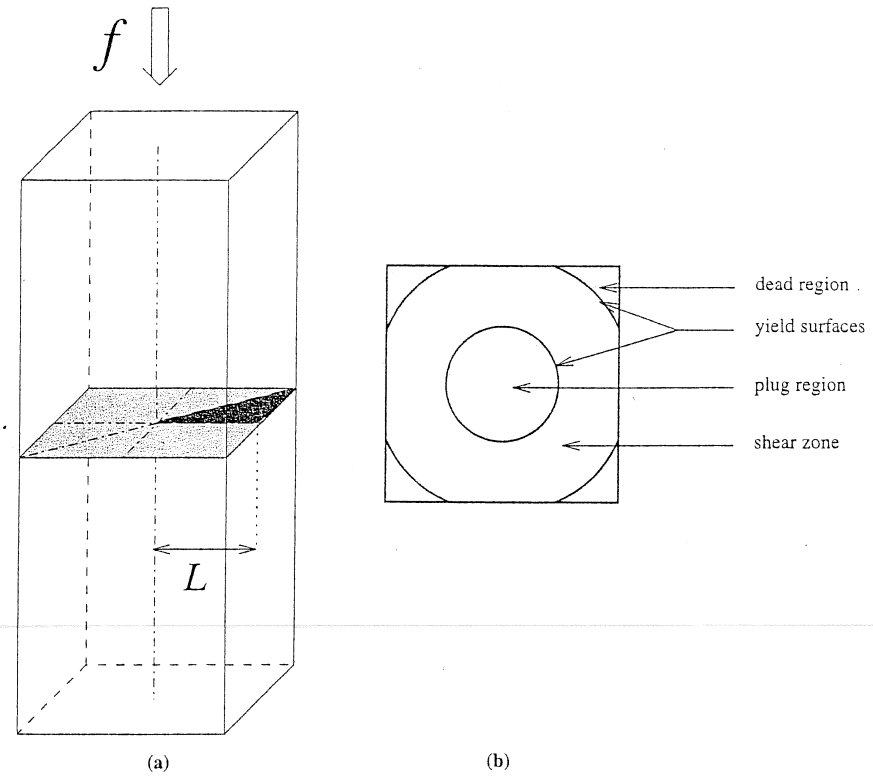

Fig. 1. Square tube cross-section: (a) tri-dimensional view; (b) schematic view of the cross-section.

problem increases when the regularization parameter approaches zero, i.e., when the regularized model approaches the less regular viscoplastic model. Furthermore, the computational time grows very rapidly when the regularization parameter approaches zero. Finally, all rigid zones disappear completely as soon as the regularized model is used, and the notion of zones with *small deformations* may be introduced. As a consequence, regularized model studies encounter difficulties to provide accurate solutions, especially in the most interesting case where yield properties become important. Nevertheless, biviscosity models are widely used, since most available numerical codes for solving Newtonian flows with a non-constant viscosity function can directly be re-used. Recently, Taylor and Wilson [6] explored the resolution of the Bercovier and Engelman [3] regularized model in square and rectangular tube sections. These authors exhibited some dead regions. Nevertheless, unexpected situations were exhibited: the concavity of the dead regions were inverted, and dead and plug regions was connected. The dramatic effect of the regularization parameter on the inversion of concavity has been analyzed by Wang [7]. The author showed that these unexpected effects were caused by an insufficient accuracy of the numerical simulation.

The replacement of the Bingham model by regularized one can be avoided in practical computations: in the framework of variational inequalities, Fortin [8] proposed an algorithm to solve the flow of a Bingham fluid in a square cross-section. Moreover, the author exhibited results for the flow in a square section. Nevertheless, meshes were rough, and a dead region was represented by only one triangular element. The augmented Lagrangian framework introduced by Fortin and Glowinski [9], later developed by Glowinski and LeTallec [10], has furnished efficient algorithms for solving viscoplastic flow problems. Since this approach does not require the use of a regularized model, an accurate prediction of rigid zones could be expected. Huilgol and Panizza [11] applied this approach to the resolution of a Bingham model in a L-shaped tube section. A plug region was found at the center of the section. Nevertheless, as pointed out by Wang [12], the flow field in the corner regions was not clearly resolved by these authors.

Even when using augmented Lagrangian method for solving the exact Bingham model, the finite element prediction of the yield surface is not accurate enough. The first improvement is to increase the polynomial degree used by the finite element method. The second improvement is to increase mesh refinement. A uniform mesh refinement increases the computational time rapidly, while the accuracy increases slowly in terms of the yield surface determination. The idea of anisotropic auto-adaptive mesh generation, introduced in 1990 by Vallet [13] and developed by Borouchaki et al. [14] has been recently used for the simulation of Euler and Navier–Stokes equation by Castro-Diaz et al. [15] to capture shocks accurately, i.e. surfaces where the solution is discontinuous. By analogy, in the context of viscoplastic flows, the second derivatives of the velocity field are generally discontinuous across yield surfaces. Since such surfaces are a priori unknown, mesh refinement requires an iterative process to catch the solution and obtain a high precision for yield surfaces.

In this paper, the flow of a Bingham fluid along a pipe of square cross-section is considered. The numerical technique combines the augmented Lagrangian method that takes rigorously into account the yield stress constitutive equation, and the auto-adaptive mesh procedure for the capture of surfaces associated with abrupt variations of the solution.

The second section presents the Bingham model and states the problem of the flow along a prismatic tube. Numerical methods and tests are grouped in the third section. The augmented Lagrangian algorithm is recalled. Then, the stress-and-velocity mixed finite element approximation is introduced. The validation uses a circular tube section. The efficiency of the mesh adaptation strategy is tested on both circular and cross-square sections. The fourth section presents results on a square cross-section, including rigid zone enhancement and velocity and stress profiles. The limit case where rigid zones invade the whole section, related to the *limit load analysis*, is treated using an extrapolation procedure. Finally, a scaling procedure extends the flow curve of a circular pipe to the case of the squared pipe. Two short appendixes group explicit expressions of some constants.

2. Problem statement

The Bingham model [16,17] is characterized by the following property: the material starts to flow only if the applied forces exceed a certain limit σ_0, called the yield limit. The total Cauchy stress tensor is expressed by

$$\sigma_{\text{tot}} = -p \cdot I + \sigma,$$

where σ denotes its deviatoric part, and p is the pressure. The conservation of momentum is

$$\rho\left(\frac{\partial \mathbf{u}}{\partial t} + \mathbf{u} \cdot \nabla \mathbf{u}\right) - \mathbf{div}\ \sigma + \nabla p = 0,$$

where $\mathbf{u}$ is the velocity field, and ρ the constant density. Since the fluid is assumed to be incompressible, the mass conservation leads to

$$\text{div}\ \mathbf{u} = 0.$$

The constitutive equation can be written as:

$$\sigma = 2\eta D(\mathbf{u}) + \sigma_0 \frac{D(\mathbf{u})}{|D(\mathbf{u})|} \quad \text{if } |D(\mathbf{u})| \neq 0,$$
$$|\sigma| \leqslant \sigma_0 \quad \text{if } |D(\mathbf{u})| = 0,$$

or equivalently:

$$D(\mathbf{u}) = \begin{cases} \left(1 - \frac{\sigma_0}{|\sigma|}\right)\frac{\sigma}{2\eta} & \text{if } |\sigma| > \sigma_0, \\ 0 & \text{otherwise,} \end{cases}$$

where $\sigma_0 \geqslant 0$ is the yield stress, $\eta > 0$ is the plastic viscosity, $D(\mathbf{u}) = (\nabla\mathbf{u} + \nabla\mathbf{u}^{\mathrm{T}})/2$ is the rate-of-deformation tensor, and, for any tensor $\tau = (\tau_{ij})$, the notation $|\tau|$ represents the following matrix norm:

$$|\tau| = \sqrt{\frac{\tau : \tau}{2}} = \frac{1}{\sqrt{2}} \left(\sum_{ij} \tau_{ij}^2 \right)^{1/2}.$$

Notice that $\sigma_0 = 0$, one is led to the classical viscous incompressible fluid. When $\sigma_0 > 0$, rigid zones in the interior of the fluid can be observed. As σ_0 becomes larger, these rigid zones develop and may completely block the flow when σ_0 is sufficiently large.

We consider the fully developed flow in a prismatic tube (see Fig. 1(a)). Let (O_z) be the axis of the tube and (O_{xy}) the plane of the bounded section $\Omega \subset \mathbb{R}^2$. The pressure gradient is written as $\nabla p = (0, 0, -f)$ in Ω, where $f > 0$ is the constant applied force density. The velocity is written as $\mathbf{u} = (0, 0, u)$, where the third component u along the (O_z) axis depends only upon x and y, and is independent of t and z. The problem can be considered as a two-dimensional one, and the stress tensor σ is equivalent to a two shear stress component vector: $\boldsymbol{\sigma} = (\sigma_{xz}, \sigma_{yz})$. We also use the following notations:

$$\nabla u = \left(\frac{\partial u}{\partial x}, \frac{\partial u}{\partial y} \right),$$

$$\operatorname{div} \boldsymbol{\sigma} = \frac{\partial \sigma_{xz}}{\partial x} + \frac{\partial \sigma_{yz}}{\partial y},$$

$$|\boldsymbol{\sigma}| = \sqrt{\sigma_{xz}^2 + \sigma_{yz}^2}.$$

Finally, the so-called Mosolov problem can be summarized as:

(P): find $\boldsymbol{\sigma}$ and u defined in Ω such that

$$\nabla u = \begin{cases} \left(1 - \frac{\sigma_0}{|\boldsymbol{\sigma}|}\right) \frac{\boldsymbol{\sigma}}{\eta} & \text{if } |\boldsymbol{\sigma}| > \sigma_0, \\ 0 & \text{otherwise}, \end{cases} \tag{1}$$

$$\operatorname{div} \boldsymbol{\sigma} = -f \text{ in } \Omega, \tag{2}$$

$$u = 0 \text{ on } \partial\Omega. \tag{3}$$

Here, (1) expresses the constitutive equation, (2) the conservation of momentum and (3) the no-slip boundary condition. In the case of a square cross-section, we reduce the domain of computation by using symmetries (see Fig. 1(a)). Thus, in this paper, results for the square cross-section are represented in a triangular domain.

Let L be a characteristic length of the cross-section Ω, i.e., the half-length of an edge of a square section, or the radius of a circular section (also denoted by R for convenience in that case). A characteristic velocity is given by $U = L^2 f/(2\eta)$ and a characteristic viscous stress by $\Sigma = \eta U/L = Lf/2$. The Bingham dimensionless number is defined by the ratio of the yield limit σ_0 by a representative viscous stress Σ

$$Bi = \frac{2\sigma_0}{Lf}. \tag{4}$$

This is the only dimensionless number of the problem.

3. Numerical methods and tests

The augmented Lagrangian method, applied to the Mosolov problem (1)–(3), is briefly introduced in this appendix. Then, the delicate problem of the choice of a mixed finite element is carefully treated. Next, the validation of our numerical methodology on a circular pipe with uniform meshes is presented. Finally, our mesh adaptation strategy is tested and discussed.

3.1. Augmented Lagrangian algorithm

Let $H_0^1(\Omega)$ denote the classical functional space [18] and J the functional defined for all $v \in H_0^1(\Omega)$ by

$$J(v) = \frac{\eta}{2}\int_\Omega |\nabla v|^2 \,\mathrm{d}x + \sigma_0 \int_\Omega |\nabla v| \,\mathrm{d}x - \int_\Omega fv \,\mathrm{d}x.$$

Glowinski et al. [19] showed that the solution u of problem (P) expressed as a minimization point of J on $H_0^1(\Omega)$

$$\min_{v\in H_0^1(\Omega)} J(v). \tag{5}$$

Since J is non-differentiable on $H_0^1(\Omega)$ when $\sigma_0 > 0$ due to the term $\int_\Omega |\nabla v| \,\mathrm{d}x$, the problem cannot be described by an equation and thus requires a specific convex optimization approach (see also [20]).

Let

$$\gamma = \nabla u \in L^2(\Omega)^2. \tag{6}$$

The linear constraint (6) is handled by using a Lagrange multiplier that coincides with the stress $\sigma \in L^2(\Omega)^2$

$$\mathscr{L}(u,\gamma;\sigma) = \frac{\eta}{2}\int_\Omega |\gamma|^2 \,\mathrm{d}x + \sigma_0 \int_\Omega |\gamma| \,\mathrm{d}x - \int_\Omega fv \,\mathrm{d}x + \int_\Omega (\nabla u - \gamma)\cdot\sigma \,\mathrm{d}x.$$

For all $a > 0$, the augmented Lagrangian

$$\mathscr{L}_a(u,\gamma;\sigma) = \mathscr{L}(u,\gamma;\sigma) + \frac{a}{2}\int_\Omega \nabla u - \gamma|^2 \,\mathrm{d}x$$

becomes quadratic and positive-definite with respect to u. This implies that, with σ and γ fixed, $\mathscr{L}_a$ can be minimized with respect to u on $H_0^1(\Omega)$, whereas this operation becomes in practice impossible for $a = 0$. This transformation becomes helpful since we can solve the saddle-point problem of $\mathscr{L}_a$, that coincides with those of $\mathscr{L}$, by an appropriate algorithm proposed in [9]:

Algorithm (Uzawa)

initialization: $n = 0$

Let σ^0 and γ^0 arbitrarily chosen in $L^2(\Omega)^2$.

loop: $n \geqslant 0$

- *Step 1*: Let σ^n and γ^n being known, find $u^{n+1} \in H_0^1(\Omega)$ such that

$$-a\Delta u^{n+1} = f + \operatorname{div}(\sigma^n - a\gamma^n) \text{ in } \Omega, \tag{7}$$

$$u^{n+1} = 0 \text{ on } \partial\Omega. \tag{8}$$

- *Step 2*: compute explicitly:

$$\gamma^{n+1} := \begin{cases} \left(1 - \frac{\sigma_0}{|\sigma^n + a\nabla u^{n+1}|}\right)\frac{\sigma^n + a\nabla u^{n+1}}{\eta + a} & \text{if } |\sigma^n + a\nabla u^{n+1}| > \sigma_0, \\ 0 & \text{otherwise .} \end{cases} \tag{9}$$

- *Step 3*: compute explicitly:

$$\sigma^{n+1} := \sigma^n + a(\nabla u^{n+1} - \gamma^{n+1}). \tag{10}$$

end loop

The interest of this algorithm is that it transforms the global non-differentiable problems (5) into a family of completely standard problem (7), (8) and local explicit computation (9), coordinated via the Lagrange multiplier in (10).

3.2. Stress–velocity mixed finite element approximation

Let A and B be the two bilinear forms defined by

$$A(\gamma,u;\xi,v)=(\eta+a)\int_\Omega \gamma\cdot\xi\,\mathrm{d}x-a\int_\Omega \nabla u\cdot\xi\,\mathrm{d}x-a\int_\Omega \nabla v\cdot\gamma\,\mathrm{d}x+a\int_\Omega \nabla u\cdot\nabla v\,\mathrm{d}x,$$

$$B(\xi,v;\tau)=-\int_\Omega \xi\cdot\tau\,\mathrm{d}x+\int_\Omega \nabla v\cdot\tau\,\mathrm{d}x.$$

The saddle point of $\mathscr{L}_a$ is characterized as the solution of a problem expressed by the following variational inequalities:

(FV): find $(\gamma,u;\sigma)\in L^2(\Omega)^2\times H_0^1(\Omega)\times L^2(\Omega)^2$ such that

$$\sigma_0\int_\Omega(|\xi|-|\gamma|)\,\mathrm{d}x+A(\gamma,u;\xi-\gamma,v)+B(\xi-\gamma,v;\sigma)\geqslant\int_\Omega fv\,\mathrm{d}x,$$

$$B(\gamma,u;\tau)=0$$

for all $(\xi,v;\tau)\in L^2(\Omega)^2\times H_0^1(\Omega)\times L^2(\Omega)^2$.

Let $D_h\subset L^2(\Omega)$, $V_h\subset H_0^1(\Omega)$, and $T_h\subset L^2(\Omega)$ be some finite dimensional spaces. The finite dimensional version of the variational inequalities is simply obtained by replacing functional spaces by their finite dimensional counterparts:

(FV)$_h$: find $(\gamma_h,u_h;\sigma_h)\in D_h\times V_h\times T_h$ such that

$$\sigma_0\int_\Omega(|\xi|-|\gamma_h|)\,\mathrm{d}x+A(\gamma_h,u_h;\xi-\gamma_h,v)+B(\xi-\gamma_h,v;\sigma)\geqslant\int_\Omega fv\,\mathrm{d}x,$$

$$B(\gamma_h,u_h;\tau)=0$$

for all $(\xi,v;\tau)\in D_h\times V_h\times T_h$.

For $\sigma_0=0$ the problem reduces to a linear one that fits the theory of mixed finite elements (see, e.g., [21]). The choice $D_h=T_h$ leads to $\gamma_h=R_h\nabla u_h$, where R_h denotes the projection from $L^2(\Omega)^2$ on T_h, defined for all $\xi\in L^2(\Omega)^2$ by:

$$R_h\xi\in T_h \text{ and } \int_\Omega R_h\xi\cdot\tau\,\mathrm{d}x=\int_\Omega\xi\cdot\tau\,\mathrm{d}x\quad\forall\tau\in T_h.$$

See also [22] for the use of the properties of R_h in the context of stabilized mixed finite element approximation. An investigation of stress–velocity mixed finite element space combinations that satisfies $R_h=I$ is

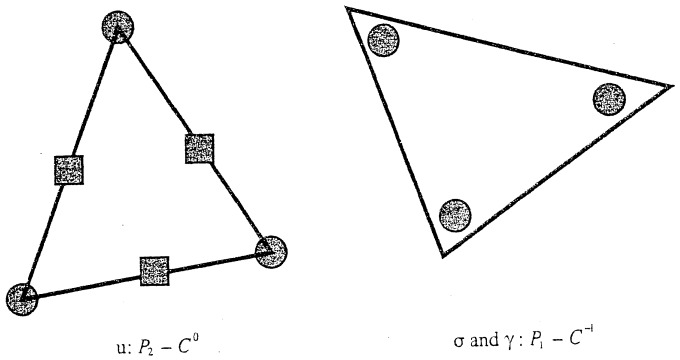

Fig. 2. Mixed finite element approximation.

presented in [23] and applied in the context of viscoelastic fluid flows [24]. Thus, the case $\sigma_0 = 0$ leads to $\boldsymbol{\sigma}_h = \eta R_h \nabla u_h$ and the problem reduces to the following linear elliptic one:

$(Q)_h$: find $u_h \in V_h$ such that

$$\eta \int_\Omega R_h \nabla u_h \cdot R_h \nabla v \, \mathrm{d}x + a \int_\Omega (I - R_h) \nabla u_h \cdot (I - R_h) \nabla v \, \mathrm{d}x = \int_\Omega f v \, \mathrm{d}x \quad \forall v \in V_h.$$

When $R_h \neq I$ i.e. $T_h \neq \nabla V_h$, the discrete solution u_h depends upon the numerical parameter $a > 0$ of the augmented Lagrangian method. This property is not desirable. A necessary and sufficient condition for the solution u_h to be independent of the parameter a is $T_h = \nabla V_h$.

Let $\mathcal{T}_h$ be a finite element mesh composed of triangles. We introduce the space V_h, composed of continuous piecewise polynomial quadratic functions ($P_2 - C^0$). Thus, $T_h = D_h = \nabla V_h$ is the set of discontinuous piecewise linear functions ($P_1 - C^{-1}$). Fig. 2 represents the corresponding degrees of freedom. In a preliminary version, the space V_h was implemented by continuous piecewise linear functions ($P_1 - C^0$), and $T_h = D_h$ by discontinuous piecewise constant functions ($P_0 - C^{-1}$). The quadratic implementation leads to a better approximation, and thus, is well-suited to exhibit fine flow patterns.

3.3. Validation on a circular tube

This subsection presents the validation of the numerical methodology on a circular pipe, since the analytical solution is known. Let Ω be a section of a circular pipe of radius R and center $(x, y) = (0, 0)$. Let $r = \sqrt{x^2 + y^2}$ for convenience. The Bingham number is defined by $Bi = 2\sigma_0/(fR)$. For $2\sigma_0 \geqslant fR$, i.e. $Bi \geqslant 1$, the flow is completely blocked and the velocity field is zero. When $2\sigma_0 < fR$, the velocity field $u(r)$ is given by:

$$\frac{2\eta}{fR^2} \times u(r) = \begin{cases} \frac{1}{2}\left(1 - \frac{r^2}{R^2}\right) - \frac{2\sigma_0}{fR}\left(1 - \frac{r}{R}\right) & \text{when } \frac{r}{R} \geqslant \frac{2\sigma_0}{fR}, \\ \frac{1}{2}\left(1 - \frac{2\sigma_0}{fR}\right)^2 & \text{otherwise}. \end{cases}$$

Thus, a plug flow of radius $2\sigma_0/f$ exists, which translates at constant velocity in the (O_z) direction. Note that the solution $u(r)$ is only one time differentiable, since the gradient of velocity is non-differentiable at the junction between the shear and the plug zones (i.e. at $r = 2\sigma_0/f$).

Fig. 3 shows the evolution of the normalized residual term $\|\gamma_h^n - \nabla u_h^n\|_{L^2(\Omega)}$ versus the iteration number n for three values of the numerical parameter a of the algorithm. Note that $a = 20$ leads to an optimal convergence velocity. For $n \approx 1400$, the computation reaches the machine precision, roughly 10^{-30} in quadruple precision. For $a = 5$ or $a = 50$, the convergence is slower. Recall that the limit u_h of the family $(u_h^n)_{n \geqslant 0}$ does not depend upon a, since the finite element approximation for velocity and stresses are carefully chosen. Note also on Fig. 3 the asymptotic slope on the semi-logarithmic scale. This slope is related to the convergence velocity v^* defined by

$$v^* = \lim_{n \to \infty} -\frac{1}{n} \log \|\gamma_h^n - \nabla u_h^n\|_{L^2(\Omega)}.$$

Fig. 4 shows v^* versus a for various uniform mesh size h and Bingham number. Fig. 5 presents a family of three uniform finite element meshes with decreasing element size h. We observe that the optimal convergence velocity occurs for a value of a that depends upon h and Bi. The optimal a increases when $h \to 0$ and Bi increases, while the corresponding optimal convergence velocity v^* decreases. This expresses that the computation time increases with mesh size and Bi. From a practical point of view, the optimal value of a is difficult to predict, since it depends strongly upon the dimensionless number Bi, and the finite element mesh. Nevertheless, the algorithm converges for all $a > 0$. For all computations of the previous section, involving adaptive meshes, the value $a = 200$ has been used, and iterations were performed until the maximum of $|\gamma_h^n - \nabla u_h^n|$ over Ω becomes lower than 10^{-12}.

Let us turn to the convergence of u_h versus the mesh size $h \to 0$ for the uniform mesh family. The exact solution u is known for the circular pipe and Fig. 6 plots in logarithmic scale the error in L^2-norm versus h.

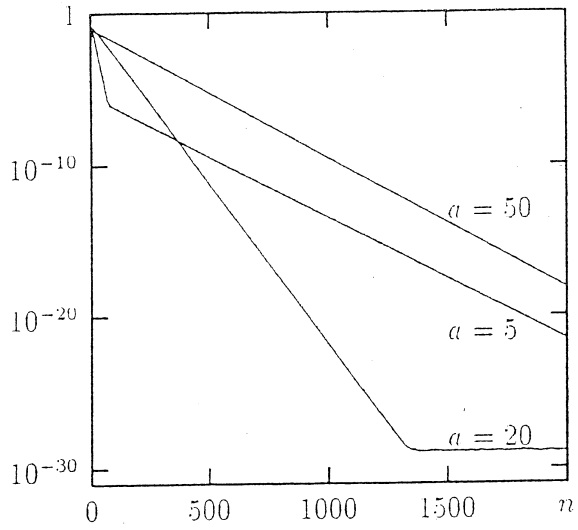

Fig. 3. Normalized residual terms $\|\gamma_h^n - \nabla u_h^n\|_{L^2(\Omega)} / \|\gamma_h^0 - \nabla u_h^0\|_{L^2(\Omega)}$ versus algorithm iteration number n.

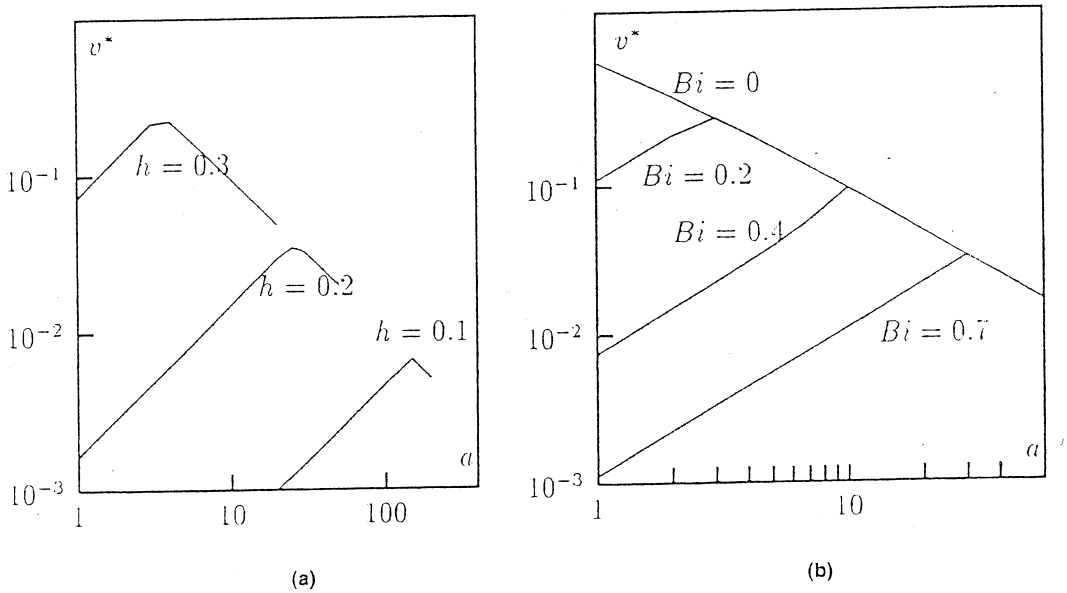

Fig. 4. Algorithm convergence velocity v^* versus a: (a) varying mesh size and for $Bi = 0.5$; (b) varying Bi and for mesh size $h = 0.2$.

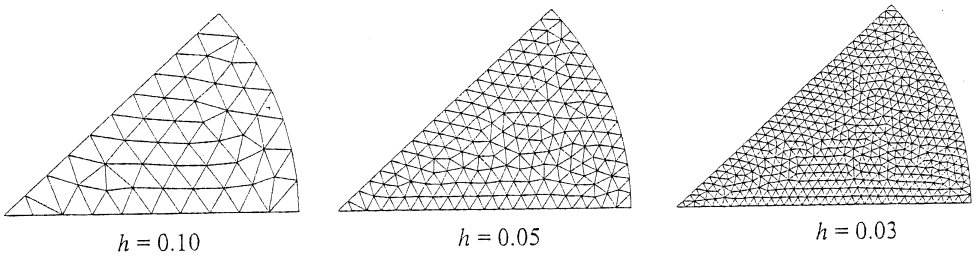

Fig. 5. The uniform mesh family used for the convergence validation.

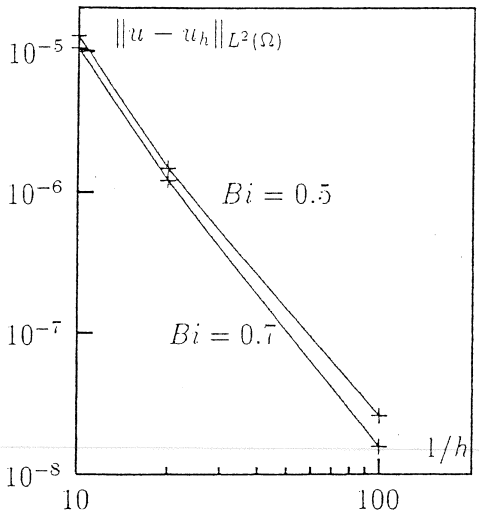

Fig. 6. Convergence of the finite element method: $\|u - u_h\|_{L^2(\Omega)}$ as a function of the mesh size h.

Observe that the error decreases rapidly with h. The error is about 10^{-8} for $h = 10^{-2}$. More generally, the error behaves as $\mathcal{O}(h^\lambda)$, where λ is in the range 2–3. The continuous P_2 finite element, used for the velocity, is responsible of this efficient convergence property. In the case of the continuous P_1 element, the convergence is slower: Glowinski [25] showed a $\mathcal{O}(h\sqrt{|\ln(h)|})$ behavior for the error in H^1-norm, and Falk and Mercier [26] showed an optimal $\mathcal{O}(h)$ estimate for the vorticity in L^2-norm when Ω is connected. When using the P_2 element, Roquet et al. [27] showed recently a $\mathcal{O}(h^2\sqrt{|\ln(h)|})$ estimate for the velocity in H^1-norm.

Finally, let us introduce the field of dissipative energy, defined in Ω by

$$E = \eta|\nabla u|^2 + \sigma_0|\nabla u|.$$

This field E is known to be non-differentiable across the border between shear and rigid zones, as can be seen with its explicit expression:

$$\frac{4\eta}{f^2R^2} \times E(r) = \begin{cases} \left(\frac{r}{R}\right)^2 - \frac{2\sigma_0}{fR} \times \frac{r}{R} & \text{when } \frac{r}{R} \geqslant \frac{2\sigma_0}{fR}, \\ 0 & \text{otherwise.} \end{cases} \tag{11}$$

Notice that E is continuous, but its first derivative is discontinuous. The following subsection, related to the mesh adaptation process, exploits this important property.

3.4. Mesh adaptation

Let $\mathcal{T}_0$ be an initial mesh and u_0 be the solution of problem $(\mathrm{FV})_h$ associated to $\mathcal{T}_0$. Next, let $\varphi_0 = \varphi(u_0)$ be the *governing field* obtained from ∇u_0 by

$$\varphi_0 = \left(\eta|\nabla u_0|^2 + \sigma_0|\nabla u_0|\right)^{1/2}.$$

Note that φ_0 is the square root of the dissipative energy. This choice will be explained in the following subsection. The governing field φ_0 is approximated by a piecewise polynomial function over each triangle $K \in \mathcal{T}_0$, and the error of interpolation in the unitary direction $\mathbf{d} \in \mathbb{R}^2$ is estimated by:

$$e_{K,\mathbf{d}} = h_{K,\mathbf{d}}^2 \left| \frac{\partial^2 \varphi_0}{\partial \mathbf{d}^2} \right| \quad \text{in } K,$$

where $h_{K,\mathbf{d}}$ is the length of K in the $\mathbf{d}$ direction,

$$\frac{\partial^2\varphi_0}{\partial\mathbf{d}^2} = \mathbf{d}^{\mathrm{T}}\cdot H(\varphi_0)\cdot\mathbf{d}$$

and $H(\varphi_0)$ denotes the Hessian of φ_0

$$H(\varphi_0) = \begin{pmatrix} \partial^2\varphi_0/\partial x^2 & \partial^2\varphi_0/\partial x\partial y \\ \partial^2\varphi_0/\partial x\partial y & \partial^2\varphi_0/\partial y^2 \end{pmatrix}.$$

Following Vallet [13], a possibility to adapt the mesh to the computation of φ_0 is to equi-distribute this error, i.e. to make it constant over all triangles and in all directions. Let λ_1, λ_2 be the eigenvalues of $H(\varphi_0)$ and $\mathbf{d}_1$ and $\mathbf{d}_2$ the associated eigenvectors:

$$\frac{\partial^2\varphi_0}{\partial\mathbf{d}_1^2} = \lambda_1 \quad \text{and} \quad \frac{\partial^2\varphi_0}{\partial\mathbf{d}_2^2} = \lambda_2.$$

The error $e_{K,\mathbf{d}}$ is independent of $\mathbf{d}$ and K when $e_{K,\mathbf{d}_1} = e_{K,\mathbf{d}_2}$, i.e. when

$$h_{K,\mathbf{d}_1}^2|\lambda_1| = h_{K,\mathbf{d}_2}^2|\lambda_2| = c_0 \quad \forall K\in\mathscr{T}_0,$$

where $c_0 > 0$ is a constant independent of K. The Hessian $H(\varphi_0)$ being known over K, we suppose that $H(\varphi_0)$ is non-singular, i.e. $\lambda_1\lambda_2 \neq 0$. The constant c_0 being known, we want to build triangles of length h_i in the $\mathbf{d}_i$ direction with $h_i = \sqrt{c_0/|\lambda_i|}$, $i = 1, 2$. Such a triangle has no privileged direction in a metric such that the two $h_i\mathbf{d}_i$ vectors, $i = 1, 2$, have the same norm. Thus, we introduce the metric $M(\varphi_0)$, the eigenvectors as column of $H(\varphi_0)$ with the corresponding $|\lambda_1|$ and $|\lambda_2|$. The induced norm $\|\cdot\|_M$ satisfies

$$\|h_i\mathbf{d}_i\|_M = h_K\sqrt{\mathbf{d}_i^T\cdot M(\varphi_0)\cdot\mathbf{d}_i} = \sqrt{c_0}, \quad k = 1, 2.$$

Thus, an isotropic mesh in the Riemann space associated to the metric $M(\varphi_0)$ is a mesh extended in the Euclidean space with a factor h_i in the $\mathbf{d}_i$ direction.

Solving a problem using a mesh adaptation is an iterative process, which involves three main steps:

1. Starting from an initial mesh $\mathscr{T}_0$, the problem is solved using the augmented Lagrangian algorithm. Let u_0 be the corresponding solution associated to the mesh $\mathscr{T}_0$.
2. Let $\varphi_0 = (\eta|\nabla u_0|^2 + \sigma_0|\nabla u_0|)^{1/2}$ be the governing field. This field must emphasize regions where the solution has high gradients, so that the mesh generator refines these regions.
3. Starting from the governing field φ_0 on the mesh $\mathscr{T}_0$, the anisotropic mesh generator (see [14,28]) generates a totally new mesh, denoted by $\mathscr{T}_1$.

Then, $\mathscr{T}_1$ is used to solve the problem, and so on, until the obtained solution gets clear limits between shear zones and rigid zones with no more jagged borders.

In the case of a circular section, the dissipative energy E is expressed by (11). Thus, as pointed out in the previous subsection, $\varphi = \sqrt{E}$ is continuous, but its first derivative is discontinuous, so the Hessian $H(\varphi)$ is defined with Dirac measures. From a numerical point of view, $H(\varphi)$ is not explicitly computed but rather approximated numerically. The numerical computation of $H(\varphi)$ will have high variations around the border of the plug flow. Then, the metric induced by φ will force the mesh generator to refine strongly the new mesh near this border.

This theoretical prediction can be verified in Fig. 7, which shows the initial mesh and the mesh obtained after ten loops of the adaptation process. Elements in the central plug zone become larger, while the mesh is strongly refined with stretched elements around the border of this zone and near the wall.

The same kind of properties are expected to extend to various cross-section geometries: numerical tests have confirmed that the square root of the dissipative energy appears to be a good governing field for both circular and square sections.

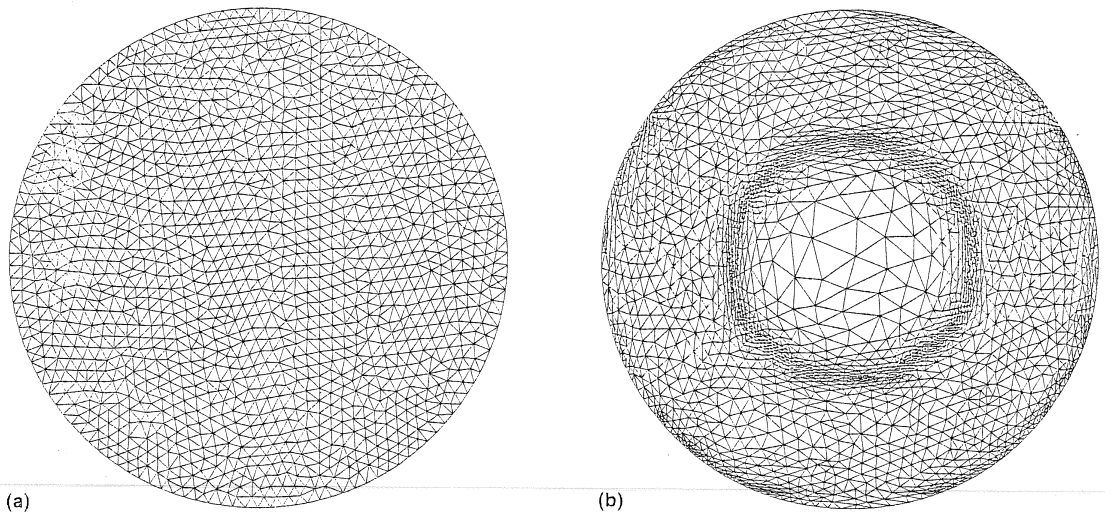

Fig. 7. Initial and adapted mesh after 10 iterations for a circular section ($Bi = 0.5$). (a) Initial uniform mesh (4000 elements); (b) adapted mesh (5000 elements).

3.5. *Efficiency of the adaptation process on the square section*

The influence of the mesh adaptation on the quality of our solution is shown in Fig. 8. The left column plots the adapted meshes while the right column represents the $|\sigma_h|/\Sigma$ field for $Bi = 1$. The grey scale represents values above 1 for dark while rigid zones from 1 to 0.9 are in dark grey and in light gray for values smaller than 0.5. The $|\sigma|/\Sigma = 1$ contour is associated with the yield surface.

The first row shows results for an isotropic regular mesh. We can see the poor accuracy of the solution, especially between shear and rigid zones, which are regions of interest. Moreover, the dead zone is unreadable.

Basing on this result, the governing field φ is computed, as described before, and then a mesh adaptation step is used. Then, the mesh plotted in the second row is obtained. This mesh is no longer regular and is slightly anisotropic. Refined regions already emphasize the shear zones. A solution to our problem can now be computed, using this mesh as a startup. The result, shown in column 2 row 2, is already better than the one computed with the initial mesh. Borders between shear and rigid zones are clearer and the dead zone in the corner has begun to be noticeable.

Going through some more cycles of adaptation loops, results are clearly improved. After 10 loops, we get the mesh and solution shown in the third row. The computational cost for 10 iterations of the adaptive process is of about one hour on an Intel/Linux (200 MHz) personal computer. The final mesh contains about 2000 triangles. Here, we have the wanted type of an anisotropic and irregular mesh. Elements are still larger in the rigid zones, both the inner plug and dead zones, while they are strongly refined in the shear zone. In particular, the regions with small element sizes are located near the wall and around the borders between shear and rigid zones. Note also that elements are stretched along these borders, as a result of the mesh anisotropy. The corresponding solution shows accurate contours and borders.

While the concavity of the separating line between shear and dead zones is turned towards the inside of the section (Fig. 8(c), right), a brutal change of concavity occurs, and concavity of contours for $|\sigma|/\Sigma = 0.9$ turns towards corners. Thus, the prediction of dead zones requires accurate numerical computation in this region, as pointed out in Section 4.

As in the case of the circular section, the field φ is here continuous but its first derivative appears to be discontinuous. Note that in 1995, Seregin [29] showed, in a more general case, the continuity of ∇u. Fig. 9(a) represents φ in elevation in the vertical direction, for $Bi = 0.7$ and after 10 iterations of adaptation loop. One can notice that rigid zones are associated with $\varphi = 0$ and the brutal transition of φ at the separation from rigid to shear zones. The representation of both the energy field in elevation and the

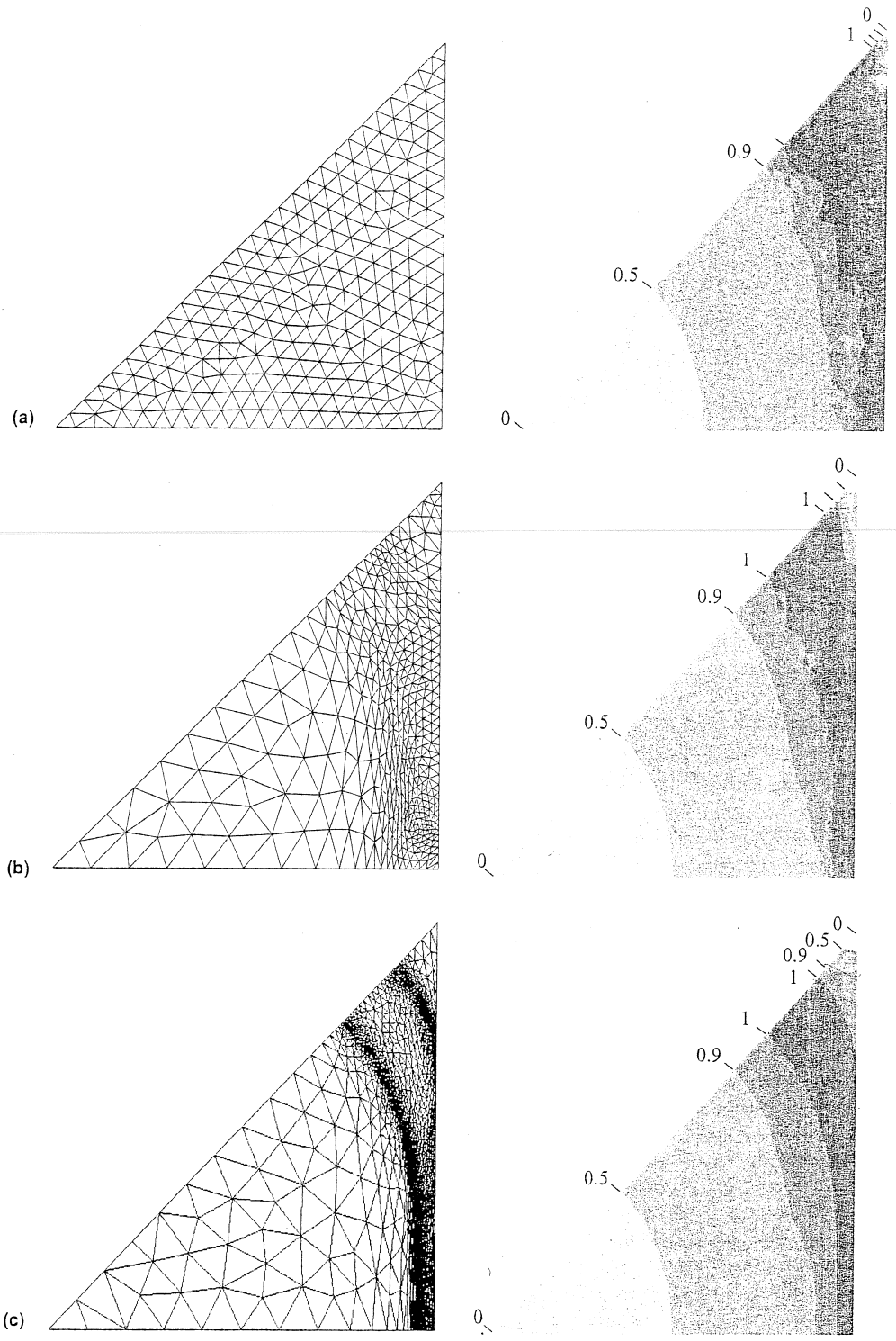

Fig. 8. Efficiency of the adaptive method: evolution of $|\sigma|/\Sigma$ during adaptation loop for $Bi = 1$. (a) Initial uniform mesh (256 vertices); (b) adapted mesh at iteration 1 (737 vertices); (c) adapted mesh at iteration 10 (1944 vertices).

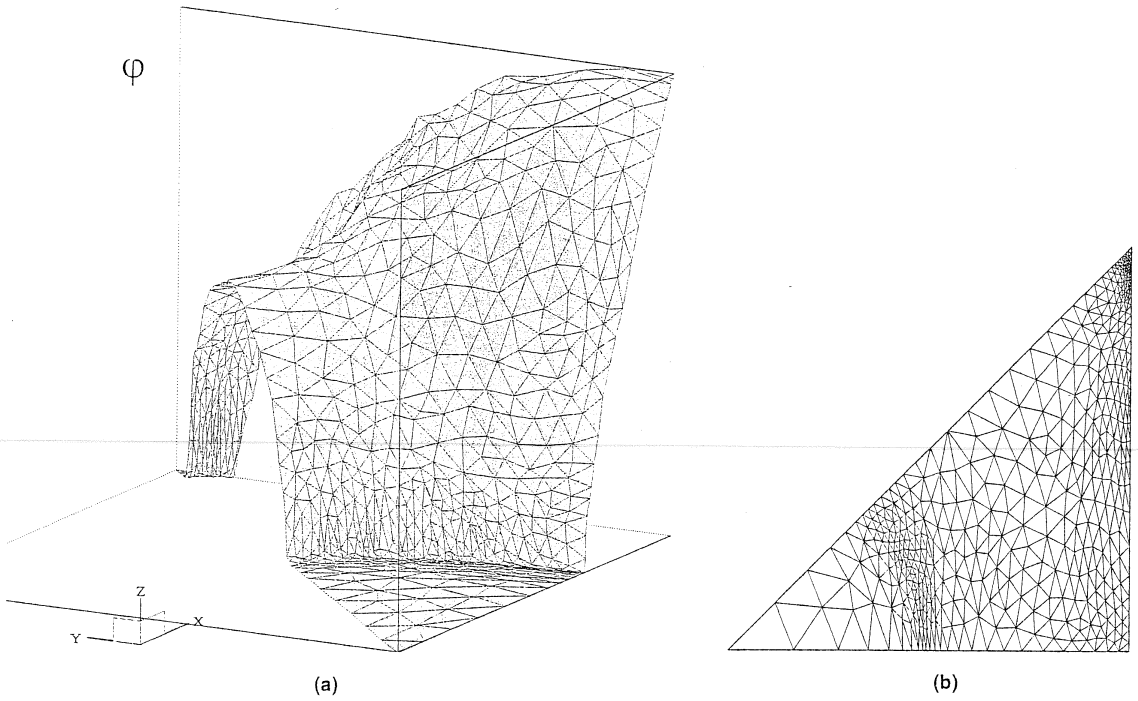

Fig. 9. (a) Elevation view of the governing field φ and the corresponding anisotropic adaptative mesh; (b) two-dimensional view of the mesh ($Bi = 0.7$, iteration 10).

corresponding anisotropic mesh shows that the mesh adapts to the surface curvature in the three dimensional space. For all computations in Section 4, 10 iterations of the adaptive process have been used.

Fig. 10 shows two successive zooms of the adapted mesh. Observe the different length scales and the anisotropy in the border of the shear zone. The first zoom shows that the mesh is able to catch in detail of the separation line between the rigid and shear zones, corresponding to $|\sigma| = \sigma_0$. The second zoom shows also that triangles becomes flat in the direction normal to the separation line, since the adaptation is anisotropic. The shortest edge of the mesh is about 10^3 times smaller than the longest one.

4. Results on a square cross-section

4.1. Yield surfaces and velocity field

Fig. 11(a)–(c) show adapted meshes and the corresponding solutions for different Bingham numbers, namely $Bi = 0.5$, 0.9 and 1.05. Dark lines indicate the velocity contours. Let us observe the shear zone ($|\sigma|/\Sigma \geqslant Bi$), in grey, and the two rigid zones, in white ($|\sigma|/\Sigma < Bi$). The first rigid zone is a dead region, close to the outer corner. The second rigid zone, at the center of the flow, is an inner plug, that translates with a constant velocity in the (O_z) direction.

Let us now consider the dead region and its evolution with Bingham number. The dead region always presents a concavity turned towards the inside of the section, as pointed out in the Section 1. Note that the plug region, associated with a rigid translation movement, and the dead region, associated with zero velocity, are always separated by the shear zone, where the velocity varies gradually. Taylor and Wilson [6, Fig. 2(d), p. 98], proposed a flow with four shear zones reduced to small regions near the middle of the walls, while dead and plug regions become connected. Using the regularized model due to Papanastasiou

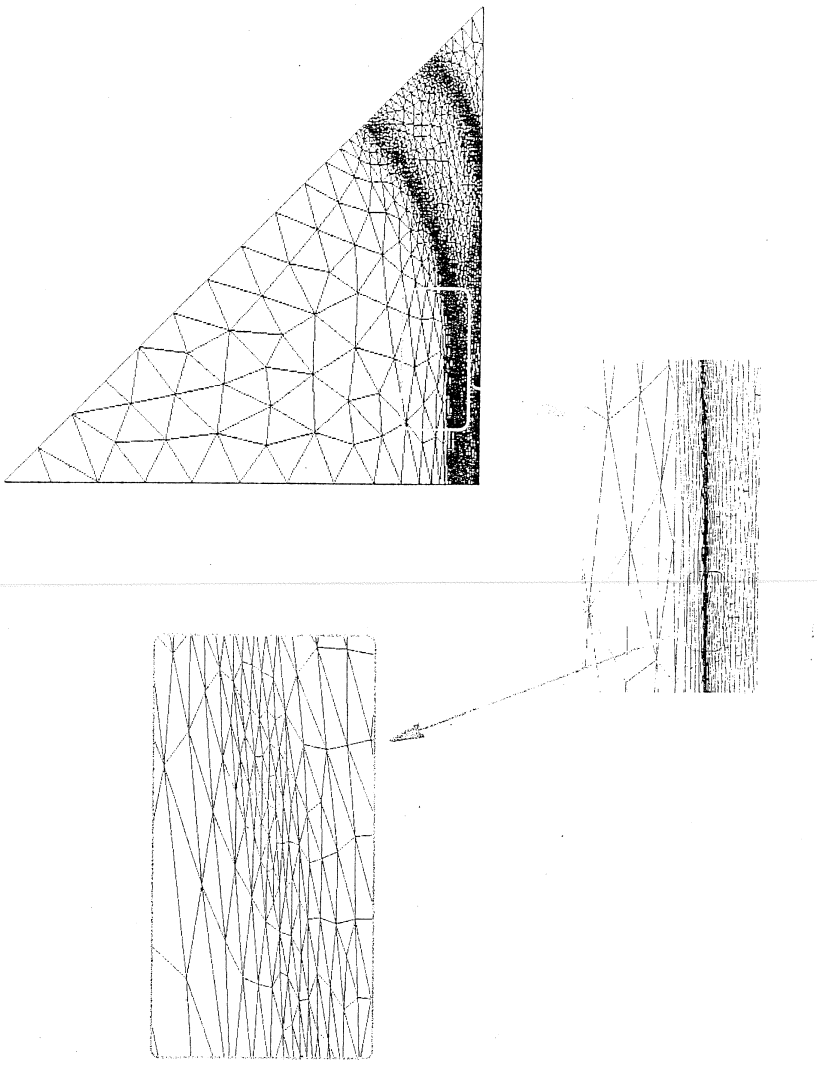

Fig. 10. Several length scales for an adapted mesh ($Bi = 1$, iteration 10).

[5], Burgos and Alexandrou [30] obtained also connected plug and dead regions (Fig. 8(d), line 1, p. 494 and Fig. 9(d), line 1, p. 495). and exhibited dead regions with inverted concavity (Fig. 8(d), line 2, p. 494). Theoretical studies showed for all $Bi > 0$ that:

1. the existence and uniqueness of the plug zone (showed by Mosolov and Mjasnikov [1]);
2. the existence of dead zones with concavity as found in the present paper (showed in 1966 by Mosolov and Mjasnikov [2]).

Our results are consistent with these properties. In particular, plug and dead zones cannot be connected before the fluid comes to a full stop. Wang [7] showed that these unexpected phenomena are due to a lack of precision in the numerical computations proposed by Taylor and Wilson [6], namely a too high value of the regularization parameter.

The inner plug is circle-like when small enough. As it grows, the inner plug gets flat due to its facing the wall. The shear zone near the middle of the wall is thinner than the one along the diagonal, but it also decreases slowly, so that the shear zone finally vanishes everywhere for the same critical Bingham number. This phenomena will be studied in detail in the following section.

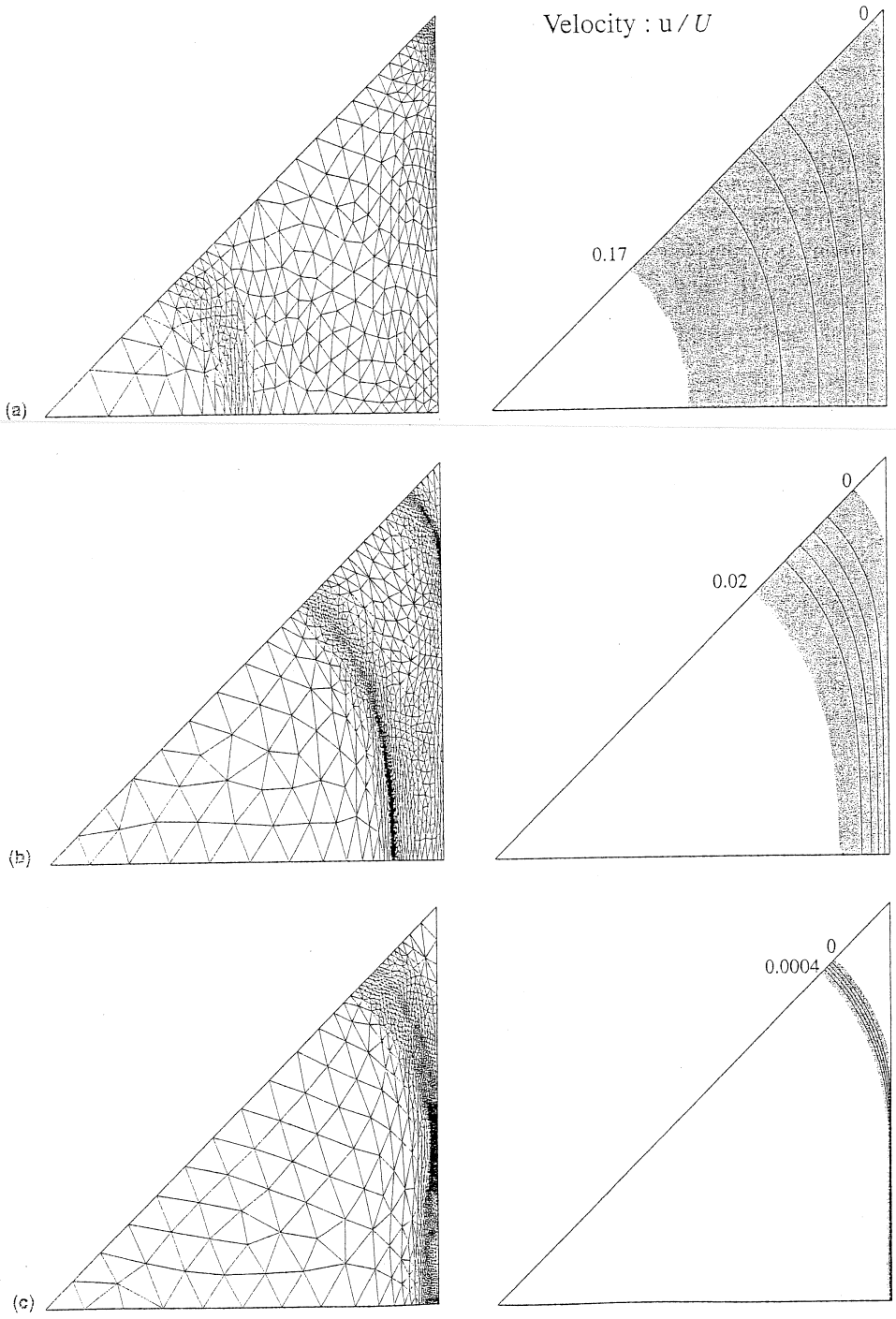

Fig. 11. Evolution versus Bi of velocity contours and shear (in gray) and rigid (in white). (a) $Bi = 0.5$; (b) $Bi = 0.9$; (c) $Bi = 1.05$.

The entire evolution of shear and rigid zones is described here. The fluid comes to a full stop for a Bingham number slightly greater than 1.05. For $Bi = 1.05$ (see Fig. 11(c)), an almost totally yielded cross-section appears, with only a thin shear zone. The maximum velocity, i.e velocity of the inner plug, is in this

case roughly 10^3 times smaller than the corresponding one in the Newtonian case, which is associated with a wide area of the flow.

4.2. Velocity and stress profiles

Fig. 12(a)–(d) represent the velocity u and the yield criteria $|\sigma|/\Sigma - Bi$ profiles along the median line $x = 0$ and the diagonal line $x = y$. A curvilinear abscissa $s = \sqrt{x^2 + y^2}$ is used along the diagonal, varying from zero at the center to $\sqrt{2}L$ at the outer corner. For each cut, the evolution for several Bingham numbers, ranging from the Newtonian case ($Bi = 0$) to the full stop case is represented. Fig. 12(a) shows the growth of the inner plug region for non-zero Bingham numbers. This corresponds to the plateau that grows in size and decreases in intensity while Bi increases. The Newtonian case $Bi = 0$ is associated with a gradually varied flow. The diagonal cut of the velocity is represented on Fig. 12(b). One can observe also

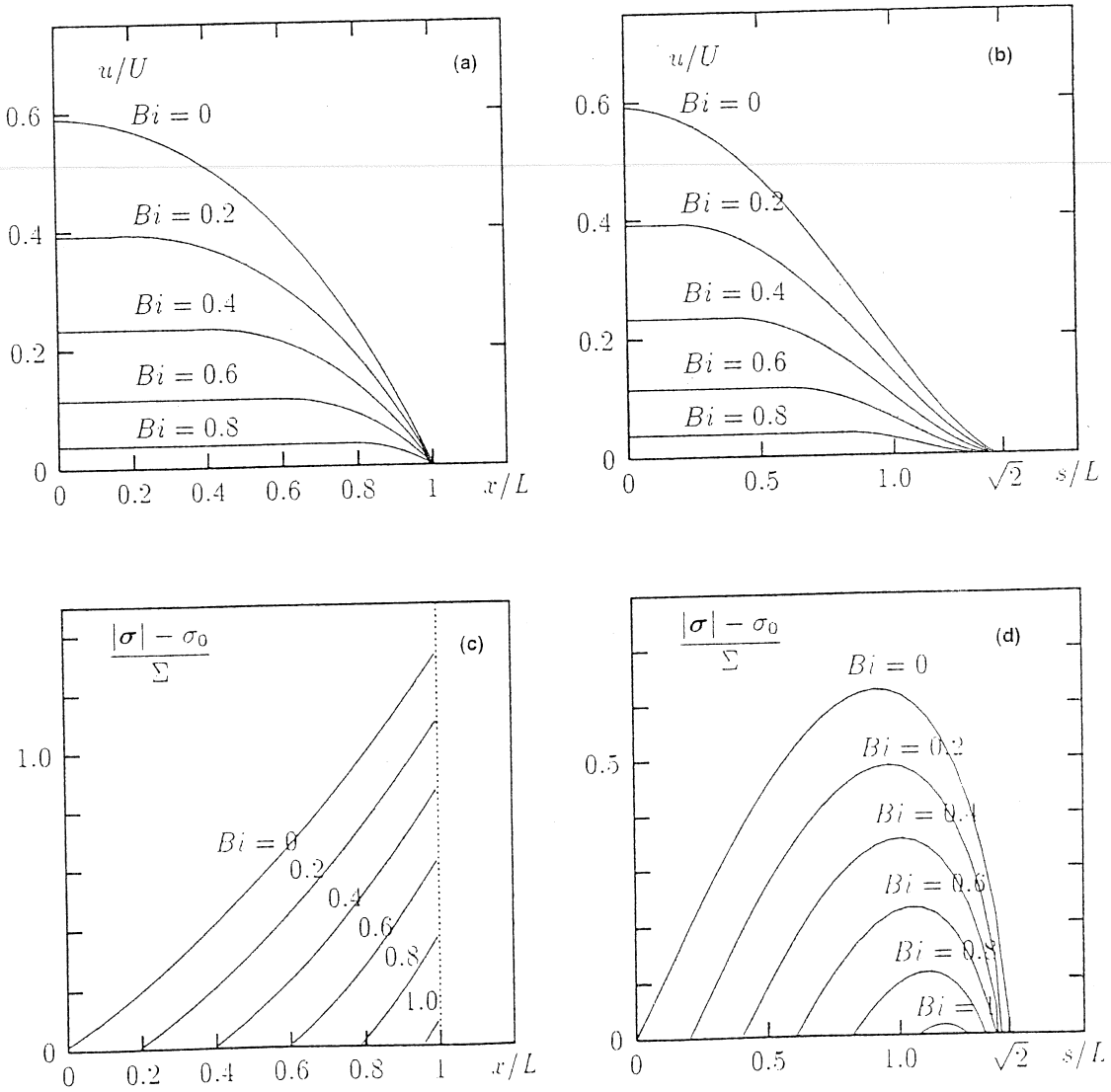

Fig. 12. Velocity profiles: (a) along the median; (b) along the diagonal; yield criteria profiles; (c) along the median; (d) along the diagonal.

the plug, represented as a plateau, and the formation of the dead region, which corresponds to curves approaching gradually the zero velocity axis as Bi increases.

Fig. 12(c)–(d) show the yield criteria. Only the positive parts of this quantity are represented, corresponding to shear zones.

In the median cut (Fig. 12(c)), one can see that the shear zone gets closer to the wall, as Bi increases. Note that the maximum value of the yield criterion over the whole section Ω is reached at the wall, i.e. along the median cut. Then, until this maximum gets to zero, there still exists a shear zone, at least at the middle of the wall, at $x = 1$. When this maximum reaches the zero value, the plug flow touches the wall, and the fluid stops.

On the diagonal cut (Fig. 12(d)), observe that the shear zone decrease, related to the expansion of both the inner plug region and the dead region. The local maximum along the diagonal cut also decreases. When this maximum reaches zero, there is no more separation between the two types of rigid zones: the plug and the dead region come into contact and the fluid stops.

4.3. Limit load analysis

The evolution described in the previous section shows that the fluid comes to a full stop for a critical Bingham number, namely Bi_c. For values of the Bingham number greater than Bi_c, the flow is totally stopped, whereas for values smaller than Bi_c it can be described by our results. When Bi increases and approaches Bi_c, the shear zone reduces to a surface, referred as the *limit yield surface*. In this section, we are interested in determining Bi_c and plotting the limit yield surface. This is done using extrapolations from data computed for several Bingham numbers, from $Bi = 0$ to $Bi = 1.05$, which is the current limit in solving the problem.

Let s_{plug} (resp. s_{dead}), as on Fig. 13(a), be the distance along the diagonal from the center of the section to the plug region border (resp. to the dead region border). Fig. 13(b) shows s_{plug} and s_{dead} as a function of the Bingham number. These distances computed numerically are interpolated by third-degree polynomials, where the coefficients are provided by a non-linear least squares fitting procedure. The intersection of the two third-order polynomial curves can also be computed, and occurs for $Bi = Bi_c \approx 1.07$ and $s_{plug} = s_{dead} \approx 1.22$ on Fig. 13(b).

By using variational methods, Mosolov and Mjasnikov [1] showed that: $Bi_c = 4/(2+\sqrt{\pi}) \approx 1.0603178\ldots$; this exact value confirms, to our point of view, the accuracy of our numerical computations.

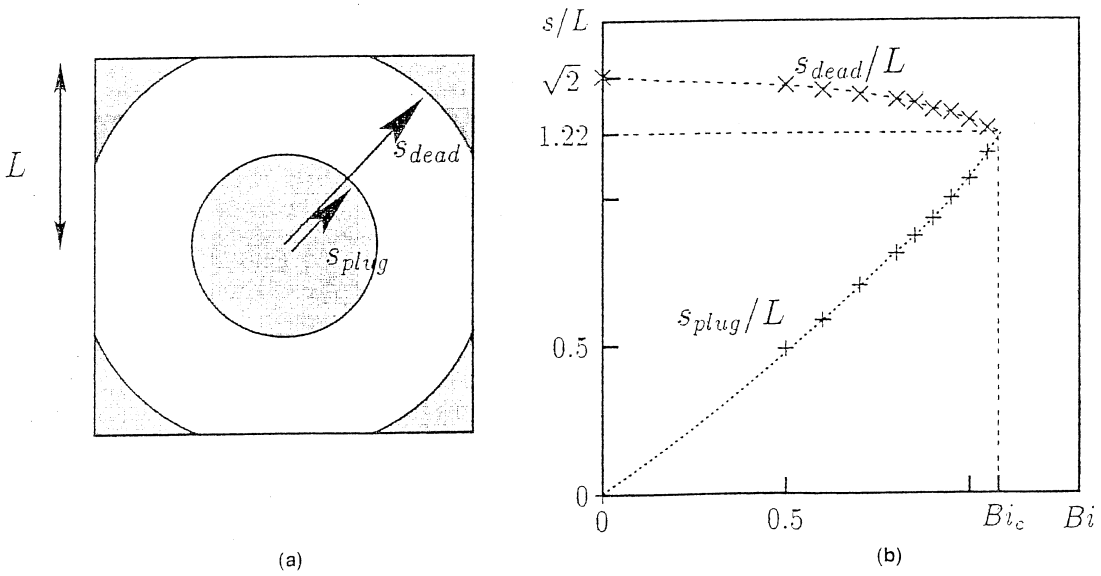

Fig. 13. Intersection of the yield surface with the diagonal: (a) schematics and notations; (b) computations and extrapolation.

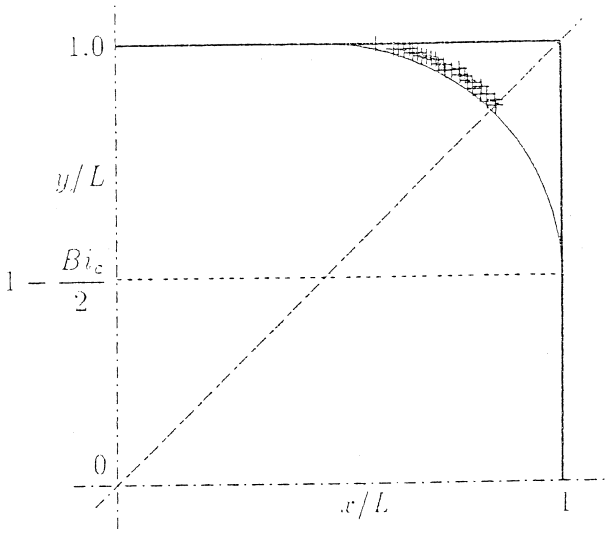

Fig. 14. The limit yield surfaces.

Taylor and Wilson [6], by using a regularized model, predicted a critical Bi_c value of 1.12. Note that these authors used another dimensionless number: $\lambda = Bi/4$ and obtained $\lambda_{crit} = 0.28$.

The previous extrapolation procedure along the diagonal is extended to other cutting directions, as shown in Fig. 14. Each cutting direction furnishes a point of the limit yield surface in the square cross-section. In Appendix A, we show that the limit yield surface is an arc of circle tangent to the wall. The radius r_c and the center (x_c, y_c) of the arc describing the limit yield surface express:

$$r_c = \frac{Bi_c}{2} \approx 0.53015890,$$

$$x_c = y_c = 1 - \frac{Bi_c}{2} \approx 0.46984110.$$

The exact yield surface is drawn in solid lines on Fig. 14, while the numerical extrapolations are represented by the + symbol. We observe that the extrapolation procedure slightly overestimates the exact coordinates. We point out that the extrapolation procedure developed here applies systematically to an arbitrary shape section while the exact yield surface can be easily explicitly expressed only for some particular section geometries (such as circle, square and rectangles).

4.4. Hydraulic analogy

This subsection aims at bringing out simple laws for use in practical designs. A classical engineering problem is to get the flow-rate as a function of the pressure drop in the pipe, given the fluid properties and the duct geometry. This result can easily be expressed by an explicit equation for a viscoplastic fluid of Bingham type, when the pipe is of a circular cross-section. Results for both circular and square pipes are compared by using the fraction $Bi/Bi_c \in [0, 1]$. This has been done for the mean velocity u_{mean}, and for the the maximum velocity u_{max}, which is the velocity of the inner plug region:

$$\frac{2\eta}{L^2 f} u_{mean}(Bi) = \frac{C_{mean}}{4}\left(1 - \frac{4}{3}\frac{Bi}{Bi_c} + \frac{1}{3}\left(\frac{Bi}{Bi_c}\right)^4\right), \tag{12}$$

$$\frac{2\eta}{L^2 f} u_{max}(Bi) = \frac{C_{max}}{2}\left(1 - \frac{Bi}{Bi_c}\right)^2, \tag{13}$$

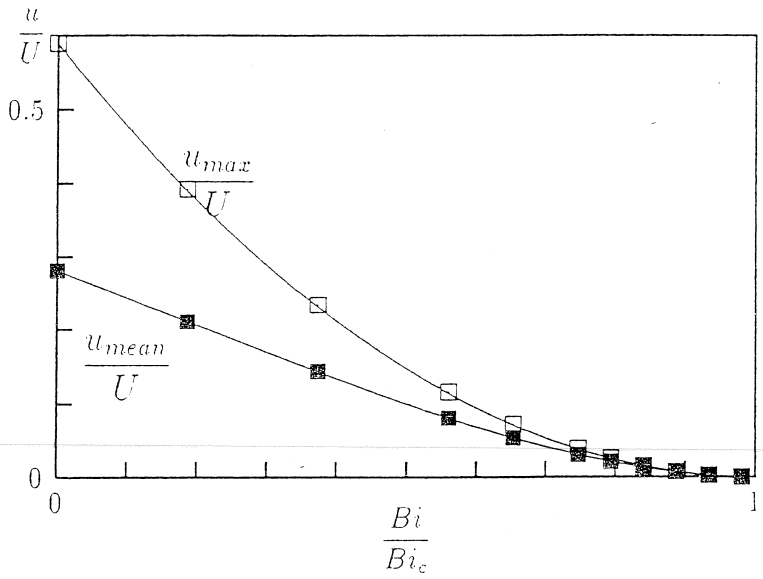

Fig. 15. Mean and maximal velocities.

where Bi is expressed by (4). The above expressions are exact for a circular section with $Bi_c = 1$ and $C_{max} = C_{mean} = 1$. In the case of a square section, Bi_c is known from the previous subsection. Moreover, C_{mean} and C_{max} can also be computed since the Newtonian solution $u(x,y)$, associated with $Bi = 0$, can be expressed using a Fourier expansions. The computation of these constants is reported in Appendix B. Fig. 15 compares u_{mean} and u_{max} as obtained by direct numerical computations in a square cross-section, and by using (12) and (13). Recall that relations (12) and (13) are not a priori exact in the case of a square cross-section. Nevertheless, the maximum of the relative error is of about 10^{-3} and cannot be seen on the plot. These relations are of practical interest for most engineering problems.

The pressure drop in a pipe of length $\mathscr{L}$ is given by $\delta p = f \times \mathscr{L}$ (see also Fig. 1(a)) and is usually compared with the kinetic energy $\rho u_{mean}^2/2$ by introducing the hydraulic coefficient Λ:

$$\delta p = \Lambda \frac{\mathscr{L}}{D_H} \frac{\rho u_{mean}^2}{2},$$

where D_H is the hydraulic diameter, defined to be four times the ratio of the section to the wetted perimeter, i.e. $D_H = 2R$ for the circular section and $D_H = 2L$ for the square section. By introducing the Reynolds number $Re = \rho u_{mean} D_H/\eta$ and using the previous expression of u_{mean}, we get:

$$\Lambda = \frac{64}{C_{mean} Re} \times \frac{1}{1 - \frac{4}{3}\frac{Bi}{Bi_c} + \frac{1}{3}\left(\frac{Bi}{Bi_c}\right)^4}.$$

5. Conclusion

The objective of this work is to examine the development of macroscopic features, such as flow curves and rigid zone enhancements, for the fully developed flow of a yield stress fluid in a square pipe. Our numerical resolution of the Bingham model leads to results that are qualitatively and quantitatively in good agreement with previous theoretical and numerical studies. An important result is the precision of the yield surface prediction, especially when the fluid comes close to the full stop. In that case, an extrapolation procedure leads to the limit yield surface at the full stop. Moreover, a scaling procedure extends the flow curve of a circular pipe to the case of the square pipe, interpreted as an approximate law.

The results of the present paper fully validate, to our opinion, the robustness and the accuracy of our numerical strategy. Validated on a circular cross-section and applied to a square cross-section, this approach could be applied to a tube section of any shape. Our approach combines a high order mixed finite element approximation, an anisotropic auto-adaptive mesh procedure, and the augmented Lagrangian method. The adaptive strategy allows accurate capture of the yield surfaces. This approach also eliminates the regularized parameter introduced frequently in numerical computations, and associated with a loss of accuracy.

Solving viscoplastic fluid flows in a square pipe is not only of interest as an appropriate test problem for developing the fluid mechanics of yield stress fluids, but it is also of practical interest and great importance in food and petroleum industries. In most of these cases, optimization tends to eliminate dead regions by modifying the pipe section geometry. In addition, the numerical methods used for solving this problem is of interest for various fluid and solid mechanics problems involving variational inequalities.

Appendix A. Computation of the limit yield surface and Bi_c

Mosolov and Mjasnikov [1] gave a geometric mean for the computation of Bi_c:

$$\frac{Bi_c}{2} = \sup_{\omega \subset \Omega} \frac{\mathrm{mes}(\omega)}{\mathrm{mes}(\partial\omega)}$$

they claim in [1, Lemma 2.3, p. 250], that there exists $\omega_c \subset \Omega$ such that the supremum in the previous relation is achieved. Moreover, every such ω_c satisfies the following property (Lemma 2.3, proof pp. 269–270):

> If $P \in \partial\omega_c \setminus \partial\Omega$, then the connected part of $\partial\omega_c \setminus \partial\Omega$ containing P is an arc of circle touching the wall $\partial\Omega$ and tangent to $\partial\Omega$ at the touching points.

In addition, such ω_c can be taken as the limit plug region A_c. This is obtained thanks to the Theorem 2, in [31, p. 611], that claims, in particular:

$$\frac{Bi_c}{2} = \frac{\mathrm{mes}(A_c)}{\mathrm{mes}(\partial A_c)}.$$

Hence, in the present case of a square Ω, it is established that the limit yield surface is an arc of circle tangent to $\partial\Omega$. More precisely, let us consider the subdomain $\omega(r) \subset \Omega$, obtained by replacing the corners of the square by arcs of circle of radius r and center $(1-r, 1-r)$, as shown in gray, Fig. 16. Let

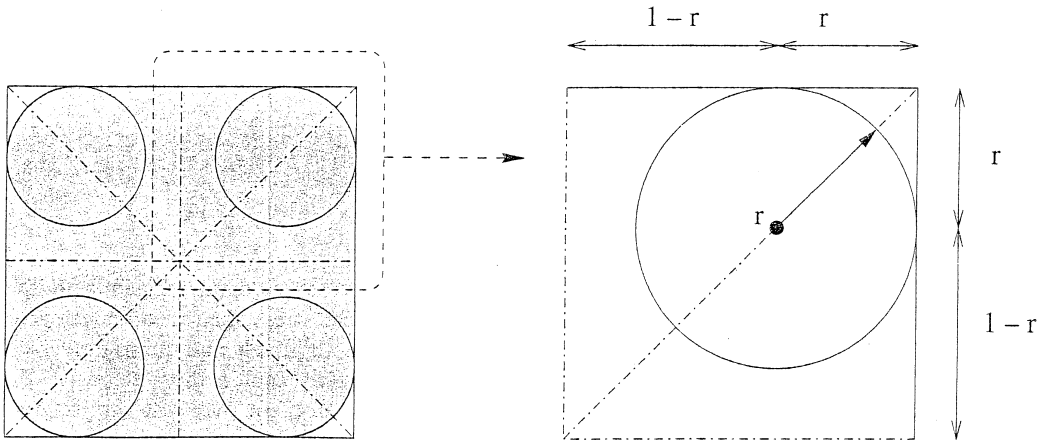

Fig. 16. Computation of Bi_c and the limit yield surface.

$$\Phi(r) = \frac{\mathrm{mes}(\omega(r))}{\mathrm{mes}(\partial\omega(r))} = \frac{(\pi-4)r^2+4}{2(\pi-4)r+8}, \quad 0 < r < 1.$$

The limit plug region A_c is an $\omega(r)$ that achieves the supremum of Φ. In particular, A_c is an $\omega(r)$ that maximize Φ. In other words, there exists $r_c \in]0,1[$ such that $A_c = \omega(r_c)$ and

$$\frac{Bi_c}{2} = \sup_{r\in]0.1[} \Phi(r) = \Phi(r_c).$$

Finally, a straightforward computation shows that

$$\frac{Bi_c}{2} = \frac{2}{2+\sqrt{\pi}} \text{ and } r_c = \frac{Bi_c}{2}.$$

Appendix B. Expression of C_{mean} and C_{max}

The solution u for $Bi = 0$ satisfies $-\Delta u = 2$ in $\Omega = [-1,1]^2$ and $u = 0$ on $\partial\Omega$. Fourier expansion leads to:

$$u(x,y) = 1 - y^2 - 4\sum_{k=0}^{\infty} \frac{(-1)^k \cosh(a_k x)\cos(a_k y)}{a_k^3 \cosh(a_k)}$$

where $a_k = (2k+1)\pi/2$. Thus, we get:

$$C_{\mathrm{mean}} = \frac{8}{3} - 16\sum_{k=0}^{\infty} \frac{\tanh(a_k)}{a_k^5} = 1.12461611964122972470774985\ldots,$$

$$C_{\mathrm{max}} = 2 - 8\sum_{k=0}^{\infty} \frac{(-1)^k}{a_k^3 \cosh(a_k)} = 1.17874165250422104902304040\ldots$$

References

[1] P.P. Mosolov, V.P. Mjasnikov, Variational methods in the theory of the fluidity of a viscous-plastic medium, PMM, J. Appl. Math. Mech. 29 (1965) 545–577.

[2] P.P. Mosolov, V.P. Mjasnikov, On stagnant flow regions of a viscous-plastic medium in pipes, PMM, J. Mech. Appl. Math. 30 (1966) 841–854.

[3] M. Bercovier, M. Engelman, A finite element method for incompressible non-newtonian flows, J. Comput. Phys. 36 (1980) 313–326.

[4] E.J. O'Donovan, R.I. Tanner, Numerical study of the Bingham squeeze film problem, J. Non-Newtonian Fluids Mech. 15 (1984) 75–83.

[5] T.C. Papanastasiou, Flow of materials with yield, J. Rheol. 31 (1987) 385–404.

[6] A.J. Taylor, D.R. Wilson, Conduit flow of an incompressible, yield-stress fluid, J. Rheol. 41 (1997) 93–101.

[7] Y. Wang, Comment on Conduit flow of an incompressible, yield-stress fluid, J. Rheol. 41 (1997) 93–101, 1387–1391.

[8] M. Fortin, Calcul numérique des écoulements des fluides de Bingham et des fluides newtoniens incompressibles par la méthode des éléments finis. thèse, Paris VI, 1972.

[9] M. Fortin, R. Glowinski, Méthodes de lagrangien augmenté. Applications à la résolution numérique de problèmes aux limites, Méthodes Mathématiques de l'Informatique, Dunod, 1982.

[10] R. Glowinski, P. Le-Tallec, Augmented Lagrangian and operator-splitting methods in nonlinear mechanics, Stud. Appl. Math., Soc. Ind. Appl. Math., 1989.

[11] R.R. Huilgol, M.P. Panizza, On the determination of the plug flow region in Bingham fluids through the application of variational inequalities, J. Non-Newtonian Fluid Mech. 58 (1995) 207–217.

[12] Y. Wang, Finite element analysis of the duct flow of Bingham plastic fluids: an application of the variational inequality, Int. J. Numer. Methods Fluids 25 (1997) 1025–1042.

[13] M.G. Vallet, Génération de maillages anisotropes adaptés. Application à la capture de couches limites, Rapport de Recherche no 1360, INRIA, 1990.

[14] H. Borouchaki, P.L. George, F. Hecht, P. Laug, E. Saltel, Delaunay mesh generation governed by metric specifications. Part I: Algorithms, Finite Elem. Anal. Des. 25 (1997) 61–83.

[15] M.J. Castro-Diaz, F. Hecht, B. Mohammadi, O. Pironneau, Anisotropic unstructured mesh adaption for flow simulations, Int. J. Numer. Methods Fluids 25 (1997) 475–491.
[16] E.C. Bingham, Fluidity and Plasticity, Mc Graw-Hill, New-York, 1922.
[17] J.G. Oldroyd. A rational formulation of the equations of plastic flow for a Bingham solid, Proc. Cambridge Philos. Soc. 43 (1947) 100–105.
[18] R.A. Adams, Sobolev Spaces, Academic Press, New York, 1975.
[19] R. Glowinski, J.L. Lions, R. Trémolières, Numerical Analysis of Variational Inequalities, North Holland, Amsterdam, 1981.
[20] I.R. Ionescu, M. Sofonea, Functional and Numerical Methods in Viscoplasticity, Oxford University Press, Oxford, 1993.
[21] F. Brezzi, M. Fortin, Mixed and Hybrid Finite Element Methods, Springer, Berlin, 1991.
[22] F. Brezzi, M. Fortin, R. Stenberg, Error analysis of mixed-interpolated elements for Reissner-Mindlin plates, Research Repport no 780, Instituto di Analisi Numerica, Pavie, 1991.
[23] P. Saramito, Numerical simulation of viscoelastic fluid flows using incompressible finite element method and a θ-method, Math. Model. Numer. Anal. 28 (1994) 1–35.
[24] P. Saramito, Efficient simulation of nonlinear viscoelastic fluid flows, J. Non-Newtonian Fluid Mech. 60 (1995) 199–223.
[25] R. Glowinski, Numerical Methods for Nonlinear Variational Problems, Springer, Berlin, 1984.
[26] R.S. Falk, B. Mercier, Error estimates for elastoplastic problems, RAIRO, série Analyse Numérique 11 (1977) 135–144.
[27] N. Roquet, R. Michel, P. Saramito, Errors estimate for a viscoplastic fluid by using P_k finite elements and adaptive meshes, C. R. Acad. Sci. Paris Sér. I 331 (7) (2000) 563–568.
[28] F. Hecht, Bidimensional anisotropic mesh generator, INRIA, 1997.
[29] G.A. Seregin, Continuity for the strain velocity tensor in two-dimensional variational problems from the theory of the Bingham fluid. Preprint 402, SFB 256 Universität Bonn, 1995.
[30] G.L. Burgos, A.N. Alexandrou, Flow development of Herschel–Bulkley fluids in a sudden three-dimensional square expansion, J. Rheol. 43 (1999) 485–498.
[31] P.P. Mosolov, V.P. Mjasnikov, On qualitative singularities of the flow of a viscous-plastic medium in pipes, J. Mech. Appl. Math. (P.M.M.) 31 (1967) 609–613.